Department of Meteorology

University of Maryland
College Park, MD 20742

Multidisciplinary Research Program in Atmospheric Science

NSG 5209

Final Report

to

National Aeronautics and Space Administration

Owen E. Thompson

April 1982

division of mathematical & physical sciences & engineering

TABLE OF CONTENTS

I. Introduction

This document represents the final technical report of research sponsored under NASA Grant NSG 5209, Multidisciplinary Research Program in Atmospheric Science. The present document consists of ten individual research reports involving studies of satellite and radar based indirect sensing of the atmosphere; aspects of atmospheric radiative transfer through cloudy atmospheres; and numerical modeling of large scale atmospheric flow. Combined with a previous report*, there are, thus, twenty-two extensive reviews of research conducted during the period of this grant.

In addition to the individual research projects, the grant has sponsored joint NASA-U. Maryland Summer Research Colloquia in atmospheric science each summer since 1977, and a special working seminar on atmospheric blocking during the past 15 months. The grant has also supported developmental research involving remote computer graphics capabilities. This has led to system software development which will support graphics on three separate types of plotting equipment for the dozen or so remote university user groups of the NASA-Goddard Modelling and Simulation Facility.

*Multidisciplinary Research Program in Atmospheric Science-A Quasi-Biennial Report. Department of Meteorology, University Maryland, College Park, MD. April, 1980. (O. E. Thompson, Principal Investigator.)

II. HIRS-AMTS Satellite Sounding System Test-Theoretical Vertical Resolving Power

by

Owen E. Thompson

ABSTRACT

A theoretical analysis of the vertical resolving power of the High resolution Infra-red Radiation Sounder (HIRS) and the Advanced Meteorological Temperature Sounder (AMTS) is carried out. First, the infra-red transmittance weighting functions, and associated radiative transfer kernels, are analyzed through singular value decomposition. The AMTS is found to contain several more pieces of independent information than HIRS when the transmittances are considered, but the two instruments appear to be much more similar when the temperature sensitive radiative transfer kernels are analyzed.

The HIRS and AMTS instruments are also subjected to a thorough analysis using the theoretical methods of Backus and Gilbert. From this analysis, it is found that the two instruments should have very similar vertical resolving power below 500mb but that AMTS should have superior resolving power above 200mb. In the layer 200-500mb, the AMTS shows badly degraded spread function which may or may not be a realistic assessment of vertical resolving power there.

1. Introduction

This paper concerns the vertical resolving power of satellite borne temperature sounding instruments. Specifically, we wish to present information on the capabilities of the High Resolution Infra-red Radiation Sounder (HIRS) and a proposed sounding instrument called the Advanced Moisture and Temperature Sounder (AMTS) designed following the work of Kaplan, Chahine, Susskind and Searle (1977). In this paper and the one which follows, we discuss two quite different methods for assessing the vertical resolving power of satellite sounders. The first is the theoretical method of Conrath (1972) which was patterned after the work of Backus and Gilbert (1968). In this method, vertical resolving power is defined in terms of certain properties of the transmittance weighting functions corresponding to the sounding channels of the satellite radiometric device. Resolving power defined in this theoretical approach deals with the characteristic thickness of averaging kernels which relate a temperature estimate, at a given atmospheric level, to the distribution of temperature throughout height as it exists to produce the radiation measurements. The relation between the two is an integral relation deriving from the atmospheric radiative transfer equation with a presumed linear dependence between estimated temperature and measured radiance. The Backus-Gilbert-Conrath (BGC) approach includes a formalism for deriving a retrieval algorithm for optimizing the vertical resolving power. However, a retrieval algorithm constructed in the BGC optimal fashion may not necessarily be optimal as far as actual temperature retrievals are concerned. This is due to the fact that integral averaging kernels which have minimum thickness may also have undesirably large side-lobes which degrade the overall retrieval of a profile of temperature.

For the reasons introduced above, we have developed an independent criterion for vertical resolving power which is based on actual retrievals of signal structure in the temperature field. (See the following paper by the present author.) The criterion is patterned after that introduced by Lord Rayleigh for testing the resolving power of optical instruments. Specifically, in the paper which follows, we define the vertical resolving length of a satellite based temperature sounding system as the minimum separation of two distinct signals in the "field of view" (that is, along the vertical profile) which can just be resolved as distinct signals by the observing system.

In what is to follow in this paper, we present an analysis of the vertical resolving power of the HIRS and AMTS instruments using the theoretical criteria developed by Backus and Gilbert and Conrath. The two studies taken together will provide a comparison of theoretical and empirical results concerning vertical resolution of satellite temperature sounders. It will also yield a fairly consistent comparison of the vertical resolution of HIRS and AMTS instruments, but will also reveal some important discrepancies in the two methods of analysis. Since vertical resolving power is expected to be a strong function of instrument noise characteristics, we will carry out our analysis for the most representative estimates of instrument noise available for these very high technology instruments.

2. The concept of vertical resolving power

It is worth a few paragraphs to discuss the general concept of vertical resolving power of a satellite temperature sounding system. Even for radiosonde measurements of the temperature profile, it is not immediately clear what the vertical resolving power actually is. For a sensor of low thermal inertia (quick response to temperature change) the resolving power should be closely related to the "least count" of the system; that is, the vertical spacing between successive measurements. If the sensor has large thermal inertia so that its response time exceeds the time to ascend to the next measurement level, the resolving length would exceed the least count. If the sensor or its attendant electronic package were noisy, then the true resolving length becomes a statistical function of the instrument noise as well. Further, if the telemetering system is not perfect, then even the least count distance is imperfectly known and the true resolving length also depends on the errors in the telemetering system.

In a satellite temperature sounding system, the situation is even more complex. The integral nature of the radiative transfer physics of the atmosphere assures that true temperature signals are grossly smoothed into bulk radiation measurements. (See, for example, Thompson, Eom and Wagenhofer (1976).) While narrowing the spectral bandwidth of the radiometric instrument will sharpen the transmittance weighting functions, one can never design an instrument with a true Dirac delta-function relationship to the temperature profile. Thus, the integral smoothing is always real and significant and vertical resolution will always suffer because of it. The integral nature of atmospheric radiative transfer also makes the least count of the system (in this case, the spacing between adjacently positioned

transmittance weighting functions) a poor measure, in and of itself, of vertical resolving power. We need only compare N channels of the NIMBUS III SIRS instrument with N similarly positioned channels of the HIRS or AMTS instruments to appreciate this fact. The channels of the SIRS instrument so overlapped that it could not resolve vertical structure as well as a similar number of channels of the current HIRS instrumentation. Thus, the width of the transmittance weighting functions as well as the least count, or number of separately located channels, affect the vertical resolving power of the system.

Noise in a satellite borne sounding instrument will also degrade its vertical temperature resolving power just as it would in a radiosonde system. Such instrument noise is factored explicitly into the Backus-Gilbert-Conrath resolving power analysis where there is a trade-off between the characteristic width of integral averaging kernels and the sensitivity of a retrieval to instrument noise.

A very important aspect of vertical resolving power is the algorithm for transforming satellite radiometer measurements into temperature profile estimates. Unlike an <u>in situ</u> direct measuring system, such as the radiosonde, where the sensor signal is directly related to the temperature, the satellite radiation measurement is indirectly and integrally related to the vertical distribution of temperature and must be unraveled by some sort of inverse solution to the integral relationship. The solution is not unique and there are many possible temperature estimation algorithms, each performing some sort of complex transformation of radiance into temperature. The importance of this step is dramatized by the fact that one can construct an algorithm which transforms all radiometric measurements of a satellite sounding instrument into a coarse vertical mean value of temperature. In such a case, the resolving length is the entire depth of the atmosphere. (For example, the inverse solution given by Conrath (1972) for the case q=0 does essentially this.) In such an example, what inherent resolving power there may have been in the satellite radiometer measurements has been deadened by the temperature retrieval algorithm. The minimum information solution of Smith, Woolf and Fleming (1972) can be tuned to merely reproduce the first guess field itself, thereby completely nulling the resolving power of the radiometer measurement. To one extent or another, all temperature retrieval algorithms will modify what may be considered an inherent resolving capability of a satellite sounding instrument.

It is for the above reasons that we consider the satellite temperature sounding problem to involve two separate components of a sounding "system". The first is the intrument with its inherent characteristics of spectral bandpass, least count, signal sensitivity, noise, etc. The second is the mathematical algorithm used to map the measured radiances into estimates of the temperature profile, with its intrinsic smoothing and mathematical stability characteristics.

There is one final aspect of the issue of vertical resolving power which is important. That is, the vertical resolution of à priori data used in the sounding. Rodgers (1976) has spoken to this point by showing that à priori data increases the overall vertical resolution of temperature profiles derived from satellite measurements. In an even simpler example, the minimum information method, tuned as discussed above, yields a vertical resolution for the system which is just the vertical resolution of the à priori data. In practice, it is upon this initial vertical resolution that the sounding system may improve, or degrade. Even such gross information as correct tropopause level can make substantial improvements to retrieval accuracy (Thompson and Wolski (1977), Westwater and Grody (1981)). In our studies, the issue of the resolution of à priori data is specifically and carefully removed from our analysis so that we may address only the question of the latent characteristics of the instrument and a retrieval algorithm, which incorporates only a gross a priori depiction of the vertical structure of the atmosphere.

3. Channel characteristics of HIRS and AMTS

Figure 1 shows the transmittance weighting functions, $d\tau(\nu_i)/dx$, for the HIRS and AMTS instruments. These functions were computed for a standard atmospheric temperature profile using transmittance data kindly provided by J. Susskind, NASA/GLAS, and are normalized by their maximum values. We show here 11 selected channels of each instrument in the 4.3μm or 15μm CO2 absorption band. The circled labels indicate 4.3μm channels. These sub-sets of channels were selected so that there are the same number of 4.3μm and 15μm channels in each set and their distribution with height is as uniform as possible. The AMTS channels are generally narrower than the HIRS and there would appear to be more information gathered above 100mb by the AMTS measurement channels. We note the region from about 150mb to 300mb in which each instrument appears to have lower vertical sensitivity.

Figure 2 shows a comparison of the radiative transfer kernels, $\{dB(\nu_i, T(z))/dT^s(z)\}\{d\tau^s(\nu_i)/dz\}$, which have been computed for a standard atmosphere, and normalized. These functions are particularly relevant to the empirical test of vertical resolving power discussed in the companion paper (Thompson, (1981)) where they are used in linearized inverse retrieval algorithms. The temperature dependence of the transformation to radiative transfer kernels causes some significant differences between the functions in Figures 1 and 2. Channels 1-6 of the AMTS are only slightly modified but 7-11 are drastically changed. The levels at which the radiative transfer kernels peak are significantly lower than corresponding levels of the transmittance weighting functions. These latter channels are also sharpened when rendered as radiative transfer kernels. However, the combined effect is to create an information "gap" around 200mb for the AMTS instrument. For the HIRS, channels 1-3 are only slightly modified, channels 4-9, 11 have their peaks significantly lowered and sharpened. Channel 10 completely changes character in the transformation. The main peak is lowered from near the 100mb level to 300mb with only a secondary peak near 100mb where the transmittance weighting function peaks. Also, the radiative transfer kernel for Channel 10 shows sensitivity at very high levels (~1mb) which adds to the information collected in Channel 1 of the HIRS.

The distribution of radiative transfer kernels for the HIRS also shows an information gap around 200mb although Channels 4 and 10 help to supply information in this region. One of the most significant differences in the sets of kernels is that HIRS has 8 channels strongly sensitive below 200mb and 3 or 4 strongly sensitive above. AMTS shows 6 channels sensitive to the higher levels and 5 sensitive below 200mb.

To further analyze the information measured by the two instruments, we performed a singular value decomposition of the weighting functions and radiative transfer kernels of each. Figure 3 shows the cumulative sum of normalized, ranked eigenvalues as a function of index for the HIRS and AMTS. The solid curves refer to characteristics of the transmittance weighting functions while the dashed curves refer to the radiative transfer kernels. The results show that about 99% of the information gathered by a HIRS instrument could be explained by only three or four orthogonal eigenfunctions of the transmittances while six to seven eigenfunctions of the AMTS would be required to explain the same amount of information. This implies that the AMTS instrument should possess more vertical resolving power since the information in the weighting functions is spread over more

orthogonal dimensions of radiance space.

The situation with radiative transfer kernels for the HIRS and AMTS is quite different. The information distribution for the kernels is very nearly the same for each instrument. The AMTS instrument shows perhaps only one more significant eigenfunction than the HIRS when information is rendered in terms of radiative transfer kernels. For each instrument, only about 3 or 4 eigenfunctions are necessary to account for most the information contained in the radiative transfer kernels.

4. Theoretical analysis of vertical resolution

The work of Backus and Gilbert (1968) opened a theoretical approach to the subject of resolving power in inverse geophysical problems. Conrath (1972) adapted the work of Backus and Gilbert specifically to the satellite temperature retrieval problem. In this section, we present an analysis of vertical resolving power following this theoretical approach.

In the notation of Conrath, the measurements of spectral radiation by a satellite radiometric device may be represented by the equation

$$\Delta I_i = \int_{x_0}^{x_T} K_i(y)\, \Delta T(y)\, dy + \epsilon_i \quad ; \quad i=1,2,\ldots,N \qquad (1)$$

where I_i is the measured radiance at each of N frequencies, ν_i, less the surface contribution, which is contaminated by errors ϵ_i, $T(y)$ is the atmospheric temperature at some vertical level y, $K_i(y)$ are the radiative transfer kernels defined earlier for the sounding frequencies ν_i. The (Δ) indicates that differences have been taken between true and background values, (e.g. $\Delta T(y)=T(y)-T^*(y)$; $\Delta I = I_i - I_i^*$). If one considers the class of linear temperature retrieval algorithms, yielding estimates of temperature at levels x, expressible by

$$\widehat{\Delta T}(x) = \sum_{i=1}^{N} a_i(x)\, \Delta I_i \qquad (2)$$

then, the retrieval estimate, $\widehat{\Delta T}(x)$, is integrally related to the ambient profile, $\Delta T(y)$, by

$$\widehat{\Delta T}(x) = \int_{x_0}^{x_T} \sum_{i=1}^{N} a_i(x)\, K_i(y)\, \Delta T(y)\, dy \qquad (3)$$

In (3), the estimate of temperature at each level, x, in

the atmosphere is given by a weighted average of the entire ambient vertical profile, $\Delta T(y)$. The fidelity of this estimate depends on the narrowness of the averaging kernel, or spanning function, $A(x,y) = \sum_i a_i(x)\, K_i(y)$, and the amount of transfer of measurement errors, ϵ_i, into the temperature retrieval. The error transfer also depends on the narrowness of the averaging kernel so that resolution and error transfer are not independent but, rather, play against each other.

The Backus-Gilbert-Conrath (BGC) analysis defines two properties of the sounding system. The characteristic vertical width of the averaging kernel, or "spread", is given by

$$s(x) = 12 \int_{X_0}^{X_T} (x-y)^2 \,(A(x,y))^2 \, dy \qquad (4)$$

The errors of radiance measurement, ϵ_i, in (1) will contaminate the retrieval through (2). The mapping of measurement errors into temperature retrieval space may be expressed as an error variance,

$$\sigma^2(x) = (1/M) \sum_{k=1}^{M} \sum_{i=1}^{N} \sum_{j=1}^{N} a_i(x)\, \epsilon_i^k\, \epsilon_j^k\, a_j(x) \qquad (5)$$

where we imagine that M soundings have been made with ϵ_i^k the measurement error in the i'th radiometric channel during the k'th sounding. In matrix notation, the spread and error variance may be written

$$s(x) = (\tilde{a})^T (\tilde{S})\ (\tilde{a})$$

$$\sigma^2(x) = (\tilde{a})^T (\tilde{E})\ (\tilde{a})$$

where $(\tilde{a})$ is a column vector whose elements are the selected retrieval coefficients $a_i(x)$, and matrices $\tilde{S}(x)$ and $\tilde{E}$ are given by

$$\tilde{S}(x) = (S_{ij}) = 12 \int_{X_0}^{X_T} (x-y)^2\, K_i(y)\, K_j(y)\, dy$$

$$\tilde{E} = (E_{ij}) = (1/M) \sum_{k=1}^{M} \epsilon_i^k\, \epsilon_j^k$$

Therefore, the spread function depends on instrument design ($K_i(y)$) and retrieval coefficients $a_i(x)$ while the noise transfer depends on the retrieval coefficients and the noise

covariance matrix of the radiometric instrument.

For the theoretical analysis of resolving power, we compare the two instruments - the HIRS and AMTS - using appropriate matrices $\tilde{S}(x)$ and $\tilde{E}$ for each.

To proceed with the analysis, we specify the radiative transfer kernels, $K_i(y)$, and noise characteristics, $(\tilde{E})$, for each instrument. Figure 2 shows the radiative transfer kernels $K_i(y)$ for the infra-red sounding channels selected for the HIRS and AMTS test. For the noise characteristics, we specify two noise covariance matrices for the AMTS and three for the HIRS. All are diagonal and the first in each set is what we shall call the 1% set. The noise values are approximately 1% of radiance values emanating from a standard atmosphere. The values are actually rounded so that there is a single characteristic value for the 15μm channels and a single value for the 4.3μm channels. The second set of noise values for each instrument were provided by L. McMillin of NOAA/NESS and represent a more realistic set of noise values based on NOAA/NESS investigations. A third set of noise values are used in the HIRS test which simulate the noise levels of a HIRS instrument assuming its detectors were cooled in a way similar to the proposed AMTS sensors. McMillin(*) has estimated that cooling the HIRS detectors in a manner similar to that specified for the AMTS would reduce the noise values by a factor of approximately 2.5-3.0. We use here a reduction factor of 2.5. Table 1 summarizes the noise characteristics of the simulated instruments tested in this paper and the paper to follow.

Figure 4 shows spread and noise variance as a function of height for the HIRS1 instrument with 1% radiometer noise. Spread is shown here in terms of geometric length rather than a pressure related variable. Graphs are shown for various values of the retrieval parameter q. For comparison, Figure 5 shows corresponding curves for AMTS1. In all cases, varying the retrieval parameter has a larger effect on reducing noise variance than on increasing the spread function. The spread function curve for q=1.000 is a minimum limit on spread function values. The spread function varies from a few kilometers in the troposphere to greater than 15 or 20 kilometers in the stratosphere. At 500mb, the curves indicate that in order to reduce noise variance to a tolerable level -say, less than 1K - the spread function must take on a value roughly twice as large as the

---

(*) Personal communication

theoretically minimum value. (About 5km for q=0.990 rather than 2.5km for q=1.000.)

The 1% AMTS1 instrument shows a better stability of its spread characteristics over the range of solution parameters used. For example, the degradation in spread function which occurs when q is reduced to 0.990 from 1.000 is not startling even though the associated reduction in noise variance is significant. The spread function for AMTS1 is significantly smaller than for HIRS1 at high levels above 100mb but the two instruments show comparable response in the troposphere. The most notable feature of the AMTS1 curves is the apparent degradation of resolving power in the layer 200-400mb which is not exhibited in the HIRS1 channels.

Figures 6 and 7 show similar spread-variance curves for HIRS2 and AMTS2 instruments which incorporate more realistic values of radiometer noise. An important thing to notice is that reducing instrument noise certainly improves the noise transfer characteristics of an instrument but does not lead to order of magnitude improvements in the spread function characteristics. This is particularly true for AMTS2 as compared with AMTS1: the spread function curves, if super-imposed, are clustered very close together. For HIRS2 compared with HIRS1, there is an improvement of 2 to 3km in the spread function between the surface and 100mb for comparable noise variance levels. (E.g. compare HIRS1 with q=0.990 with HIRS2 with q=0.998.) As with HIRS1 and AMTS1, the AMTS2 theoretical spread characteristics are superior to HIRS2 in the stratosphere, comparable to HIRS2 in the lower troposphere but worse than HIRS2 in the layer 200-400mb.

At the suggestion of L. McMillin, NOAA/NESS, we also tested a simulated cooled version of the HIRS instrument wherein radiometer noise levels were reduced by a factor of 2.5 of current noise estimates. The resulting spread and variance curves are shown in Figure 8. Such cooling would produce a modest improvement in the theoretical spread characteristics; about 1-2km in the stratosphere and less than that in the troposphere. By this analysis, the HIRS3 would be more competitive with an AMTS2 in the stratosphere and comparable in the troposphere.

As a convenience to the reader, spread and error variance for the five simulated sounding instruments are compared in Figure 9 for values of the trade-off parameter, q, leading to similar traces of instrument noise transfer.

5. Summary and conclusions

In this paper, we have given a discussion of the concept of vertical resolving power of a satellite temperature sounding system. We have noted that the vertical resolving power should depend on the number, separability, and sharpness of transmittance weighting functions, the noise levels of the instrument channels, the resolution of a priori information used in the retrieval, and, importantly, on the retrieval algorithm used to transform radiance information into temperature information. We suggest two independent methods of assessing vertical resolving power, one of which was carried out in this paper, the other appearing in a companion paper.

In the present study, we have obtained measures of vertical resolving power using the theory of Backus and Gilbert. That is, we have presented distributions of the spread function, corresponding to the Backus-Gilbert integral averaging kernel, and the error variance function representing the transfer of radiometer noise into the temperature retrieval. Such results have been presented for three simulated versions of the HIRS instrument and two simulated versions of the AMTS; the versions differing only in the assumed noise levels of the radiometric channels of the instruments.

In analyzing the transmittance weighting functions of the HIRS and AMTS instruments, we find that the AMTS has one or two more pieces of significant information in its CO2 channels than does HIRS. This conclusion is based on a singular value decomposition of the transmittance weighting functions. However, when the instrument characteristics are rendered in the form of temperature sensitive radiative transfer kernels, we find that the amount of information collected by each instrument is very nearly the same, but with AMTS still showing a slight advantage.

In the spread function analysis, we find that the optimum parametric condition (q=1) leading to averaging kernels with minimum spread generally allows too much noise transfer for both instruments. When the trade-off parameter is set to reduce the noise transfer to tolerable levels, the corresponding spread function increases a significant amount. This tuning degradation is much less severe for the higher precision versions of the sounding instrument where noise levels are extremely small to begin with.

Generally speaking, the theoretical analysis of vertical resolving power indicated that the AMTS instrument should be superior to a HIRS instrument at high levels above 200mb

where the spread function for AMTS is only 50-60% of that for HIRS. The two instruments should be comparable below 500mb having spread function of order 2 or 3 km. In the layer from 200-500mb, the AMTS instrument shows a disturbing surge in spread function not evident in the HIRS instrument. The theory yields a spread function for the AMTS from 5 to 10 km in this layer, but only 4 to 6 km for the HIRS.

Now Newman (1979) and Newman and Sagan (1978) discussed some deficiencies of the Backus-Gilbert method of analysis of vertical resolving power. In particular, they have shown anomalous behavior of the spread function to the extent that as defined here, the spread function may not be an accurate measure of the resolving ability of the averaging kernels. In the context of our present comparison of HIRS and AMTS, this issue is important especially in light of the rather large values of spread function for AMTS in the 200-400mb layer.

To help resolve the issue, the author has developed a test for vertical resolving power which deals specifically with retrievals of temperature signal structure. This empirical test indicates that the vertical resolving power of AMTS around 300mb is much better than indicated by the BGC analysis. This test, with a comparison with Backus-Gilbert theory, is discussed in the paper which follows.

Acknowledgements

The author wishes to acknowledge the extensive help of Mr. David Hogan, currently with the Government Systems Division, RCA Corporation, Princeton, who developed much of the basic computer software used in this project while pursuing graduate studies at the University of Maryland. Also, the help of J. Susskind, NASA/Goddard Laboratory for Atmospheric Sciences and J. Rosenfield, Sigma Data Corporation in providing data and guidance for calculating transmittance functions for HIRS and AMTS is gratefully acknowledged. A debt of thanks is owed to L. McMillin, NOAA/NESS for kindly providing measurement noise estimates for each instrument. The author wishes to thank H. Fleming, NOAA/NESS and L. Kaplan, NASA/GLAS for helpful discussions of the topic. This research was sponsored by the NASA Goddard Laboratory for Atmospheric Sciences under Grant NSG-5209.

REFERENCES

Backus, G.E., and J.F. Gilbert, 1968: The resolving power of gross earth data. Geophys. J. Roy. Astron. Soc., 16, 169-205.

Conrath, B.J., 1972: Vertical resolution of temperature profiles obtained from remote radiation measurements. J. Atmos. Sci., 29, 1262-1272.

Kaplan, L.D., M.T. Chahine, J. Susskind, and J. Searle, 1977: Spectral bandpasses for a high precision satellite sounder. Appl. Optics, 16, 322-325.

Newman, W.I., 1979: The application of generalized inverse theory to the recovery of temperature profiles. J. Atmos. Sci., 36, 559-565.

Newman, W.I., and C. Sagan, 1978: Five micron limb-darkening and the structure of the Jovian atmosphere. Icarus, 36, 223-239.

Rodgers, C., 1976: The vertical resolution of remotely sounded temperature profiles with a priori statistics. J. Atmos. Sci., 33, 707-709.

Smith, W.L., H. Woolf, and H.E. Fleming, 1972: Retrieval of atmospheric temperature profiles from satellite measurements for dynamical forecasting. J. Appl. Meteor., 11, 112-122.

Thompson, O.E., 1979: Vertical resolving power of a satellite temperature sounding system. (COSPAR) Remote Sounding of the Atmosphere from Space. (H.J. Bolle, ed.) Pergamon Press, Oxford and New York. 143-147.

Thompson, O.E., J.K. Eom, and J.R. Wagenhofer, 1976: On the resolution of temperature profile finestructure by the NOAA satellite vertical temperature profile radiometer. Monthly Weather Review, 104, 117-126.

Thompson, O.E., 1981: HIRS-AMTS satellite sounding system test - Empirical vertical resolving power. Submitted to Journal of Applied Meteorology

Thompson, O.E., and R.J. Wolski, 1977: Nonlinear functions of satellite measured spectral radiances as estimators of tropopause height. J. Appl. Meteor., 16, 281-289.

Westwater, E.R., and N.C. Grody, 1980: Combined surface- and satellite-based microwave temperature profile retrieval. J. Appl. Meteor., 19, 1438-1444.

TABLE 1

Characteristics of the simulated HIRS and AMTS instruments.

	HIRS				AMTS		
Channel	Center (cm^{-1})	HIRS1 (1%)	HIRS2 (Noise Values)* (Current)	HIRS3 (Noise Values)* (Cooled)	Center (cm^{-1})	AMTS1 (1%)	AMTS2 (Noise Values)* (Current)
1	668.60	0.63	0.82	0.328	667.50	0.50	0.222
2	679.05	0.63	0.15	0.060	668.70	0.50	0.220
3	689.70	0.63	0.11	0.044	667.00	0.50	0.220
4	703.80	0.63	0.08	0.032	666.00	0.50	0.222
5	716.70	0.63	0.05	0.020	652.75	0.50	0.222
6	731.85	0.63	0.06	0.024	646.75	0.50	0.250
7	2192.50	0.0044	0.0011	0.00044	2383.74	0.0025	0.000282
8	2211.65	0.0044	0.0012	0.00048	2386.10	0.0025	0.000360
9	2237.35	0.0044	0.0009	0.00036	2388.19	0.0025	0.000293
10	2271.20	0.0044	0.0007	0.00028	2390.19	0.0025	0.000336
11	2506.60	0.0044	0.0005	0.00020	2392.34	0.0025	0.000298

*(Noise values are in units of $mw/(m^2-sr-cm^{-1})$)

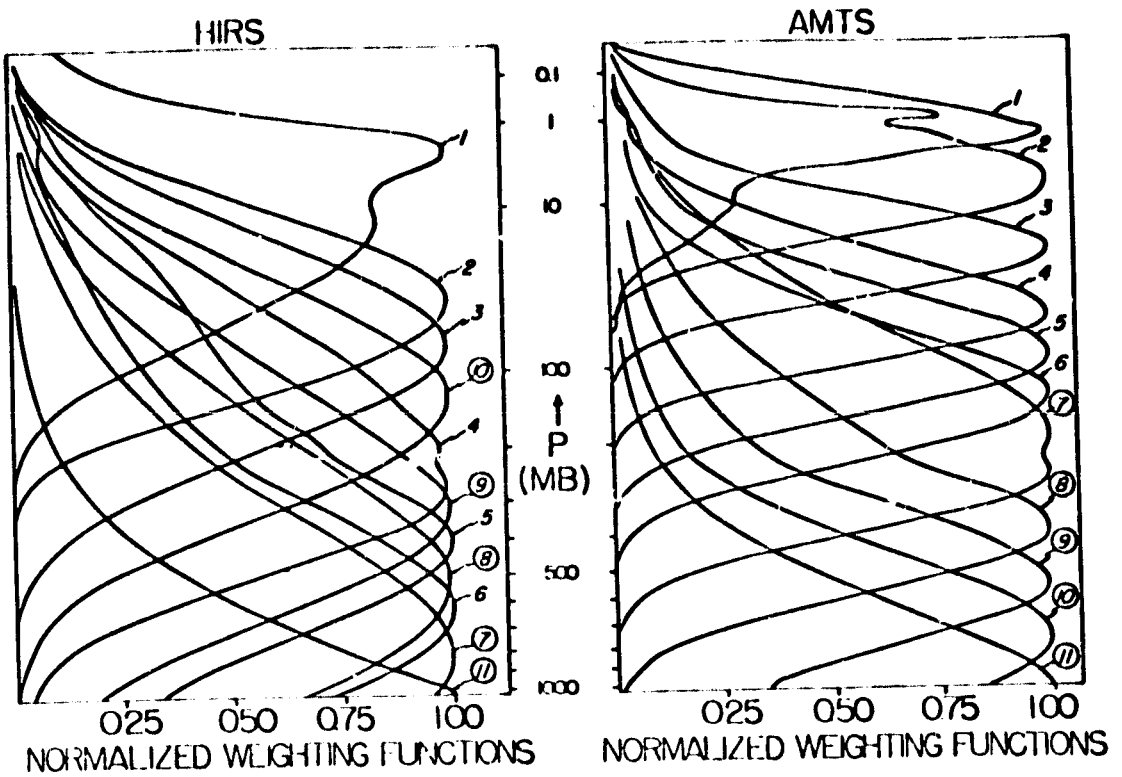

Figure 1. Transmittance weighting functions for eleven comparable channels of the HIRS and AMTS instruments. Circled curves refer to channels in the 4.3μm CO2 absorption band, while the others refer to channels in the 15μm CO2 absorption band.

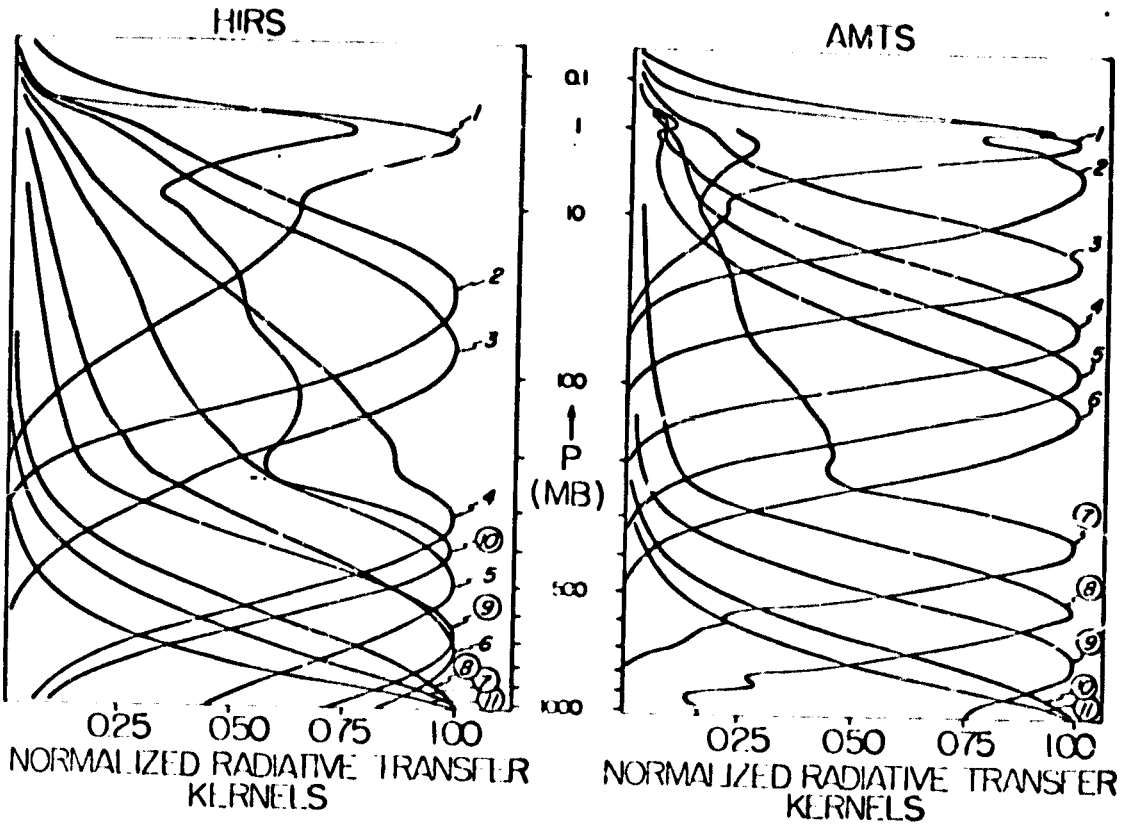

Figure 2. Radiative transfer kernels for the eleven channels of the HIRS and AMTS instruments shown in Figure 1.

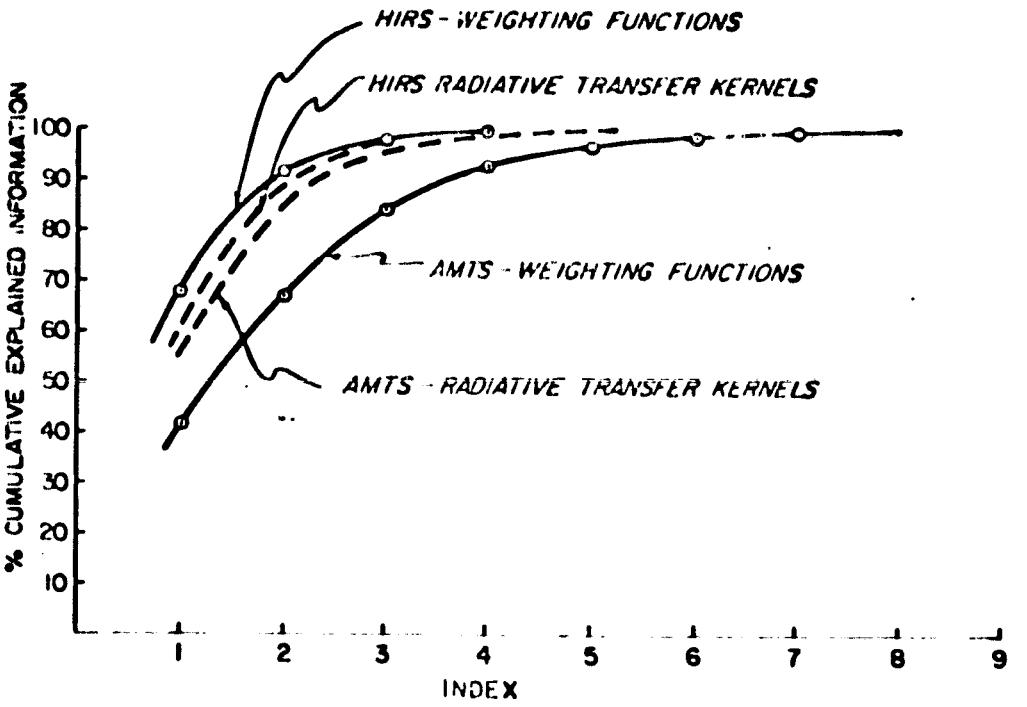

Figure 3. Cumulative distribution of normalized eigenvalues for transmittance weighting functions and radiative transfer kernels for the HIRS and AMTS.

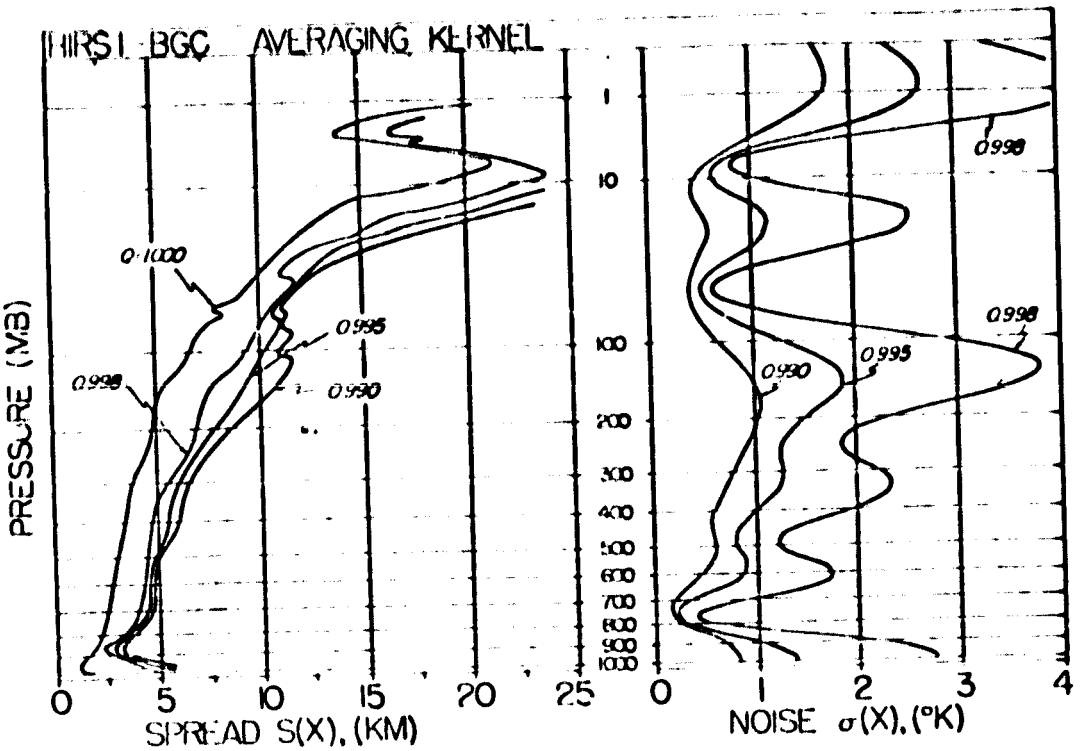

Figure 4. Spread and error variance functions for the HIRS1 instrument.

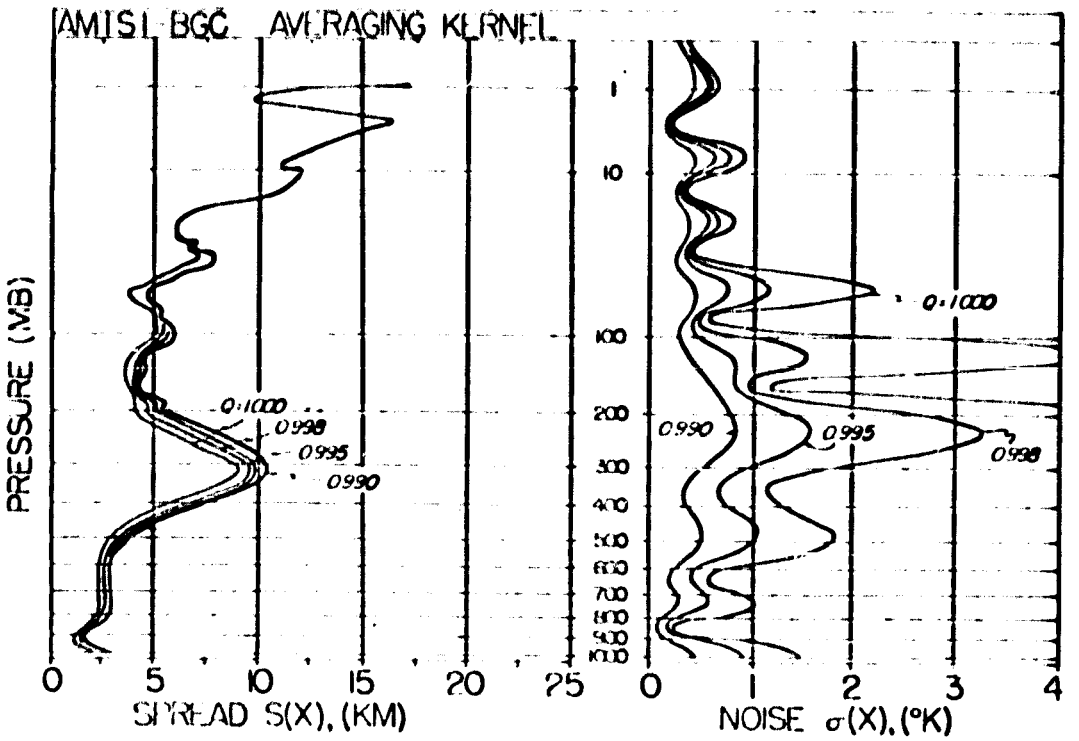

Figure 5. Spread and error variance functions for the AMTS1 instrument.

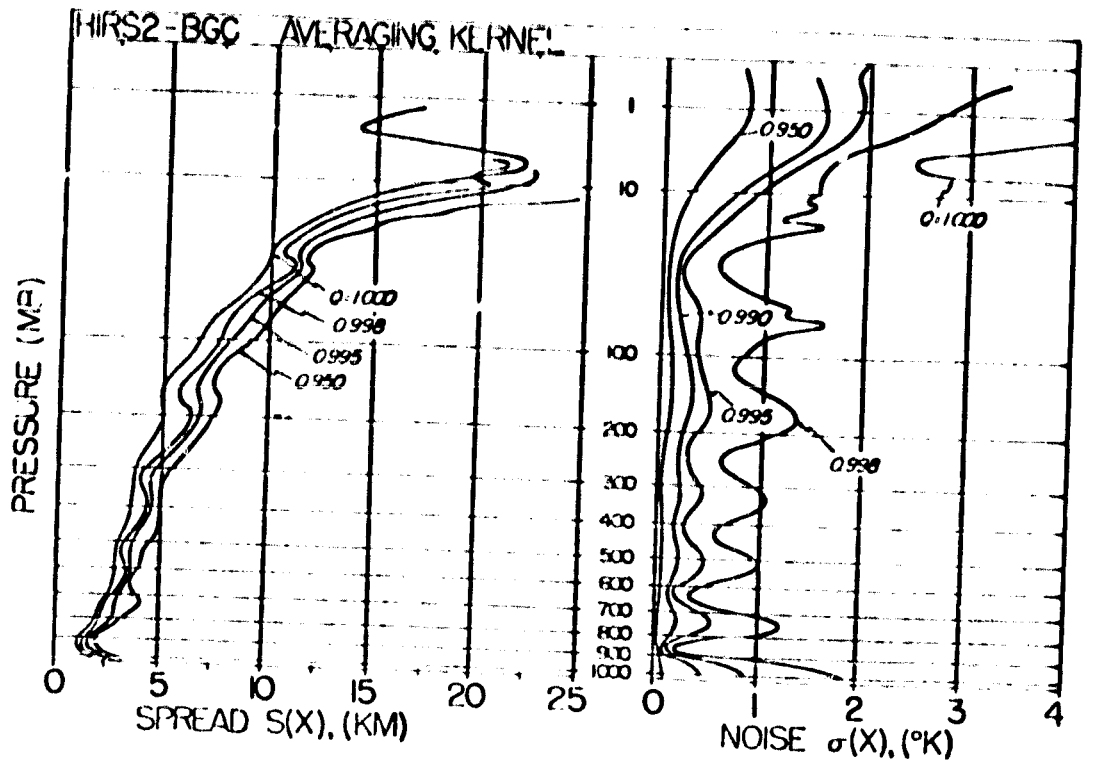

Figure 6. Spread and error variance functions for the HIRS2 instrument.

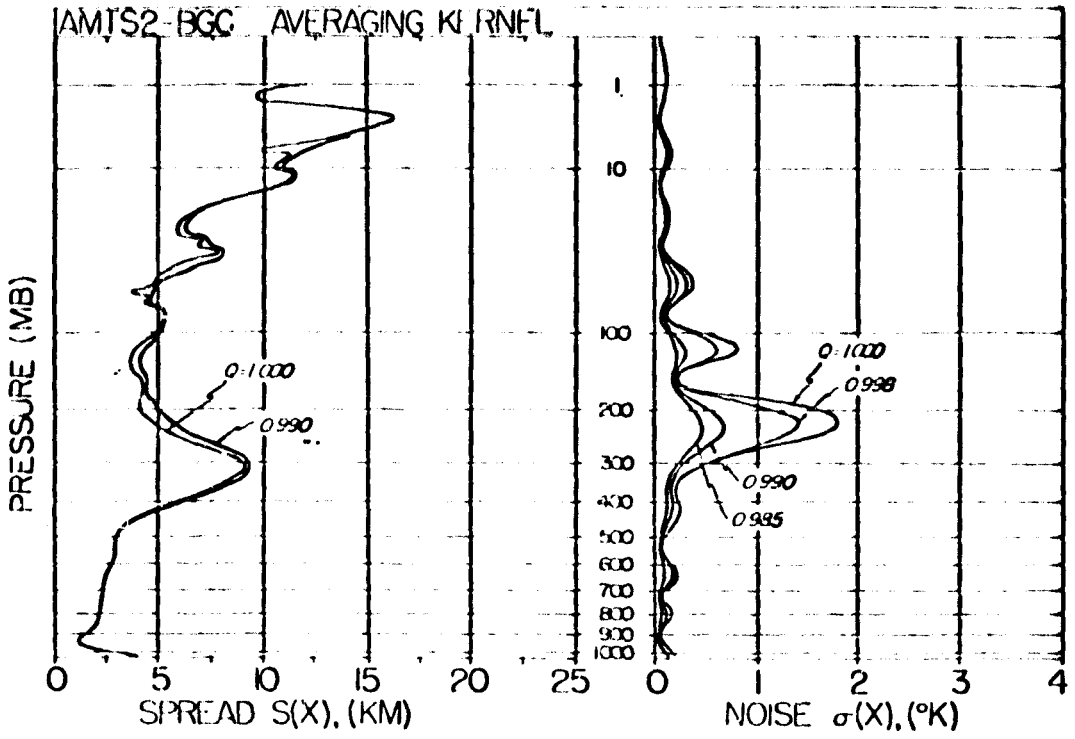

Figure 7. Spread and error variance functions for the AMTS2 instrument.

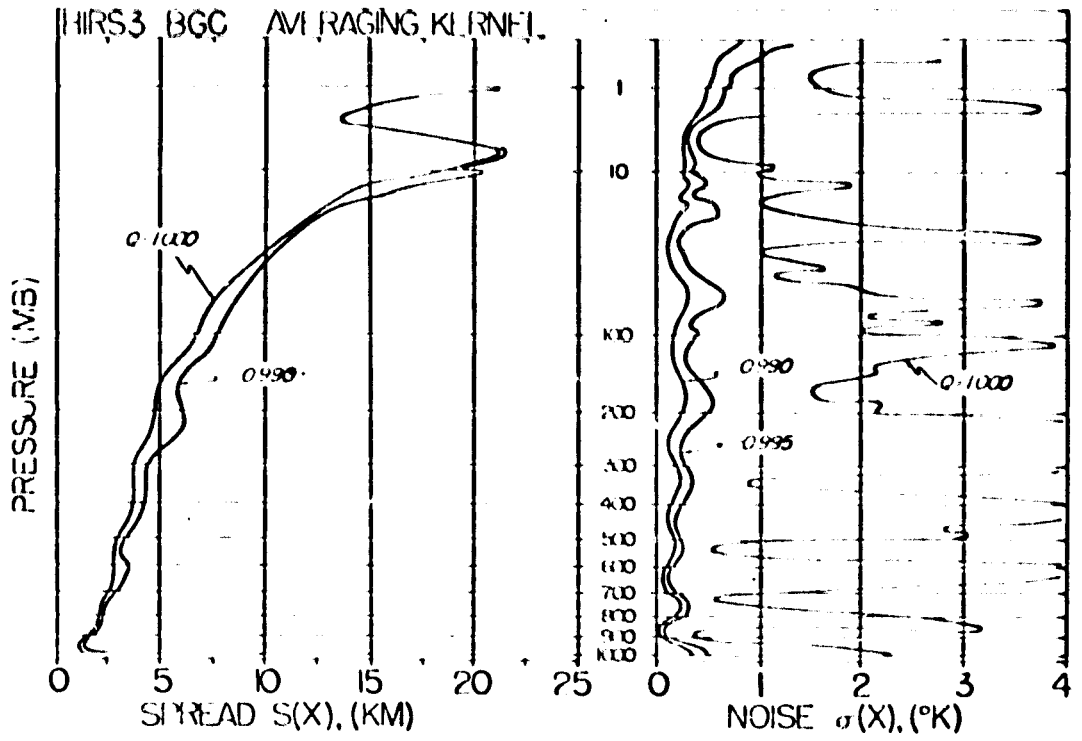

Figure 8. Spread and error variance functions for the HIRS3 instrument.

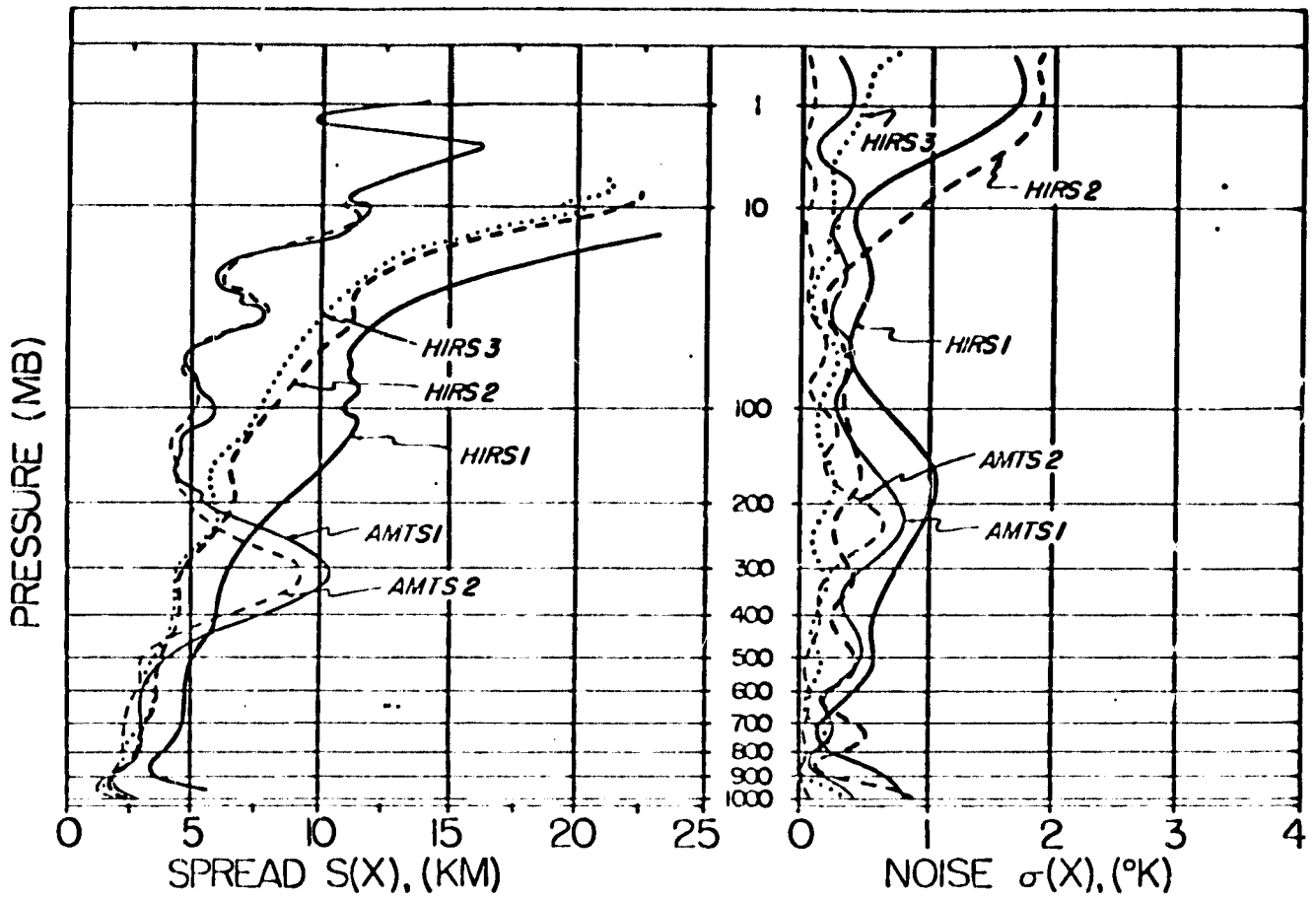

Figure 9. Spread and noise variance functions for HIRS1, HIRS2, HIRS3, AMTS1, and AMTS2 for q-values yielding similar noise variance values.

III. HIRS-AMTS Satellite Sounding System Test-Empirical Vertical Resolving Power

by

Owen E. Thompson

ABSTRACT

An empirical method for assessing vertical resolving power of satellite temperature sounders is developed and applied to the High resolution Infra-red Radiation Sounder (HIRS) and the Advanced Meteorological Temperature Sounder (AMTS). The empirical method involves carrying out the resolution assessment in a temperature retrieval mode rather than in a theoretical mode. Results are compared with the standard theoretical Backus-Gilbert analysis.

Using two well known, physical inverse retrieval algorithms, the empirical test demonstrates that the Backus-Gilbert spread function does not represent the minimum separation of resolvable signals in the atmospheric temperature profile. We find that the HIRS and AMTS should have similar vertical resolution in the troposphere with vertical resolving length around 2 or 3 km, quite consistent with theory. The AMTS exhibits a slight advantage over the HIRS above 200mb, a result which is qualitatively consistent with theory also. In the layer 200-500mb, the two instruments appear to have very similar resolution characteristics with AMTS showing a slight advantage over HIRS. This is totally contrary to theoretical results which would indicate that AMTS should be very poor in this layer.

1. Introduction

In the previous paper (Thompson (1981)), the author discussed the vertical resolving power of the HIRS and AMTS satellite temperature sounding instruments from a theoretical viewpoint. The spectral channel and noise characteristics of each instrument were subjected to an analysis derived from the work of Backus and Gilbert (1968; 1970) and Conrath (1972). In this paper, we wish to expand upon the study by deriving independent measures of vertical resolving power of satellite sounders which are based on the actual retrieval of fine scale structure in the temperature profile.

Thompson, Eom and Wagenhofer (1976) conducted an empirical test of the NOAA/VTPR sounder in a retrieval mode. In that study, a single smooth perturbation on a mean temperature profile was retrieved in a simulation mode and the smoothing characteristics of the retrieval system were analyzed. There are at least two major limitations to that study. First, it involved a sounder whose spectral channels and measurement noise characteristics are far inferior to current instruments, such as HIRS and the proposed AMTS. Secondly, the retrieval of a single smooth input perturbation does not tell us whether <u>two</u> or more closely spaced perturbations could be sensed by the satellite system. In this paper, we will generalize the simulations to come closer to the real issue of vertical resolving power.

2. Empirical resolving power

The Backus-Gilbert-Conrath analysis provides very useful information about the transmittance weighting functions of a radiometric sounder. However, Newman (1979) has discussed some limitations of this approach and has demonstrated that one may obtain spurious values of spread function which do not accurately reflect true vertical resolving power. Moreover, when one uses such a satellite sounding device in practice, one normally attempts to retrieve temperature structure from the radiance measurements. The fidelity of those retrievals certainly depends on the nature of the transmittance functions but also is very sensitive to the range of difficulties with the inverse problem. Thus, it is relevant to develop a resolving power test which is carried out in the retrieval, or inverse mode of the problem.

In developing an empirical retrieval resolving power test, we appeal to concepts of Lord Rayleigh. The resolving length of an optical system, such as a telescope, is the

minimum separation of two point sources (say, stars) which could just be detected as two distinct signals by the telescope. Adapting this concept to a satellite sounding system, one may define the resolving length of a sounding system as the minimum separation of two temperature signals along a vertical profile which can just be retrieved as two separate signals by the retrieval system. It is important to reemphasize that the retrieval system consists of both the instrument, with its transmittance functions and noise characteristics, and the mathematical algorithm for analyzing the measurements.

In the version of the empirical test of vertical resolving power to be discussed here, we wish particularly to omit the issue of the resolution of à priori temperature information which might be used for a retrieval. Although Rodgers (1979) has shown that à priori data can be used to further decrease the spread function below the minimum values established by the Backus-Gilbert theory, we wish to focus here on the resolving power of the radiance measurements alone without adding any additional information except a knowledge of the mean temperature profile and a good model of atmospheric transmittance. For this reason, we sought a retrieval algorithm which does not use à priori statistical data but does explicitly use the atmospheric transmittance function information. In fact, in our tests we used two algorithms meeting these requirements: A Backus-Gilbert-Conrath (BGC) retrieval algorithm and a modified minimum information algorithm, called Moderate Information (MI) here, which is patterned after Foster (1961) or Smith, Woolf and Fleming (1972). This algorithm uses different noise levels for each channel of the radiometric device and a single (temperature variance) tuning parameter, s^2. Further, we biased the problem towards the ideal so that we could obtain upper limits to system capabilities. Accordingly, no cloud effects or other error contamination of the simulated radiance meaurements were considered, although the noise characteristics of the instruments are explicitly included in the retrieval algorithms and the convergence criteria.

The simulations to define a resolving length were constructed as follows. Two carefully defined gaussian temperature signals separated by a known vertical distance were super-imposed on a standard atmospheric temperature profile. Exact radiances for each channel of the HIRS and AMTS instruments were computed for this profile. These radiances, in turn, were submitted to each of the retrieval algorithms mentioned above to produce a retrieved estimate of the double peaked signal.

For each retrieval, the first guess field was a temperature profile everywhere 2K cooler than the base profile upon which the temperature signals were super-imposed. Thus, the first guess profile contains no information about the temperature signal. Each of the two retrieval algorithms involve the transmittance weighting functions and a covariance matrix representing radiometer noise information. The noise covariance matrix was assumed diagonal with noise variances for each channel for each particular instrument as specified in Table 1 of Thompson (1981) distributed along the diagonal. Preliminary tests were run on each of several versions of each algorithm using different methods of handling temperature updating and linearization. Generally speaking, the retrieval algorithms were iterated until the root mean square deviation between actual and retrieved temperature profiles reached a first minimum. This convergence criterion is not identical to requiring that radiances corresponding to the retrieval converge to the measurements to within the instrument noise level for each channel, nor to requiring that the radiances converge in a least squares sense. When linearized, physical matrix inverse algorithms are used with high precision instruments, such as HIRS or AMTS, it may well happen that the algorithm will diverge, in the rms temperature sense, before reaching an acceptable level of convergence in a radiance sense. This, presumably, is due to a conglomeration of difficulties related to the linearization approximation applied to such high precision instruments, and to the implicit ill-conditioning of the linearized solution. Although the temperature convergence criterion could not be used in practice, we feel comfortable in using it in this analysis of optimum resolving power.

3. The simulation approach

Figure 1 illustrates the general nature of a determination of empirical resolving length for a given instrument (AMTS), a given retrieval algorithm (BGC), at a particular atmospheric level (100mb). In Figure 1, the base atmosphere has been subtracted from both the input and retrieved signals so that only the perturbations are shown. The input perturbation is a super-position of two gaussian curves each of amplitude 10K and half-width of 8 levels (8 equal increments of p**2/7) separated by a distance L. The separation L is set at some small value, radiances are computed and the retrieval algorithm is iterated until convergence. At that point, a determination is made of whether the input signal has been resolved. This resolution criteria is as follows:

(a) There must be two local maxima with an intervening minimum in the retrieval "near" the input perturbation.

(b) Given (a), if the maxima are denoted $(\hat{t}_1)$ and $(\hat{t}_2)$ and the minimum $(\hat{t}_o)$, then the perturbation is considered to be resolved if

$$(1/2)\{(\hat{t}_1) + (\hat{t}_2)\} - (\hat{t}_o) \geq (e)$$

where (e) is an rms deviation between input and retrieved signals "away from" the perturbation. The region over which (e) is computed is from the surface to 10mb but excluding the region between (x_T) and (x_B) where

$$(x_T) = (x_2) - H$$

$$(x_B) = (x_1) + H$$

(c) Given that (a) and (b) are met, a simple measure of the quality of vertical resolution of the input signal is given by $\rho = P/Q$ where P is the rms deviation between the input and retrieved signals between 1000mb and 10mb, and Q is the rms signal strength of the input signal calculated between 1000mb and 10mb.

In Figure 1, results for three successively larger values of L are shown. It is clear that the input signal is not resolved, by the criteria above, for the first two experiments. In the third, the input signal has been separated by a sufficient distance so that the retrieval system resolves it although with reduced amplitude, shifted center, and separated maxima.

4. Retrieval method test

In the course of completing the research reported here, we encountered many difficulties in carrying out retrievals using the two linearized physical inverse methods applied to the high resolution, low noise sounders. The convergence criterion mentioned earlier had to be used, instead of one

requiring that radiances converge to simulated measurements, because of certain over-relaxation properties of the inverse solutions. In some experiments, the last channel to converge would converge so reluctantly - or possibly not at all - that the algorithm either would diverge altogether, in the sense of rms retrieval error, or would swing away only to begin a slow convergence again. Twomey (1977, Section 9.1) showed a similar example of residual error oscillation, although with a direct rather than physical inverse solution. Further, in some cases, a solution satisfying the radiance convergence criteria would be worse, from the vertical resolution criteria, than one which had not converged in the radiance sense. The difficulty lies, in part, with the linearization used in the retrieval algorithms applied to instruments with low noise levels, and possibly due, in part, to the algorithm for temperature updating of the transmittances. Put simply, a sequence of linearized solution iterations incorporating temperature correction of the transmittances may not converge, within the very small tolerances of the HIRS or AMTS, to a correct solution of the full non-linear problem. Further, a linearized solution which does produce radiances within noise levels of the measurements may not, in fact, be optimal in temperature space.

For the empirical test of the AMTS and HIRS instruments, we began by using iterated retrieval algorithms which start with the first guess temperature field and with transmittances also computed for this profile. At each iteration step, transmittances were recomputed using the NASA/GLAS algorithms, provided to us by J. Susskind, and the new estimate of temperature. In this paper, this is called Version 1 of either algorithm. In our experiments, we experienced inordinate difficulties with this version of the MI retrieval algorithm applied to HIRS2 and HIRS3. Of course, to obtain the sharpest possible vertical resolving power, the algorithm was tuned as close to a high resolution limit as feasible. Generally, the algorithm was mostly unstable for the higher values of s^2 tried. When s^2 was lowered, so as to stabilize the solution, the resolving power was sufficiently reduced so as to produce no meaningful determinations. The moderate information regularization of the inverse problem does not seem to be an optimal solution for the HIRS when very low noise levels are incorporated into the solution; at least in the case of these simulations. Therefore, we used an alternate version of the MI solution for the HIRS2 and HIRS3 in which kernels corrected to the true input perturbation temperature profile are used in the iterative solution. (This is called Version 2 of either algorithm.) For the AMTS2, we used both versions of the MI algorithm for comparison. Version 2 ought to represent an

ideal optimum case since it contains correct kernels from the outset even though the algorithm operates on the smooth first guess temperature field at the first iteration. While Version 1 does not achieve these optimum results, it gives some indication of how close to optimum one can get operating objectively with no à priori information whatever.

In our trials, each solution was iterated until the rms deviation between input and retrieved temperature reached its first relative minimum. (Generally speaking, this "final" solution does not necessarily produce radiances within the noise level of the input radiances, but does produce the best solution in temperature space.) Also, optimum retrieval parameters were determined for each instrument and each algorithm by extensive tuning tests.

5. Empirical resolving length results

Figure 2 shows empirical resolving length as a function of height for the HIRS2 instrument. The two curves shown were obtained by using each of the retrieval algorithms discussed above. The dots appearing on the diagram represent smallest resolvable differences at each level in our determinations of empirical resolving length. The successive dots at a given level represent successive increases by two levels (two increments of "p**2/7) of the separation of the input perturbations. Also, shown as a dotted line is the theoretical spread function of Backus and Gilbert, taken from Thompson (1981), for the same q parameter as used in the BGC retrieval. Though the BGC retrieval results were limited to the troposphere, they follow very closely the theoretical spread function. The empirical resolving length using the BGC retrieval is smaller than the theoretical spread function in the layer 200-500mb and only slightly greater below that. The result for the MI-Version 2 solution shows an empirical resolving length less than the theoretical spread function at almost all levels. At 200mb, for example, the MI-2 empirical resolving length is only about half as great as the theoretical spread. These results give us our first indication that the theoretical spread function does not represent the minimum resolving length possible for a remote sounding device. Even though the MI-2 is an idealized algorithm, it is one which should be approachable in practice.

The panel to the right in Figure 2 shows the normalized retrieval error ρ as a function of height corresponding to the retrievals in the left panel. The MI-2 retrievals were very good at all levels producing an rms retrieval error from 1000-10mb varying from 10-35% of the rms temperature

input signal strength. Thus, not only were the input perturbations resolved, but they were resolved with reasonably high quality. The quality of the BGC retrievals was somewhat lower and the result near 400mb was of particularly low quality, even though it also yielded an empirical resolving length less than the theoretical spread function.

Figure 3 shows a similar display of results for the AMTS2 instrument. In this series of experiments, we were able to obtain excellent, and quite comparable results from Version 1 of both retrieval algorithms. We also show results for Version 2 of the MI algorithm so that the most optimum case is shown as well. The curves show that retrievals using the AMTS2 instrument come very close to the ideal in the lower troposphere with resolving length - by any measure - being 2 to 3 km. Above 200mb, the empirical results fall short of the theoretical result. Even the MI-2 retrievals have vertical resolving length significantly larger than the theoretical spread function. The BGC-1 and MI-1 algorithms yield quite comparable results throughout the entire atmosphere with the largest discrepancy around 100mb where the BGC algorithm shows a decided advantage. Elsewhere, the MI algorithm produced sharper resolution with lower retrieval error.

The most striking feature of Figure 3 is that the large peak in the theoretical spread function between 200-400mb appears to represent a gross underestimate of the actual vertical resolution of the AMTS2. On the other hand, the right panel of Figure 3 shows a substantial increase in the retrieval error for both the BGC-1 and MI-1 algorithms in this same region. This means that while the input signals are resolved - by the criteria set out for this study - the quality of the retrieval is not as high in this layer as in the troposphere. Note, however, that the idealized MI-2 algorithm yielded higher quality retrievals through this same region. This is near the region where the distribution of the AMTS radiative transfer kernels leaves an apparent information gap and the ability to retrieve fine structure in the profile was expected to be degraded. (*) The large discrepancy in theoretical and empirical measures of

---

(*) It shcuild be emphasized here that our test of AMTS is not altogether fair since we used only 11 sounding channels, fewer than are actually available. Susskind, in personal communication, has pointed out that an additional AMTS CO_2 channel near 300mb would be available to an operational version of the instrument.

vertical resolution in this region calls for a deeper look into the matter.

Figure 4 shows the AMTS2 averaging kernels appropriate to the 300mb level computed for the BGC and MI retrieval coefficients. The amplitudes of these curves are arbitrarily normalized so that only the shape is important here. The kernel for the BGC coefficients is separated into two prominences, one slightly above 200mb and one between 400-500mb. The 300mb level itself is a local minimum for the BGC averaging kernel. Figure 5 shows the series of BGC retrieval for perturbations centered at 300mb, and for separations ranging from 6 levels (1.94km) to 16 levels (5.16km). The resolution criteria is met for a separation of 16 levels, nearly exactly the separation of the prominences in the BGC averaging kernel. This suggests that this experiment may only be a "resonance" phenomenon where perturbations are only retrieved when they become synchronized with prominences or side lobes of the averaging kernels. However, the averaging kernel in Figure 4 for the MI retrieval coefficients is sharp, at 300mb, with no such prominences. The corresponding series of retrieval experiments are shown in Figure 6 where the input signal is also resolved at separations of 14 and 16 levels: even better than for the BGC retrievals. We conclude, therefore, that the resolution of these signals by both methods is an event more fundamental than resonance with kernel side lobes. That is, the empirical resolving lengths determined between 200 and 400mb are just as significant as those determined at other atmospheric levels.

The empirical resolving length results for the HIRS3 instrument are shown in Figure 7. Once again, we had difficulty in producing stable, highly resolving retrievals with the MI-1 algorithm. Even with the BGC algorithm, the interplay between the high sensitivity tuning of the algorithm and the temperature correction of the kernels produced unstable retrievals at many of the levels investigated. Those BGC-1 results obtained are consistent with the MI-2 results and we take the pattern of both to be representative. By comparing Figure 7 with Figure 2, one sees that lowering the noise level of the HIRS instrument should produce an increase in the vertical resolving power, even though the theoretical spread functions shown for HIRS2 and HIRS3 in these figures are virtually indistinguishable. The empirical resolving length for HIRS3 is significantly better than HIRS2 above 200mb and slightly better in the troposphere. As with HIRS2, HIRS3 shows consistently better MI-2 results than are predicted by Backus-Gilbert theory. Even the few BGC-1 results obtained suggest that the high empirical vertical resolution may not be solely due to the

priori information in the kernels for method MI-2.

For convenience to the reader, the MI-2 results for each instrument tested here are grouped together in Figure 8 for instrument comparison. The three instruments behave comparably in the troposphere with the HIRS3 generally showing the highest quality resolution of input signals and AMTS2 generally outperforming HIRS2. Between 200mb and 50mb, the HIRS3 appears to have a decided advantage over AMTS2 even though the theoretical spread function results would lead one to believe just the opposite. The present version of HIRS (HIRS2) would appear to be inferior to the AMTS2 in this layer. Above 50mb, the AMTS produces higher resolution than either version of HIRS.

6. Conclusions

In this paper, we have developed and presented a method for assessing the vertical resolving power of satellite borne temperature sounders which is carried out in a retrieval mode. The method is conceptually similar to methods of defining resolving power of telescopes and microscopes. The advantage of this method over the theoretical method of Backus and Gilbert is that the retrieval algorithm itself plays a strong role in the determination of resolution properties. The method could be used for any retrieval algorithm, including direct relaxation methods and non-linear methods, since assessment is carried out in temperature retrieval space. Moreover, in light of certain known limitations of the theoretical Backus-Gilbert approach, the empirical method shows directly - instead of inferentially - the minimum separation of signal perturbations on the temperature profile which car be resolved by a temperature sounding system.

The most significant disadvantage of the method is that the simulation used to define resolving length is decidedly unatmospheric. On the contrary, isolated signals are retrieved centered around specific levels instead of a more natural super-position of irregular signals such as might be encountered in nature.

Nevertheless, the approach developed here is reasonably objective and does yield a baseline measure of the vertical resolving power of satellite spectral radiation measurements absent the expectation of structure derived from independent à priori information.

The empirical method has been applied to two high technology sounding instruments, the HIRS and AMTS, using each

of two standard, well known physical inverse retrieval solutions. These results, in turn, have been compared with the standard theoretical assessment given by the Backus-Gilbert method.

We have found that the empirical resolving length of a sounding system may be either smaller than or larger than the Backus-Gilbert spread function, depending on instrument, retrieval method, and atmospheric level. That the empirical resolving length may be smaller than the theoretical spread gives evidence that the latter may not comprise the best test of vertical resolving power. That the empirical measure may often be larger than the theoretical measure gives evidence that a given retrieval algorithm will not always extract the most temperature structure information incorporated in the radiation measurements from satellite sounders.

Based on our empirical tests of vertical resolving power, we have found that the HIRS and AMTS instruments should have nearly comparable vertical resolution in the troposphere -- AMTS showing a slight advantage -- with vertical resolving length varying around 2 or 3 kilometers. The AMTS instrument also exhibits a slight advantage over the present version of HIRS, from the resolution standpoint, above 200mb with maximum advantage occurring near 20mb. If, however, the sensors of a HIRS instrument were cooled in a fashion similar to the proposed AMTS, our results show that the vertical resolving power above 200mb would be substantially improved, perhaps exceeding the capabilities of the AMTS. The effect of sensor cooling for improving tropospheric retrievals by HIRS does not appear to be dramatic. In the layer 200-500mb, we find a significant difference between our empirical results for the AMTS and the theoretical, Backus-Gilbert results. The empirical resolving length is much less than the Backus-Gilbert spread function in this layer and is also generally smaller than the resolving length for the HIRS. We conclude that the spread function for the AMTS is misleading in this layer and that the AMTS instrument is superior to HIRS between 200 and 500mb, rather than inferior as would be inferred from Backus-Gilbert theory.

Finally, it is important to note that we experienced many difficulties in conducting empirical tests of vertical resolving power using the high precision HIRS and AMTS instruments. Some of these difficulties can be traced to the linearization of the fundamentally non-linear problem which is incorporated into the physical inverse retrieval solutions used in our tests. The present author, therefore, considers the comparisons between HIRS and AMTS shown here to be tentative and very much in the context of the approximate

retrieval methods used. We suggest that a testing approach similar to ours be adapted for more sophisticated retrieval algorithms before final assessment of the merits of each instrument are made.

ACKNOWLEDGEMENTS

The author wishes to acknowledge the extensive help of Mr. David Hogan, currently at Government Systems Division, RCA Corporation, Princeton in developing much of the computer programming used in this project while pursuing graduate studies at the University of Maryland. Also, the author acknowledges the assistance of J. Susskind, NASA/Goddard Laboratory for Atmospheric Science, J. Rosenfield, Sigma Data Corporation, and L. McMillin, NOAA/NESS for providing information on HIRS and AMTS transmittances and measurement noise estimates. This research was sponsored by the NASA/Goddard Laboratory for Atmospheric Sciences through Grant NSG-5209.

REFERENCES

Backus, G.E., and J.F. Gilbert, 1968: The resolving power of gross earth data. Geophys. J. Roy. Astron. Soc., 16, 169-205.

Conrath, B.J., 1972: Vertical resolution of temperature profiles obtained from remote radiation measurements. J. Atmos. Sci., 29, 1262-1272.

Foster, M., 1961: An application of the Wiener-Kolmogorov smoothing theory to matrix inversion. J. SIAM, 9, 387-392.

Newman, W.I., 1979: The application of generalized inverse theory to the recovery of temperature profiles. J. Atmos. Sci., 36, 559-565.

Rodgers, C., 1976: The vertical resolution of remotely sounded temperature profiles with a priori statistics. J. Atmos. Sci., 33, 707-709.

Smith, W.L., H. Woolf, and H.E. Fleming, 1972: Retrieval of atmospheric temperature profiles from satellite measurements for dynamical forecasting. J. Appl. Meteor., 11, 112-122.

Thompson, O.E., 1979: Vertical resolving power of a satellite temperature sounding system. (COSPAR) Remote Sounding of the Atmosphere from Space. (H.J. Bolle, ed.) Pergamon Press, Oxford and New York. 143-147.

Thompson, O.E., J. K. Eom, and J.R. Wagenhofer, 1976: On the resolution of temperature profile finestructure by the NOAA satellite vertical temperature profile radiometer. Monthly Weather Review, 104, 117-126.

Thompson, O.E., 1981: HIRS-AMTS satellite sounding system test - Theoretical vertical resolving power. Submitted to Journal of Applied Meteorology

Thompson, O.E., and R.J. Wolski, 1977: Nonlinear functions of satellite measured spectral radiances as estimators of tropopause height. J. Appl. Meteor., 16, 281-289.

Twomey, S., 1977: Introduction to the Mathematics of Inversion in Remote Sensing and Indirect Measurements. Elsevier Co., Amsterdam, Oxford, and New York. 243p.

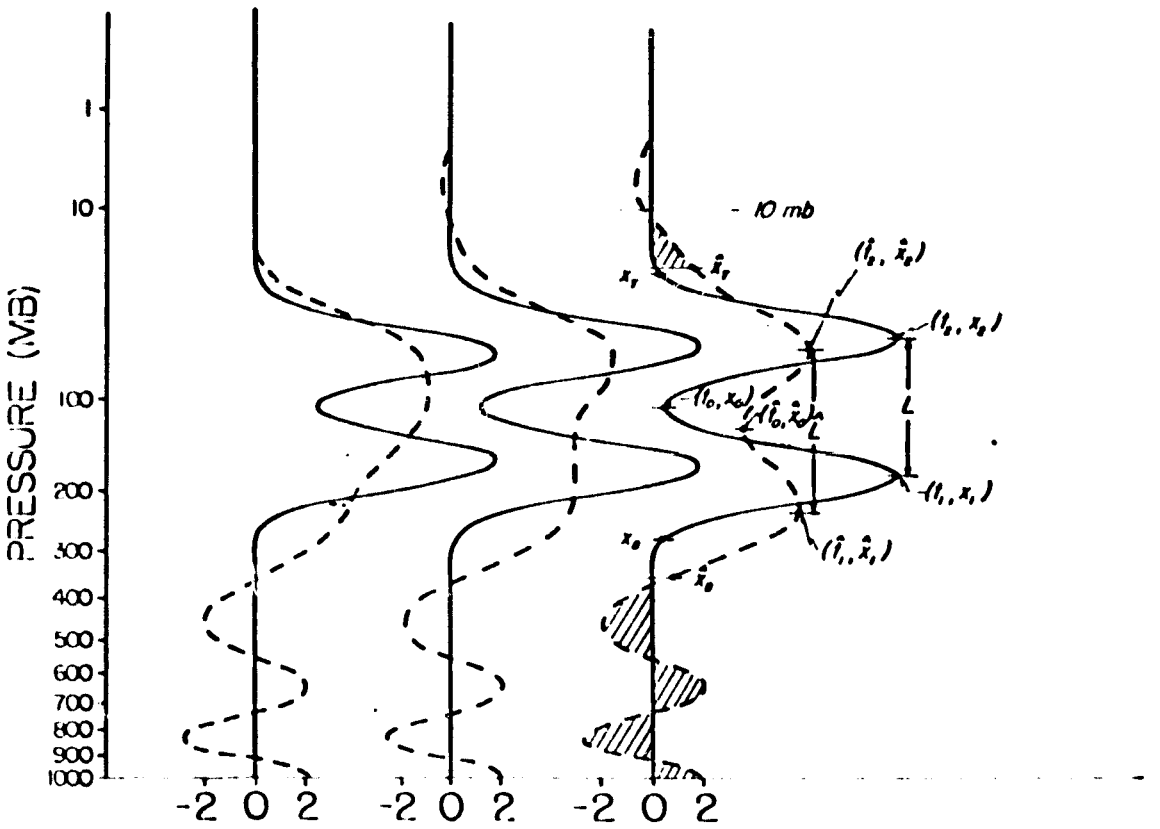

Figure 1. Illustration of the determination of empirical resolving length.

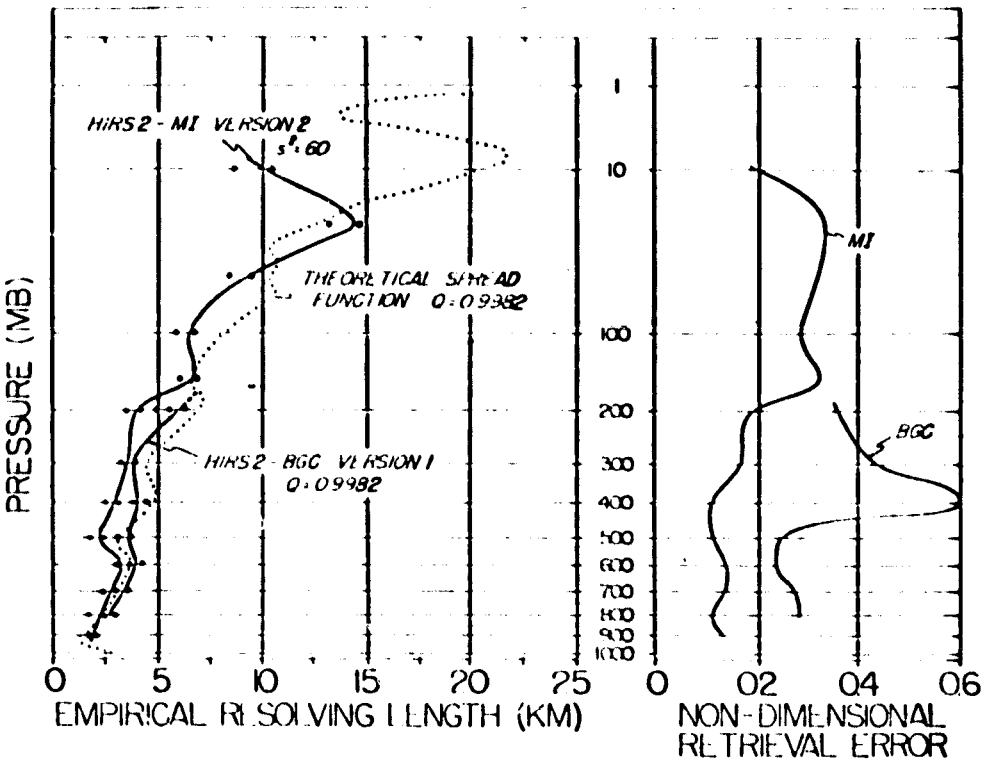

Figure 2. Empirical resolving length and quality for HIRS2.

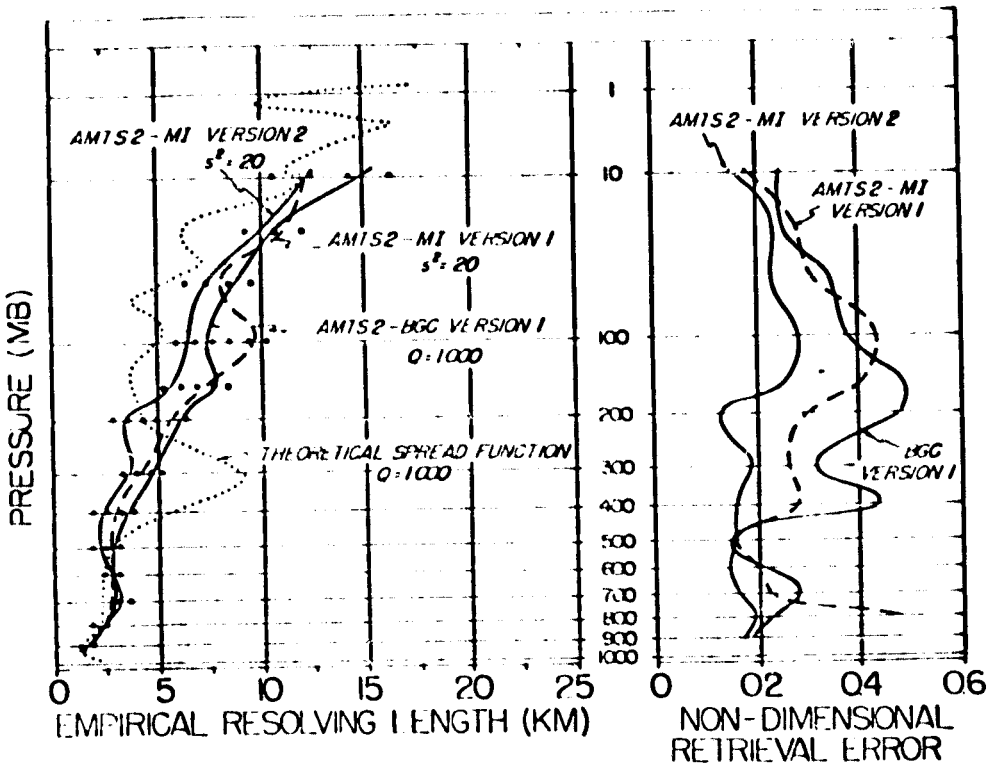

Figure 3. Empirical resolving length and quality for AMTS2.

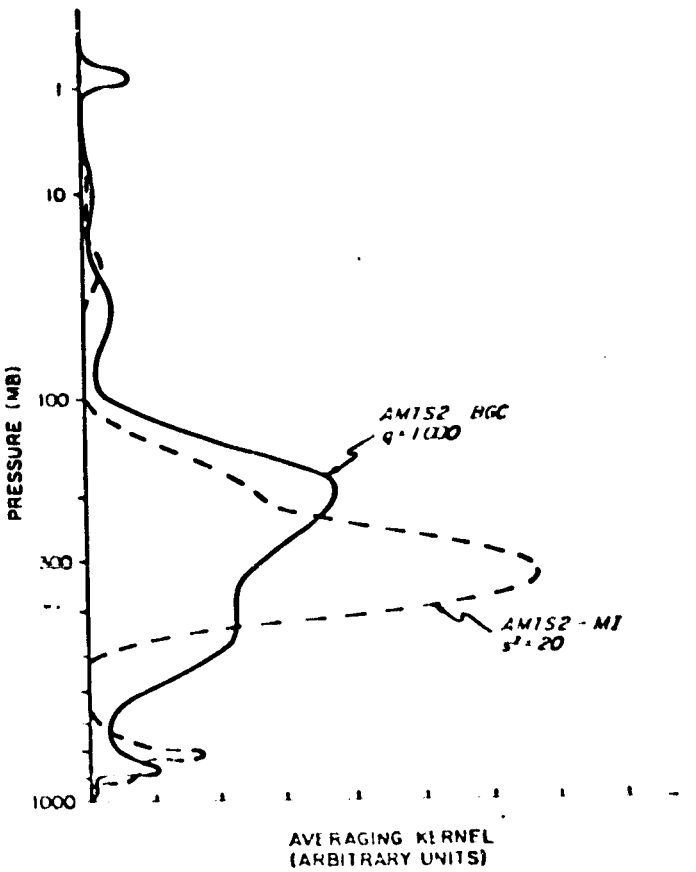

Figure 4. AMIS2 averaging kernel at 300mb for BGC and MI retrieval coefficients.

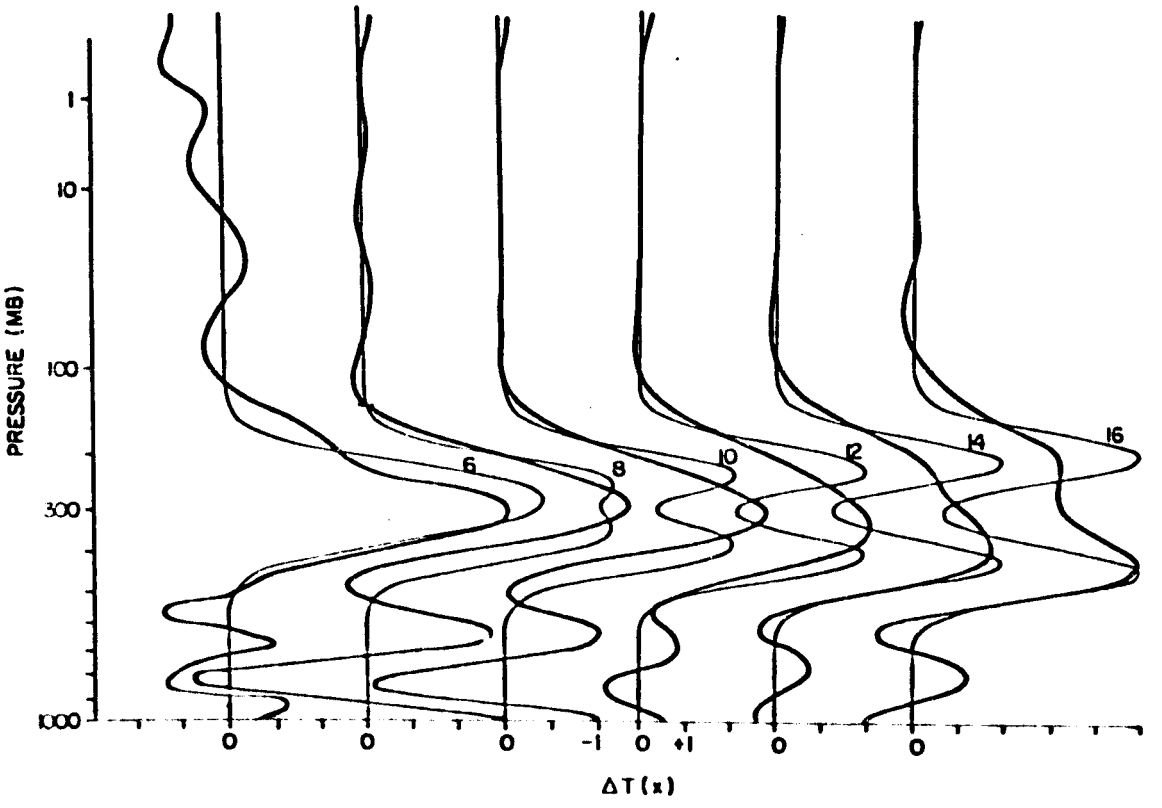

Figure 5. BGC retrieval experiments at 300mb for the AMTS2 corresponding to Figure 3.

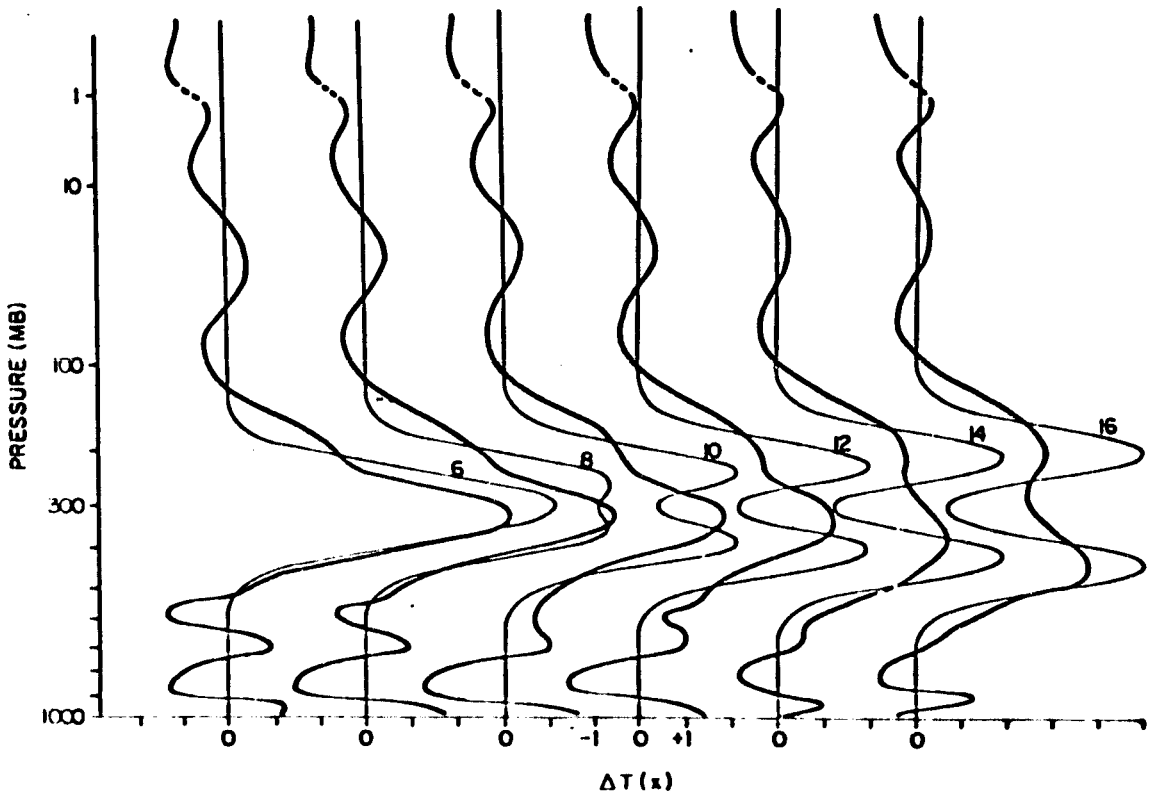

Figure 6. MI retrieval experiments at 300mb for the AMTS2 corresponding to Figure 3.

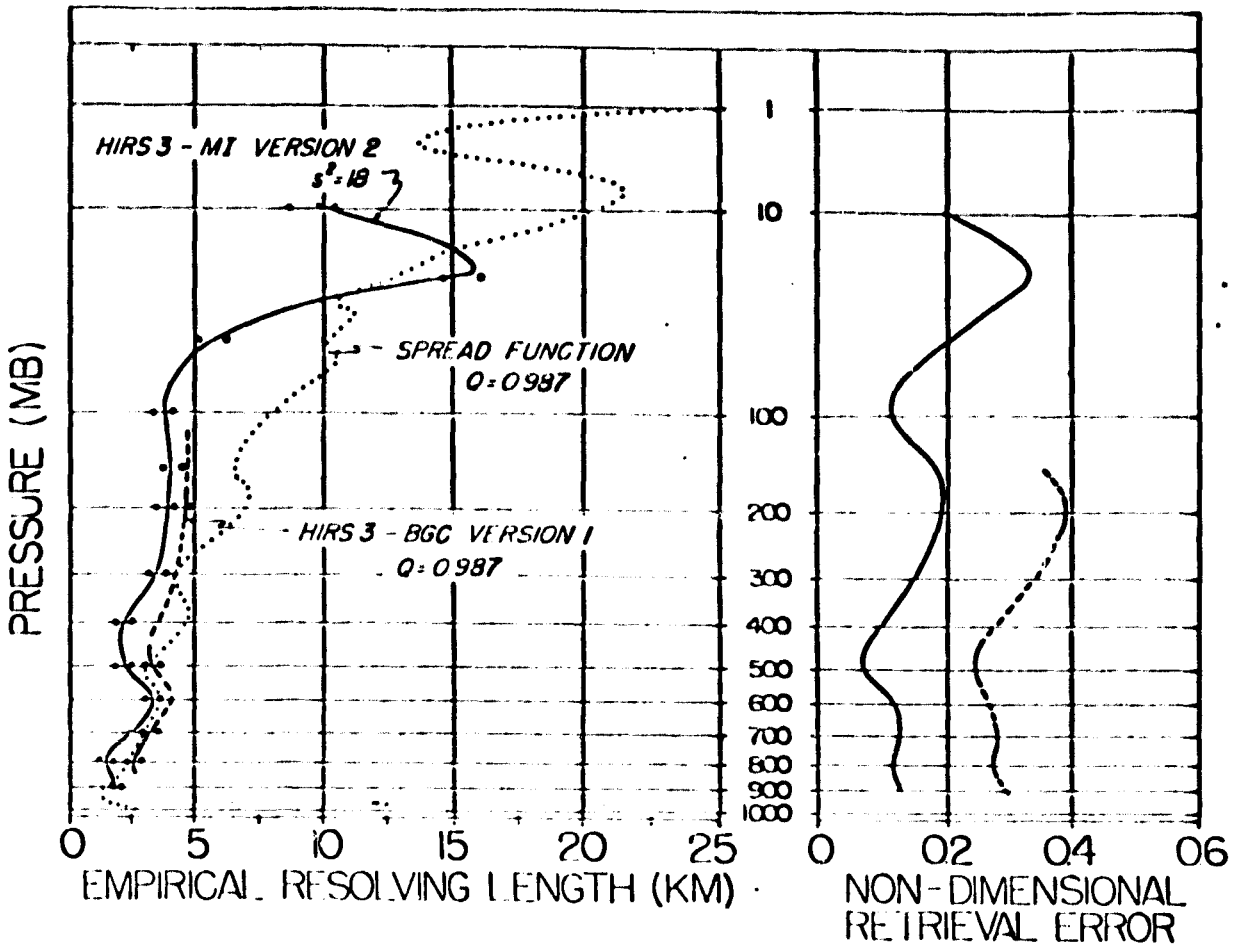

Figure 7. Empirical resolving length and quality for HIRS3.

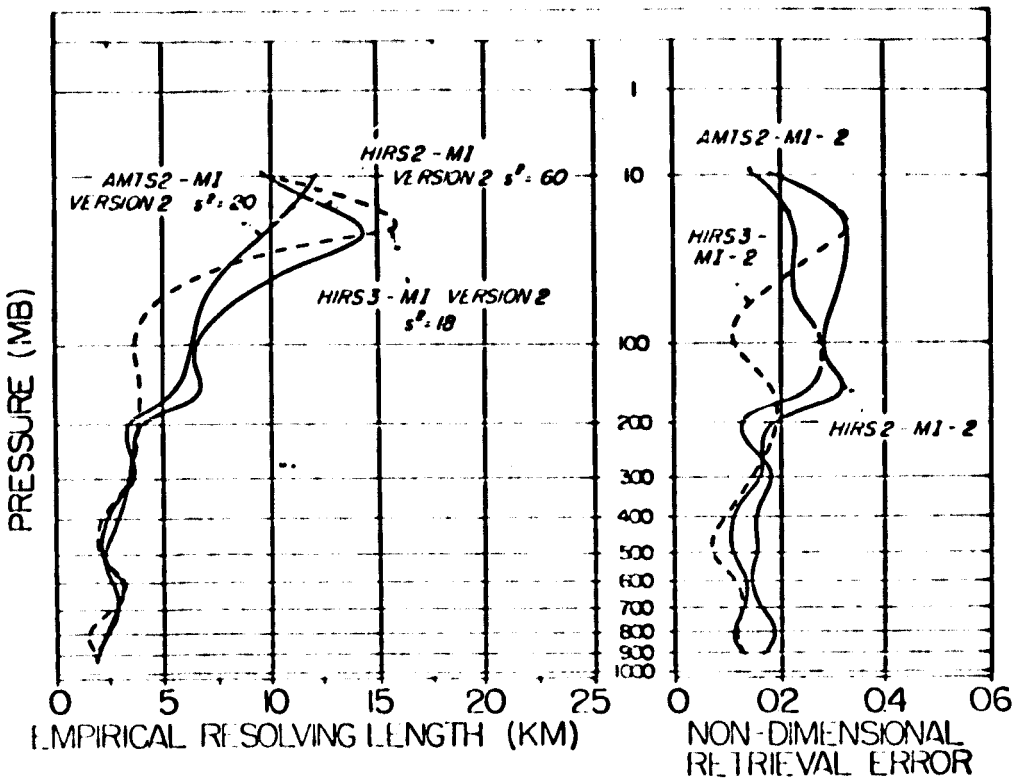

Figure 8. Comparison of empirical resolving length and quality for HIRS2, HIRS3, and AMTS2.

IV. Transfer and Distortion of Information in a Satellite Temperature Sounding System

by

Owen E. Thompson

Donald Wark

Information concerning the ambient atmospheric thermal structure can be severely distorted by satellite temperature retrieval systems and subsequent analysis algorithms. Generally speaking, we know that a finite set of spectral radiance measurements bears only a coarse, integrated relationship to the ambient temperature structure which emits the radiation. Temperature retrieval algorithms may smooth, add, or further distort information depending on how stable is the algorithm, and how heavily influenced it is by à priori data. Further analysis of retrievals in preparation for a final meteorological study will generally distort the information further.

In this paper, the transfer and distortion of the basic ambient temperature information is discussed. The approach is to examine the variance spectrum of information as it takes different forms in the retrieval-analysis cycle.

It is shown that the (total) adjusted variance of radiative brightness temperatures measured by the HIRS satellite instrument is only about half the variance of corresponding atmospheric temperature profiles in middle latitudes, and only about 30% in the tropics. For statistical (regression) temperature retrievals, about 48-49% of the information content is attributable to à priori data while for physical retrieval methods, only about 25-27% is attributable to prior information (such as transmittances). Other retrieval methods lie between these extremes. The distortion of information is explicitly shown by examining empirical orthogonal functions of corresponding RAOB and retrieval profiles.

The impact of remote sensing data on global and mesoscale models of atmospheric behavior depends fundamentally on the quantity and quality of new observational information provided by the remote sensing device. In particular, satellite based soundings of temperature and moisture should have an impact on diagnostic and prognostic models proportional to the amount of new observational information imbedded in the retrievals. However, owing to the well known difficulties with the inverse problem, satellite derived soundings are most always a complex blend of the new radiometric measurements with à priori information on the atmospheric structure. This à priori information may involve climatological mean structure, statistical or probabilistic information, in situ measurements nearby in time and space, numerically forecasted structure, and so on.

In this paper, an analysis of information transfer for the satellite sounding problem is presented. Of particular interest is the distortion of the atmospheric information - the information content of the ambient atmospheric thermal field - as it naturally produces the outgoing radiance field, and the further distortion of this information as the radiation field is transformed back into thermal structure information through the retrieval step. The amount and quality of new information about the ambient atmosphere provided by this satellite sounding process is not always clear but is of fundamental relevance to the meteorological impact of that observing system.

Figure 1 schematically illustrates how information embodied in, say, the ambient temperature structure is transformed into different forms of that information in a satellite temperature retrieval and analysis system. The variables enclosed in ovals in Figure 1 represent various versions of the original temperature information which are expected to be moderately to highly distorted versions compared with the original information in the ambient temperature structure. In the retrieval-analysis system illustrated in Figure 1, the original information has been transformed into various kinds of radiance ensembles or temperature estimate ensembles by the various steps in the retrieval-analysis procedure. In order to know how accurate is the depiction of a meteorological phenomena described by some variate based on remote radiation measurements, one must know how the original information in the ambient temperature field has been degraded by the natural radiative transfer integration, by the error contamination of radiance measurements, and by subsequent processing and analysis of that radiance dat (See, for example, Thompson, Eom and Wagenhofer (1976), Thompson (1982a, 1982b).) The radiative transfer physics and the finite, spectral resolution of a

radiometer assure that substantial vertical averaging has been done to the actual temperature data in transferring that information to the radiance domain. Temperature retrieval algorithms, often involving à priori or forecasted temperature information which is independent of the radiance observation, supply their own information transfer properties so that the retrieval is a distorted version of the ambient signal. The distortion is partly due to bias by the à priori information used and partly due to the inherent mathematical properties of the retrieval algorithm. Further analysis of the retrieved temperature profiles contribute even more distortion of the information.

The information can be examined at each step of the process illustrated in Figure 1 - either in the temperature domain or the radiance domain - and the quality and quantity of information existing at each step compared with the original ambient temperature information. A systematic approach to this comparison is given in section 3.

2. Previous relevant work

Satellite meteorologists have sought to retrieve the structure information of the ambient temperature field by a variety of techniques. Retrieval algorithms based on the methods of Backus and Gilbert (1968) seek to optimize the vertical resolution of structure in the temperature field by sharpening the integral everaging kernels so as to extract the structure information directly from the radiance data in some optimal sense. Another method seeks to recover structure by optimizing the construction of a first guess field using, say, a numerical forecast model, and then constraining the retrieval to deviate minimal amounts from that field, (Smith, Woolf and Fleming (1972) for example). Other methods constrain the retrievals statistically so that they have the structure of an independent, but presumably representative, set of temperature data derived from RAOBs (Smith, Woolf and Jacob (1970), Smith and Woolf (1976) for example), or by performing a final interpolation or fitting of radiance based temperature information by empirical orthogonal functions derived from an independent set, (J. Susskind, personal communication). In methods utilizing à priori information independent of the radiance measurements, it is sometimes difficult to know how much of the final information has actually been synthesized from à priori data and how much is new information contributed by the radiance measurements themselves.

The issue of information content has been studied by several investigators. Crosby and Weinreb (1974) analyzed information content of satellite retrievals based on statistically optimized solutions and have further shown how incorrect independent statistics incorporated in a retrieval

solution can distort the information produced from radiances by that solution. Spanküch, Timofeyev and Güldner (1977) also showed the distortion of measured radiance information that can occur if one uses incorrect statistics to produce retrievals.

In a discussion of early TIROS-N temperature retrievals, Phillips, McMillin, Gruber and Wark (1979) showed, among other things, that the variance of satellite derived temperatures about their mean is often significantly less than the variance of co-located RAOB temperatures about their mean for most layers in the atmosphere. The ratio of variance of TIROS-N soundings to the variance of RAOBs are shown to be as low as 0.2-0.3 in the higher layers and generally range somewhere between 0.5 and 0.9. This implies that actual temperature information gets filtered by the satellite sounding system, often severely.

Schlatter (1981) showed the results of comparisons of TIROS-N temperature soundings with an NMC (optimum interpolation) analysis of RAOB data. The TIROS-N soundings were done using procedures described by Smith, Woolf, Hayden, Wark, and McMillin (1979). The NMC analysis, done without satellite soundings during the period of Schlatter's comparisons, is described by Bergman (1979) and McPherson, Bergman, Kistler, Rasch and Gordon (1979). Schlatter's comparisons showed a significantly different pattern of error between TIROS-N soundings and analyzed RAOB data than one normally sees in comparisons of satellite soundings directly with co-located RAOBs. The rms differences between TIROS-N soundings and NMC analyzed temperatures shown by Schlatter did not exhibit the larger values at tropopause level that many other studies have shown. (Eg. Fig. 6 from Schlatter as compared with Fig. 4 from Smith, Woolf, Hayden, Wark and McMillin (1979)). Schlatter showed rms errors of about 2K from 700-70 mb with no apparent strong maximum near the tropopause. Smith, et al (1979) showed rms deviations between TIROS-N soundings and co-located RAOBs which achieved local maxima around 200mb of 2.5- 3.0K. While somewhat mixed, the results of Phillips, et al (1979) also show local maxima in errors at tropopause level when considering deviations between TIROS-N soundings and co-located radiosondes. Halem, Ghil, Atlas, Susskind and Quirk (1978) examined NIMBUS-6 soundings during two periods of the Data Systems Test and also found prominent errors at tropopause level ranging to as much as 3K.

Schlatter's result, when compared with the other studies cited above, illustrates the smoothing of the RAOB information which is effected by the NMC analysis and which leaves a result involving the comparison of two fields each of which are smoother than the original RAOB data. The two smoothed fields (TIROS-N and analyzed RAOB) seem to agree with each other better, most likely, than either would

compare with the original RAOB information. That is, the original information in the ambient temperature field has been transformed into the smoother information contained in the analysis. Further, the radiative transfer physics and the retrieval algorithm also transforms the ambient temperature structure information into smoothed temperature retrieval information. The comparison of these two fields, then, is that of two smoothed and distorted versions of the original temperature information possessing much more structure.

In an earlier study, Schlatter and Branstator (1979) showed, in fact, that the degree of accuracy in comparing NIMBUS-6 temperature retrievals to analyzed radiosonde profiles depends significantly on the amount of smoothing performed on the radiosonde data during the analysis cycle. If satellite retrievals are subjected to a further analysis routine - alone or mixed with radiosonde data - the information content of the radiance measurements would be further distorted.

The issue of the transformation of atmospheric temperature information through the various stages of distortion which it encounters in a particular application, is quite important to meteorologists. Satellite temperature soundings will continue to be used in observing the structure of atmospheric systems. It is important to know rather accurately what the relationship is between the retrieved temperature structure and the ambient temperature structure. Sounding systems such as VAS will be providing data from which meteorologist will hope to infer the thermal structure of mesoscale phenomena. The inference of structure and variation on that scale will undoubtedly pose an even more difficult problem than the large scale weather prediction problem. Moreover, one may generally expect that satellite soundings constructed to analyze mesoscale systems, or to initialze models thereof, will need to possess more detailed, accurate vertical and horizontal structure than is now obtained for the global problem in order to have a positive impact in that arena.

In the section to follow, a systematic approach to investigating the transfer and distortion of information in the temperature retrieval problem is discussed.

3. The flow of information

To quantitatively analyze the flow of information, it is necessary first to define information for this study. A large ensemble of RAOB profiles and corresponding satellite radiometer observations will form the basis of the data to be analyzed. The RAOB data have been assembled under the guidance of N. Phillips, NOAA/NMC to serve as the basis of

several tests of satellite sounding systems. Using this data, we have synthesized radiance observations that would be gathered by the HIRS and AMTS(*) sounding instruments. Information for this study is defined to be the variance spectrum of empirical orthogonal functional representation of the ensembles of either temperature profiles or radiance values in each oval in Figure 1. While the data in each oval in Figure 1 may be taken as a representation of the data in any other oval, it is certainly expected that the corresponding variance spectra will be quite different. For example, Figure 2 shows plots of cumulative percent explained variance plotted as functions of the number of empirical orthogonal functions used in representing the ensemble of RAOBs and corresponding (synthesized) satellite radiances for 200 wintertime observations between 30 and 60 north latitude. The broad spectrum of RAOB information is compressed into fewer significant orthogonal functions of radiance.

Clearly, Fig. 2 demonstrates the significant smoothing of information which occurs even before a satellite measurement is made. A temperature retrieval method based only on the radiative transfer physics (that is, not incorporating a priori information on the atmosphere's thermal structure) should exhibit the same drastic smoothing of information.

Now, in fact, satellite temperature sounding algorithms generally add structure information to the radiance information in producing retrievals. For example, highly statistical temperature retrieval methods, such as the regression method of Smith, Woolf and Jacob (1970) or its structured variant (Smith and Woolf (1976)) will add a good deal of structure information by using historical knowledge of the atmosphere's thermal structure and its relationship to satellite radiance measurements. In fact, since the physics of radiative transfer is not explicitly included in these algorithms, such methods produce retrievals with atmosphere-like thermal structure even though they operate on the much smoother radiance fields. In the middle of the spectrum of retrieval methods, there are physical-statistical methods, such as minimum rms (Foster (1961), Strand and Westwater (1968)), known also as maximum probability (Rodgers (1970)), statistical regularization (Tichonov, as quoted by Kondratiev and Timofeyev (1970)), which blend historical thermal information with the radiative transfer physics to produce a retrieval possessing more structural detail than is provided solely by the radiances. Finally, there are methods which are mostly physical in the sense that no a priori statistics are used at all. Such physical methods include the minimum

---

(*) See Kaplan, Chahine, Susskind and Searle (1977)

information inverse method (Foster (1961), Smith, Woolf and Fleming (1972)), and direct, relaxation methods such as those by Chahine (1968) and Smith (1970) or Smith and Woolf (1981). These physical methods, as with some of the others above, do make use of à priori transmittance data, and all methods use some à priori first guess field.

Statistical methods (pure or mixed) add historical thermal information to the radiance information in producing an estimate of the atmosphere's thermal field. If the impact of the satellite observation on some analysis or forecast is to be fairly assessed, then it is important to distinguish how much of the retrieval is really due to the radiance observation and how much is due to the climatology of the atmosphere.

4. The method of analysis of information flow

Let us imagine an ensemble of RAOBs which we consider to define 100% of the thermal structure information for a given situation. For the present study, we will restrict our view to only the vertical dimension so that this original information may be described by the empirical orthonormal functions of the ensemble (eigenfunctions of the covariance matrix of the RAOBs) and the corresponding eigenvalues which give the variance described by each orthonormal structure function. We consider that the eigenvalues are normalized by the total variance of the ensemble (the trace of the covariance matrix) so that they represent fractions of total variance explained by each eigenfunction. If these eigenvalues are ranked from highest to lowest value and accumulated, one obtains curves such as those in Fig. 2 labeled TEMPERATURE.

Now, suppose radiances for some given satellite sounding instrument are synthesized using the radiative transfer equation. Then, that ensemble may be similarly decomposed to produce a variance spectrum such as that labeled RADIANCE in Fig. 2. The variance spectra for the ensemble of retrievals may be compared with the spectra for the RAOBs to assess the distortion of information as it passes through the radiative transfer equation and through the retrieval algorithm.

In the remainder of this paper, four temperature retrieval algorithms distributed between the extremes of pure statistical to pure physical will be tested to discover their information transfer characteristics. The methods are the Regression Method (Smith, Woolf and Jacob (1970)), Statistical Regularization (Foster (1961)), Minimum Information (Foster (1961), Smith, Woolf and Fleming (1972)) and the iterative, physical method of Smith (1970), as modified by Smith and Woolf (1981). The Smith iterative algorithm is generally a numerically stable, physical method. It involves no sensitive matrix inverse step, and no

à priori statistics except for a first guess profile and à priori estimates of atmospheric transmittances. The regression algorithm is also mathematically stable but possesses the greatest statistical influence of à priori data with virtually no explicit radiative transfer physics involved. The statistical regularization method involves a matrix inversion of the linearized radiative transfer equation - hence, has the possibility of numerical instability through ill-conditioning -- but is efficiently regularized through the use of à priori statistical information derived from historical temperature data. The minimum information special case of statistical regularization also involves matrix inversion of the radiative transfer physics with regularization obtained through a minimal amount of à priori statistical information; namely, a single, mean value of atmospheric temperature variance.

In the analysis to be presented here, several important simplifications or approximations are involved. First, satellite measurements were synthesized from RAOB profiles without any moisture, ozone or cloud effects. For some experiments, random errors were added to these simulated measurements while other experiments were conducted with "perfect" measurements. Thus, our simulation of satellite measurements is much cleaner than actual measurements would be. Also, only results for the HIRS sounding instrument are included in this paper. Retrievals involving transmittance weighting functions made use of exactly the same functions as those used to synthesize the radiance measurement. Thus, even in iteration cycles of a retrieval algorithm, "correct" transmittances were used throughout. Next, the surface contribution to the radiance measurements is subtracted exactly from the problem so that the integral term in the radiative transfer equation is isolated perfectly. The minimum information and statistical regularization methods apply to linearized versions of the radiative transfer equation in which radiative transfer kernels and temperature deviations about the current temperature estimate replace the transmittance weighting functions and Planck function profiles. (See Conrath (1972) for the linearized version of the direct problem used here.) These two methods are also iterated with the required statistical information recomputed at each step of the iteration (either the whole temperature covariance matrix about the current estimate, for statistical regularization, or the average diagonal element for minimum information). Finally, eleven CO2 sounding channels of the HIRS instrument are used in this study -- the same used by Thompson (1982a). The instrument weighting functions are computed for each object profile rather than being computed for the current (or first) estimate. The noise covariance matrix for the HIRS was formed as a diagonal matrix using values supplied by L. McMillin of NOAA/NESS and are explicitly given by Thompson

(1982a) as HIRS2. Finally, in Fig. 2, the eigenvalues were normalized by the total variance of the appropriate ensemble. In considering an ensemble of temperature retrievals, it is more interesting to normalize on the total variance of the original RAOB information so that one can discuss the relative amount of original information which is explained by the ensemble of retrievals. Thus, if P is the total variance of a given ensemble of retrievals, and Q is the total variance of the original RAOB ensemble, then an adjustment factor F=P/Q may be applied to each eigenvalue to convert explained test ensemble variance to explained RAOB ensemble variance. It should be explained that a singular value decomposition is performed on each retrieval ensemble independent of the RAOB information, except that the covariance matrix contains variances and covariances about the RAOB mean rather than the mean of the given retrieval ensemble. The scaling performed by the multiplication by (P/Q) merely transforms the retrieval covariance matrix eigenvalues to numbers which reflect a percentage of total variance as though the total variance was that of the RAOB ensemble. The ensemble covariance matrix and the structure of the eigenfunctions, however, reflect the variability of the retrievals and not the variability of the RAOB information. Thus, to speak in terms of how much RAOB variance is "explained" by a given eigenfunction of the retrieval covariance matrix is, strictly speaking, an incorrect phrasing but will be used here anyway.

5. Results

RAOB data from the Phillips data set collected over ocean surfaces in January were partitioned into a tropical set (30S,30N) and a mid-latitude set (30N,60N). Radiance measurements were synthesized and each of the retrieval algorithms were applied to the result. For this study, à priori statistical information was derived using one-half of each ensemble, and retrievals were performed on the independent remaining half. There were 200 mid-latitude profiles divided into dependent and independent sets of 100 each, and 218 tropical profiles divided into sub-sets of 109 each. As described in the previous section, a singular value decomposition was performed on each ensemble, and eigenvalues were F-adjusted.

Fig. 3 shows a spectra of F-adjusted, cumulated eigenvalues of the information for the mid-latitude data. The RAOB curve shows a rather broad spectrum of structure information in which 99% of the variance information is spread over about 15 orthogonal eigenfunctions. Radiances were converted to brightness temperatures using the Planck relationship, and the spectrum of this information is labeled BRIGHT. Since there are 65 levels of RAOB information but only 11 channels of radiance information, the total variance of the brightness temperature ensemble

was further adjusted by the factor (65/11) in order that results could be compared to RAOBs and retrievals. Comparing the RAOB and BRIGHT curves, one sees the substantial smoothing of information effected by the radiative transfer physics of the atmosphere. The integration of the detailed thermal structure of the atmosphere into 11 channels of radiometric information is, indeed, a drastic process. The brightness spectrum is assymptotic to the value 51.5 which means that the total variability of information in the radiance data is only about 51.5% of the total variability of the information in the RAOB data. This is a significant reduction of information content. Temperature retrieval algorithms can extract no more information than this from the radiance data alone. The corollary is, of course, that any extra information in an ensemble of retrievals has to come from other sources, such as à priori data.

The curve labeled SMITH represents the spectrum of information in the retrieval ensemble using the Smith physical iterative method. As discussed earlier, the Smith method does not use à priori statistics as such but, as the other methods, does use a first guess profile, which is the RAOB mean profile here. Further, the transmittance information, which here has been computed exactly for each RAOB profile to be retrieved, is a form of à priori information and helps to expand the spectrum of information. Hence, the SMITH spectrum is assymptotic to 69.8% of the total variability of RAOB information, which is somewhat more than just the brightness information alone.

On the other end of the range of retrieval methods, regression retrieval results form the spectrum labeled REGRESSION in Fig. 3. The regression method does not use à priori estimates of atmospheric transmittances but does use à priori statistical information in the fullest possible way. The information spectrum is the broadest of any shown. In fact, in this case the regression retrievals exhibit slightly more total variance than the RAOB data. The difference between the REGRESSION and BRIGHT spectra reflects the amount of à priori information <u>added</u> to the satellite measurement in producing the temperature retrieval. Evidently, this added information is a significant amount of the total information in those retrievals. For example, the total RAOB variance is 2340(K^2). The adjusted total variance of the brightness temperatures is only about 51.5% of that. Adding à priori RAOB statistics through the regression approach brings the total variance of the regression retrievals to 2350(K^2). Thus, the à priori statistics imbedded in the regression method contributes about 1145(K^2) to the total variance of the retrieval ensemble which means that the regression retrievals are about 51.3% satellite information and 48.7% à priori radiosonde information. One should keep this in mind when assessing the impact of "satellite temperature

retrievals" on, say, numerical prediction models since the satellite data seems to have only a limited impact on "satellite temperature retrievals" depending on the method used.

The information spectra curves for statistical regularization and minimum information retrieval methods are also shown in Fig. 3. The minimum information algorithm yields a similar, although slightly broader information spectrum in comparison with the Smith method. The minimum information method is almost a pure physical method except for the mild influence of the à priori vertical mean temperature variance included in the retrieval matrix. Thus, the spectrum is assymptotic to a slightly larger percentage (73.0%) of total RAOB variance than the Smith method. The statistical regularization which includes both the physics of radiative transfer and the covariance statistics of the à priori radiosonde information gives a broader spectrum than either the minimum information or Smith method, but one which is flatter than the regression results. The total variance of the ensemble of statistical regularization retrievals is 2085(K^2) , about 89.1% of the total variance of the original RAOB set.

The stability and reliability of a retrieval method can be assessed by examining the error characteristics of the method. Fig. 4 shows vertical profiles of the root mean square retrieval errors for the results in Fig. 3. The error traces are similar with regression and statistical regularization methods showing better accuracy than minimum information and Smith iterative methods. Thus, a combination of results, such as contained in Figs. 3 and 4, are necessary to make a reasonable assessment of the fidelity of information transfer.

Figs 5(a)-(f) show the actual empirical orthogonal eigenfunctions of the various covariance matrices for the mid-latitude data. These figures clearly show the smoothing and distortion of the structure information due to the radiative transfer integration and the retrieval, or inverse step. The Smith and minimum information methods show the most smoothing of the vertical structure. Once again, these two methods make minimal use of à priori data from past radiosonde observations. Thus, the structure shown, even though drastically smoothed, exhibits the vertical thermal structure information contained in the radiance measurements. On the other hand, the regression and statistical regularization retrieval methods recovers more accurately the vertical structure of the thermal field, but clearly this is due to the incorporation of historical data on that structure. By the third or fourth eigenfunction, the structure of the original RAOB data is very poorly represented by any of the retrieval methods. A curious feature of these results should be pointed out. As the

spectra in Fig. 3 become flat, there is an ambiguity in ranking the eigenvalues. That is, successive eigenvalues are small and not significantly different from each other in this limit. Thus, objective ordering of the eigenvalues may actually lead to an incorrect ordering of the structure functions. In Fig. 5(d), for example, the fourth structure function of the Smith retrievals is shown in comparison with the third structure function of the RAOBs. In Fig. 5(e), the third Smith function and the fifth minimum information function bore the closest resemblance to the fourth RAOB function. In Fig. 5(f), the sixth minimum information function is shown in comparison with the fifth RAOB function. These events are not particularly troublesome but indicate that care should be taken in truncating sets of eigenfunctions in representing atmospheric soundings. Of course, since degradation of the structure functions begins with the first function itself, one expects that it grows continually worse through higher order functions.

Figs 6 and 7 show results for the mid-latitude case when random errors are added to the synthesized measurements. Errors were drawn randomly from a population whose standard deviations were equal to the expected noise levels of the channels of the HIRS instrument. These noise values were the current estimates for HIRS and were provided by L. McMillin of NOAA/NESS. For the results in Figs 6 and 7, the same error contaminated radiances were presented to each algorithm.

Now the variance of the set of random errors added to the synthetic measurements is significantly less than the variance, over the mid-latitude ensemble, of the synthetic measurements themselves. Thus, the impact of this noise on the information spectrum for <u>brightness temperatures</u> is rather minor. The error contaminated brightness temperatures have total variance of 1214(K^2), only slightly larger than the 1205(K^2) for the uncontaminated measurements. Yet, the temperature retrieval algorithms respond to these errors in various ways. The regression, statistical regularization, and minimum information variance spectra are flattened in this experiment in comparison with Fig. 3, while the Smith variance spectrum is slightly broadened. This result was unexpected for it implies that, except for the Smith method, the temperature retrieval algorithms actually overcompensated for the radiometer noise and produced retrievals with less overall variance than the retrievals using error-free measurements. On the other hand, the error profiles shown in Fig. 7 for these experiments clearly show a degradation of accuracy for retrievals using error contaminated radiances. Curiously, the Smith method behaved very well in this experiment with only a very minor degradation in overall accuracy. Thus, in analyzing the information transfer and distortion in sounding systems, it is of importance to first examine noise-free cases in order

to establish a baseline which involves only the radiative transfer integration and the retrieval method.

It was also of interest to test the effect of radiometer noise level estimates on the information transfer. The statistical regularization, minimum information, and Smith methods were iterated until either the root mean square, instrument noise scaled deviations between estimated and actual radiances fell below 1, or until the rms temperature retrieval error reached a minimum. In addition, the statistical regularization and minimum information methods contain the radiometer noise covariance matrix explicitly in the inverse solution. Thus, assumed radiometer noise values will have an impact on the results.

A series of experiments for the mid-latitude band was performed in which the radiometer noise values were increased to values approximately equal to 1% of spectral radiances produced by a mean atmospheric profile. (*) These noise values are used both in the noise covariance matrix and in the convergence criteria. Figs 8 and 9 show the results, for noise-free radiances, which should be compared with results in Figs 3 and 4. The RAOB, BRIGHT and REGRESSION results are not changed by the change in radiometer noise characteristics. The remaining three retrieval methods each produced smoother variance spectra with less total variance when the expected noise values were increased.

Figs 10 and 11 show results for the tropical latitude band using noise-free synthetic radiance measurements. The total RAOB variance for the tropical data set was 3810(K^2) as compared with 2340(K^2) for the mid-latitude data. Notice also that the brightness temperature variance was a much smaller fraction of RAOB variance in the tropics: only 27.3% or slightly more than one-fourth. Consequently, all retrieval methods in the tropics recovered smaller fractions of the RAOB information than in mid-latitudes because the information was more drastically filtered by the radiative transfer physics. A comparison of Fig. 11 with Fig. 4 shows that the tropical RAOB variance was smaller in the troposphere but larger in the stratosphere when compared with mid-latitudes. Generally speaking, the retrieval errors exhibit this same behavior with the regression retrievals showing the most reliability, even in the tropical stratosphere.

(*) The noise values are rounded so that there is a single value for the 15μ CO2 channels and a single value for the 4.3μ CO2 channels which are, respectively, 0.63 and 0.0044 $mw/(m^2-sr-cm^{-1})$.

Figs 12 and 13 show tropical results with synthesized radiances which have been contaminated by random errors. As in the mid-latitude test, all methods except the Smith method showed a slight flattening of the information spectrum and an increase in overall rms error. The Smith method showed an increase in overall variance and handled the radiance errors reasonably well.

Experiments in the tropics using the larger "1%" instrument noise values behaved in a manner similar to those experiments in mid-latitudes. The results are not shown here.

To summarize our experiments, Table 1 shows values of the 10-1000mb mean value of overall rms retrieval errors for each latitude band, each simulated version of the HIRS instrument, for both noise-free and noise-contaminated measurements. As seen, the regression retrieval method gave the best overall results. This is to be expected when the à priori statistics at hand are truly representative of the profiles to be retrieved. The Smith iterative method exhibited highly favorable results for all categories. This is a particularly important finding because that method depends least on à priori data and, hence, should suffer least if object profiles are not well represented by à priori data. The two matrix inverse methods exhibit less stability to radiometer errors, although the statistical regularization method operated best for error-free measurements and "correct" à priori statistics.

Table 2 shows what we shall call the impact of satellite data on satellite temperature retrievals. The entries are the ratio of the (adjusted) total variance of brightness temperatures to the total variance of various temperature profile ensembles. The brightness temperatures represent the information measured by a satellite device. As seen in Table 2, this information is only about one-half the RAOB information in mid-latitudes, and only about one-fourth the RAOB information in the tropics. Retrieval methods using a lot of à priori information (Eg. regression) get much of their variance structure from this à priori information. Thus, the satellite data contributes only a relatively small amount of the total retrieval information in this method. Physical methods (Eg. Smith iterative) are more faithful to the satellite measurement information - hence, the satellite data contributes a relatively large fraction of the total retrieval information. In mid-latitudes, the regression and Smith methods show least sensitivity to measurement noise while all but the Smith method show mild sensitivity in the tropics. The Smith and minimum information methods would exhibit the least sensitivity to "incorrect" à priori statistics.

6. Conclusions and discussion

In this paper, we have had an extensive look at the transfer and distortion of information concerning the atmosphere's thermal structure as this information takes on the different forms relevant to the satellite temperature retrieval problem. The contribution, here, has been to quantify this transfer process since most workers in the field understand that distortion takes place. Our analysis method has been to perform singular value decompositions of the various ensembles of information and then to compare the variance spectra of each version of the information and to compare ensemble averaged errors between representations. Specifically, the goal has been to quantitatively assess the distortion of atmospheric thermal information as it acts through the physics of radiative transfer to produce the outgoing radiation which is measured by a satellite radiometer, and the further distortion caused by various, classical temperature retrieval algorithms operating on these radiation measurements.

We have shown that the process of radiative transfer in the atmosphere -- being an integral process transforming atmospheric temperature into outgoing radiation -- causes a drastic smoothing of information. That is, the total variance of outgoing radiation (rendered as a finite set of brightness temperatures) is half or less of the total variance of the atmospheric thermal field, even when values have been adjusted for the different numbers of measuring intervals for the two quantities.

Temperature sounding systems which produce retrievals with a large amount of variance, and with greater apparent vertical resolution than simple profiles of brightness temperature, generally do so by adding à priori information (virtual measurements in the language of Rodgers (1976)), taken usually from past observations of the temperature profile, or from a numerical forecast model. While passing no judgement on the usefulness of this technique in any given case, we have attempted to quantify how much à priori information is added in each of several types of temperature retrieval scheme. Thus, for mid-latitude retrievals using a statistical correlation-regression technique, with representative à priori statistics, about 48-49% of the total variance in an ensemble of retrievals is attributable to the à priori data. The total variance of the regression retrievals themselves is about the same as the total variance of the atmospheric thermal field producing the radiances upon which the retrievals are based. Using a physical retrieval technique, such as the iterative method of Smith (1970), about 73-75% of the total variance of the retrievals is attributable to radiance information, while only 25-27% is attributable to à priori information such as atmospheric transmittance functions. However, the total variance of these retrievals is only about 70% of the total variance of the original thermal field. Retrieval algorithms

such as minimum information, or statistical regularization produce results between these two extremes, and reflect the effective mix of physics and à priori statistics of those methods.

In examining the average temperature retrieval errors, we find results consistent with other investigators. Namely, of the four retrieval methods tested, the ranking by overall accuracy and stability to measurement errors is regression (highest), Smith iterative, statistical regularization, minimum information.

The vertical profiles of the empirical orthogonal eigenfunctions of each retrieval ensemble were compared against the same for the RAOB data defining the original information. The smoothing and distortion of these functions has been specifically illustrated. Generally speaking, we have shown that fidelity of the vertical structure of satellite retrieved temperature profiles is rather low for physical retrieval methods. The increase in fidelity for physical-statistical or pure statistical retrievals is attributable, therefore, to the inclusion of à priori data. As suggested by the work of Crosby and Weinreb (1974) and of Spanküch, Timofeyev and Güldner (1977), the validity of this process of "fleshing out" the vertical structure in satellite temperature retrievals is only as good as the correctness of the atmospheric statistics for each object retrieval.

We end this paper with a few philosophical remarks. There is, and should continue to be, a question concerning the impact of satellite observing systems on the analysis and prediction of atmospheric behavior. The Data Systems Test presented our first comprehensive look at the impact on the large scale numerical prediction problem. This test has produced a mixture of results (See Tracton, Desmaris, VanHarren, and McPherson (1980), Ghil, Halem and Atlas (1979)) which indicates that the impact is a complicated function of initialization and assimilation procedures and the numerical forecast model itself (Atlas, et al (1981)). Our results here show that even the question of the impact of satellite data on satellite temperature soundings is one which produces a mixture of results depending on the type of retrieval algorithm used and the representativeness of à priori data. Because of the nature of the data set used here, we were not able to simulate the initialization-assimilation step to measure the further smoothing of the original measurements in preparation for the large scale problem. We strongly recommend that this be done. The results shown here indicate that statistically optimized satellite temperature retrievals are very heavily influenced by the statistics so that impact tests may be assessing the effect of à priori statistics on weather forecasting as much as they are assessing the impact of satellite observations

on forecasting. It would be interesting to conduct an impact test using, say, a physical method such as the Smith iterative method. Alternatively, one could seek a way to conduct the assimilation step in radiance space instead of temperature space, perhaps avoiding the inverse problem altogether.

We expect that these issues will become even more pointed as one delves deeper into mesoscale applications of satellite soundings. To achieve mesoscale observations from satellites in the horizontal or temporal sense such as through VAS, (Smith, Suomi, et al (1981)) is significantly different than to achieve the correspondingly relevant vertical scales for these meteorological systems. Presumably, the interesting vertical structure of mesoscale systems will have to be gotten from à priori data, from independent observations such as discussed by Westwater and Grody (1980), or, possibly, from a significantly different incorporation of radiosonde observations (Fritz (1977)). To the extent that atmospheric mesoscale systems are not merely miniatures of the global scale system, we suggest that global scale satellite sounding procedures are not necessarily the optimum techniques for sounding mesoscale weather systems.

Acknowledgements

The authors would like to acknowledge the help of J. Susskind of NASA/GLAS and J. Rosenfield, Sigma Data Corp. for extensive help in getting HIRS instrument weighting function algorithms together and L. McMillin of NOAA/NESS for providing NESS-estimates of radiometer noise values for HIRS. This research was supported by the National Aeronautics and Space Administration through the Goddard Laboratory for Atmospheric Sciences under Grant NSG-5209.

REFERENCES

Atlas, R., M. Halem, and M. Ghil, (1981): The effect of model resolution on satellite sounding data impact. Submitted to XXXXX

Backus, G.E., and J.F. Gilbert, (1968): The resolving power of gross earth data. Geophys. J. Roy. Astron. Soc., 16, 169-205.

Bergman, K., (1979): Multivariate analysis of temperatures and winds in using optimum interpolation. Mon. Wea. Rev., 107, 1423-1444.

Chahine, M.T., (1968): Determination of the temperature profile in an atmosphere from its outgoing radiance. J. Opt. Soc. Amer., 58, 1634-1637.

Conrath, B.J., (1972): Vertical resolution of temperature

profiles obtained from remote radiation measurements. J. Atmos. Sci., 29, 1262-1272

Crosby, D.S., and M. P. Weinreb, (1974): Effect of incorrect atmospheric statistics on the accuracy of temperature profiles derived from satellite measurements. J. Statist. Comput. Simul., 3, 41-51.

Foster, M., (1961): An application of the Wiener-Kolmogorov smoothing theory to matrix inversion. J. SIAM, 9, 387-392.

Fleming, H.E., and W.L. Smith, (1972): Inversion techniques for remote sensing of atmospheric temperature profiles. Proc. Fifth Symp. on Temperature, Washington, DC. 2239-2250. Inst. Soc. Amer., 400 Stanwix St., Pittsburg, PA.

Fritz, S., (1977): Temperature retrievals from satellite radiance measurements - an J. Appl. Meteor., 16, 172-176.

Ghil, M., M. Halem and R. Atlas, (1979): Time continuous assimilation of remote sounding data and its effect on weather forecasting. Mon. Wea. Rev., 107, 140-171.

Halem, M., M. Ghil, R. Atlas, J. Susskind, and W. Quirk, (1978): The GISS sounding temperature impact test. NASA Technical Memorandum 78063. NASA/GSFC, Greenbelt, MD. 421p.

Kaplan, L.D. M.T. Chahine, J. Susskind, and J. Searle, (1977): Spectral bandpasses for a high precision satellite sounder. Appl. Optics, 16, 322-325.

Kondratiev, K. and J.M. Timofeyev, (1970): Termiceskoe Zondirovanic Atmosfery so Sputnikov. Gidroizat, Leningrad.

McPherson, R.D., K. Bergman, R. Kistler, G. Rasch, and D. Gordon, (1979): The NMC operational global data assimilation system. Mon. Wea. Rev., 107, 1445-1461.

Phillips, N., L. McMillin, A. Gruber, and D. Wark, (1979): An evaluation of early operational temperature soundings from TIROS-N. Bull. Amer. Meteor. Soc., 60, 1188-1197.

Rodgers, C., (1970): Remote sounding of the atmospheric temperature profile in the presence of cloud. Q. J. Roy. Meteor. Soc., 96, 654-666.

Rodgers, C., (1976): The vertical resolution of remotely sounded temperature profiles with a priori statistics. J. Atmos. Sci., 33, 707-709.

Schlatter, T.W., (1981): An assessment of operational TIROS-N temperature retrievals over the United States. Mon. Wea. Rev., 109, 110-119.

Schlatter, T.W., and G.W. Branstator, (1979): Estimation of errors in NIMBUS-6 temperature profiles and their spatial correlation. Mon. Wea. Rev., 107, 1402-1413.

Smith, W.L., (1970): Iterative solution of the radiative transfer equation for the temperature and absorbing gas profile of an atmosphere. Appl. Optics, 9, 1993-1999.

Smith, W.L., V. Suomi, W. Menzel, H. Woolf, L. Sromovsky, H. Revercomb, C. Hayden, D. Erickson, F Mosher, (1981): First sounding results from VAS-D. Bull. Amer. Meteor. Soc., 62, 232-236.

Smith, W.L., and H.M. Woolf, (1976): The use of eigenvectors of statistical covariance matrices for interpreting satellite sounding radiometer observations. J. Atmos. Sci., 33, 1127-1140.

Smith, W.L., and H.M. Woolf, (1981): Algorithms used to retrieve surface-skin temperature and vertical temperature and moisture profiles from VISSR Atmospheric Sounder (VAS) radiance observations. Proc. AMS Fourth Conf. on Atmos. Rad., 13-17.

Smith, W.L., H.M. Woolf, and H.E. Fleming, (1972): Retrieval of atmospheric temperature profiles from satellite measurements for dynamical forecasting. J. Appl. Meteor., 11, 112-122.

Smith, W.L., H.M. Woolf, C.M. Hayden, D.Q. Wark, and L.M. McMillin, (1979): The TIROS-N operational vertical sounder. Bull. Amer. Meteor. Soc., 60, 1177-1187.

Smith, W.L., H.M. Woolf, and W.J. Jacob, (1970): A regression method for obtaining real-time temperature and geopotential height profiles from satellite spectrometer measurements and its application to NIMBUS-III SIRS observations. Mon. Wea. Rev., 98, 582-603.

Spänküch, D., Y.M. Timofeyev, and J. Güldner, (1977): Comparison of different inversion methods for the determination of vertical temperature profiles from simulated satellite measurements in narrow spectral intervals. Zeitschrifte fur Meteorologie, 27(4), 234-242.

Strand, O.N., and E. R. Westwater, (1968a): Statistical estimation of the numerical solution of a Fredholm integral equation of the first kind. J. Assoc. Comp. Mach., 15, 100-114.

Strand, O.N., and E.R. Westwater, (1968b): Minimum rms estimation of the numerical solution of a Fredholm integral equation of the first kind. on S.I.A.M. J. Numer. Anal., 5, 287-295.

Thompson, O.E., J. Eom, and J. Wagenhofer, (1976): On the resolution of temperature profile fine structure by the NOAA satellite VTPR. Mon. Wea. Rev., 104, 117-126.

Thompson, O.E., (1932a): HIRS-AMTS satellite sounding system test - Theoretical vertical resolving power. Submitted to J. Appl. Meteor. October, 1981.

Thompson, O.E., (1982b): HIRS-AMTS satellite sounding system test - Empirical vertical resolving power. Submitted to J. Appl. Meteor. October, 1981.

Tracton, S., A. Desmaris, R. Van Haaren, and R. McPherson, (1980): The impact of satellite soundings upon the National Meteorological Center's analysis and forecast system - The Data Systems Test results. Mon. Wea. Rev., 108, 543-586.

Westwater, E.R. and N.C. Grody, (1980): Combined surface and satellite based microwave temperature profile retrieval. J. Appl. Meteor., 19, 1438-1444.

TABLE 1. 10-1000mb mean of root mean square retrieval errors.

30N-60N	RAOB MEAN	REGRESSION	STAT. REG.	MIN. INF.	SMITH IT.
HIRS2 no error	6.042(K)	1.730	1.625	2.882	2.702
HIRS2 errors	-	2.073	3.517	4.047	2.703
HIRS1 no error	6.042	1.730	2.208	2.747	3.049
HIRS1 errors	-	2.440	3.332	3.322	2.989

30S-30N	RAOB MEAN	REGRESSION	STAT. REG.	MIN. INF.	SMITH IT.
HIRS2 no error	4.885	1.627	2.896	3.656	2.703
HIRS2 errors	-	1.679	3.141	3.896	2.647
HIRS1 no error	4.885	1.627	2.006	3.190	3.088
HIRS1 errors	-	2.176	2.879	3.394	3.217

TABLE 2. The impact of satellite data on satellite temperature soundings. Ratio of adjusted total variance of satellite brightness temperature ensemble to total variances of other temperature profile ensembles.

	[TOTAL VARIANCE X]/[TOTAL VARIANCE Y]			
	MID-LATITUDES 30N - 60N		TROPICS 30S - 30N	
[X/Y]	No Errors	Errors	No Errors	Errors
BRIGHT/RAOB	51.4%	51.9%	27.3%	27.1%
BRIGHT/REGRESSION	51.4	53.5	28.8	28.7
BRIGHT/STAT. REG.	57.7	76.2	36.7	38.4
BRIGHT/MIN. INF.	70.5	96.8	64.1	65.0
BRIGHT/SMITH IT.	73.8	73.9	84.3	66.1

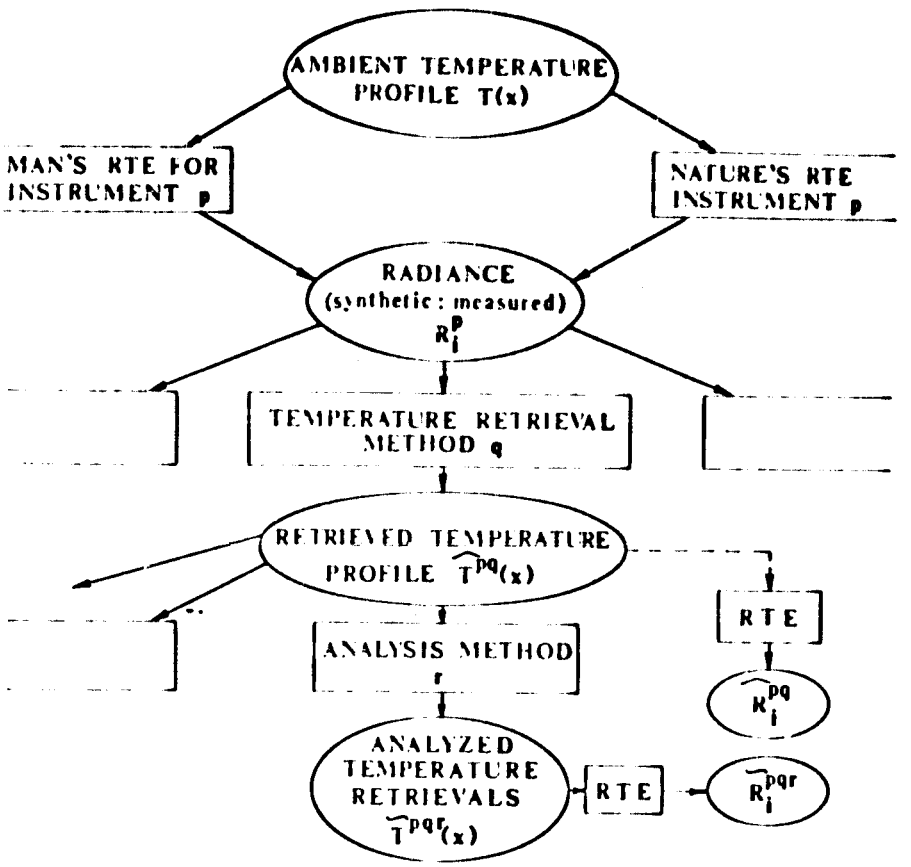

Figure 1. The flow of information through a satellite temperature retrieval and analysis system. Ovals represent different versions of information concerning the atmospheric thermal structure.

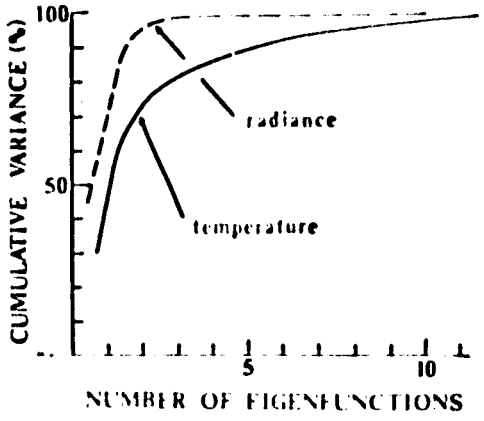

Figure 2. Singular value decomposition of temperature and corresponding satallite measured radiance information. Shown is the spectrum of cumulative percent explained variance in the empirical orthogonal functional representation of the information of each type.

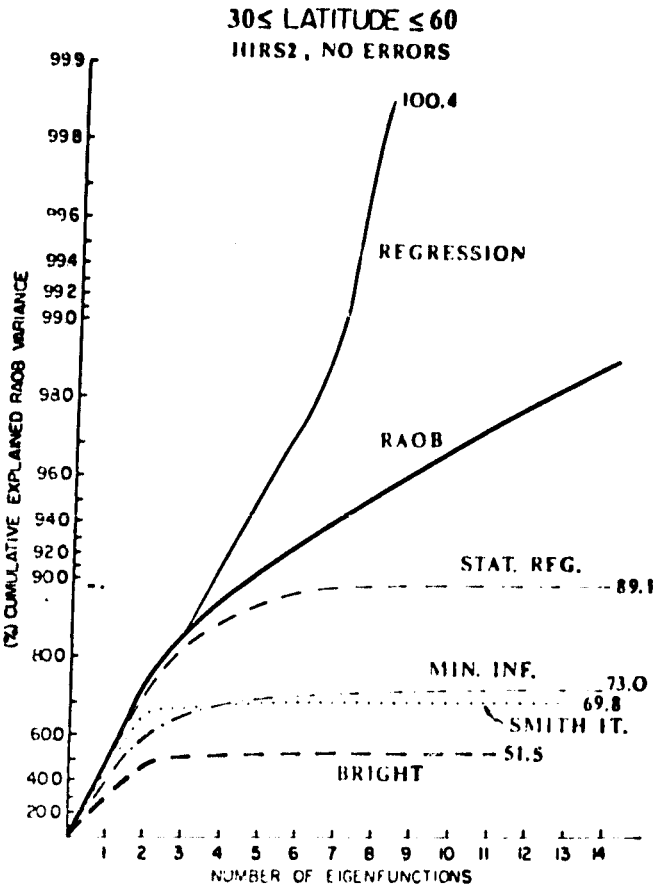

Figure 3. Cumulative percent explained RAOB variance for various satellite temperature retrieval methods in mid-latitudes (30N, 60N) for January. Also shown are RAOB and satellite brightness temperature information spectra. Radiance measurements are synthesized for the HIRS sounder with no errors. (See text for explanation.)

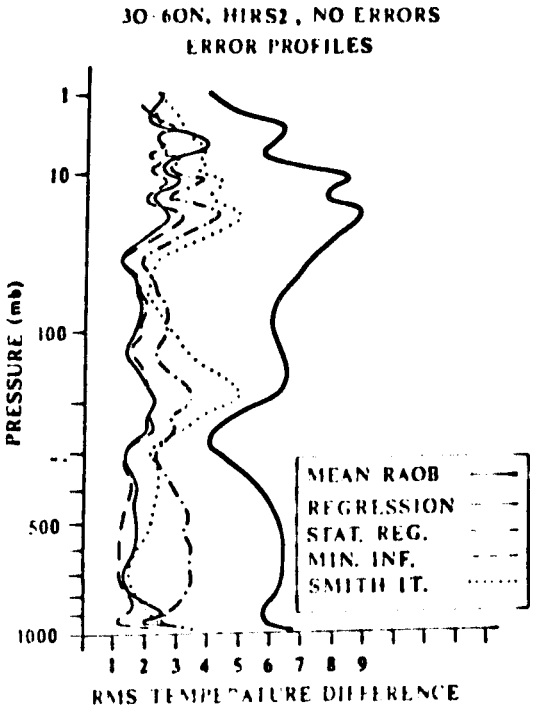

Figure 4. Vertical profiles of root mean square temperature retrieval errors for mid-latitude cases included in Fig. 3.

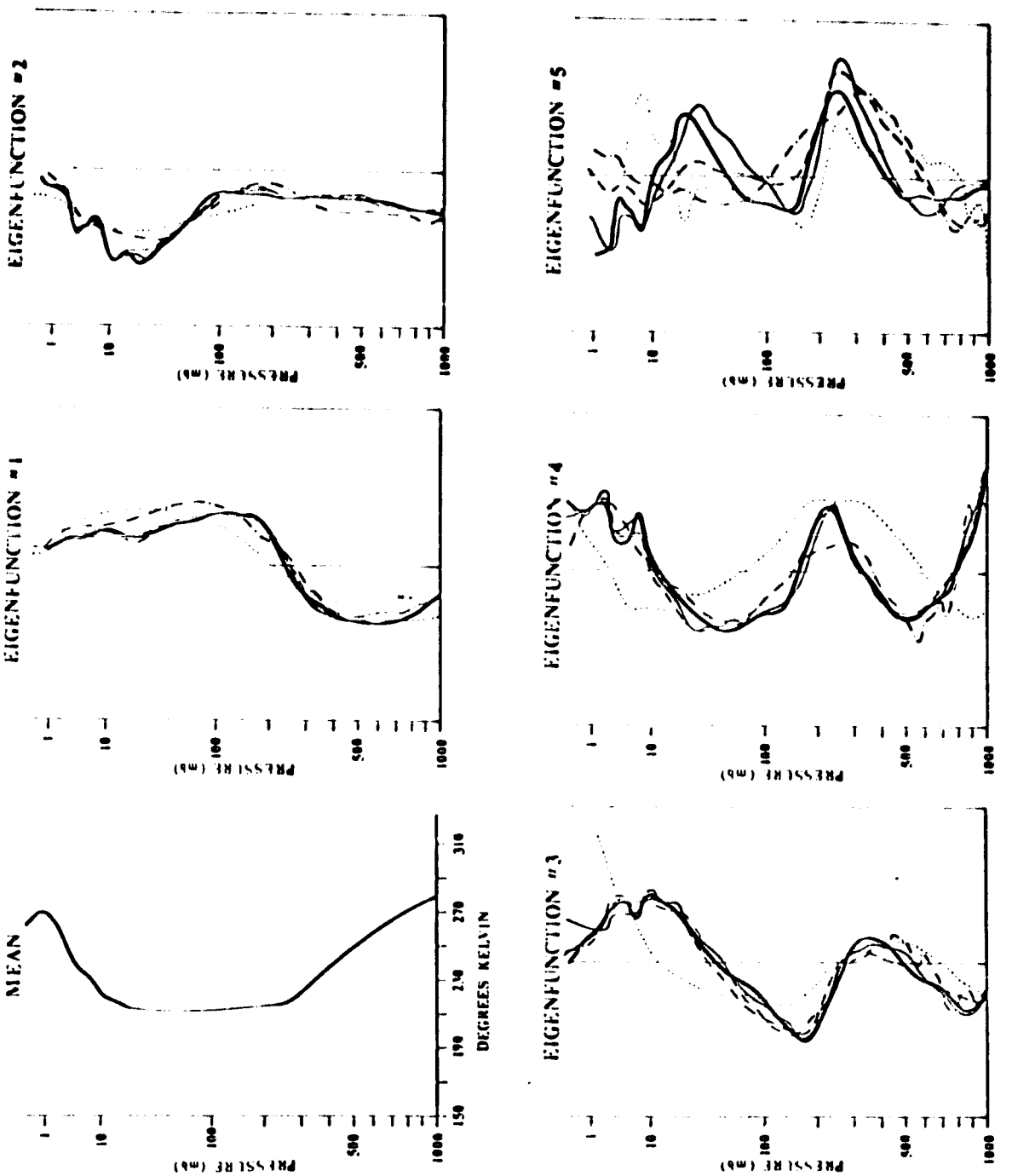

Figures 5(a)-(f). Mean profile and first five empirical orthogonal functions of RAOB temperature profiles and corresponding satellite temperature retrieval ensembles in mid-latitudes corresponding to Figs. 3 and 4.

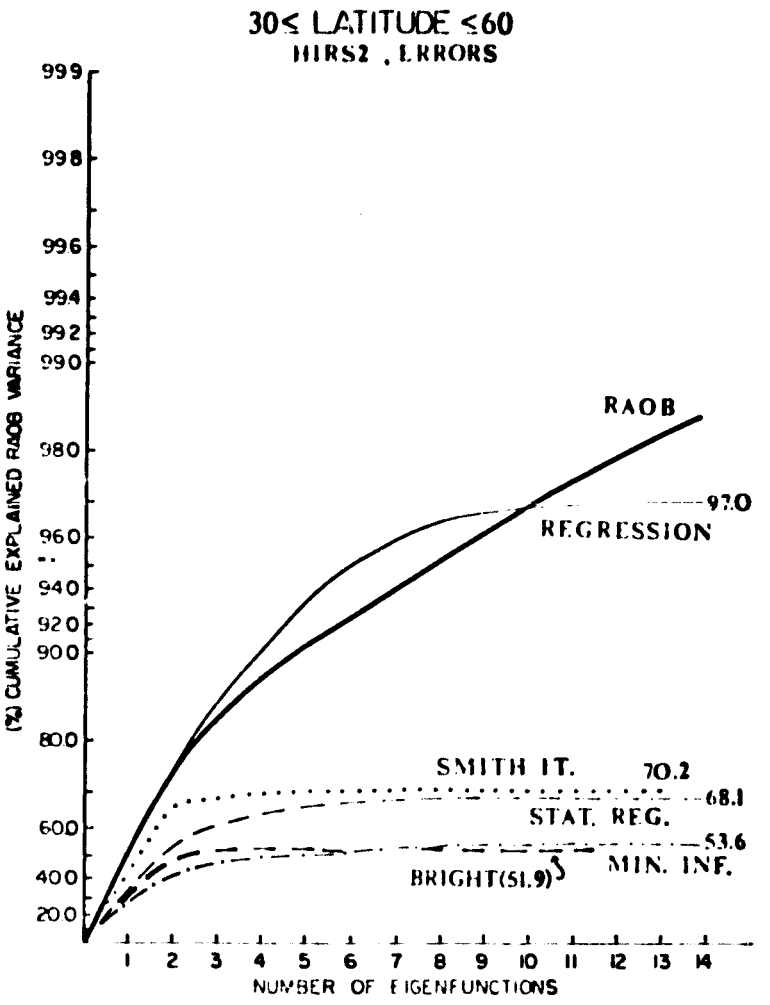

Figure 6. Information spectra for mid-latitudes as in Fig. 3 except using error contaminated HIRS synthetic radiance measurements.

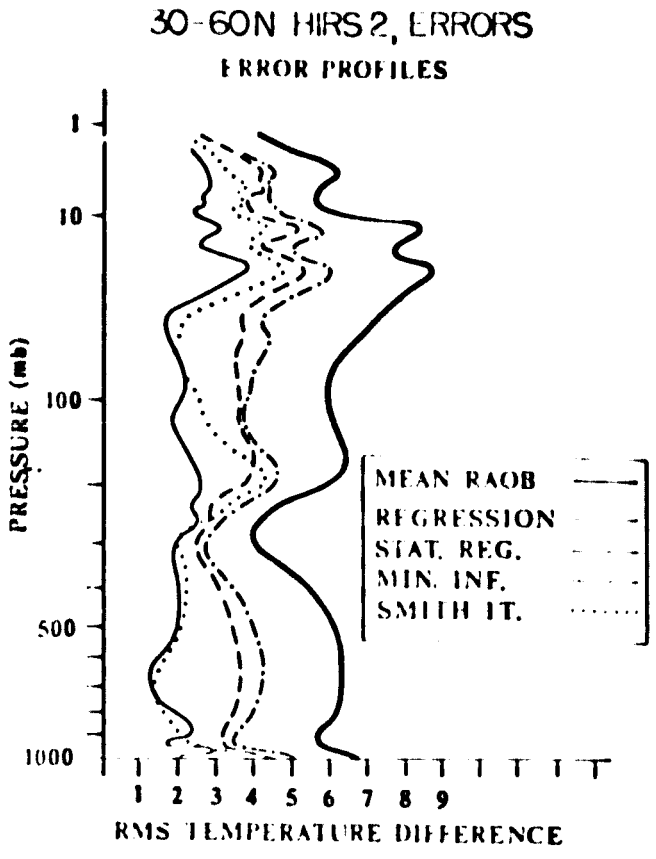

Figure 7. Vertical profiles of temperature retrieval errors in mid-latitudes for the noise contaminated experiments of Fig. 6.

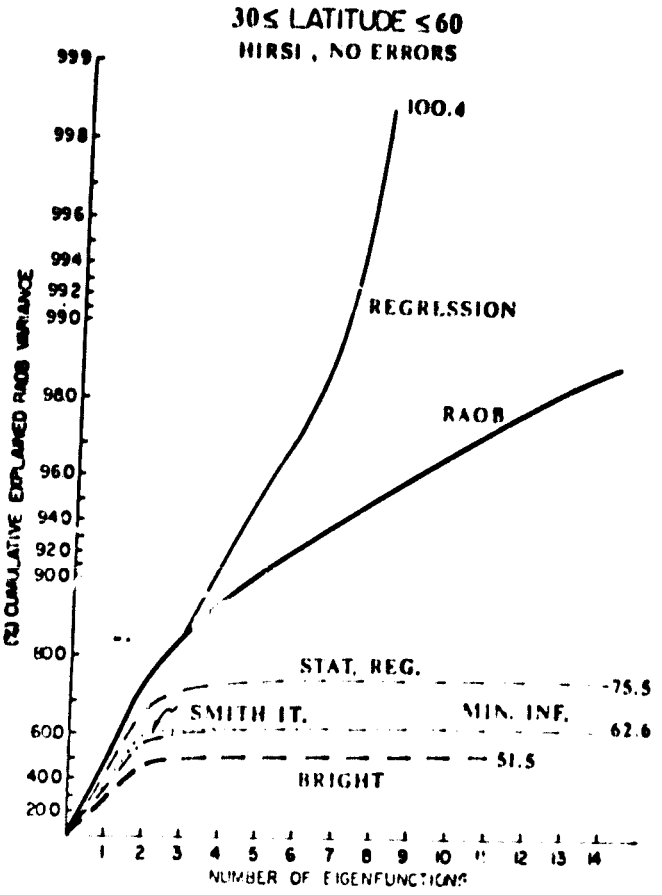

Figure 8. Information spectra for mid-latitudes, as in Fig. 3, except using radiometer noise values equal to approximately 1% of standard radiances.

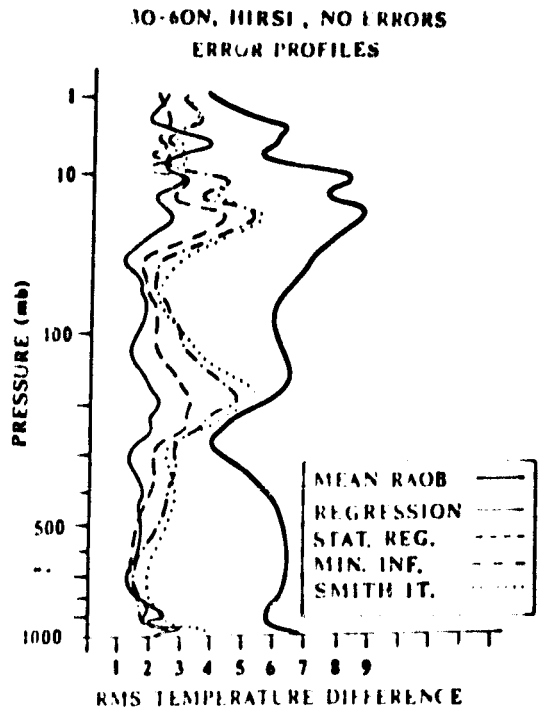

Figure 9. Vertical profiles of temperature retrieval errors in mid-latitudes for the experiments in Fig. 8.

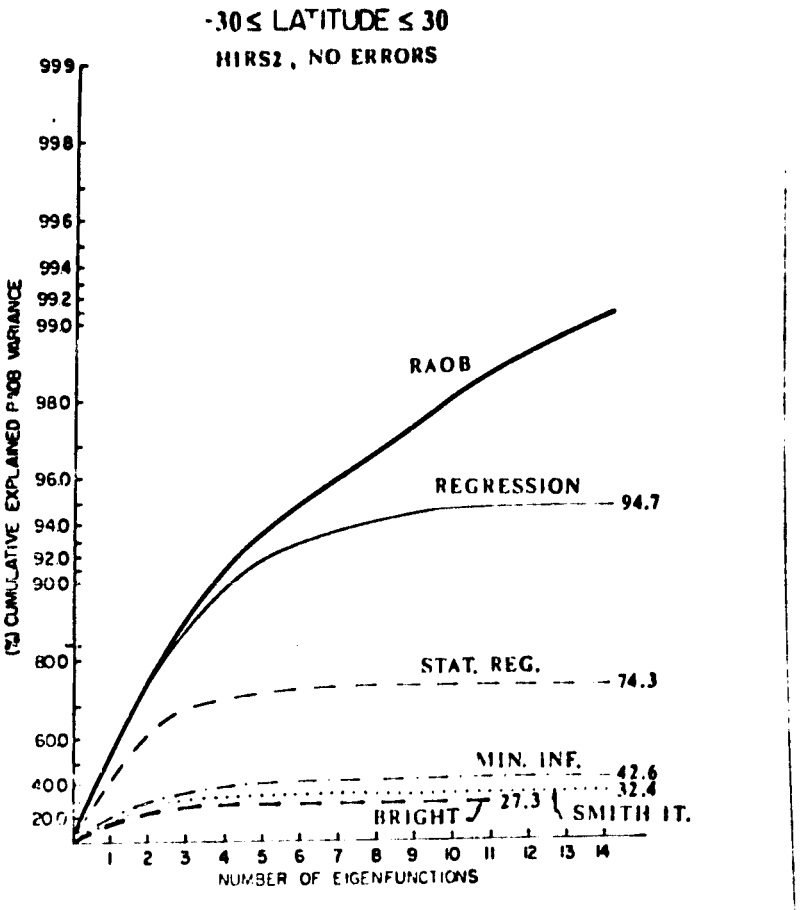

Figure 10. Same as Fig. 3 except for tropical latitudes (30S, 30N) in January.

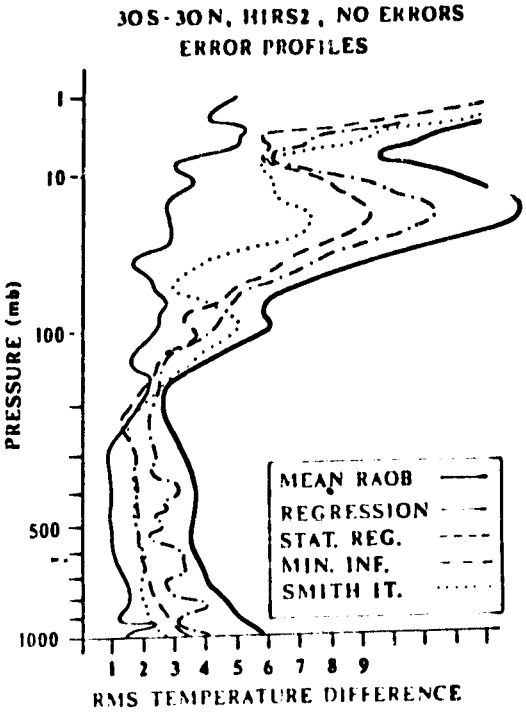

Figure 11. Same as Fig. 4 except for tropical latitudes (30S, 30N) in January.

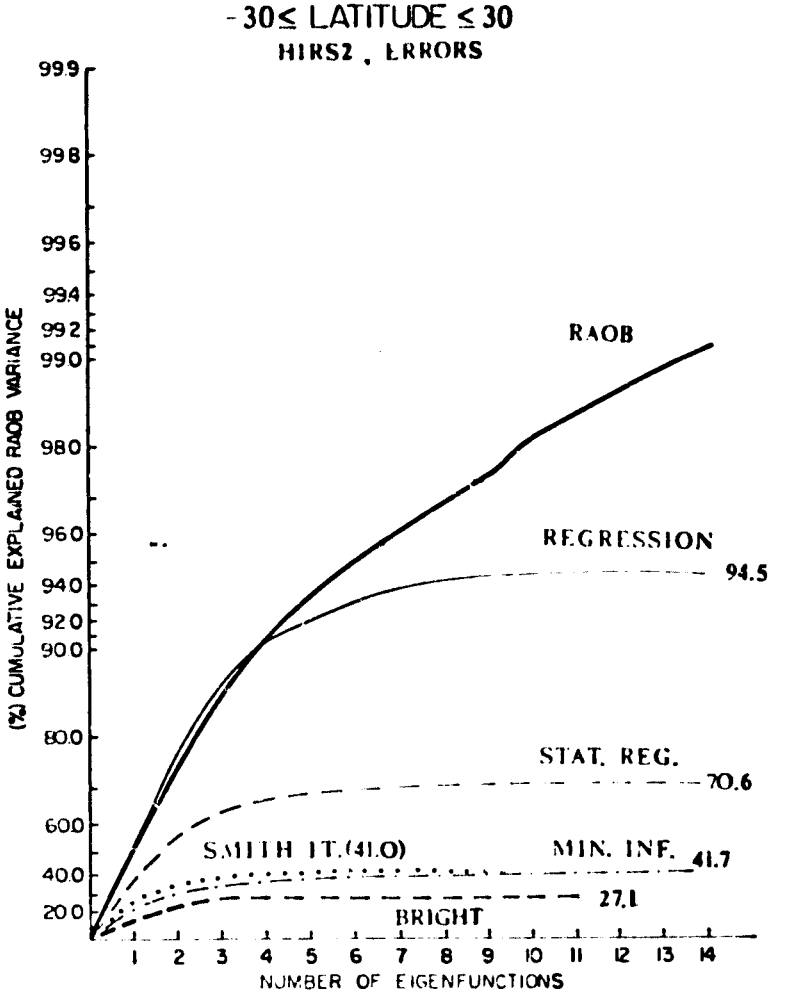

Figure 12. Same as Fig. 10 except using error contaminated synthetic HIRS radiance measurements.

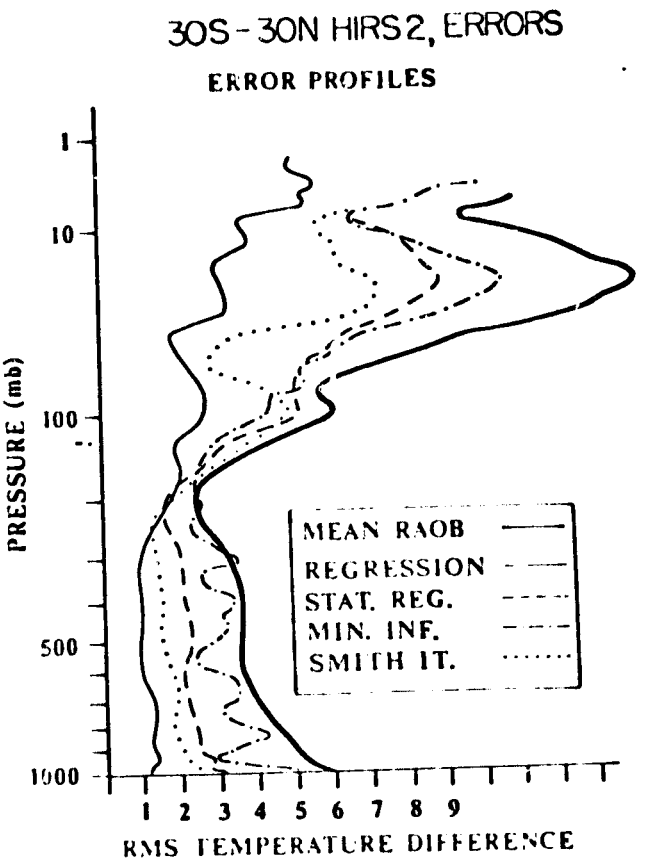

Figure 13. Same as Fig. 11 except using error contaminated synthetic HIRS radiance measurements

V. Satellite Temperature Soundings in Cyclones (Microwave Satellite Observations)

by

Sigmund Fritz

ABSTRACT

Satellite TIROS-N microwave radiances were used to derive temperatures and thickness over a cyclone in the Gulf of Alaska. The radiances were used in conjunction with the closest radiosonde data to the cyclone.

The method employed solves three equations in three unknowns. The unknowns are the three coefficients which are needed at each pressure level, to multiply the measured radiances in order to retrieve the vertical temperature distribution. From the derived vertical temperature distributions, the thickness between 700 and 300 mb were computed. Maps of the thicknesses were compared with NMC maps and with thicknesses derived from NESS operational soundings.

From a few soundings the tropopause height is seen to have a minimum near the Gulf of Alaska cyclone.

Satellite Temperature Soundings in Cyclones

(Microwave Satellite Observations)

by Sigmund Fritz

1. Introduction

Cyclonic areas over the Pacific Ocean are among the most significant regions for weather analysis and forecasting for North America.

However, in such important regions, it is difficult to make accurate temperature soundings with infra-red satellite measurements because clouds greatly influence the emission to space. Consequently, satellite measurements do not represent the effect of atmospheric temperatures alone and it becomes difficult to extract the atmospheric temperature from the satellite observations.

We have therefore restricted our investigation to the use of microwave satellite observations. At some frequences microwave observations are usually hardly influenced by the presence of clouds. Nevertheless, recently, Phillips (1980) has raised a cautionary flag regarding the influence of precipitation areas on the measureed microwave data; we shall address this problem later.

On April 6, 1979 a cylcone was located over the Gulf of Alaska (Fig. 1) and TIROS-N microwave observations were available. From the observed radiances, temperature soundings can be derived by many methods. This case was also studied by Brodrick (1980). Brodrick used NESS operational soundings which depend on certain parameters; these parameters are derived from statistical relations between satellite soundings and radiosondes which are mainly located far from the Gulf of Alaska, and also preceed the April 6, 1979 date by a week or more. Yet according to Grody (1980) "temperature profiles, having large amplitude small scale fluctuations relative to the a-priori mean, result in the largest retrieval errors". This leads to his further conclusion that the "a-priori" vertical temperature sounding should be based on a particular synoptic situation rather than on "a-priori" statistics according to three basic latitude bands. It is partly for that reason that Fritz (1976), and Hillger and Vonder Haar(1977,1979) used radiosonde data together with satellite data to derive vertical temperature structure in specific synoptic situations.

The method we have selected does not depend on any statistics. Instead the available radiosondes closest in space and time to the cyclone are accepted as basic true imput data. The satellite data are then used to interpolate the temperature soundings between the radiosonde stations.

In this method, there is no error at the radiosonde stations because we have assumed that the radiosondes are perfectly correct. The retrieval results can be compared everywhere with the results from operational methods discussed by Brodrick (1980), and with the data used in NMC analyses.

2. The Method

Solving 3 equations in 3 unknowns. The method used here has been described earlier (Fritz, 1976, 1977(a), (b), 1978). The method assumes as do most linear methods, that the temperature, at any height or pressure level in the atmopsherè, can be expressed as a linear combination of satellite observations.

Thus, we compute a temperature deviation, ΔT, from the relation

$$\Delta T_r(k) = \sum_j F(k,j) \cdot \Delta R(j) \qquad (1)$$

and find the temperature, T, from

$$T_r(k) = T_g(k) + \Delta T_r(k) \qquad (2)$$

Here T is temperature, R is radiance measured by the satellite, and the F's are a set of coefficients. The subscript, "r" , means the retrieved value, "g" means the "guess" or initial value. The letter, "k" refers to a pressure level in the atmosphere, and "j" refers to the spectral frequency of the radiation measured.

$$\Delta R(j) = R_m(j) - R_g(j) \qquad (3)$$

where the subscrpt "m" means the measured value.

The problem is to select the "best" values of F(k,j).

In general the values of F(k,j) depend on the vertical temperature structure of the atmospheres from which they are derived. Thus, in statistical methods the F's depend on the lapse rates of the sample of soundings which are used in the statistical sample. However, if the F's could be related to vertical temperature distibution in the cyclone under investigation, the temperature retrievals might be more accurate than the retrievals which depend upon a relatively unrelated statistical sample.

Therefore, in the study we selected the nearest radiosondes available. Figure 1 shows a picture of the cloud distribution over the cyclone; the dots locate the radiosonde stations (Table 1) used to derive the F's. The cyclone center was located on the surface synoptic map at 1200Z at about 54N, 167W. The center of the cloud spiral seems to be at about 53N, 165W.

The Microwave Sounding Unit (MSU) on TIROS-N has four channels

Those are:

Microwave Sounding Unit Frequencies

Channel No.	Frequency (GHz)
1	50.30
2	53.74
3	54.96
4	57.94

The radiance in channel 1 is strongly influenced by clouds. Therefore channel 1 was not used to sound the atmosphere. Channel 2 may be affected somewhat by clouds where rain is occuring. (Phillips, 1980). It may have been raining at Ship Papa, when TIROS-N viewed the area, however we shall show that channel 2, radiance did not seem noticeably affected in this case.

The remaining channels, channels 3 and 4, are presumably affected only by changes in atmospheric temperature.

We therefore have radiances available from 3 MSU channels namely, channels 2,3, and 4.

The method used here is therefore limited to the solution of 3 equations in 3 unknowns. The equations are 3 equations like Eq.(1). To generate the $\Delta T(k)$ at 3 radiosonde stations, we select one radiosonde station as the "first guess" station. We selected station #70308 (St. Paul, Alaska). We then selected 3 additional stations "surrounding" the cyclone. These three stations are listed in Table 1.

Table 1 - "First Guess" and dependent radiosonde stations.

Station	Station name	Lat.	Long.	
70308	St Paul	57.15N	170.22W	(G)
70454	Adak	51.88	176.65	
70316	Cold Bay	55.20	162.72	
C7P	Ship Papa	50.00	145.00	

(G) = "First Guess" Station, #70308

TIROS-N viewed the area at about 1320Z and 1500Z on April 6, 1979; the observed radiances over the four stations (Table 2) were selected from maps of MSU radiances for each of the channels. No adjustment was made for the difference in time from the radiosonde data, nominally at 1200Z.

Table 2 -MSU radiances over Radiosonde stations. (^{o}K)

Station	Channel Number			
	2	3	4	
70308	245.5	229.5	222.0	(G)
70454	244.0	228.5	222.1	
70316	245.3	230.6	221.5	
C7P	248.7	225.5	215.3	

(G) = "First Guess" stations

Table 3 -- Values of ΔR(^{o}K)

Station	Channel Number		
	2	3	4
70454	-1.5	-1.0	0.1
70316	-0.2	1.1	-0.5
C7P	3.2	-4.0	-6.7

The radiance values, expressed in equivalent degrees K, were subtracted from the values at the "First Guess" station, to obtain the values of $\Delta R(j)$ shown in Table 3.

The radiosonde temperature data were available at standard levels up to 100 mb, except that at Ship "Papa", the data were given to 30 mbs. In order to use a program already available, fictitious temperatures were added at the 5 mb and 0.1 mb level. The radiosonde temperatures were then interpolated to 100 pressure levels from 1000 mbs to 0.01 mb level according to a $p^{2/7}$ law.

This interpolation retains the measured temperature values at the standard levels exactly. Incidently, the surface pressure was generally lower than 100 mbs; e.g., it was 967 mb at station #70316.

Having now obtained temperatures at 100 pressure levels (actually only those at 50 levels, from 1000 to 104 mbs were meaningful) it was a simple matter to solve the 3 equations like Eq(1), separately at each pressure level, k, to obtain 3 values of F(k,j) at each pressure level.

An example of the distributions of F(k,j), is given in Fig. 2. Below about 400 mbs, the coefficients are fairly small never exceeding an absolute value of 2. However near the 300 mb level, the coefficient for channel 3 reaches a value of +5. This may be too large to give stable values of retrieved temperature for independent radiance measurements, if substantial random errors exist in the radiance observations. For that pressure level, errors in the radiance measurements would be amplified more because they would be multiplied by the large values of F(70,3); (k=70 corresponds to 299 mb). However, when we derive the thickness over the layer 700-300 mbs, as we shall do later, the coefficients are quite small when averaged over that thickness layer.

In spite of the variations of the F(k,j) in Fig. 2., obviously when the F(k,j) are multiplied by the $\Delta R(j)$ at the radiosonde stations (Table 3), and then added to "guess" temperatures, we obtain exactly correct temperatures at all levels at each radiosonde station. With this method there are no errors in the temperature at the dependent radiosonde stations. Since there are no errors in the temperatures, there are no errors in the heights of the pressure surfaces or of the layer thicknesses at those dependent radiosonde stations.

3. Application to independent data.

Having obtained values of F(k,j), we are now ready to apply them to all the TIROS-N MSU measurements over the cyclone. We derive temperatures at all 50 levels from 1000 mbs to 100 mbs. From those derived temperatures, we can compute the heights of pressure surfaces, and then compute the "thickness" between any two pressure levels.

This was done for an area larger than the region surrounding the Gulf of Alaska cyclone (Fig. 1). For that, data from two TIROS-N orbits were used. The times of those observations were approximately 1320Z and 1500Z.

The thickness of the 700-300 mb layer is shown in Figures 3 (1320Z) and Fig. 4. (1500Z). The dots in Fig.3 show the locations of the MSU observations at about 1320Z; in Fig. 4., the dots show the locations at about 1500Z. Along the latitude 50N, the thickness increases from 175E eastward. The thickness is about 5850 m at 175E, about 6000 m at 156W, and reaches a maximum of 6230 m, at 140W. At 53N, 170W, just west of the cyclone center, as shown in Fig. 1., the thickness gradient is quite small, in fact a low thickness of 5925 m was located there, surrounded by somewhat larger values of thickness.

How do these values compare with other results? Mr. H Brodrick of NESS, kindly supplied values of 700-300 mb thicknesses derived from "operational" retrievals. Unfortunately those retrievals where not made at each MSU observation spot. So Brodrick's values were interpolated between the thickness shown in Figs. 3., and 4. NMC's thicknesses, also supplied by Brodrick, were also compared in a similar manner.

Comparisons with NMC (thickness 700-300 mb) and between NESS and "3-Eqs" retrievals

It is interesting to compare the 700-300 mb thickness retrievals with NMC's thicknesses. This is done in figs. 5(a) and 5(b), for 1500Z observations, and in fig. 6(a) and 6(b) for 1320Z observations. Let's call the methods described above the "3-Eqs" method. Fig. 5(a) compares the TIROS-N 1500Z observation results of the "3 Eqs" method with NMC; Fig. 5(b) compares the results of the NESS statistical method with NMC (Brodrick, 1980). The largest differences from NMC occur near 45N, 155W. Near that location, both comparisons would reduce the NMC thicknesses. But the "3-Eqs" method would reduce the thickness by about 80 meters, whereas the NESS method would reduce the NMC values by about 150 meters. Thus while both methods would intensify the NMC trough at that location the "3-Eqs" method would do so less drastically. That result is doubtless influenced by the utilization of the sounding at Ship Papa (50N, 145W) in the "3-Eqs" method.

Figs. 5(a) and 5(b) are based on comparisons with interpolations by NMC and NESS to the NMC polar-sterographic grid-point locations. Moreover, in these figures, the TIROS-N observations were made near 1500Z. Mr. Brodrick kindly supplied also the NESS retrievals at specific locations. These are NESS retrievals made over an average of several satellite observations; therefore the location of the NESS retrievals, unfortunately, also do not correspond exactly to the retrievals at the MSU observation locations indicated by the dot in Figs. 5. Nevertheless the NESS retrievals were compared with the "3-Eqs" retrievals; the comparisons are shown in 5(c).

Fig. 5(c) shows that differences of about +100 m were computed near 155W from about 49N to 56N. Elsewhere the differences were smaller; near 50N, 170W the largest difference was -40 m. Doubtless some of the values in Fig. 5(c) are influenced by the interpolation made necessary because the retrievals were not made at exactly the same locations; but the patterns of positive differences near longitude 155W, and negative value near 170W is probably valid. This would of course change the gradient of thickness and, therefore, the thermal wind.

Another factor which may have affected the results, is the fact that 45N, 155W is near the satellite viewing horizon. The observed radiances are made at a large slant angle there; corrections are made for "limb effects" in an attempt to calculate what the radiances would have been if the satellite observations had been in the nadir. It was these "limb-corrected" radiances, kindly supplied by Dr. Grody, which were used in the retrievals with the "3-Eqs" method. Perhaps some variation in the "limb-corrections" made in the operational retrievals may account for some of the differences in the NESS and "3-Eqs" results. Of course near the center of Fig. 5 and Figs. 6, the satellite observes near nadir, and the differences in Figs. 5 and 6 would be due to other factors.

TIROS-N, 1320Z observations

In Figs. 6(a) and 6(b), the retrievals from the "3-Eqs" and from the NESS methods are compared both NMC for satellite observations made at about 1320Z. Near 50N, 155W, the results are similar to the ones in Figs. 5(a) and 5(b) at that location. In Fig. 6(a) the results are somewhat different than in Fig. 5(a) because no adjustment was made to make the retrievals equal at both observation times. In Fig. 6(a) near 55N, 135W, the "3-Eqs" method differs from NMC by about 100 m whereas the NESS retrievals agree with NMC almost exactly. At 57N, 130W NESS retrievals are about 28 m larger than NMC, while the "3-Eqs" method shows about +70 m. The reason for these discrepancies are not obvious, and should be investigated further. However, it should be noted that in an operational application of the "3-Eqs" method, a radiosonde (Annette Island), near 56N, 132W would have been utilized to retrieve the correct thickness at that location.

The difference between the "3-Eqs" and NESS retrievals for 1320Z, is shown in Fig. 6(c). Here again we note the relatively large differences near the horizon. Near the center of Fig. 5(c), that is, near satellite nadir, the differences are smaller although they still reach about +50 m.

Which result is better? It does not seem possible to decide from the thickness field alone. If the radiosonde measurements are accurate, obviously the results of Fig 3 and 4 must be better at the radiosonde stations. But the NESS results are also in approximate agreement with the Aleutian Is. radiosonde stations. Near Ship Papa the NESS results are not in such good agreement.

Thickness was also derived for the layer 1000-500 mb, but the results are not reported here. The average values of the coefficients which yield average temperatures over the layers are shown in Table 4.

Table 4
Average coefficients, F(k,j) averaged over pressure intervals

Pressure Intervals	Channel No.		
(mbs)	2	3	4
1000-500	1.16	-0.48	-0.21
700-300	+0.86	+0.01	-0.99

4. Tropopause

Since the retrievals yield temperatures at 50 pressure levels between 1000 and 100 mbs, it was interesting to see what the vertical temperature structure was.

It should be remembered that the vertical temperature structure at the radiosonde stations (Table 1) are accepted as true. Therefore, the tropopause at these stations, and all the temperatures at every level are assumed known. The satellite measurements merely serve as a rational way of interpolating between the radiosonde stations.

With that in mind, we see in Fig. 7 two radiosonde temperatures, and also a set of retrievals at five locations along a line from Ship Papa to Adak (#70454). It is interesting to note that the lowest tropopause height occurs just south of station #70316 which itself had the lowest tropopause height of the four radiosonde stations; namely at 394 mb.

The lowest tropopause height judging by Fig. 7, seems to have occurred just to east of the low level cyclone.

5. On the question of the value of channel 2 radiance at Ship Papa

Phillips (1980) has shown that when precipitation is occuring in the atmosphere under the satellite, the observed radiance in channel 2 may be too low. Under such circumstances the cold cloud is partially substituted for the warmer atmosphere which lies below.

In order to detect situations when precipitation is occuring, Phillips suggested comparing channel 1 with channel 2. Without precipitation, over the ocean, the radiance R_1 in channel 1, tends to be much smaller than the radiance R_2, in channel 2, but when precipitation is occuring, R_1 approaches R_2 in value, and R_1 may even exceed R_2.

Fig. 1 shows that Ship Papa was located under a frontal band; it may have been raining there. Is the radiance R_2, observed over Ship Papa too low? Should the radiance be increased somewhat? To test this a map of $R_2 - R_1$ was prepared; the data are shown in Figure 8.

The value of $(R_2 - R_1)$ at Ship Papa is about 10; Phillips suggested that when $(R_2 - R_1)$ is less than 12, then R_2 might be affected by the clouds. To test this further, and to determine by how much R_2 at Ship Papa should be increased the observed values of R_2 where compared with theoretically computed values.

The value of R_2 is given by mainly

$$R_2 = \int_0^1 T \, d\tau_2 \, . \qquad (4)$$

In Eq.4, "T" is the temperature obtained from radiosondes and τ_2 is the atmospheric transmittance for channel 2. Values of τ_2 were kindly supplied by Dr. N. Grody.

The radiosonde data were mostly available up to 100 mbs although some stations supplied temperatures to greater heights. The surface pressure at most stations was lower than 1000 mbs. Equation (4) was therefore applied for pressure levels from 970 mbs to 100 mbs at several stations. The results are shown in Figure 9. From Fig. 9 it appears that no correction should be applied to the observed value of R_2 at Ship Papa. A line fitted by eye through the Hawaiian stations and the Alaska stations passes through the point for Ship Papa. Another line which takes account of Midway Island, would indicate that the radiance at Ship Papa should be reduced, instead of increased.

Because of this analysis, the thickness shown in Fig. 3 and 4 were computed with the observed value of R_2 at Ship Papa. Computations were also made with the value R_2 increased from the observed value of

of 248.7 ^{o}K to a fictitious value of 250.5 ^{o}K. Of course, because of the method of solving 3 equations in 3 unknowns to derive F(k,j), no errors appear in the temperatures of the radiosonde stations, with either value of R_2. It is not until the retrievals are made at a substantial distance south of the radiosonde stations that a significant difference appears in the 700-300 mb thickness between the retrievals with R_2 = 248.7 and R_2 =250.5.

The coefficients $\overline{F}$ (k,j) for the average temperature from 700-300 mbs were:

	Channel No. 2	3	4
R_2 = 248.7	0.86	0.01	-0.99
R_2 = 250.5	0.82	0.08	-0.83

Since ΔR is small near the Aleutian Island stations, and the temperature errors are zero at the all dependent radiosonde stations, it is only when the ΔR's change appreciably from the value at the radiosonde stations that significant changes in the thickness can occur.

6. Further Discussion

As Grody (1980) suggests, the details of the vertical temperature structure may introduce errors in temperature retrievals from satellite data. Fritz (1969) also indicated that true deviations from assumed average temperatures make it impossible to derive error free retrievals at a given height from satellite data alone. Grody suggests that the vertical temperature structure in every synoptic situation needs to be considered separately.

Retrievals, using both radiosondes and satellite radiances, attempt to employ both types of data as a consistent data set. There are however questions raised when such methods are used. The present method depends on radiosonde data. If any radiosonde sounding is in error, that error will be propogated into the retrievals in the vicinity of the erroneous radiosonde. Moreover, if the satellite data are not made at the same time as the radiosonde, in a changing synoptic situation the two data sets would not be consistent. Therefore, the two sets of data should really be colocated in space and in time, although no attempt was made in the present study to account for the time differences between the radiosonde ascents and the satellite observations. The radiosonde data are taken, nominally, at 1200Z, although some allowance should be made for time taken by the ascent and deviations of the release time from 1200Z. The satellite data were taken in 1320Z, in Fig. 3 and near 1500Z in Fig. 4.

Doubtless, somewhat different retrieval results would have been obtained if the radiosonde data had been adjusted to the satellite times, by for example, using forecast temperatures made at hourly intervals.

In the course of the work, it was noted that the satellite radiances were substantially different during local daytime from the values during local night-time. If this is due to some instrumental error in the satellite, obviously the coefficients derived for 1200Z would not be applicable to any other times. Space interpolation might still be permissible, but extrapolation in time would not be valid. This day-night variation in the MSU data needs to be investigated further.

Another item which needs to be looked into further, is the reason for the 100 m discrepancy in Fig 6(a) between the thicknesses derived by the "3-Eqs" method and NMC's result, in the vicinity of Annette Island.

Further test's of the "3-Eqs" method can readily be devised. For example it would be interesting to substitute another station for Ship Papa, and to compute thickness retrievals again. Instead of Ship Papa we might employ a radiosonde in the Hawaiian Islands, or another one of the Alaska coastal stations.

7. Acknowledgements

It is a pleasure to acknowledge the cooperation of Dr. N. Grody, Mr. H. Brodrick, of NESS who supplied basic and derived data, discussed the work as it progressed, and supplied still unpublished manuscripts. Mr. F. Van Cleef, NESS, also supplied some MSU data, which has not yet been used. With my colleague, Dr. O. E. Thompson, I discussed various points, especially, the tropopause height retrievals. Technical help was received from three students at the University of Maryland; namely, Al Hendler, Andrew Postosky (programmer) and Ralph Ferraro, Clare Villanti drafted the figures; Donna M. Duckett typed the manuscript. Thanks are due to the University's Computer Facility for the use of the Univac 1140 computer. And finally, the National Environmental Satellite Service, NOAA and the Goddard Space Flight Center, NASA supported the work reported here. This was done under NOAA Grant NA80AA-D-00035 and NASA Grant NSG5209.

REFERENCES

Brodrick, H., 1980: Manuscript in Preparation; Private Communication.

Fritz, S., 1969: On the question of measuring the vertical temperature distribution of the atmosphere from satellites. Mon. Wea. Rev., 97(10), 712-715.

Fritz, S. 1976: Investigations with satellite data--Temperature retievals. Meteorology Program Publication no. 76-158, University of Maryland, College Park, Md. Final Report, NASA Grant NSG 5084, 35pgs.

Fritz, S., 1977(a): Temperature retrievals from satellite radiance measurements--an empirical method. J. Appl. Met., 16(2), 172-176.

Fritz, S., 1977(b): Investigations with satellite data--Temperature retievals, II. Meteorology Program Publication no. 77-174, University of Maryland, College Park, Md. Final Report MASA Grant NSG 5084, 29pgs.

Fritz, S., 1978: Temperature distribution from radiosonde and satellite measurements. In COSPAR: Space Research Volume XVIII, Ed. M. J. Rycroft and A. C. Stickland, pgs 51-52, Pergamon Press, Oxford and New York.

Grody, N. C., 1980: Analysis of satellite-based microwave retrievals of temperature and thermal winds: Effects of channel selection and a-priori mean on retrieval accuracy. In "Remote Sensing of Atmospheres and oceans," A. Deepak, editor. Academic Press, New York (in Press).

Hillger, D. W. and T. H. Vonder Haar, 1977: Deriving mesoscale temperature and moisture fields from Satellite radiance measurements over the United States. J. Appl. Meteor., 16, 715-726.

Hillger, D. W. and T. H. Vonder Haar, 1979: An analysis of satellite infrared soundings at the mesoscale using statistical structure and correlation functions. J. Atmos. Sci., 36, 287-305.

Phillips, N. A., 1980: Two examples of satellite temperature retrievals in the North Pacific, Bull. Am. Met. Soc., 61(7), 712-717.

Figure Legends

Figure 1 : Picture of spiral cloud band over the Gulf of Alaska from TIROS-N, April 6, 1979. The heavy line, surrounding the spiral, encloses the area emphasized in the report. The dots in the enclosed area show the locations of the radiosonde stations used as dependent stations. "Ship Papa" is denoted by "P," the "first guess" station by "G." Midway Island is labelled "M." Ship Papa appears to be under a frontal cloud band.

Figure 2 : Vertical distributions of the coefficients F(k,j), for 3 microwave channels. The tick marks on the pressure scale are for every 5 units of "k." k = 50 refers to p = 97 mb, k = 100 refers to p = 1000 mb.

Figure 3 : Thickness (meters) of 700-300 mb layer, computed on the basis of TIROS-N microwave radiance measurements and radiosonde data. Microwave measurements were made at about 1320Z. April 6, 1979. The dots show the locations of the microwave measurements; temperature and thickness retrievals were computed at each dot. The symbol at 50N, 145W shows the location of Ship Papa.

Figure 4 : Same as Figure 3, except for microwave measurements made at about 1500Z. The symbols denote the locations of the dependent radiosonde stations. The storm symbol denotes the approximate center of the cloud spiral in Figure 1.

Figure 5(a): Comparison with National Meteorological Center (NMC) thicknesses (meters). Thickness from Figure 4 (1500Z) minus thickness from NMC. Symbols denote locations of dependent radiosonde stations. Note about -80 m difference near 45N, 155W.

Figure 5(b): Same as Figure 5(a) except difference between NESS operational thickness and NMC thickness. Note about -150 m near 45N, 155W.

Figure 5(c): Comparison of thickness (meters) in Figure 4 with thickness from NESS operational soundings; Figure 4 thickness minus NESS thickness. Symbols show locations of dependent radiosonde stations.

Figure 6(a): Same as Figure 5(a), except for 1320Z TIROS-N observations (Figure 3).

Figure 6(b): Same as Figure 5(b), except for area further East.

Figure 6(c): Same as Figure 5(c), except for 1320Z TIROS-N observations (Figure 3).

Figure 7 : Temperature soundings. Soundings no. 1 and no. 7 are observed from radiosonde stations. Soundings no. 2 through no. 6 are retrievals from the "3-eqs." method, along latitude 50-51N, between the two radiosonde stations. Note the low tropopause near the center of the longitude interval.

Figure 8 : Radiance, R_2, minus radiance, R_1, for TIROS-N observations at 1320Z. Note tight gradient along coastal areas.

Figure 9 : Comparison of partial radiances computed from radiosonde temperature (eq. 4) versus MSU channel 2 radiances observed at the same radiosonde stations. Values "First Guess" station (computed or observed) subtracted from corresponding station value.

ORIGINAL PAGE
BLACK AND WHITE PHOTOGRAPH

FIG. 1

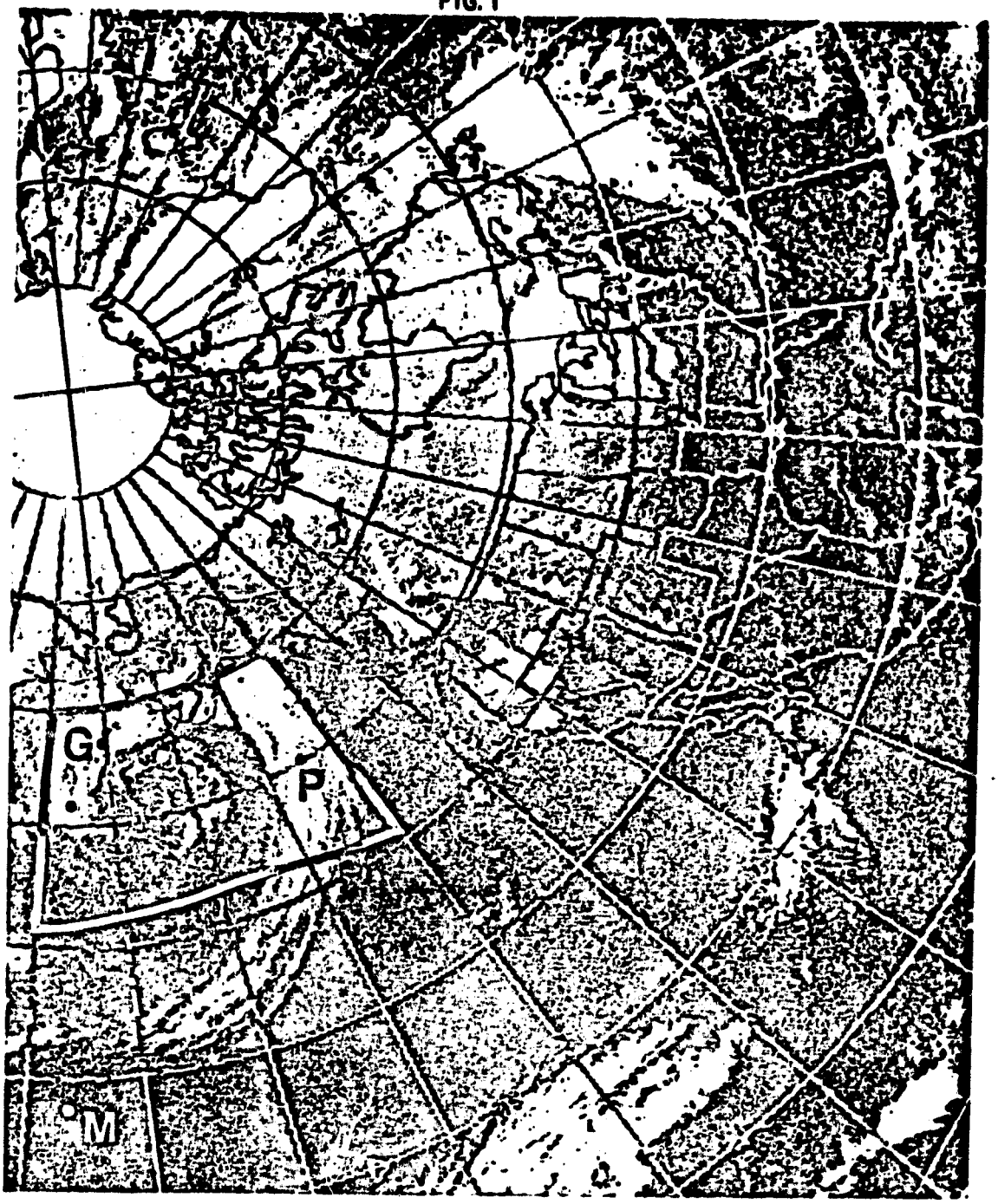

FIG. 2

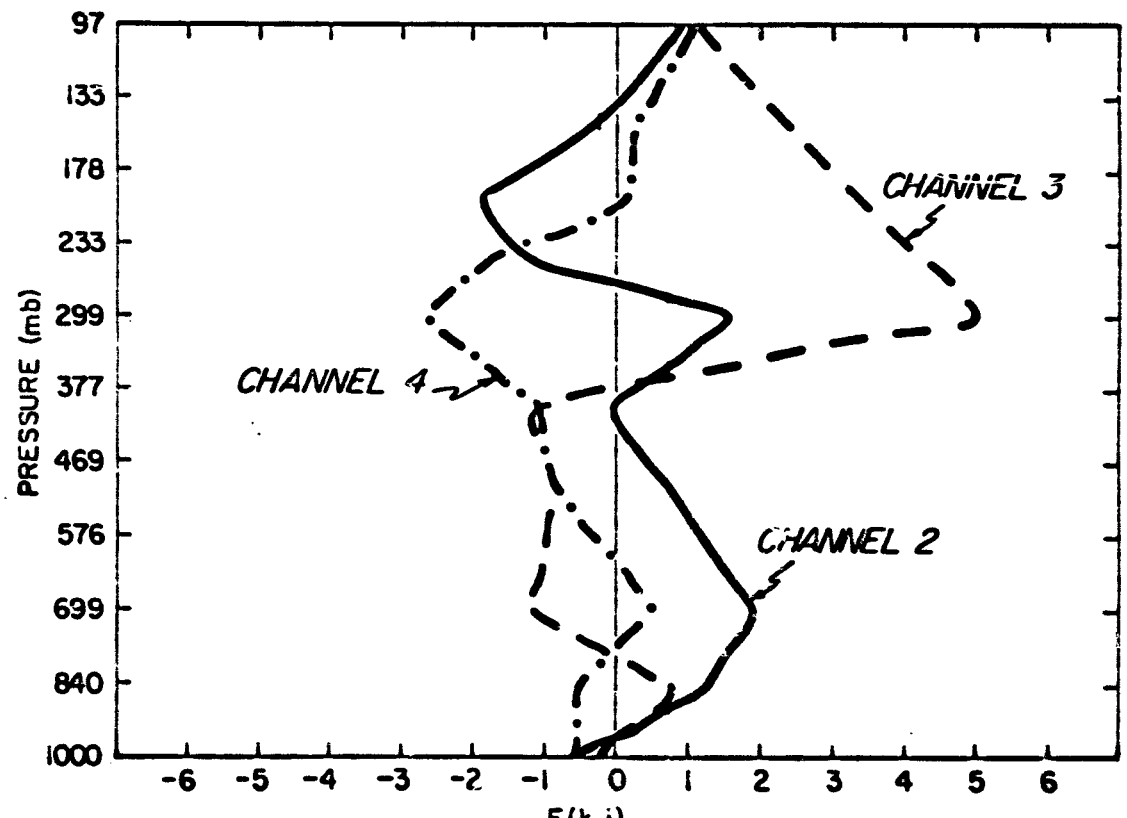
97
133
178
233
299
377
469
576
699
840
1000
PRESSURE (mb)
-6
-5
-4
-3
-2
-1
0
1
2
3
4
5
6
F(k,j)
CHANNEL 3
CHANNEL 4
CHANNEL 2

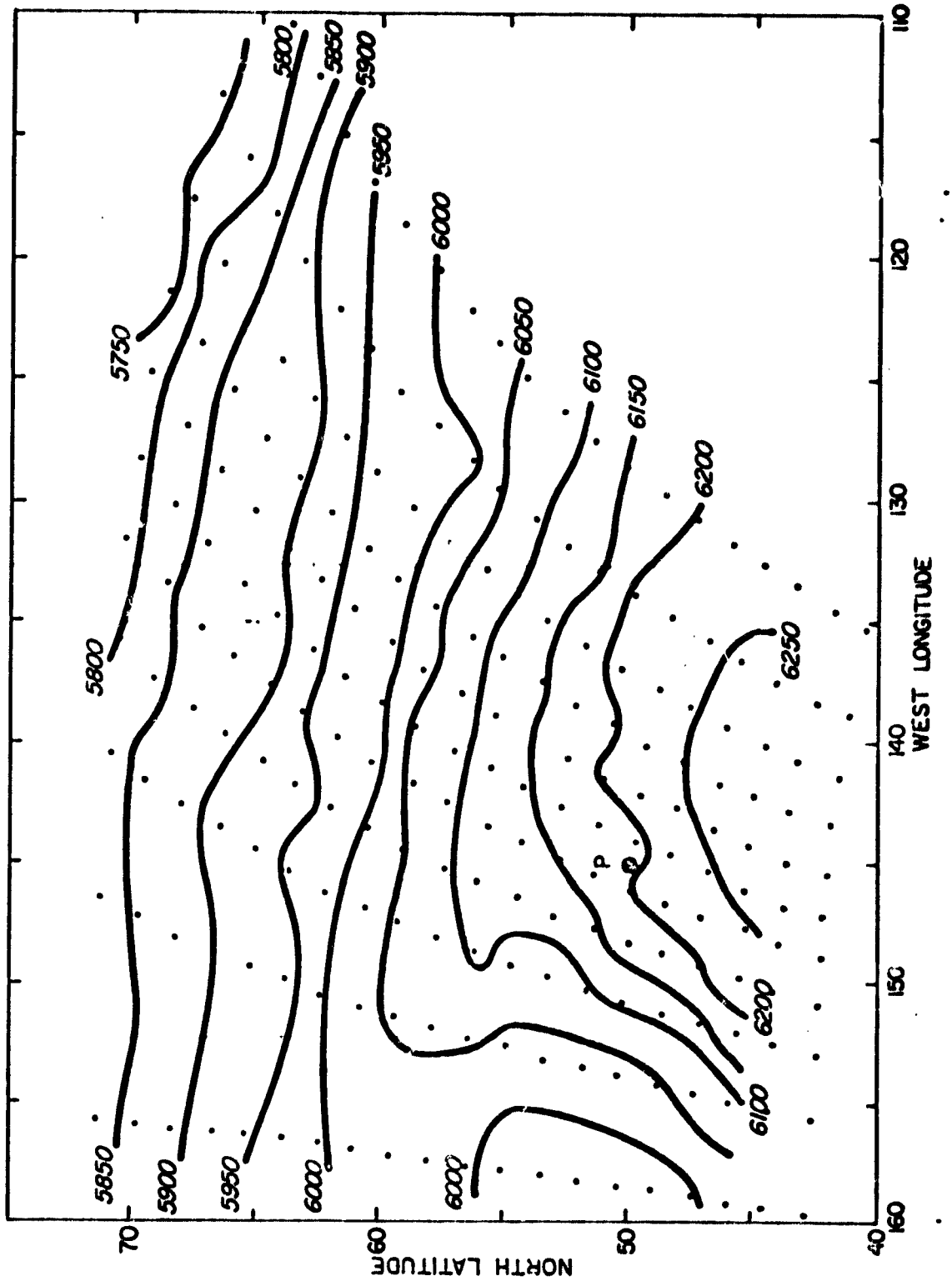
5750
5800
5850
5900
5950
6000
6050
6100
6150
6200
6250
P
NORTH LATITUDE
70
60
50
40
WEST LONGITUDE
110
120
130
140
150
160

FIG. 3

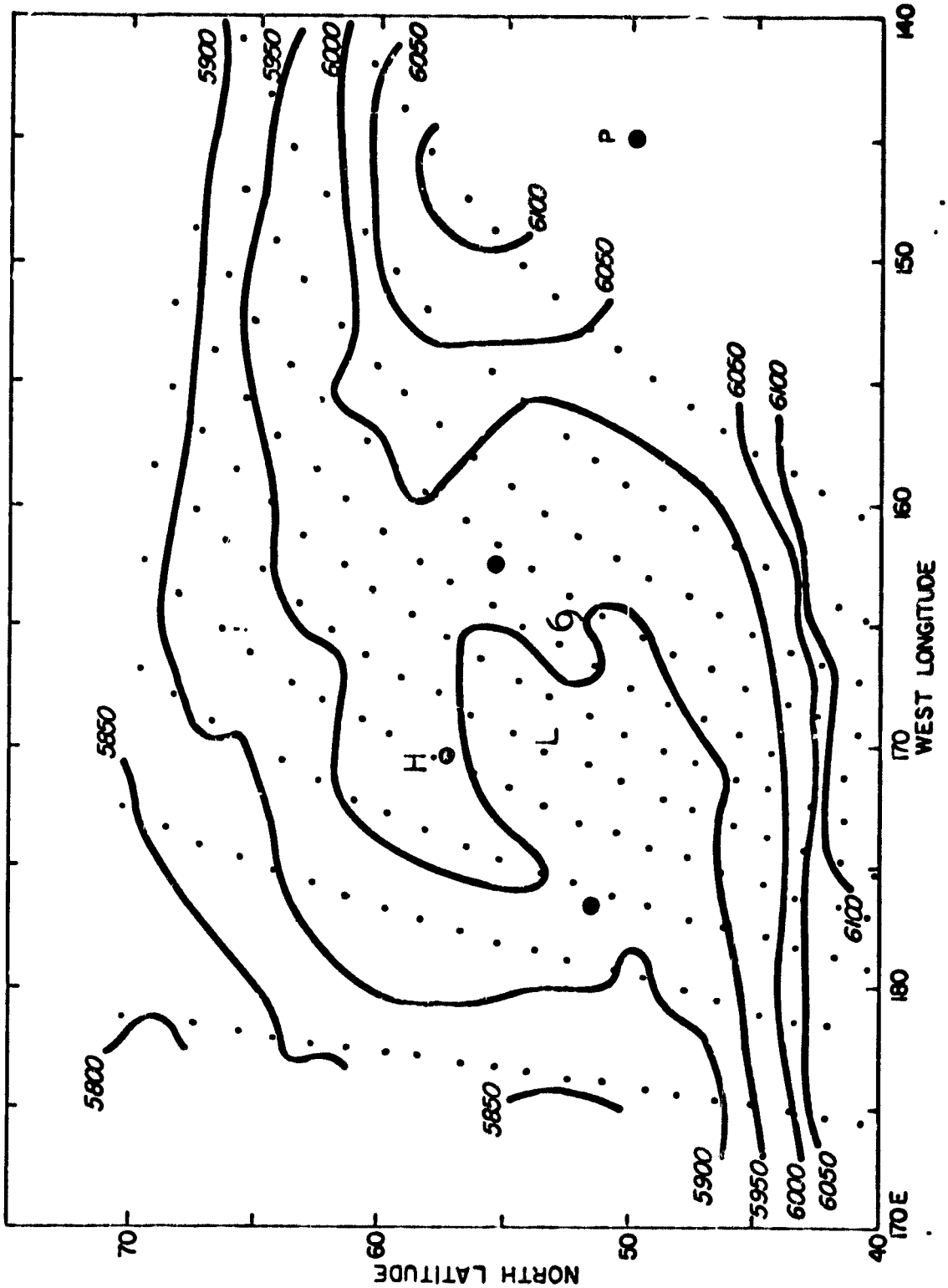
5800
5850
5900
5950
6000
6050
6100
H
L
P
70
60
50
40
NORTH LATITUDE
170E
180
170
160
150
140
WEST LONGITUDE

FIG. 4

FIG. 5(a)

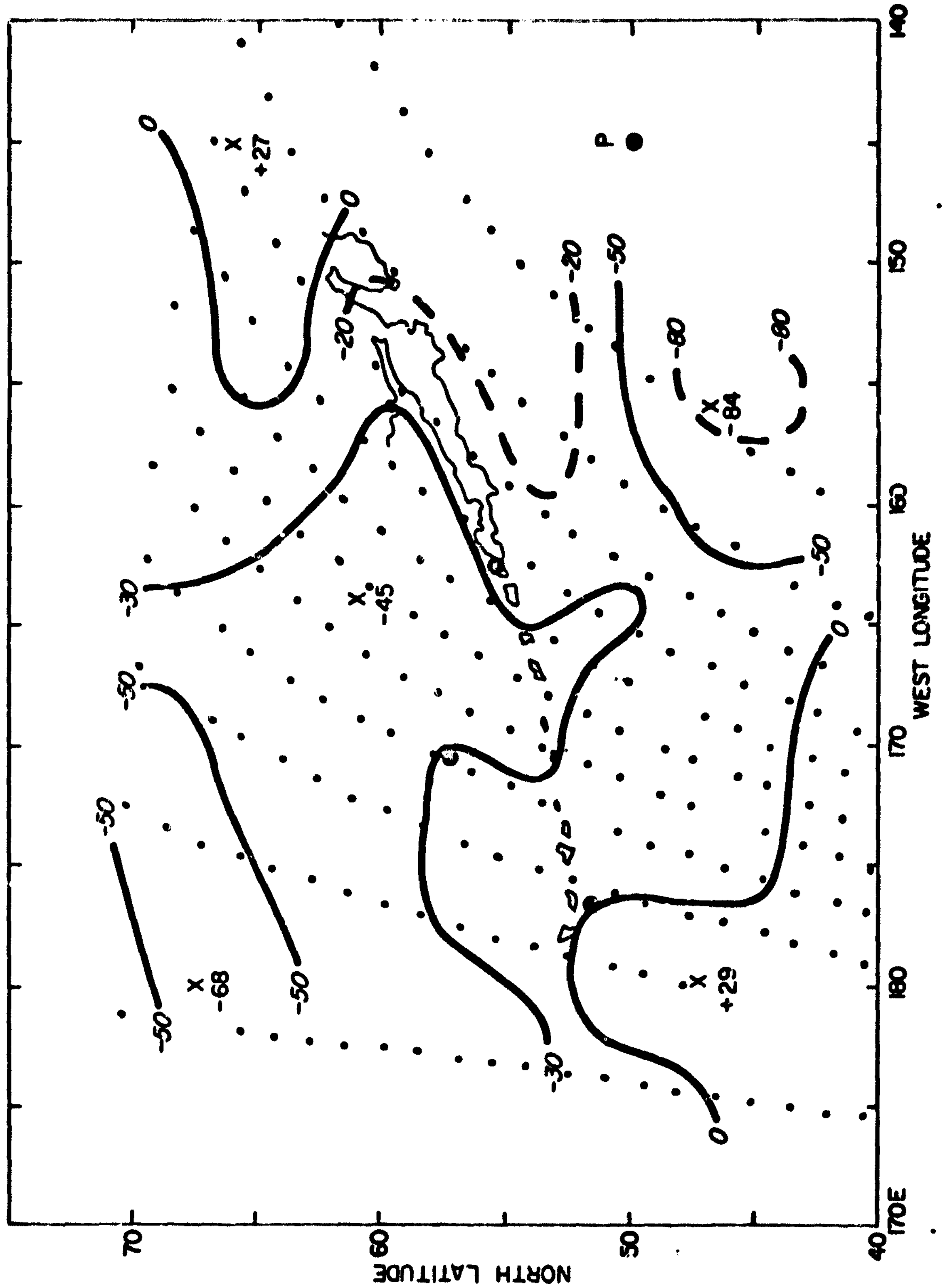
NORTH LATITUDE
WEST LONGITUDE
70
60
50
40
170E
180
170
160
150
140
0
-20
-30
-50
-80
X +27
X -45
X -68
X -84
X +29
P

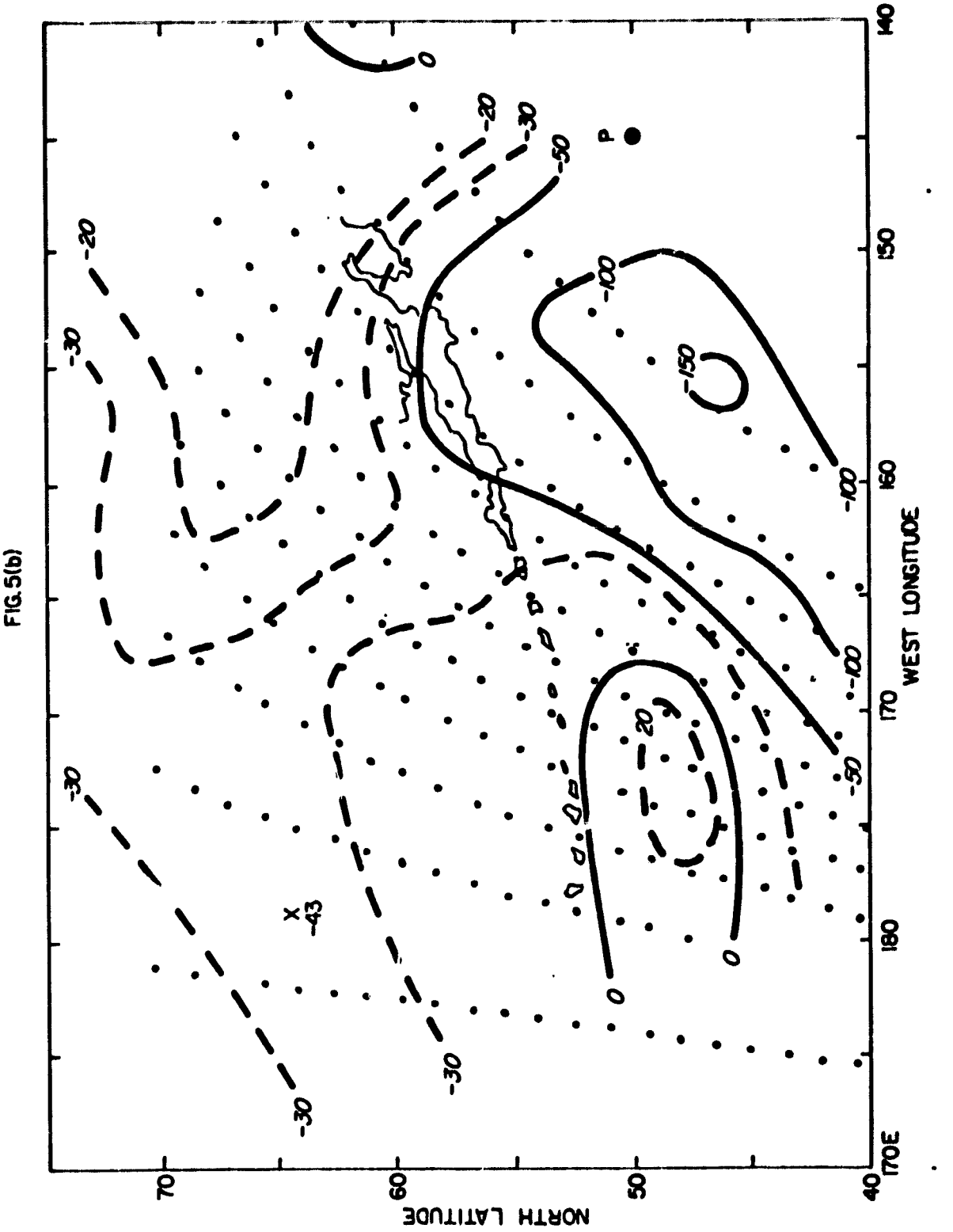
0
-20
-30
-50
-100
-150
-43
P
70
60
50
40
NORTH LATITUDE
170E
180
170
160
150
140
WEST LONGITUDE

FIG. 5(b)

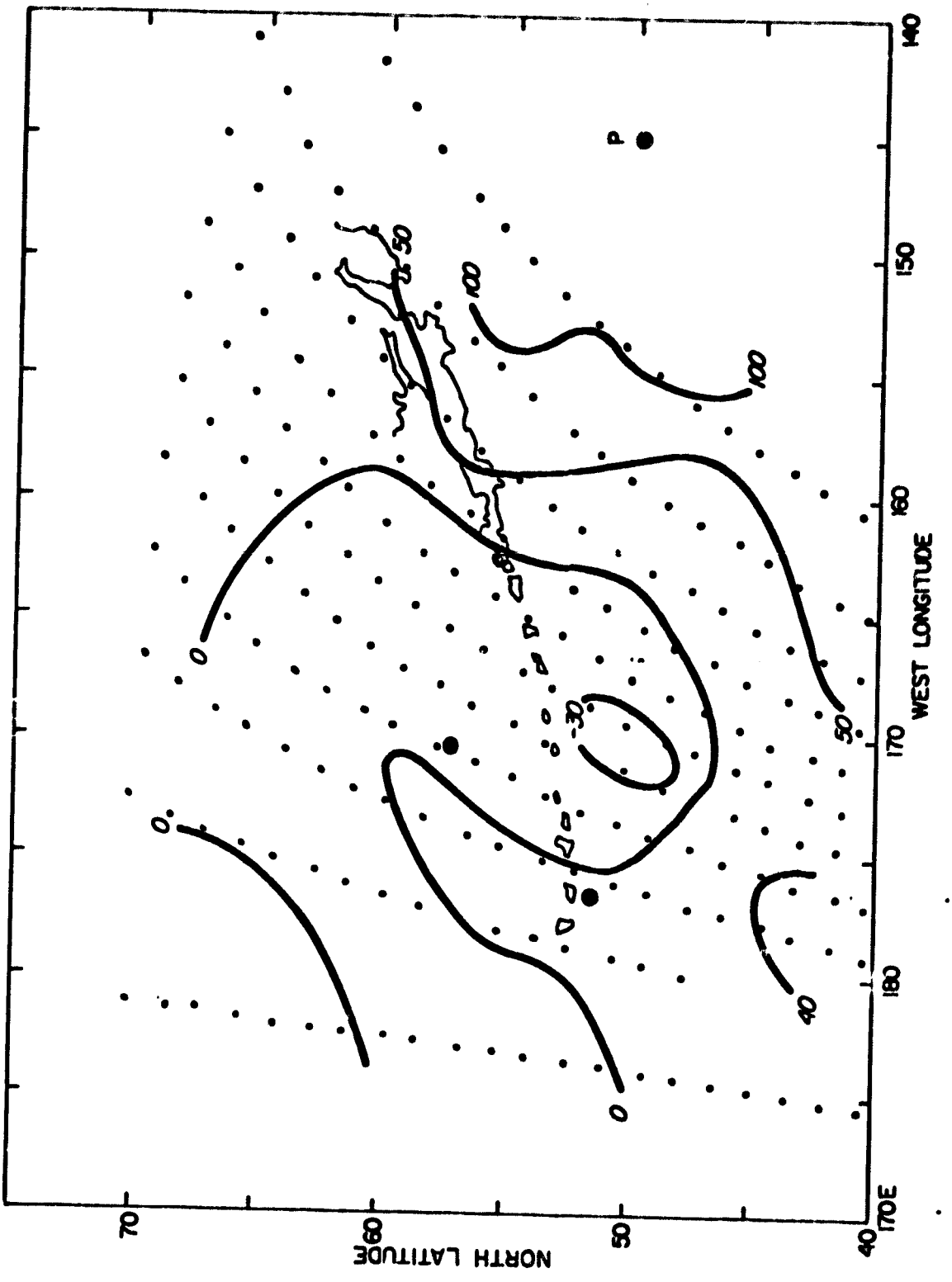
NORTH LATITUDE
70
60
50
40
WEST LONGITUDE
140
150
160
170
180
170E
0
50
100
-30
40

FIG. 5(c)

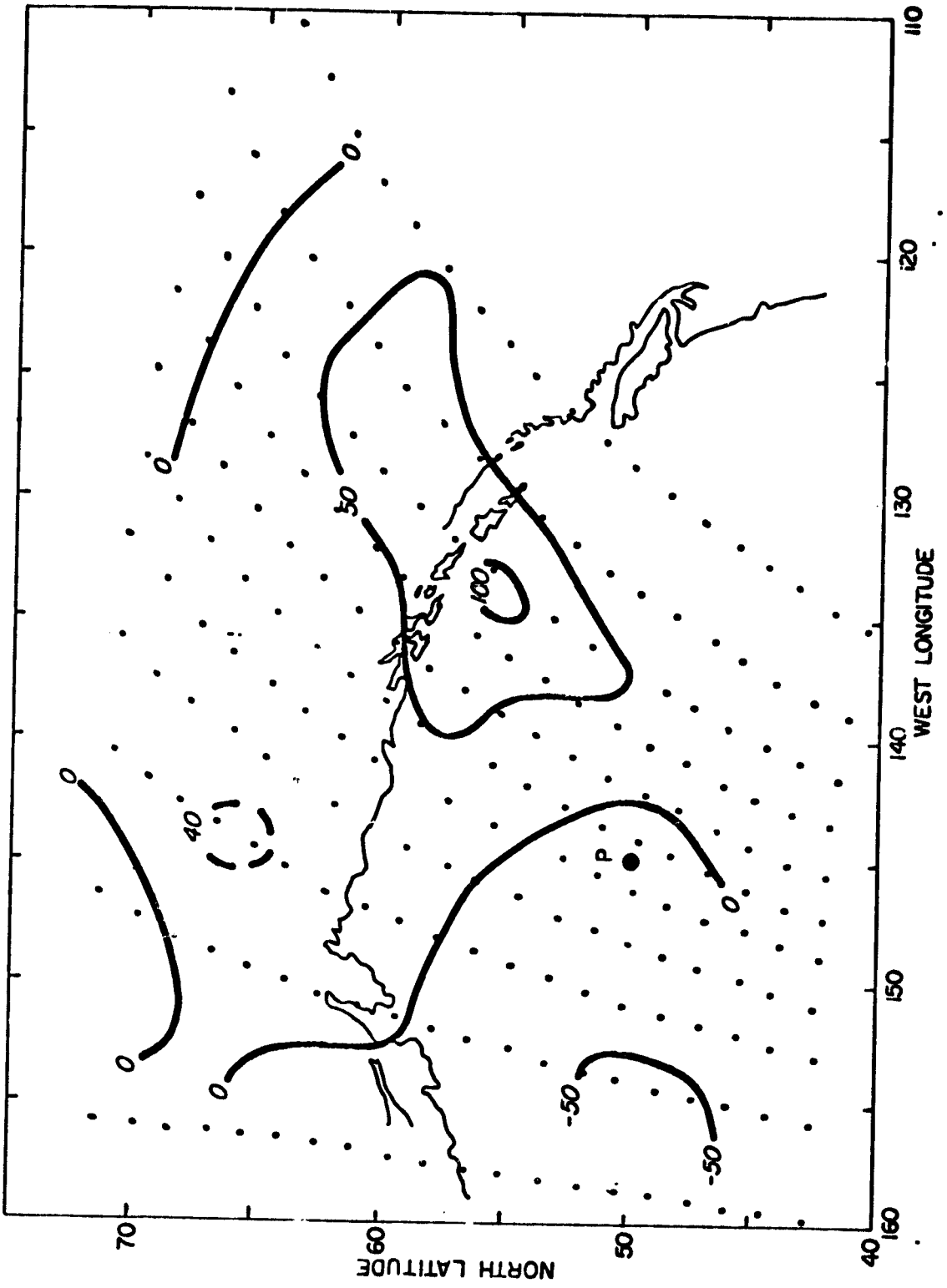
0
0
0
0
0
30
100
40
-50
-50
P
70
60
50
40
160
150
140
130
120
110
NORTH LATITUDE
WEST LONGITUDE

FIG. 6(a)

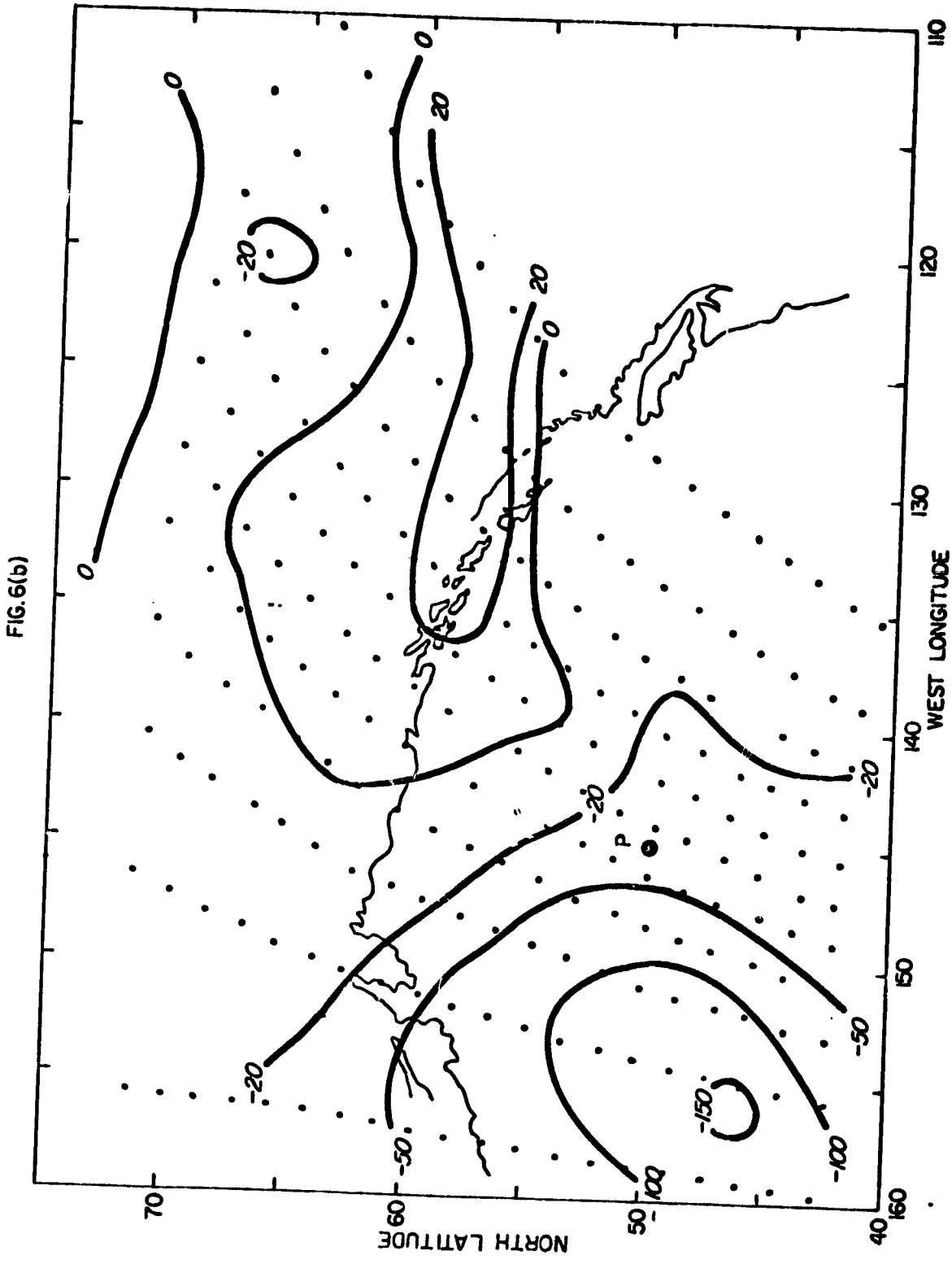
0
20
-20
0
20
0
-20
-20
-50
-150
-100
-50
-20
P
70
60
50
40
160
150
140
130
120
110
NORTH LATITUDE
WEST LONGITUDE

FIG.6(b)

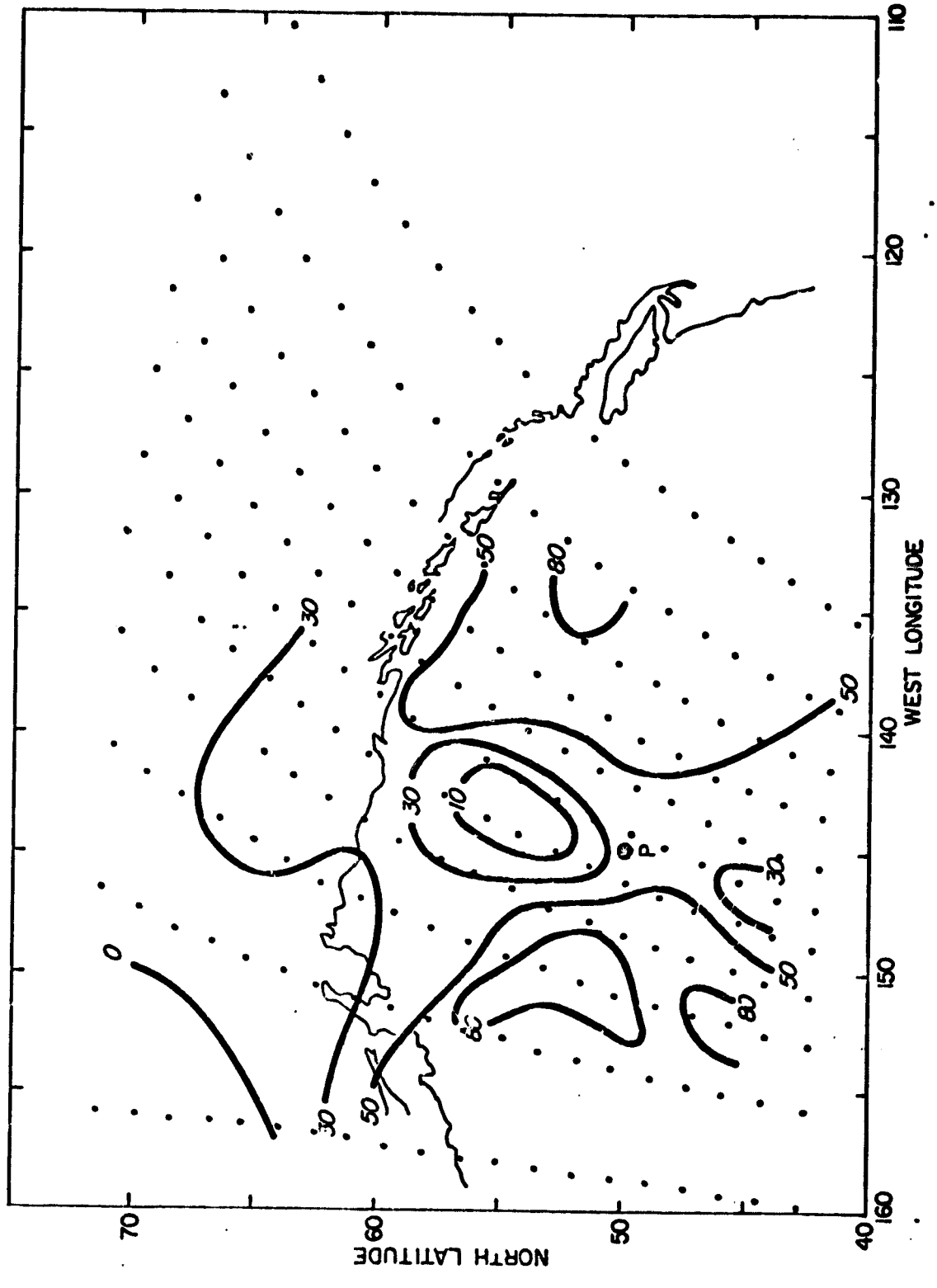
NORTH LATITUDE
70
60
50
40
WEST LONGITUDE
110
120
130
140
150
160
0
30
50
80
10
P

FIG.6(c)

FIG.7

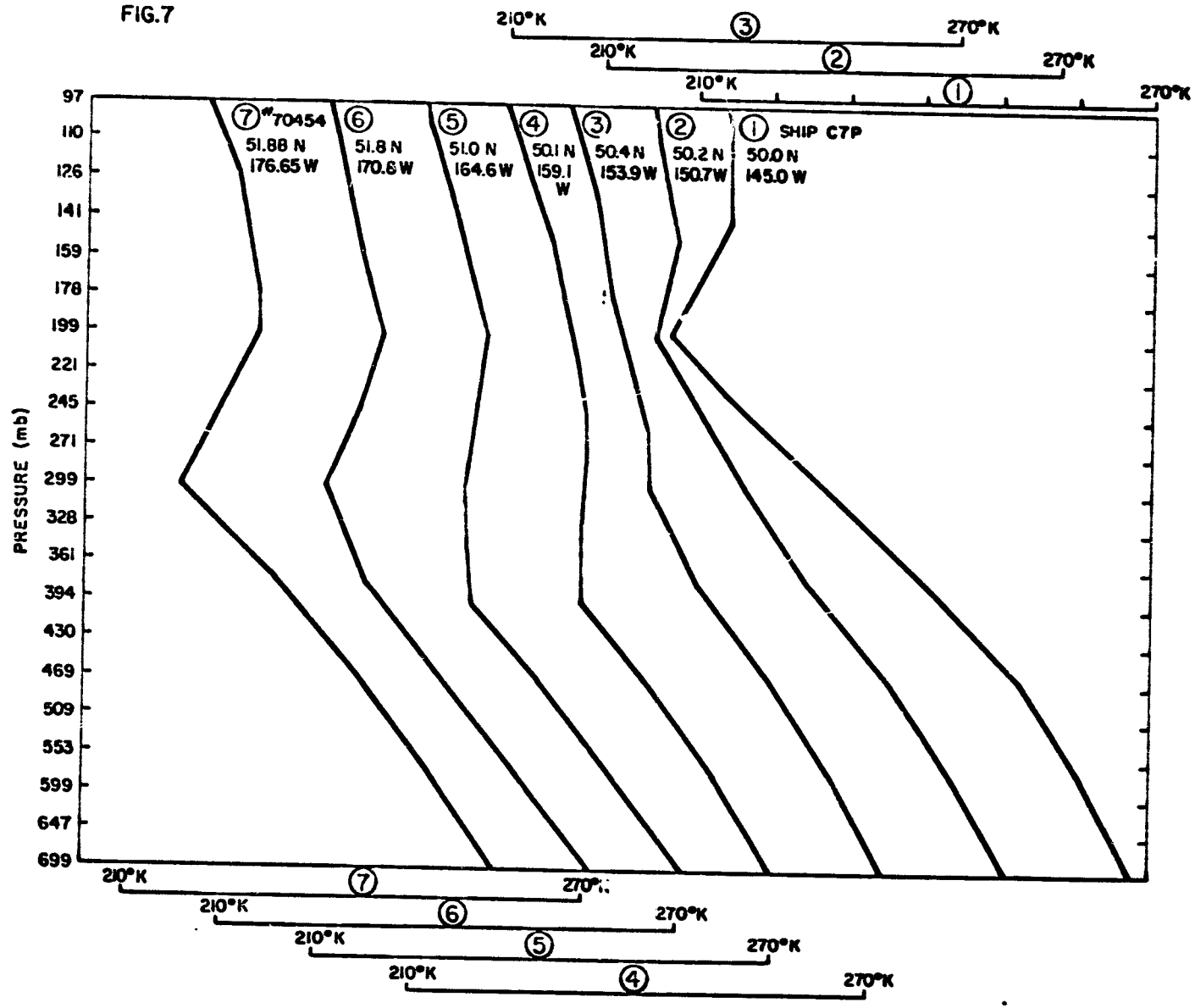
210°K
270°K
③
②
①
PRESSURE (mb)
97
110
126
141
159
178
199
221
245
271
299
328
361
394
430
469
509
553
599
647
699
⑦ "70454
51.88 N
176.65 W
⑥
51.8 N
170.6 W
⑤
51.0 N
164.6 W
④
50.1 N
159.1
W
③
50.4 N
153.9 W
②
50.2 N
150.7 W
① SHIP C7P
50.0 N
145.0 W
⑦
⑥
⑤
④

FIG. 8

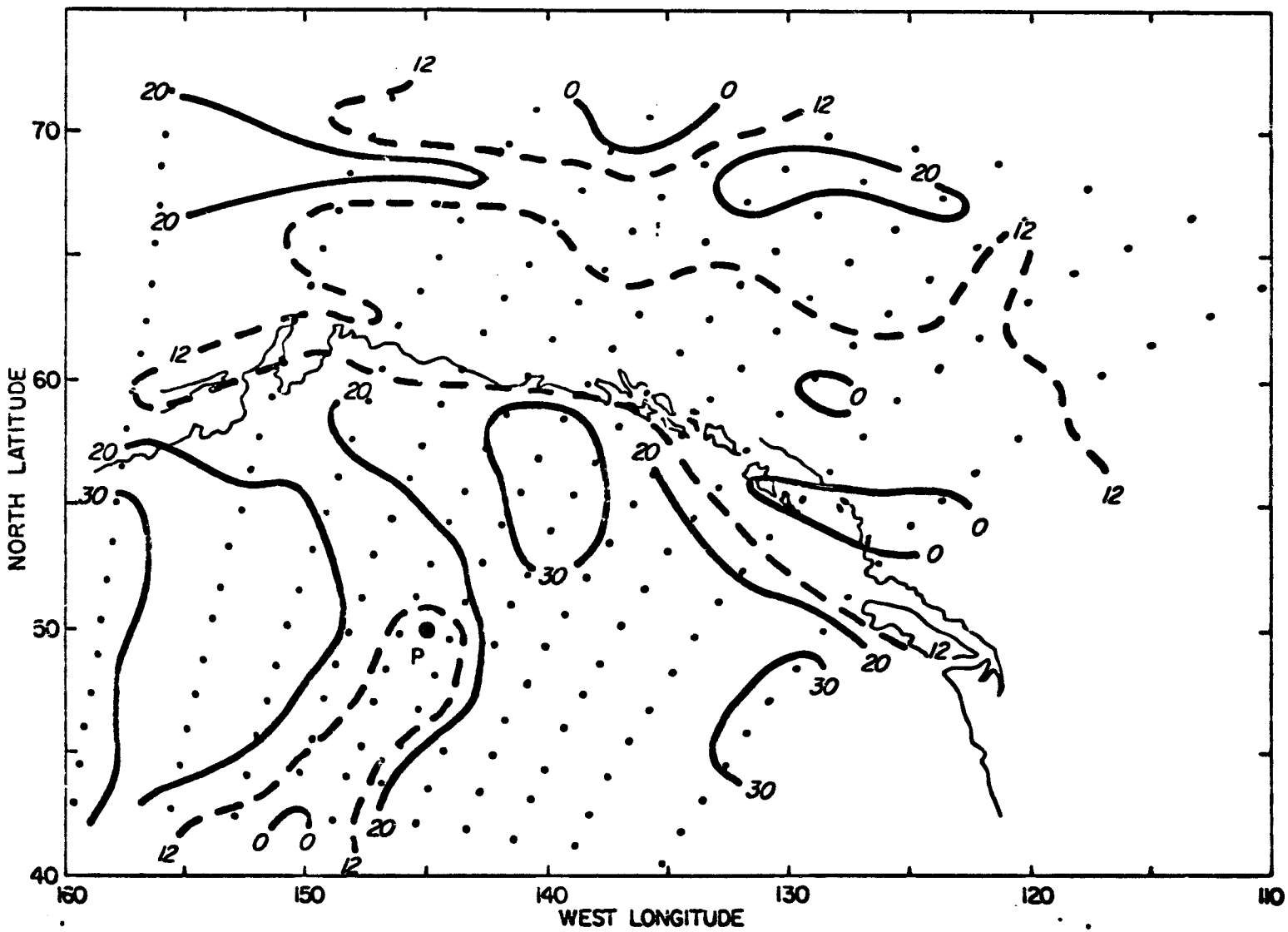
NORTH LATITUDE
70
60
50
40
160
150
140
130
120
110
WEST LONGITUDE
P
12
20
0
30

FIG. 9

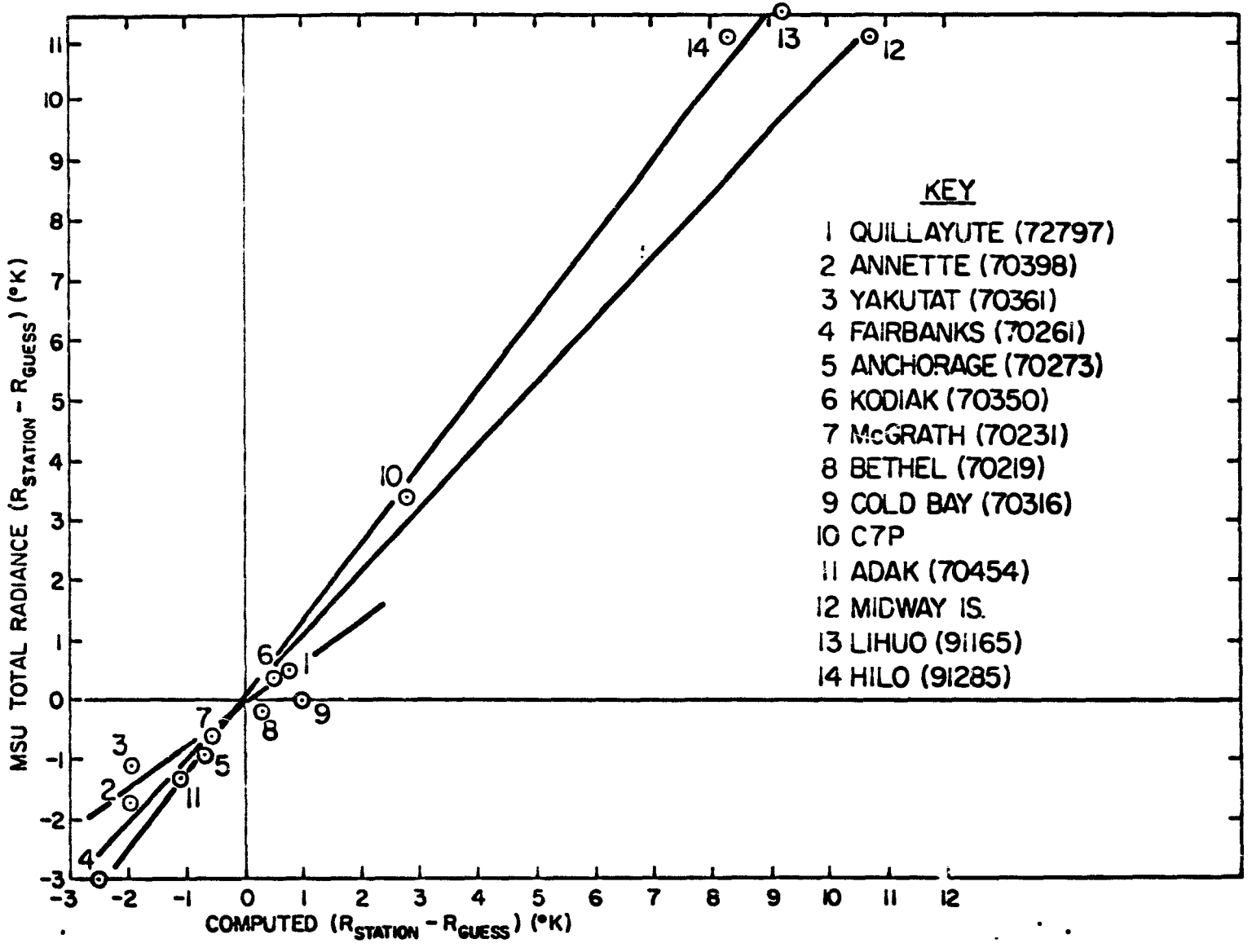
MSU TOTAL RADIANCE ($R_{STATION} - R_{GUESS}$) (°K)
COMPUTED ($R_{STATION} - R_{GUESS}$) (°K)
KEY
1 QUILLAYUTE (72797)
2 ANNETTE (70398)
3 YAKUTAT (70361)
4 FAIRBANKS (70261)
5 ANCHORAGE (70273)
6 KODIAK (70350)
7 McGRATH (70231)
8 BETHEL (70219)
9 COLD BAY (70316)
10 C7P
11 ADAK (70454)
12 MIDWAY IS.
13 LIHUO (91165)
14 HILO (91285)

VI. Northern Hemisphere 700 mb Heights and Pacific Ocean Temperatures in Winter

by

Sigmund Fritz

Abstract

Horel and Wallace (1980) show the time variations of Pacific Ocean sea-surface temperature (SST) patterns for the winter months (average for December, January, and February). The 10 years with the warmest equatorial Pacific SST and the 8 years with the coldest SST were selected from their data.

Northern hemisphere maps of the 700 mb heights, averaged for the 10 SST warm years, were computed. This was done for the mean monthly heights at each 10° latitude-longitude intersection; it was done separately for November, December, January, and February. Similar maps were prepared for the average of the 8 SST cold years. Then the difference in the 2 averaged height fields was computed. Maps for the difference are shown as Figures 1-4 in this report.

In February and in January the distribution of the height field agrees most with the correlation field shown by Horel and Wallace. Especially in February, a ring of relatively low heights surrounds the North Pole, with the ring displaced southward along 90W. This agrees also with theoretical findings cited. In January the pattern is almost as coherent, but in December and even more in November, the pattern deviates more from the "ring pattern" evident in February.

Fourier harmonic analysis shows that wave numbers 1, 2, and 3 contribute substantially to the pattern, especially in middle and high latitudes.

Finally, an interesting 10 year repetition occurs in the 700 mb heights at 60N, 90E. The cause is unknown; but the possibility is raised that SST in the Pacific and Atlantic Oceans may respond to gyres with different periods that are harmonics of 10 years.

Northern Hemisphere 700 mb Heights and Pacific Ocean Temperatures in Winter

by Sigmund Fritz

Introduction

Horel and Wallace (1980) (abbreviated H-W) show that a correlation pattern exists between the 700 mb heights over the northern hemisphere and certain patterns of the sea-surface temperatures (SST) of the Pacific Ocean. For the SST, they use an empirical orthogonal function (EOF) of Pacific SST given by Weare, Navato and Newell (1976). H-W show a time series graph of normalized SST from 1949-1979. They indicate by shading their "subjective definition of major warm SST episodes in the equatorial east Pacific." (It should be noted, however, that the EOF SST patterns characterize the SST over the whole Pacific Ocean. On the average, when the equatorial east Pacific Ocean is warm in winter, the SST is warm also in the central Equatorial Pacific; but in mid-latitudes at about 40N, the central Pacific is cold then. It is really this total pattern which characterizes the "warm" SST years selected by H-W.)

Horel and Wallace analyzed their data for winter seasons; namely for December, January and February grouped together. It is interesting to see how consistent their results are for all the warmest SST years which they selected and also for the coldest years which can be selected from their diagram (their Figure 2). They found that the largest correlation coefficient between SST and 700 mb heights for the winter season occurred near 60N, 160E. The correlation coefficient there was -0.66. To test for consistency, the departure from normal (DN) of the 700 mb heights at that location were tabulated in Table 1. There were 10 SST-warm years and 8 SST-cold years (i.e., years when the Equatorial Pacific Ocean SST was anomalously warm or cold.)

We note in Table 1 that in all 8 February months with SST cold, the 700 mb height was above normal at 60N, 160E; also in 8 out of the 10 SST warm years, the 700 mb height was below normal. In January, almost equal consistency was found. In 7 out of 8 SST cold years the 700 mb heights were above normal. In 7 out of 10 SST warm years the 700 mb heights were below normal. Persistence of the DN sign, from January to February, was more consistent in the SST cold years than in the SST warm years.

However in December, consistency was not evident. Half the 700 mb heights were above normal and half were below normal in both the SST warm years and in the SST cold years.

Therefore, the results shown in Table 1 are consistent with H-W as to the sign of the 700 mb DN, but mainly in January and February. Presumbably H-W might have found an even larger correlation coefficient at 60N, 160E, if they had confined their study to January and February, although the magnitude of the DN's are also a factor.

Table 1

Departure from Normal

Mean Monthly 700 mb Heights (m)

60N, 160E

SST warm years				SST cold years			
Years	Dec	Jan	Feb	Years	Dec	Jan	Feb
1951-52	-15	-28	- 21	1949-50	-60	+ 61	+19
57-58	-16	-31	+ 20	54-55	+59	- 20	+29
58-59	+ 1	+13	- 55	55-56	+45	+ 70	+68
63-64	-55	-57	+ 11	64-65	+29	+ 21	+ 9
65-66	-19	-61	-114	67-68	- 8	+ 43	+86
68-69	+ 5	-32	- 37	70-71	-28	+ 91	+81
69-70	-60	+80	- 34	73-74	-12	+143	+39
72-73	+15	-49	- 47	75-76	+35	+ 2	+25
76-77	+40	+14	- 59				
77-78	+48	-34	- 20				
numbers of negative cases (out of 10 possible)				number of positive cases (out of 8 possible)			
	5	7	8		4	7	8

Table 2

Departure from Normal

Mean Monthly 700 mb Heights (m)

60N, 110W

SST warm years

Years	Dec	Jan	Feb
1951-52	-51	-46	+10
57-58	-36	+59	+32
58-59	+12	-11	-8
63-64	+48	-28	-9
65-66	-15	+16	-20
68-69	+32	+4	+50
69-70	+58	+7	+23
72-73	-29	+17	+39
76-77	-3	+33	+50
77-78	-17	+89	+101
number of positive cases (out of 10 possible)	4	7	7

SST cold years

Years	Dec	Jan	Feb
1949-50	-8	-68	+36
54-55	-11	+10	-8
55-56	-1	+74	-27
64-65	-37	-4	-68
67-68	-5	+11	+78
70-71	-22	-17	-0
73-74	+32	-54	-16
75-76	-14	+16	-41
number of negative cases (out of 8 possible)	7	4	6

Horel and Wallace found a correlation coefficient of +0.45 at 60N, 110W. Table 2 shows the 700 mb DN as in Table 1. Here the results are not as consistent as they were in Table 1. In February, 6 out of 8 700 mb DN's were negative for the SST cold years, only 4 out of 8 negative DN's occured in January. In the SST warm years the number of positive DN's were 7 out of 10 in both February and January. In December, the SST cold years showed consistency with 7 out of 8 negative DN's. But for the warm SST years, December had only 4 out of 10 positive DN's; i.e., more than half with the "wrong" sign.

So over all, January and February seem to show greatest consistency and agreement with H-W as to sign of the DN, but December seems more doubtful in that respect.

Because of the month to month variation of the results at the two locations in Tables 1 and 2, we decided to examine the 700 mb height variation over most of the Northern Hemisphere separately for each calendar month. A magnetic tape had already been furnished by the NOAA Long Range Prediction Group. This tape included mean monthly 700 mb height data from January 1947 through May 1979, and had been used extensively to study the 700 mb variation, especially at 60N. (Fritz, 1980). The tapes contained data from 15N to 90N.

We accepted the SST characterization as given by Horel and Wallace for the years listed in Tables 1 and 2. For the 10 SST warm years, the average 700 mb height was computed at each 10° latitude and 10° longitude grid point from 20N to 80N. The same computation was made for the SST cold years. Then the following difference, ΔH, was computed.

$$\Delta H = \bar{H}_w - \bar{H}_c$$

where $\bar{H}_w$ is the 10 year average for the SST-warm years and $\bar{H}_c$ is the 8 year average for the SST cold years. This was done separately for each calendar month. And because Table 1 suggests that the February results are most consistent we shall describe the maps of ΔH in the order February January, December. We shall also discuss the results for November.

February ΔH.

The map of ΔH for February is shown in Fig. 1. The largest value of ΔH was -94 m at 60N, 170E. In addition there was a belt of negative heights surrounding the pole in a ring which was displaced southward approximately along longitude 90W. Along this circumpolar belt were several negative height centers. The most extensive one was the area centered near 55N, 175E; another center, with magnitude about -35 m was located just off the U.S. east coast, centered at almost 35N, 70W. A third center, with magnitude about -35 m, lay near 60N, 10E; and finally a center of about -57 m appeared near 80N, 90E. Angell (1980) also found that warm sea-surface temperature in the tropical Pacific was related to "displacement of the polar vortex toward the region 180-90° west".

An area of positive heights appeared over Northern Canada and the adjacent Arctic Ocean; its central value was about +38 m and it was located near 65N, 125W. This is not far from the center of positive correlation found by H-W for the winter months.

The striking feature of the circumpolar ring of negative ΔH, was its similarity with theory and with observation. H-W found a ring of centers of negative correlation, (as described above) lying also in a quasi-circumpolar ring with four centers of negative correlation coefficients. Two of these centers lay near the centers in Fig. 1; namely, the one already mentioned near 60N, 170E, and the one off the U.S. east coast. They show also another center in the Pacific ($r = -0.59$) near 40N; 140W, and one in the Atlantic ($r = -0.30$) near 50N, 20W.

This agreement is, of course, to be expected because both studies use the same 700 mb data as the ones used in Fig. 1. However, their results are for the whole season, December, January, February, and they presumably used all years, not only the "warm" and "cold" years. So some of the disagreement between the height distribution, ΔH, in Fig. 1 and the distribution of H-W's correlation coefficients, is doubtless due to these differences is the data base used.

Horel and Wallace also find a region of high correlation, +0.63 near 25N, 155E. In Fig. 1, a region of positive values of ΔH appears there also. Other areas of positive ΔH are evident over the Mediterranean and over Asia.

Turning to theory, Opsteegh and van den Dool (1980) have computed the geopotential height response to an SST anomaly in the tropical ocean. They also show comparison with Rowntree's GCM for 300 mbs. Both theoretical results contain the ring of low heights displaced from the pole along a meridian which is somewhat downwind from the heating area. In Rowntree's results, which refer to a tropical heating in the Atlantic, the largest negative height anomaly appears near latitude 50N, somewhat upwind (west) of the longitude of tropical heating. This too is in qualitative agreement with Fig. 1.

Thus, the February results agree with H-W's seasonal results, and with theoretical results too. In January, many of the same features appear; but differences are present also. The map for ΔH in January is shown in Fig. 2.

January ΔH.

In January, the largest negative value of ΔH was -83 m, also at 60N, 170E. This time, the band of negative ΔH, does not completely surround the North Pole; it is interrupted by a positive area which stretches from Greenland to Arabia. However, the band of negative ΔH, as in February, does reach from Kamchatka across the southern U.S. and into the Atlantic. Again a center of negative ΔH, value about -35 m, lies along the southeastern United States; this time, however, the center seems to be somewhat further west than the corresponding low center in February. The low in the Atlantic is considerably further south than in February; in January, it was located

near 40N, 25W with a value of about -25 m. The negative area which was present in February at 80N, 90E, is not present in January. Instead the region of the whole Arctic basin shows positive values of ΔH, with a maximun appearing over Greenland (value about +45 m) instead of over Canada where it appeared in February. The positive area in the Western Pacific is again present as it was in February. A high ~, +45m, appears near 55N, 40E, somewhat to the northwest of the weaker high which appeared in February near the Aral Sea.

In summary, ΔH in January appears quite similar to ΔH in February over the Pacific Ocean and over the southern United States. Elsewhere, the values of positive ΔH seem to have been displaced eastward from Western Canada to Greenland and perhaps have expanded into the Arctic Ocean bordering Siberia. And as we shall see (Figs. 10 and 11) the weak center in the Atlantic and its southward displacement, give more prominance to wave no. 1, while wave no. 2 is suppressed in amplitude.

December ΔH.

In December, further changes from February were observed. The map of ΔH for December is shown in Fig. 3. In December a center of negative ΔH appears over the Pacific near 45N, 160W. Its values was -48 m. This is considerably weaker than the values in January or February, and the center was farther to the southeast. The band of negative ΔH, again stretches across the Pacific Ocean, then weakly across Mexico. This time the negative area "trough" passes well inland over the eastern United States and eastern Canada, then to a center, (ΔH = -95 m), near 50N, 20W. It then continues across Europe to Turkey. Was the large negative ΔH in the Atlantic related to the SST's in the tropical Atlantic Ocean? It would be interesting to investigate that possibility.

The positive values of ΔH now again appear over western Canada and the adjacent Arctic Ocean (ΔH = +45 m). The high ΔH which had appeared in February near the Aral Sea and in January south of Finland, now appeared still further northwest (ΔH = +60 m) centered over Scandinavia.

To some extent then the negative pattern in the Pacific appears again, although weaker and further east. The positive area in the southwest Pacific seems to have shifted towards the northwest, with a high value of +20 m appearing over the south China Sea.

Of significance for the eastern United States is the location of the lowest ΔH there. In January and February, centers of negative ΔH lay along the east coast. Therefore, from geostrophic wind considerations one might expect below normal temperatures in SST-warm years along much of the U.S. east coast in those months; the reverse would be expected in SST-cold years. A preliminary review of the "temperature departure from normal" maps in the Monthly Weather Review indicates that in February this expectation was often fulfilled.

November ΔH.

From Pacific tropical SST kindly supplied by Dr. E. Rasmusson (Climatic Analysis Center, NOAA), it appears that SST's in November in general, had the same sign as the SST anomalies for December, January and February. It is therefore interesting to examine the November values of ΔH.

Fig. 4, shows the map of ΔH for November. Again we find a low center in the central Pacific with a value of -59 m. This center was located near 50N, 170W. There also was a weak negative area over the southern United States, with a center of about -20 m near southern Arizona. Although negative values still appear over the southeastern U.S., the values are very small. Another negative center appears over the Atlantic Ocean, (ΔH = -46 m), near 50N, 20W. The negative zone, although weak, continues across central Asia.

Several centers of positive ΔH appear around the hemisphere near latitude ? and 40N; a zone of positive ΔH lies over Greenland and the Arctic Ocean north of Siberia. One of the positive ΔH centers appears near the west coast of North America. Interestingly, the axis of positive ΔH, stretching from Greenland across the Arctic Ocean to Northern Siberia, is essentially perpendicular to the axis of positive ΔH across the Arctic in December.

In November (Fig. 4) again the negative band of ΔH is not continous around the Earth. If the SST was producing the negative area over of the North Pacific, in November and December the effect does not seem vigorous enough to produce a continuous ring of negative ΔH as it did in February. Still there is a suggestion of a continuous ring or spiral of negative ΔH that stretches from North Canada, across the Pacific into Asia, thence across Scandinavia and England into the Atlantic; after a weak break (ΔH = +5), that negative band continues across the southern United States, to Northern Mexico and into the tropical Pacific.

Summary of Pacific and Atlantic Ocean negative centers

In all four months, the negative ΔH centers in the Pacific and Atlantic are summarized in Table 3.

Table 3

Locations of negative ΔH centers

	Pacific Ocean			Atlantic Ocean		
	Lat. (N)	Long.	ΔH (m)	Lat. (N)	Long. (W)	ΔH (m)
Nov	50	170W	-59	50	20W	-46
Dec	47	170W	-48	50	20W	-95
Jan	55	180	-83	40N	20W	-25
Feb	55	175E	-94	60N	10W	-35

The patterns for all four months show persistent negative ΔH centers in the central Pacific near longitude 180°. In the Atlantic Ocean, centers of negative ΔH also appear near longitude 20°W in all four months. This suggests that wave number 2 plays a prominent role in the response of the atmosphere to the influence of the Pacific SST anomalies. However, because the magnitude of the ΔH centers in the two oceans varies, wave number 1 and other Fourier components also affect the results. To examine this further the Fourier components for February and for December were computed.

Fourier Wave Components.
The "normal height field".

Fig. 5 shows the phase and amplitude of the trough of the "normal" 700 mb heights for wave no. 1. The "normals" are the average heights for the period 1951-1973. The phase varies very little from October through March, from 20N to 60N; Eliasen (1958) had already found similar results. At latitude 70N and 80N more variation occurs, but the amplitudes are relatively small there. Fig. 5 is also in agreement with the values of van Loon, Jenne and Labitzke (1973).

The amplitudes are largest near latitude 50N, varying from about 70 m in December to 59 m in February. In October and March the amplitudes seem substantially smaller; namely, about 48 m. Therefore unless interaction of the SST with the mean circulation is very sensitive to small changes in the "normal" height field, we probably cannot depend on interactions between the SST effect and the "normal" height field to "explain" the observed difference between the December ΔH (Fig. 3) and the February ΔH (Fig. 1). Opsteegh and van den Dool (1980) found that the mean zonal wind variations between winter, fall and spring, do not produce weaker effects in the response of the SST. If anything they found even more pronounced response in fall and spring than in winter.

Fig. 6 shows the "normal" phase and amplitude for wave no. 2. Again the phase wave varies little from month to month except at latitude 30N, where the amplitude is small. It is interesting to note that the slope of the phase line in Fig. 6 is from east to west with increasing latitude this is opposite to the slope for wave no. 1 (Fig.5), a result also found by Eliasen (1958) and emphasized by Austin (1980).

The amplitude in wave no. 2 is again a maximum at 50N. Moreover, the amplitude is similar in December, January and February, i.e., between 50 m and 59 m. Now however, the amplitude in November is substantially smaller and even smaller in October; in March the amplitude is also smaller than in the winter months. So again, it might be difficult to look for differences between December and February (Fig. 1 and 3) based on variations of the "normal" height fields in those two months.

Finally, Fig. 7 shows the phase and amplitude for wave no. 3, of the normal 700 mb height field. Again there was almost no variation of the phase from month to month for October through March, this time at all

latitudes. The amplitude was somewhat smaller in December than in February (46 m verses 59 m). It is interesting to note that at latitude 50N, the amplitude for wave nos. 2 and 3 was about the same in March as in December; and the amplitudes were also mainly similar for those months at all latitudes.

Components of the ΔH field.

What about the variation of the wave number component in ΔH; i.e., in the heights for the SST warm years minus the SST cold? Fig. 8 shows the phase of the minima for ΔH for wave numbers 1 through 4, for February. Fig. 8 shows that the slope of the phase with latitude was from east to west with increasing latitude. This is the same sense as the slope of wave no. 2 in the "normal" height field; only now it is observed even in wave no. 1. At latitude 60N and 50N, especially, all the wave number components contributed to the negative values of ΔH. In fact all the phase lines appear to intersect at about 45N. Depending on the amplitudes of the Fourier components, we might find a large negative ΔH at 45N. However, the amplitude (Fig. 11) of wave no. 2 (40 m) at 60N. was a maximum, decreasing in magnitude both north and south of 60N.

Figures 10 through 14 show the amplitudes of the Fourier components of ΔH for November through March. In December, January and February, the amplitudes of wave numbers 1, 2 and 3, are usually the largest at latitudes 50 to 80. In January, as noted earlier, wave number 1 dominated. Still, depending on the phase relationships shown in Figs. 8 and 9, contributions from wave numbers 4 and 5 may also be important.

The sum of the amplitudes at 60N is not sufficent to yield the observed large negative values of ΔH, namely -94 m in Fig. 1. To attain such large values we need to include the zonal average value of ΔH; i.e., wave no. zero. The zonal mean values are shown in Table 4.

Table 4 - Zonal average value of ΔH (m)

Latitude	December	January	February
80N	+ 4	+25	- 6
70	+ 2	+ 5	-10
60	-10	- 2	-10
50	-18	-11	-11
40	- 6	-11	- 6
30	+ 6	0	+ 4
20	+ 7	+ 7	+10

Table 4 shows that for latitudes 40 to 60N ΔH was negative in all three winter months. At latitude 20 and 30N, there was a tendency for positive ΔH to appear. This effect would increase the west winds near 40N in the SST warm years relative to the SST cold years. A tendency for the subtropical jet stream to strengthen significantly in response to sea surface temperture changes in the equatorial Pacific was also noted from numerical experiments at GFDL (1980).

The slope of the phase lines in Fig. 8 suggest that one of the effects of the SST anomalies might be to strengthen the influence of wave no. 2 in the "normal" 700 mb height field. In the normal field, wave no. 2 is prominent because of the effect of mountains and continent-ocean contrast on the atmospheric circulation (Manabe and Terpstra, 1974).

Discussion

The "normal" 700 mb height field does not seem to be sufficiently different in December from February to explain the difference between the ΔH fields in those months (Fig. 1 and 3). What other effects might have done that? Of course the possibilities are very large. Among the possibilities, are the actual detailed variations in SST not only in the tropical Pacific but also in mid-latitude SST variations. Numerous empirical studies (e.g. Namias, 1979) and many theoretical studies discuss relationships between central Pacific SST and aspects of the atmospheric circulation. For example Fritz (1980) has found that the correlation between the SST in the central Pacific and the mean monthly 700 mb height at 60N, 170W was positive in all winter months and in two separate decades. Therefore it might be useful to examine the SST in the central Pacific for the "warm years" and the "cold years" in Table 1. We note again that, on average, the SST in central Pacific would tend to have opposite signs from the SST in the equatorial Pacific (Weare, et al, 1976).

Another factor might have been the SST in the Atlantic. Rowntree (1976) had shown that the SST in the Atlantic would affect the circulation of the atmosphere over the Atlantic. Perhaps a large SST anomaly in the Atlantic produced the observed large negative value of ΔH (-90 m) in the Atlantic in December (Fig. 3). Depending on whether anomaly in the Atlantic were in phase or out of phase with the SST in the Pacific, the Fourier wave number components of the ΔH pattern might be affected in different ways. Other factors might be the snow and ice distributions. These would not only vary from November to February but also from one year to the next. The southward extent of snow and ice, and the thicknesses would of course influence the surface temperatures. Can differences in the surface temperatures, due to ice and snow, also influence the general circulation of the atmosphere, in addition to sea surface temperature effects?

In December (Fig. 9), the slope of the phase line of wave no. 1 is different from the slope in February (Fig. 8). Although, there is some ambiguity about the slope direction between 60N and 50N, from 50N to 30N, the slope is opposite in December from the slope in February. In December for wave no. 1, the slope is more like the slope of the "normal" wave no. 1 phase. The shift of the wave no. 1 minimum in December from the

Pacific north of 60N to the Atlantic sector at 40N and 50N, is connected with the large negative value of ΔH (-95) in the Atlantic in December. Whether this shift was caused by a large SST anomaly in the Atlantic Ocean is unknown at present.

The possibility that the SST in the Pacific and Atlantic might affect the large scale circulation simultaneously raises many possibilities. For example, the Pacific and Atlantic Ocean gyres have different periods (Reiter, 1979). If the gyres carry with them SST anomalies, then observed cyclic variations in the atmospheric circulation might be related to combinations of two or more periodic variations of SST in the two oceans.

Earlier Fritz (1980) showed that the lowest 700 mb height anomaly at 60N, 90E tended to occur at 10 year intervals. Specifically, in the sum of wave no. 1 and wave no. 2, the lowest 700 mb height at 60N did occur at about 90E in 1948, 1957, 1958, 1967, 1968, 1977, 1978. To see what happened in all the years from 1948 to 1978, the 700 mb height departure from normal (DN), is shown in Fig. 15. The similarity in the DN's for the decade 1948-1957 and 1968-1977, is striking. Moreover even in the decade 1958-1967, the years 1958, 1959, 1966, 1967 follows the trends in the other two decades. Fourier harmonic analysis of the data in Fig. 15 show that the period 10/4 = 2.5 years had the largest amplitudes in the decades 1948-57 and 1968-1977. The time resolution of the data by Fourier analysis is not very detailed. It is nevertheless interesting to note that 2.5 years is not far from the quasi-biennial period; also 2.5 years is not very far from 28 months, twice the Chandler wobble period of about 14 months. Maksimov (1958) claimed that the surface pressure near 90E in high latitudes exhibited a periodicity which he attributed to the Chandler "polar tide" and to the non-spherical shape of the Earth. Whether periodic SST variations in the Earth's oceans, or the Chandler wobble, or some other effect is the "cause" of the regularity in Fig. 15 is at present uncertain.

In summary, the circulation change differences from November to February (Figs. 1-4) in relation to SST seem consistent in same respects but different in other respects. The cause for the difference are unknown; perhaps surface effects or atmospheric effects such as vertical stability might be causative factors. It will also be interesting to extend the analysis to other months, perhaps for the whole year July to June, extending Figures 1-4 in both time directions. It should also be interesting to examine maps such as Fig. 1-4 for sea-level pressure data.

Acknowledgements

It is a pleasure to acknowledge many useful discussions with my colleagues Dr. Alan Faller and Dr. J. D. (Theo) Opsteegh. (Dr. Opsteegh is visiting the University of Maryland from the Royal Netherlands Meteorological Institute). Dr. Faller computed the Fourier components for Fig.15.

The 700 mb data tape was kindly supplied by R. Dickson and D. Duvall of the Long Range Prediction Group, NCAA.

Programming help was received from Mr. A. Postosky, a student at the University. Thanks are due the University's Computer Facility for use of the Univac 1140 computer. Clare Villanti drafted the figures, and Sue Ernstein typed the manuscript.

Finally, the Goddard Space Flight Center, NASA, under Grant NSG 5209, supported the work reported here.

REFERENCES

Angell, J.K., 1980: Comparison of variations in atmospheric quantities with sea-surface temperature variations in the equatorial eastern Pacific. (Submitted to J. Appl. Met.)

Austin, J.F., 1980: The blocking of middle latitude westerly winds by planetary waves. Q.J.R.M.S., 106, 327-350.

Eliasen, E., 1958: A study of the long atmospheric waves on the basis of zonal harmonic analysis. Tellus, 10, 206-215.

Fritz, S., 1980: 700mb height field, December 1948-78. Chapter VIII, pgs. 122-151, in "Multidisciplinary Research Program in Atmospheric Science." O.E. Thompson, Principal Investigator. Dept. of Meteorology, University of Md., College Park, NASA Grant NSG-5209, 277 pgs.

Geophysical Fluid Dynamics Laboratory, 1980: Activities-FY 80, Plans-FY 81, with a review of 25 years of research, 1955-1980. U.S. Dept. of Commerce, NOAA, Environmental Res. Labs., 82 pgs., plus appendices.

Horel, J.D. and J.M. Wallace, 1980: Planetary scale atmospheric phenomenon associated with the interannual variability of sea-surface temperature in the Equatorial Pacific. Mon. Wea. Rev., (in press).

Maksimov, I.V., 1958: Nutational Phenomena in the high latitude atmosphere and their role in the formation of climate. In "Problems of the North" no. 1; Academy of Science, USSR Translated by National Res. Council, Ottawa, Canada, p. 103-123.

Manabe, S. and T.B. Terpstra, 1974: The effects of mountains on the general circulation of the atmosphere as identified by numerical experiments. J. Atmos. Sci., 31, 3-42.

Namias, J., 1979: Premonitory signs of the 1978 break in the west coast drought. Mon. Wea. Rev., 107, 1675-1681.

Opsteegh, J.D. and H.M. van den Dool, 1980: Seasonal differences in the stationary response of a linearized primitive equation model. J. Atmos. Sci., (in press).

Reiter, E.R., 1979: On the dynamic forcing of short-term climate fluctuations by feedback mechanisms. Envir. Res. Paper, 21, Colorado State University, Fort Collins, 62 pgs.

Rowntree, P.R., 1976: Response of the atmosphere to a tropical Atlantic Ocean temperature anomaly. Q.J.R.M.S., 102, 607-625.

van Loon, H., R.L. Jenne, and K. Labitzke, 1973: Zonal harmonic standing waves. J. Geophys. Rev., 78, 4463-4471.

Weare, B.C., A.R. Navato and R.E. Newell, 1976: Empirical orthogonal analysis of Pacific sea-surface temperatures. J. Phys. Oceanography, 6, 671-678.

FIGURE LEGENDS

Figure 1 : Map for February of ΔH for 700 mb heights. $\Delta H = \bar{H}_w - \bar{H}_c$, where $\bar{H}_w$ is the average 700 mb height for the 10 years when the tropical Pacific SST was anomalously warm, and $\bar{H}_c$ was the average height when the SST was cold. Note the circumpolar ring of negative values, displaced southward along about 90°W.

Figure 2 : Map for January of ΔH. (see Fig. 1).

Figure 3 : Map for December of ΔH. (see Fig. 1).

Figure 4 : Map for November of ΔH. (see Fig. 1).

Figure 5 : Wave number 1. Phase and amplitude (m) of the "normal" 700 mb height field. The phase is the longitude of the minimum height for that Fourier component.

Figure 6 : Wave number 2. (otherwise the same as Figure 5). The bar shows the range of phases at latitude 30N. December phase was at the western edge, January at the eastern edge.

Figure 7 : Wave number 3. (otherwise the same as Figure 5).

Figure 8 : Phase (Longitude of minima) of ΔH, for February; wave numbers 1 through 4.

Figure 9 : Phase (Longitude of minima) of ΔH for December; wave numbers 1 through 4.

Figure 10: Wave number 1. Amplitude (m) for November through March, from latitude 20N to 80N, of ΔH.

Figure 11: Same as Fig. 10, except wave number 2.

Figure 12: Same as Fig. 10, except wave number 3.

Figure 13: Same as Fig. 10, except wave number 4.

Figure 14: Same as Fig. 10, except wave number 5.

Figure 15: DNWIW2 is the sum of Fourier components for wave number 1 plus wave 2 of 700 mb height departure from normal (DN) for December, at 60N, 90E. The abscissa show the years arranged in 3 decades, 1948-1957, 1958-1967, 1968-1977. The years 1958 and 1968 are repeated in order to include 1978.

Figure 16: "Normal" 700 mb height map for February after latitudinal average heights were subtracted from mean heights. Zonal average heights shown in rectangular boxes along longitude 40E. [Note this figure not discussed in text, but included for comparison with Figure 1.]

FIG. 1

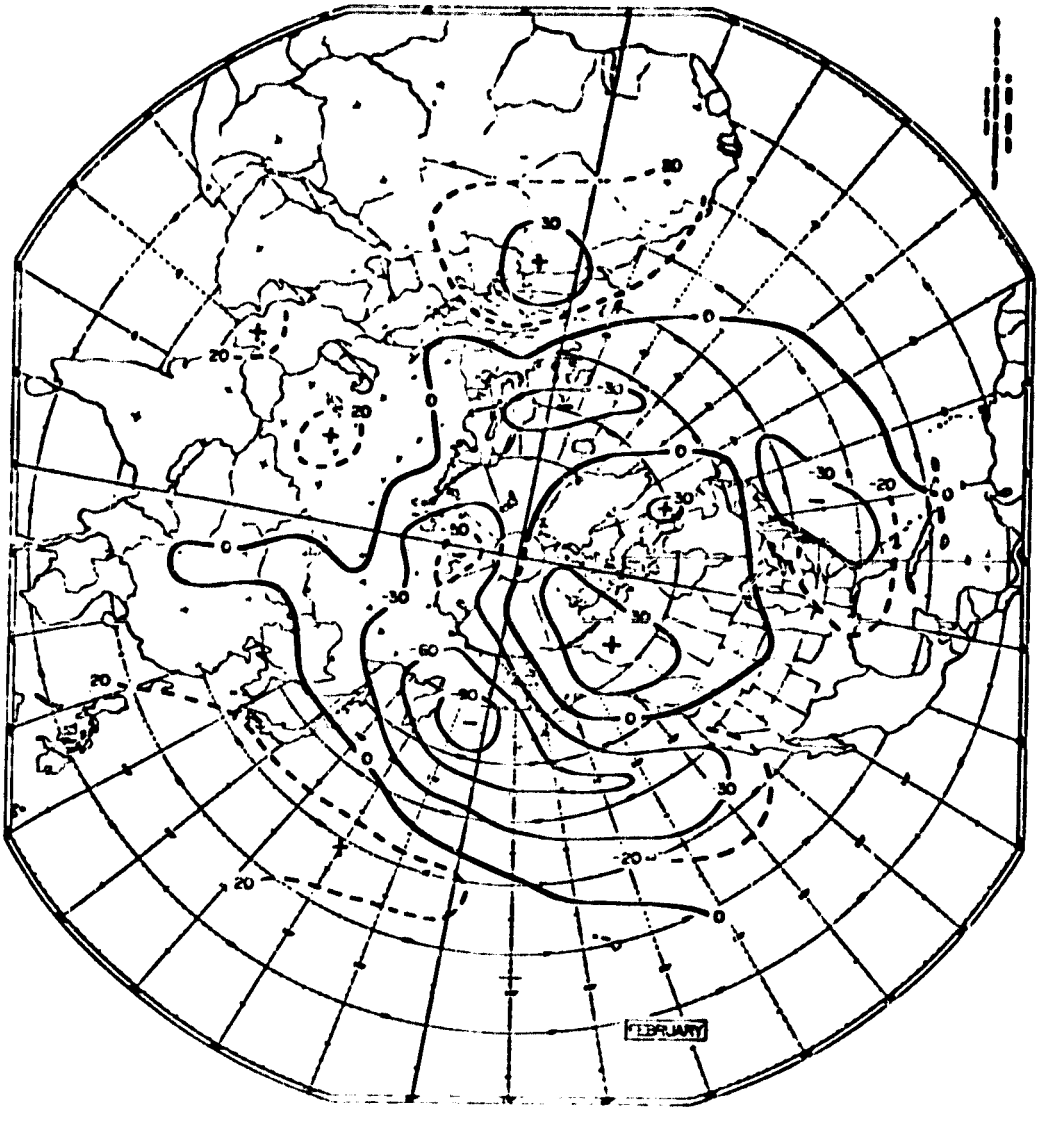

FIG. 2

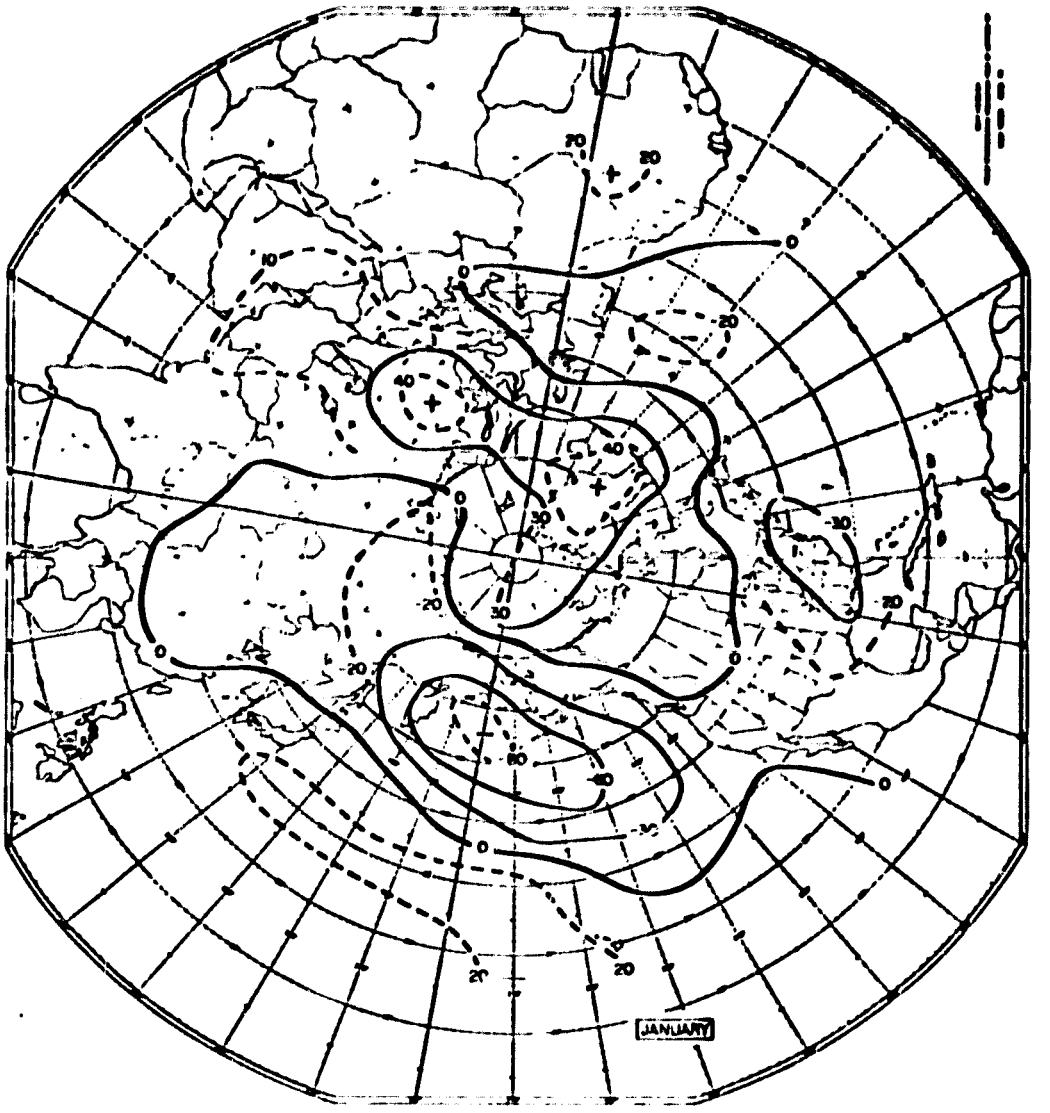

FIG. 3

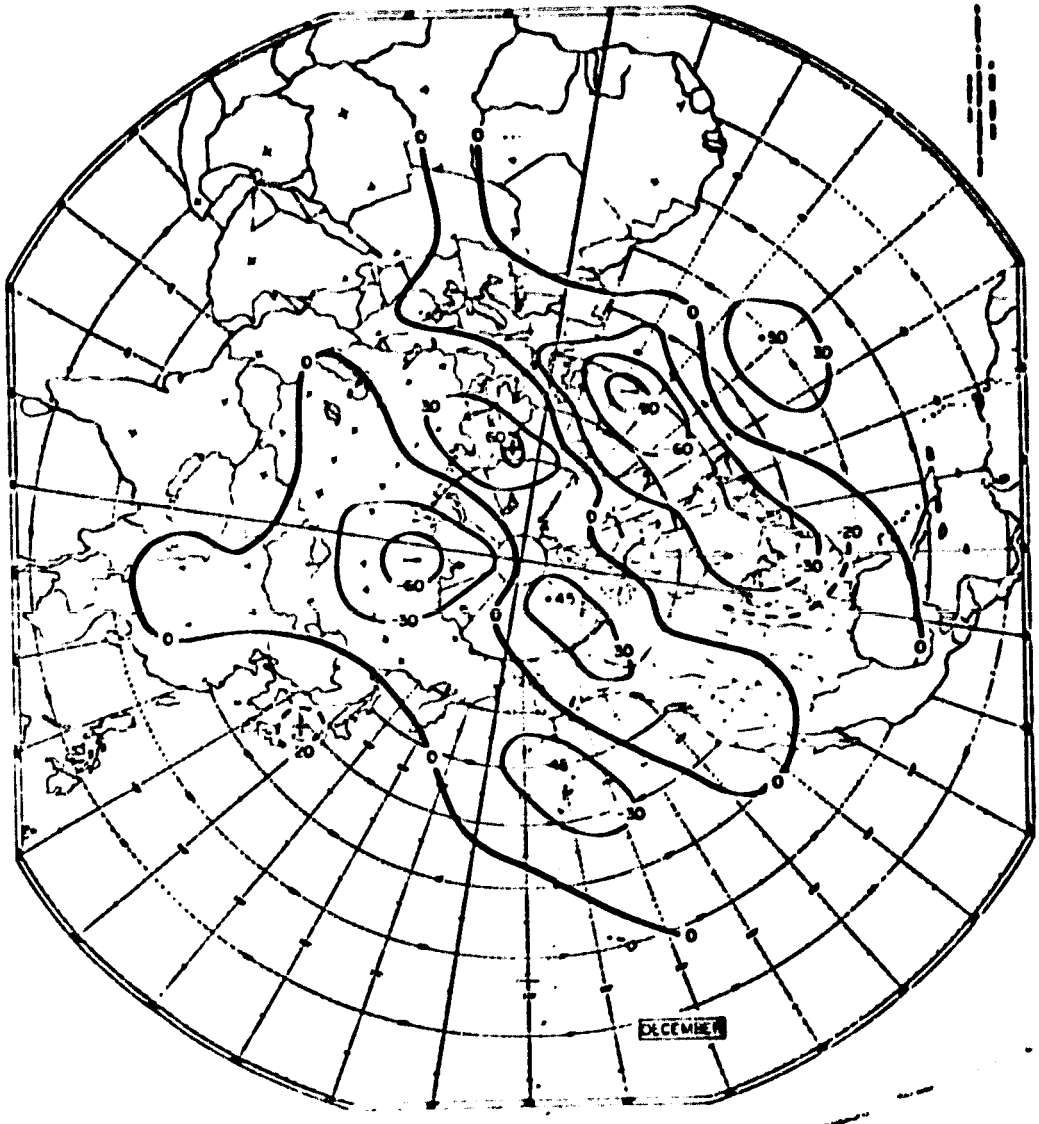

FIG. 4

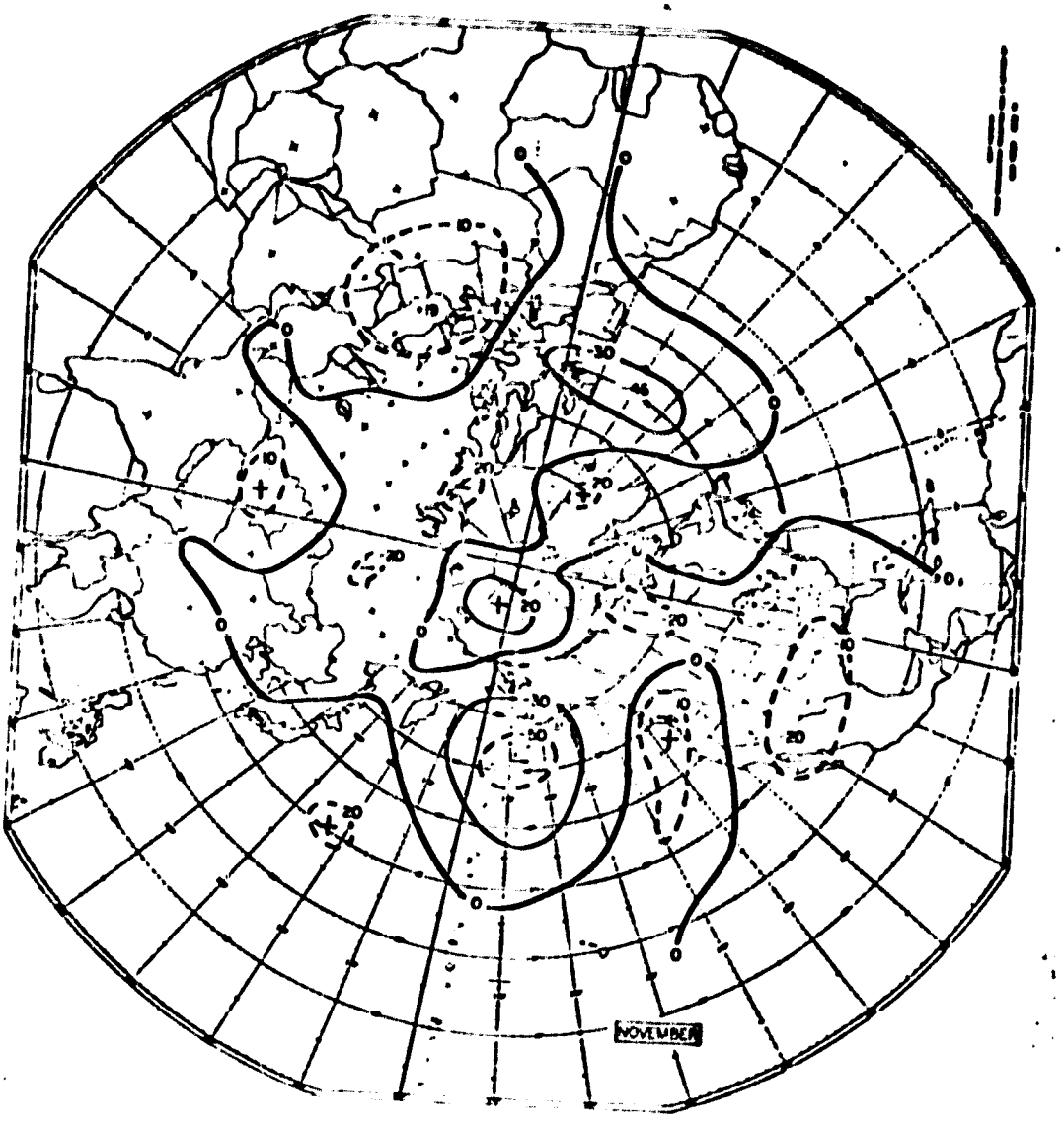

FIG.5

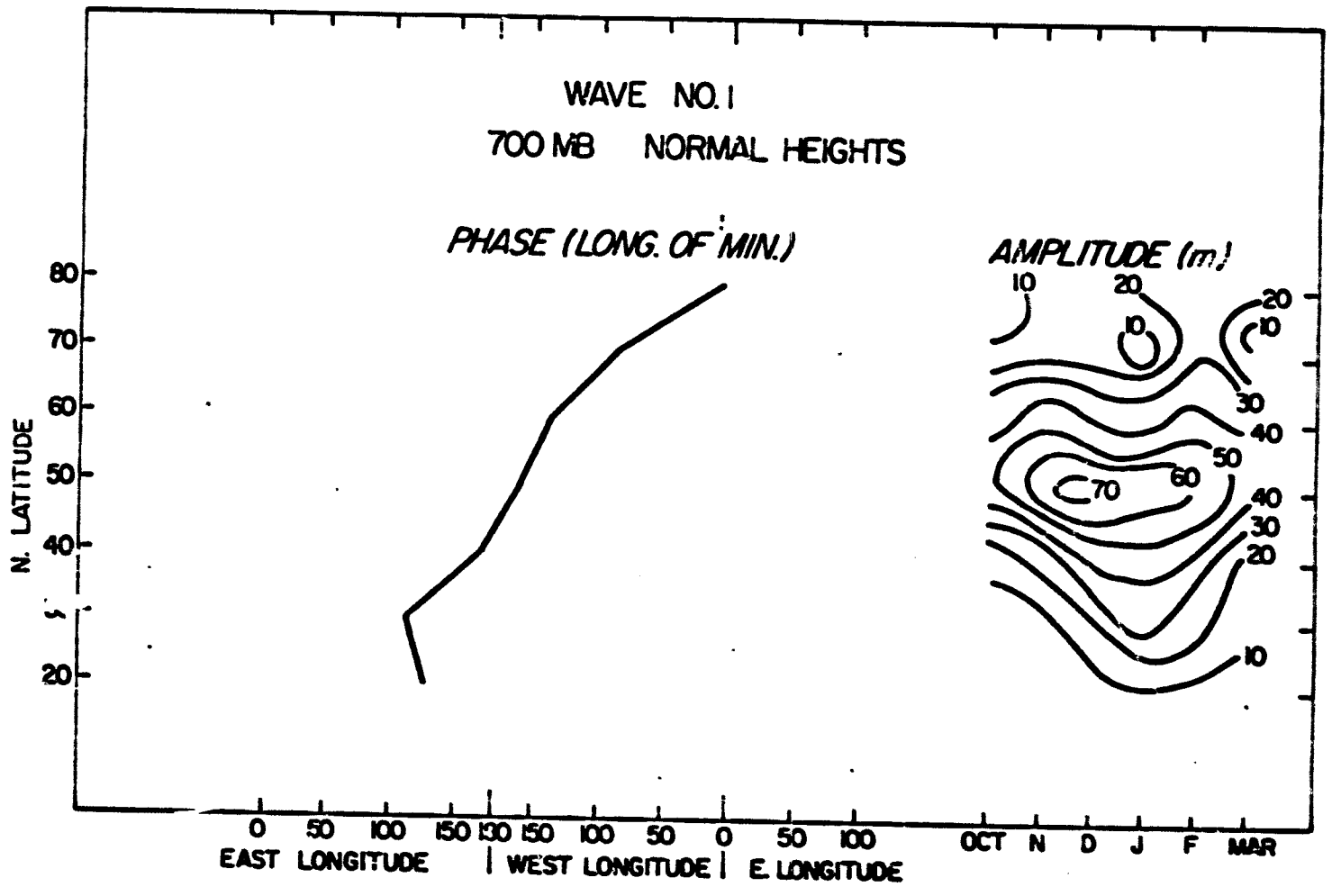
WAVE NO. 1
700 MB NORMAL HEIGHTS
PHASE (LONG. OF MIN.)
AMPLITUDE (m)
N. LATITUDE
80
70
60
50
40
20
10
20
10
20
10
30
40
50
60
70
40
30
20
10
0 50 100 150 130 150 100 50 0 50 100
EAST LONGITUDE
WEST LONGITUDE
E. LONGITUDE
OCT N D J F MAR

FIG.6

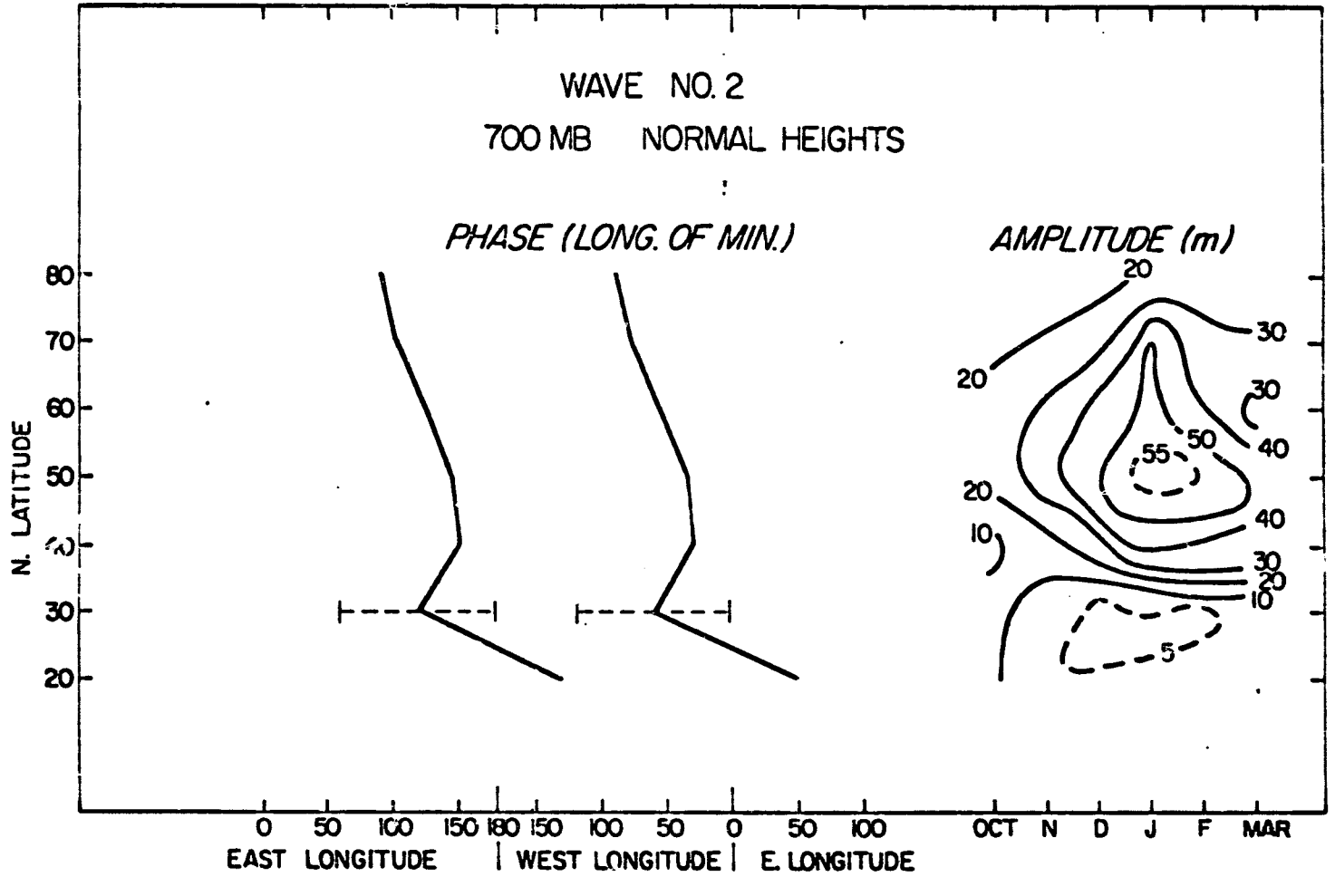
WAVE NO. 2
700 MB NORMAL HEIGHTS
PHASE (LONG. OF MIN.)
AMPLITUDE (m)
N. LATITUDE
80
70
60
50
40
30
20
0 50 100 150 180 150 100 50 0 50 100
EAST LONGITUDE
WEST LONGITUDE
E. LONGITUDE
OCT N D J F MAR
20
30
40
50
55
10
5

FIG. 7

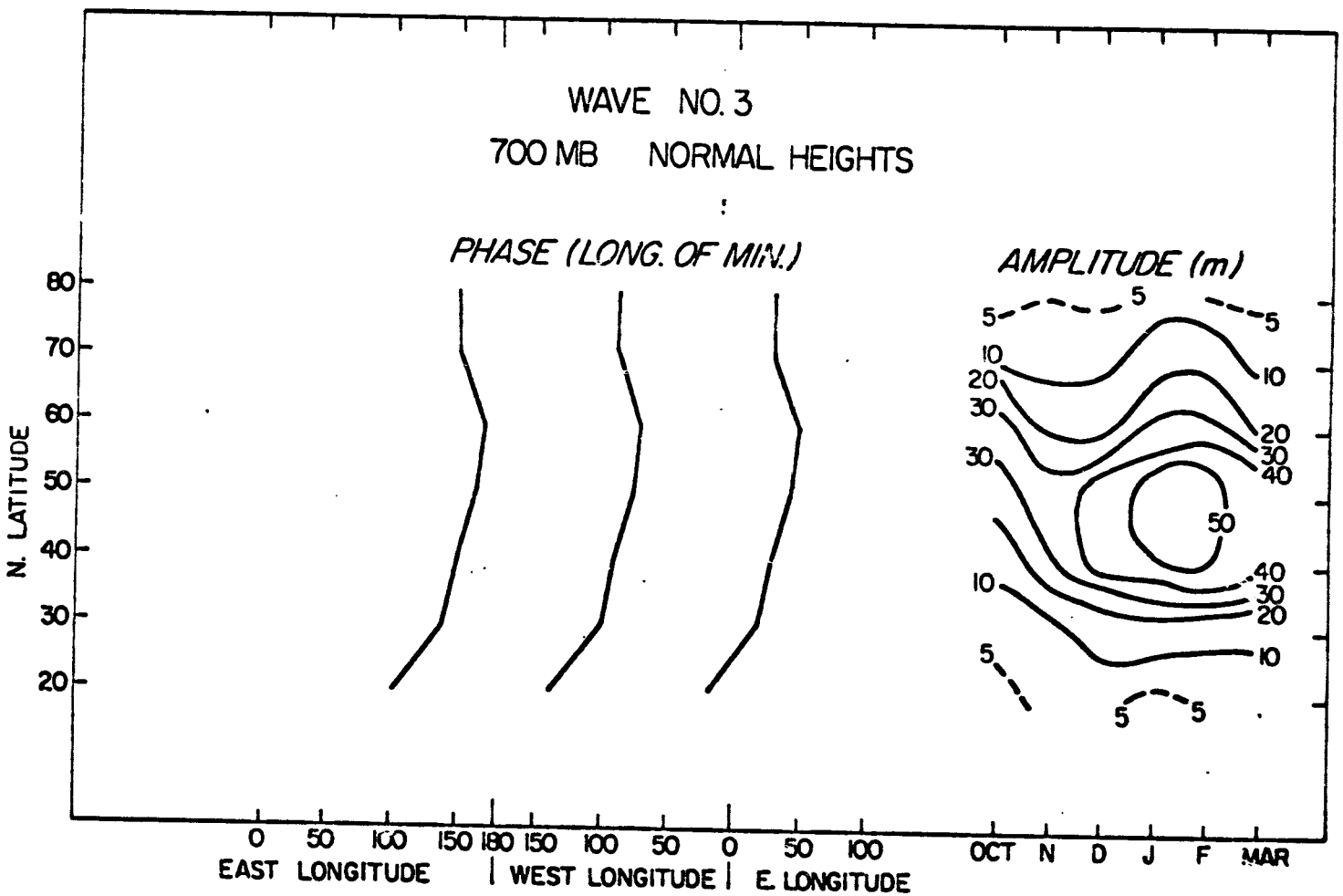
WAVE NO. 3
700 MB NORMAL HEIGHTS
PHASE (LONG. OF MIN.)
AMPLITUDE (m)
N. LATITUDE
80
70
60
50
40
30
20
0 50 100 150 180 150 100 50 0 50 100
EAST LONGITUDE
WEST LONGITUDE
E. LONGITUDE
OCT N D J F MAR
5
10
20
30
40
50

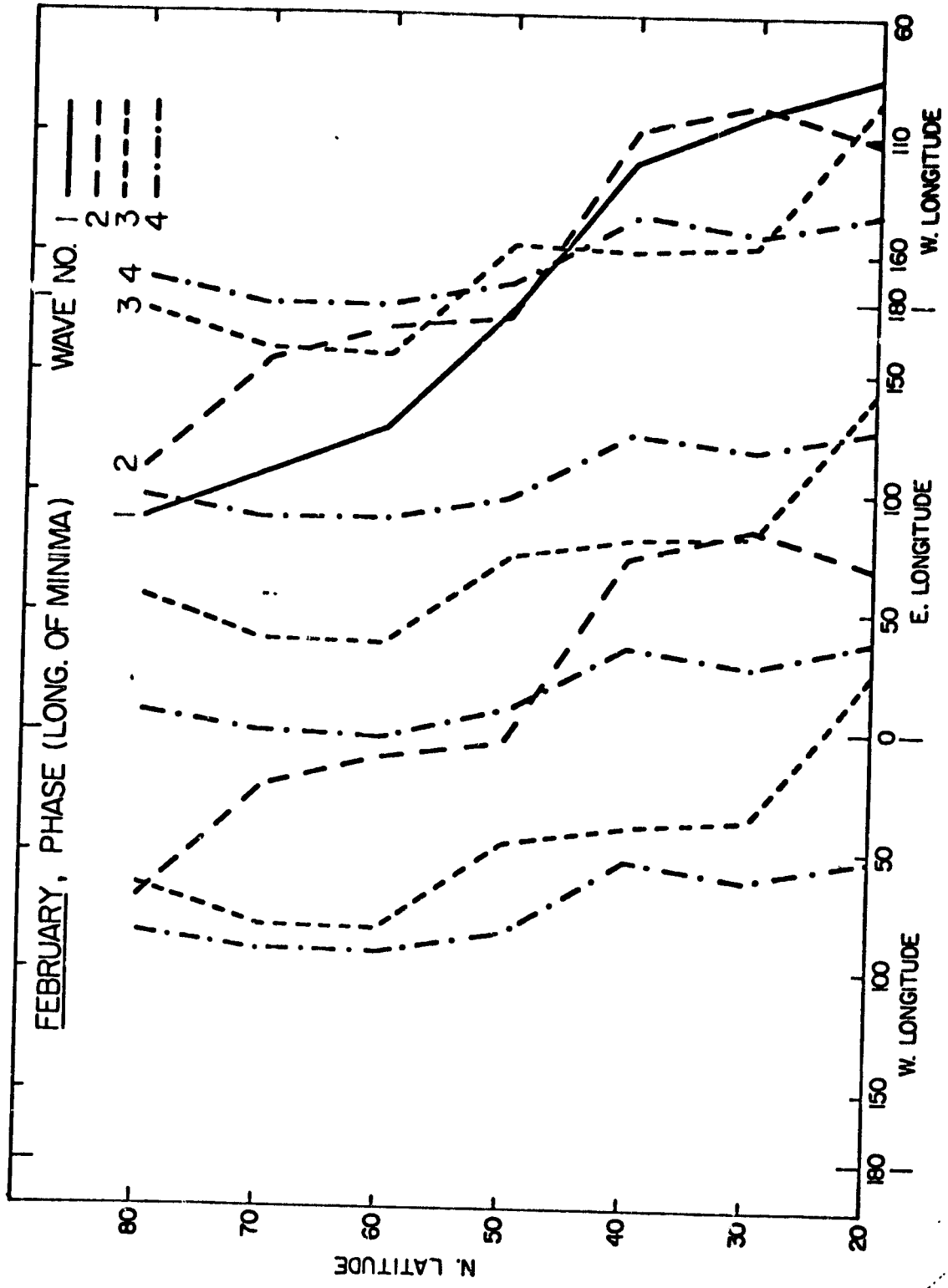
FEBRUARY, PHASE (LONG. OF MINIMA)
WAVE NO. 1
2
3
4
N. LATITUDE
80
70
60
50
40
30
20
W. LONGITUDE
180
150
100
50
0
E. LONGITUDE
50
100
150
180
W. LONGITUDE
160
110
60

FIG.8

FIG.9

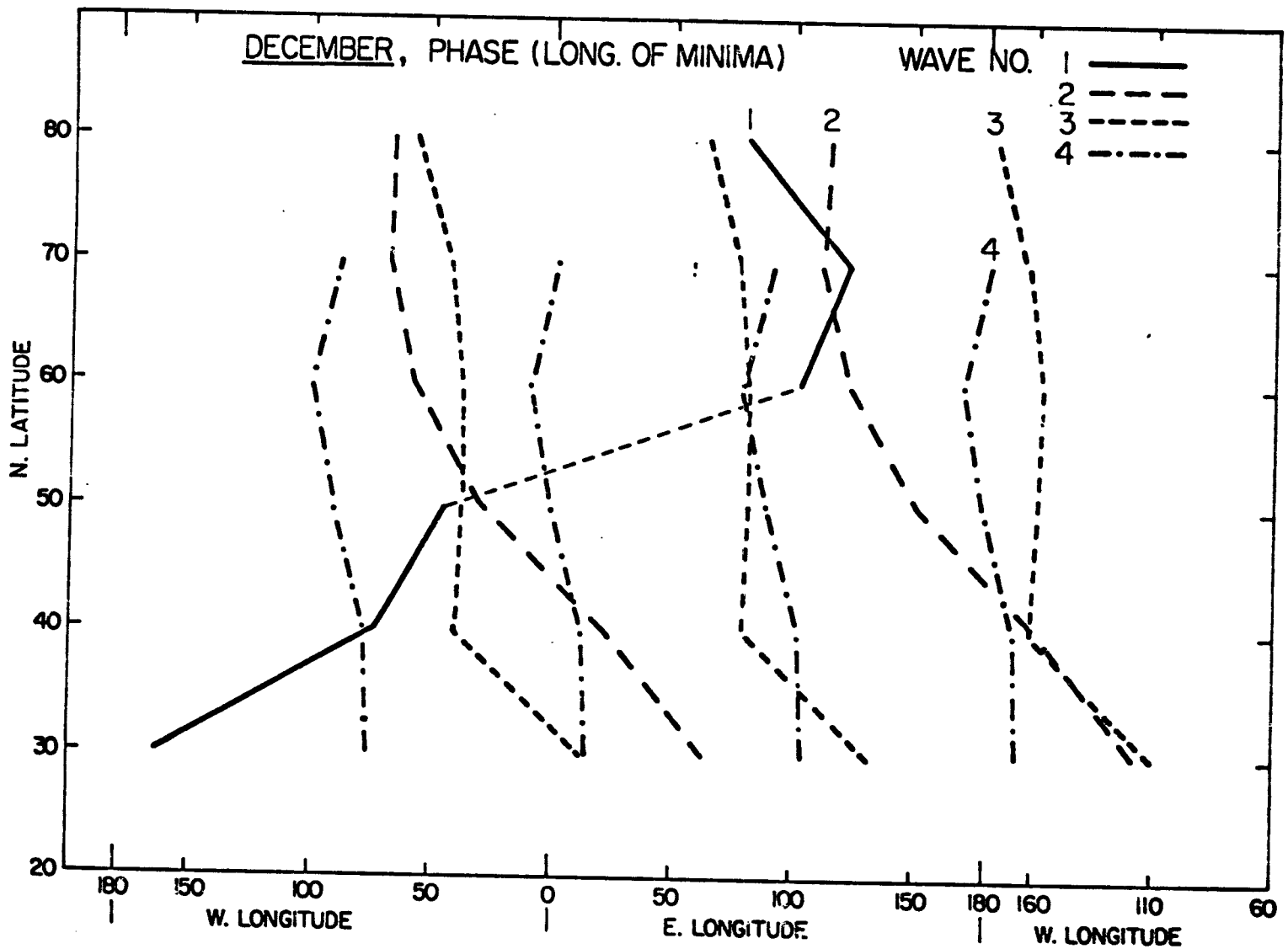
DECEMBER, PHASE (LONG. OF MINIMA)
WAVE NO. 1
2
3
4
N. LATITUDE
80
70
60
50
40
30
20
180
150
100
50
0
50
100
150
180
160
110
60
W. LONGITUDE
E. LONGITUDE
W. LONGITUDE

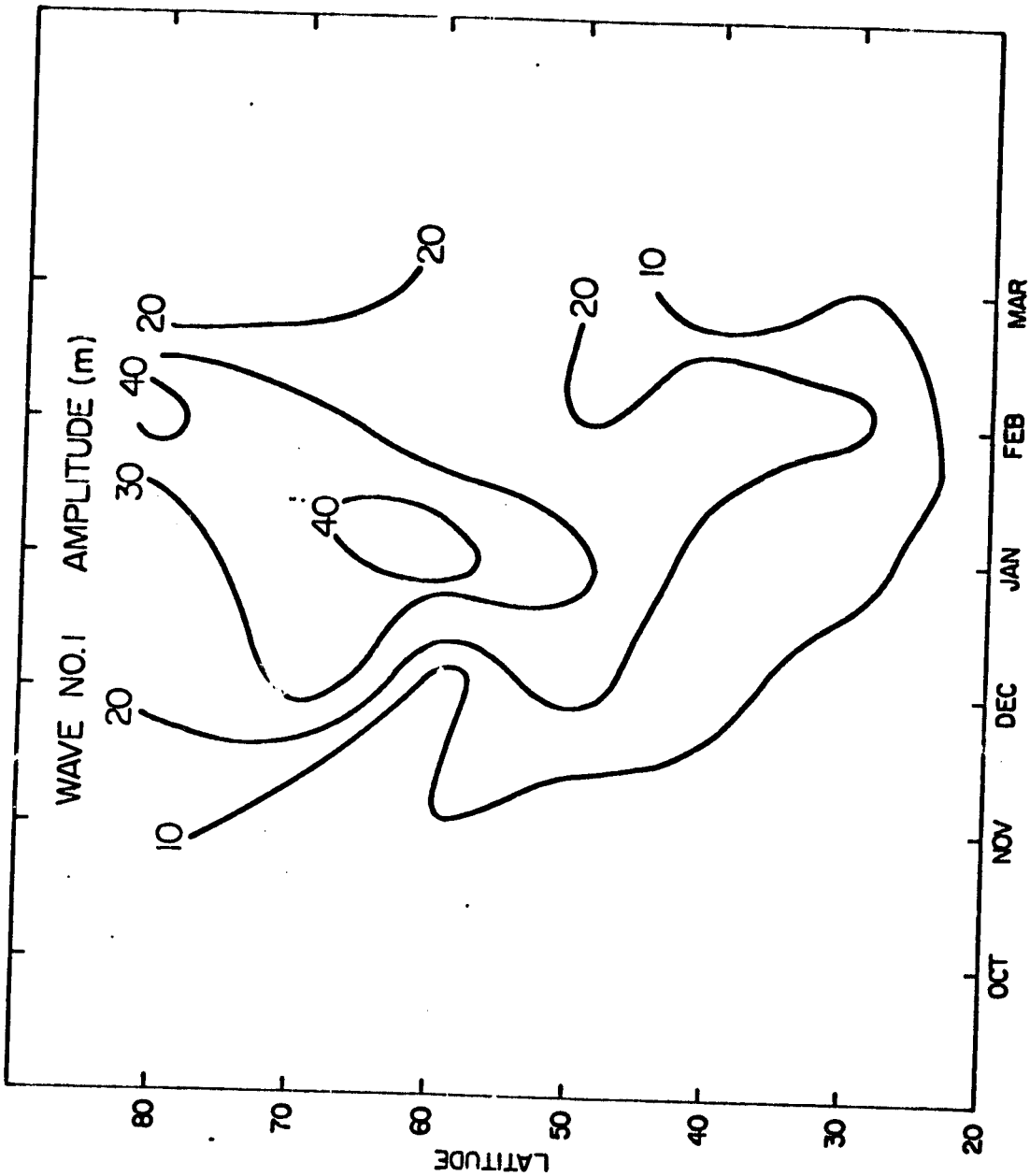
WAVE NO.1 AMPLITUDE (m)
10
20
30
40
LATITUDE
80
70
60
50
40
30
20
OCT
NOV
DEC
JAN
FEB
MAR

FIG.10

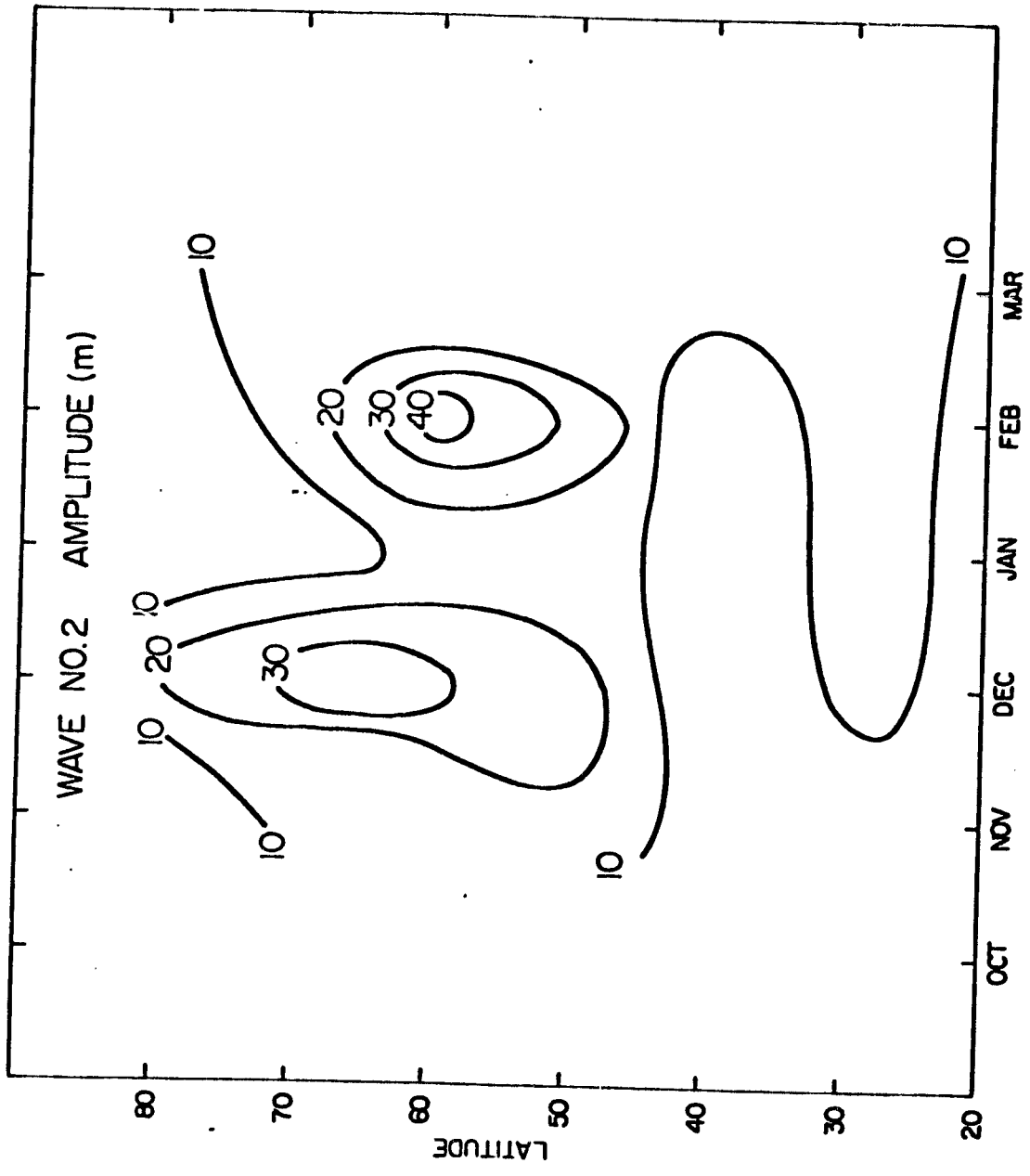
WAVE NO.2 AMPLITUDE (m)
10
20
30
40
OCT
NOV
DEC
JAN
FEB
MAR
LATITUDE
80
70
60
50
40
30
20

FIG. 11

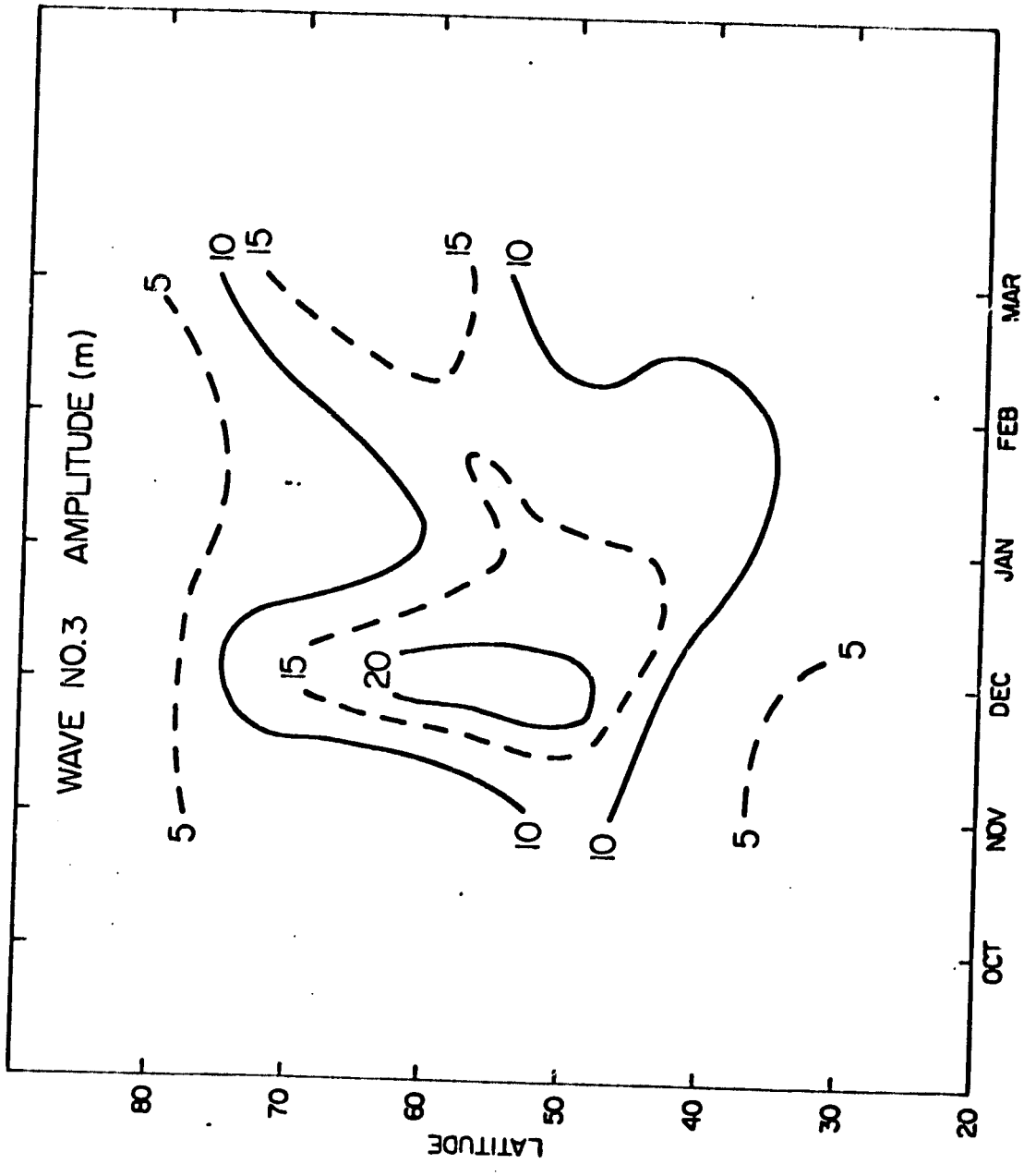
WAVE NO.3 AMPLITUDE (m)
5
10
15
20
OCT
NOV
DEC
JAN
FEB
MAR
80
70
60
50
40
30
20
LATITUDE

FIG.12

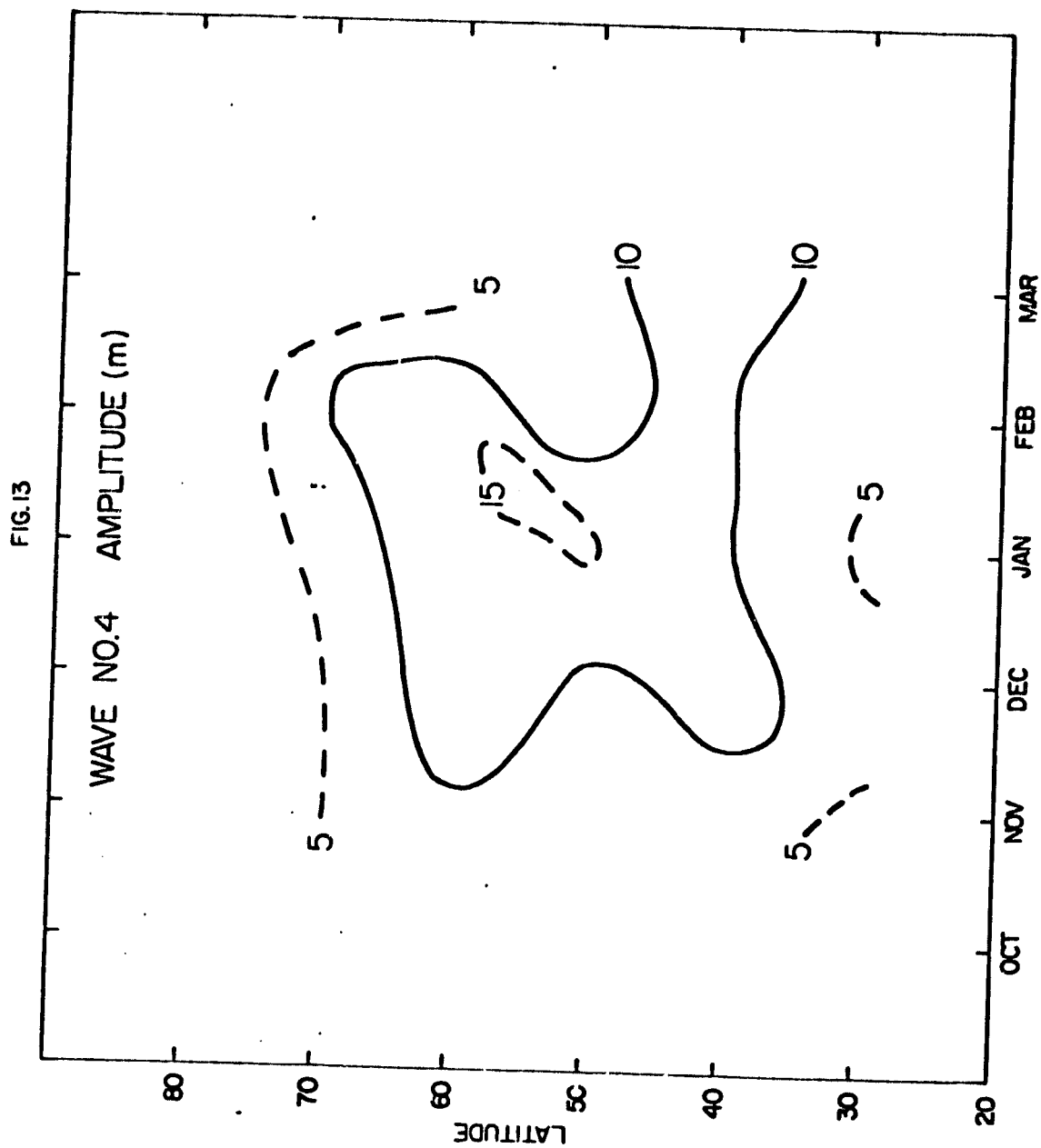
WAVE NO.4 AMPLITUDE (m)
5
10
15
10
5
5
LATITUDE
80
70
60
50
40
30
20
OCT
NOV
DEC
JAN
FEB
MAR

FIG.13

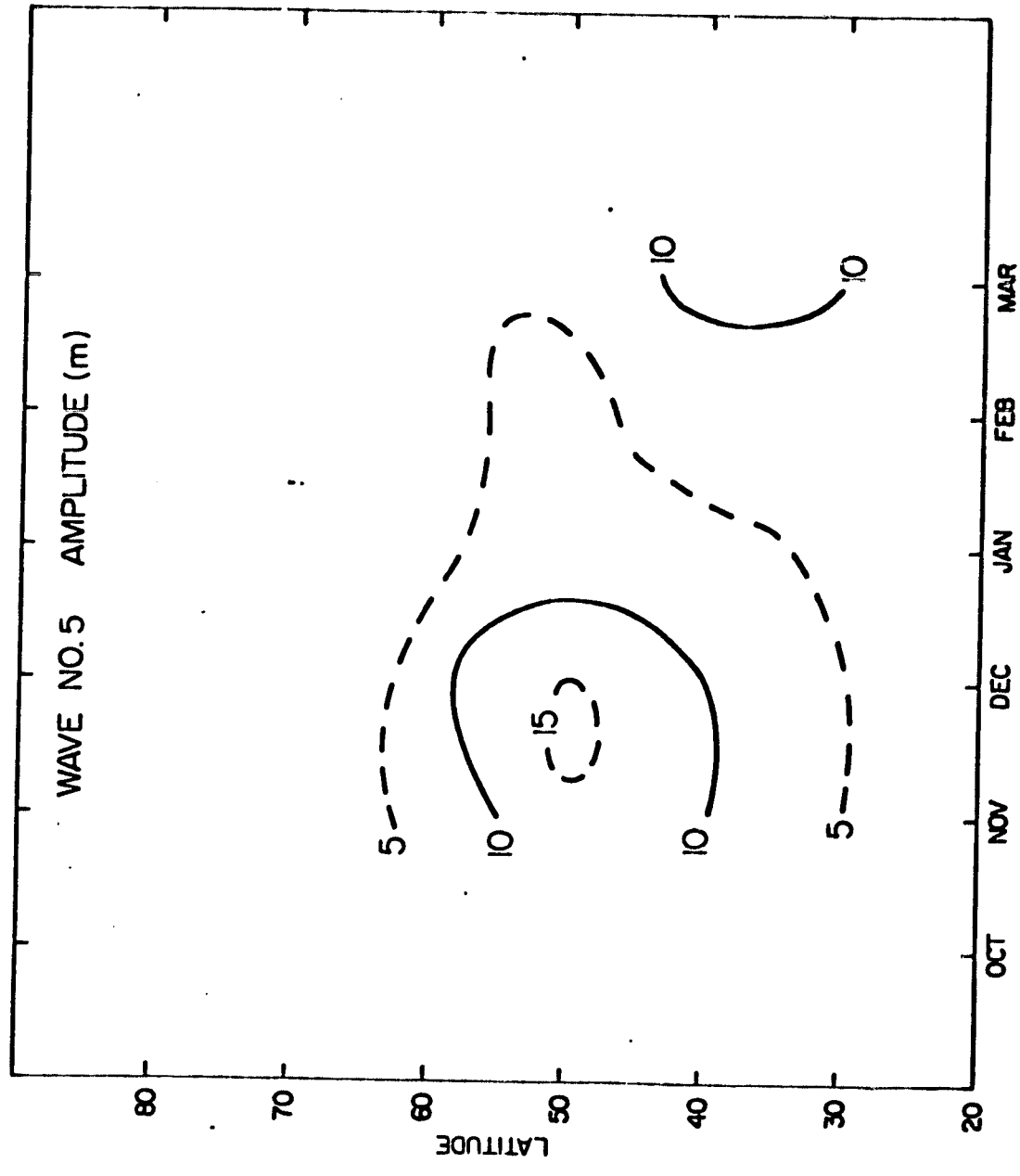
WAVE NO.5 AMPLITUDE (m)
LATITUDE
80
70
60
50
40
30
20
OCT
NOV
DEC
JAN
FEB
MAR
5
10
15
10
10
10
5

FIG.14

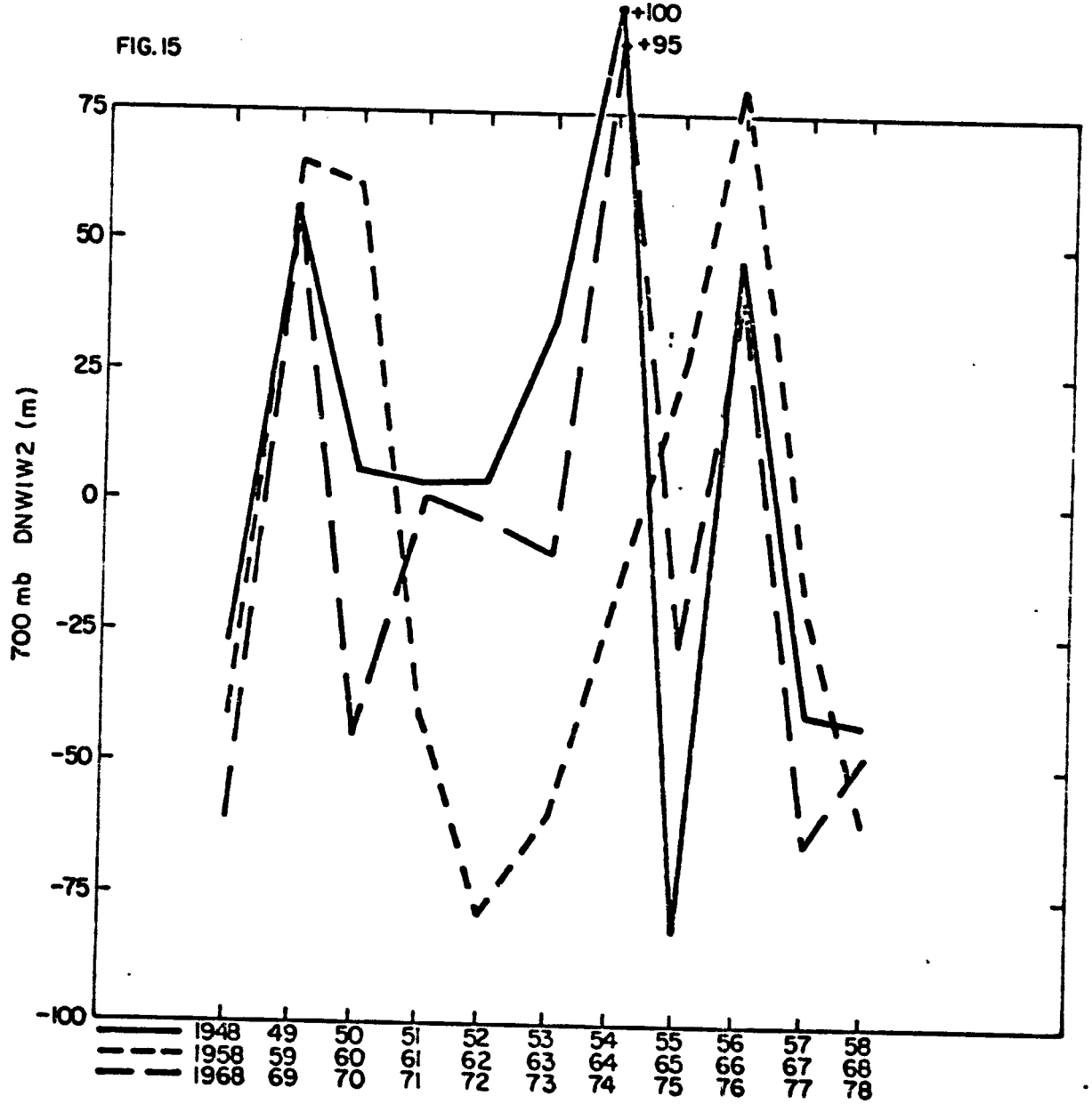

FIG. 16

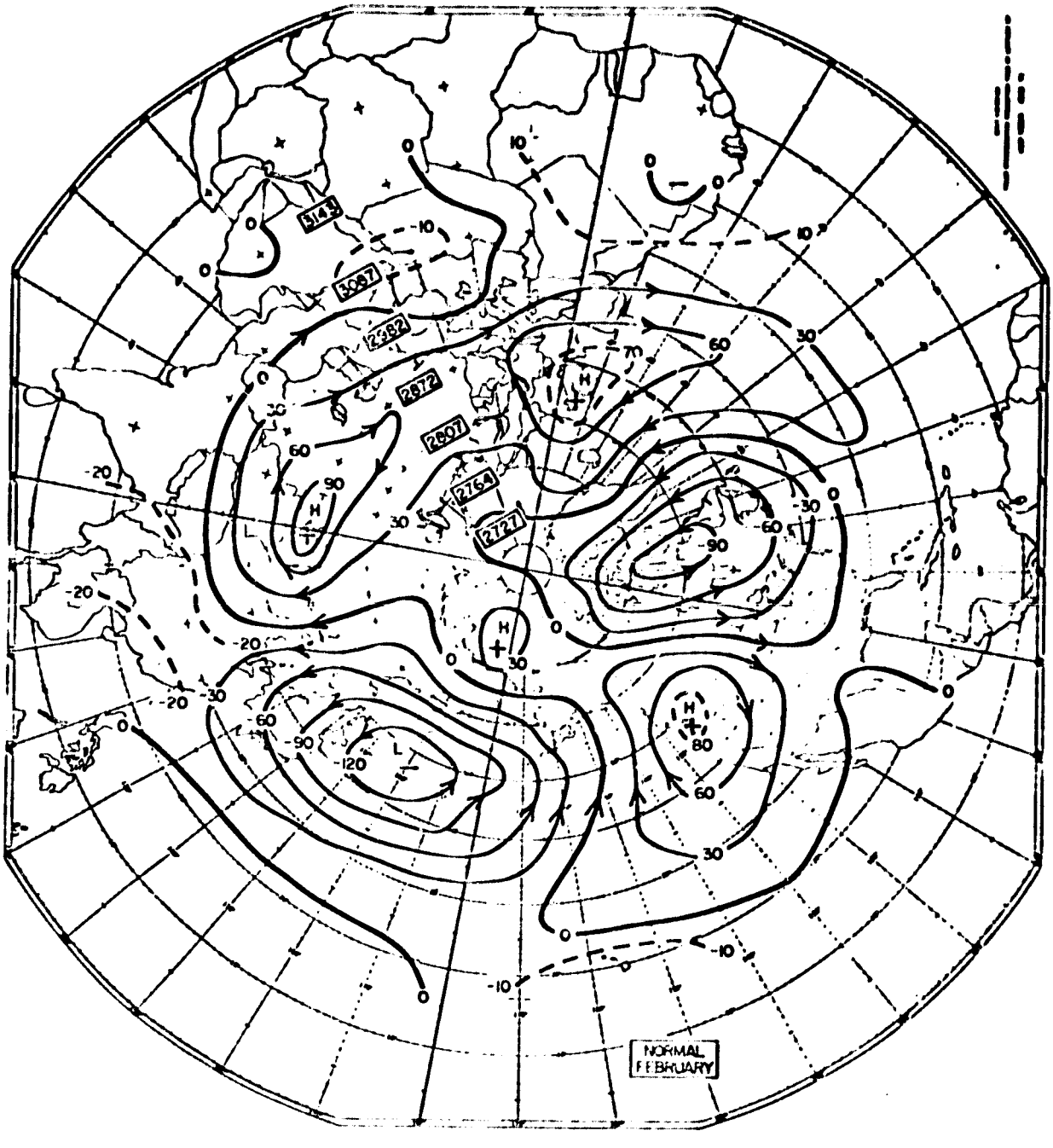

VII. Climate Modelling

by

D. Rodenhuis

J. Rivero

J. Yorke

1. Introduction

The research of this project is directed towards seasonal climate variations; that is, fluctuations in the meteorological variables on time scales of about a month and on spatial scales of 1000's of kilometers.

It is an underlying assumption that the "climate" on these scales can be resolved if the causes of planetary-scale, quasi-stationary disturbances are understood. Then, since there is a correlation between the amplitude and phase of the planetary waves and the location and intensity of synoptic-scale disturbances (e.g., Blackmon, 1976, Lau, 1979), it may be possible to predict the fluctuation in regional climate through the use of empirical statistics. Although the prediction, per se, is not the object of our project, it is the underlying motivation for the study of planetary-wave dynamics.

The causes of the planetary wave-patterns have been recognized for many years since the rather successful studies of Charney and Eliassen (1949), Smagorinsky (1953) and Doos (1963). Using linear steady-state models, they were able to explain the existence of the stationary, planetary-scale waves in middle latitudes. From these early studies the importance of topographic forcing and thermal heating were recognized.

It is somewhat of a surprise, then, that the prediction of the long waves in forecast models has been so difficult. Apparently, the nonlinear dynamics of the long waves on a sphere are a more complex process than was visualized with early models for stationary flow. Recently, there have been several developments which have illustrated the important dynamics of planetary waves.

* Spherical geometry is important in the description of ultra-long waves (Kallen, 1980; Sommerville, 1980).

* There are important "teleconnections" between the forcing in the tropics latitudes and the response in middle latitudes (Morel and Wallace, 1980; Opsteegh and van den Dool, 1980).
* Multiple equilibria in a nonlinear dynamical system may exist for some conditions of mechanical and thermal forcing (Charney and DeVore, 1979; Vickroy and Dutton, 1979; Lorenz, 1980).

These developments give some insight into the possible prediction of planetary-scale waves and their seasonal variations. That is, it may be possible to simulate the ultra-long waves beyond the time period of deterministic forecasting if we can correctly model the dynamic response of the atmosphere to slowly changing, but persistent thermal and topographic forcing. The minimum requirements of such models are:

* Global in lateral extent, two layers.
* Non-linear dynamics.
* Resolution of planetary scales.
* Balanced conditions for pressure/velocity determination.
* Capable of long-term integrations; i.e., energetically consistent and able to explain long-term changes in the distribution of mass and kinetic energy.

A low-order, spectral model with these characteristics has been developed and is operating on the GLAS computer (Section 3). A steady-state, geostrophic version of this model has recently been constructed also by Ashe (1979). This type of model recognizes the collective forcing of all scales less than planetary size only implicitly through an equivalent imposed heating function.

Of course, it is a serious limitation to ignore the explicit interaction of cyclone-scale eddy fluxes with the planetary scale steading waves. However,

if the forcing by synoptic, baroclinically unstable disturbances is really the most important forcing function of planetary-scale dynamics, efforts to make dynamic, seasonal climate forecasts are seriously impaired, since the forecast will depend on statistical products from an instability process which cannot itself be forecast more than a week or so in advance. In fact, we have some evidence that this pessimistic view is not warranted; reasonable planetary wave structures have been determined by many authors from topographic and external heating sources without resort to explicit forcing by the transient eddy fluxes. However, this question is by no means settled (Gall, et al., 1979). To predict the variations in seasonal climates, it may be necessary to have some explicit knowledge of the transient eddy fluxes. In that case, two choices are apparent; the eddy fluxes must be parameterized or specified from climatic data or contemporary analyses of synoptic-scale observations.

Another important question for a model of planetary waves concerns the mechanism of "blocking" which is usually associated with stationary waves of synoptic scale. To explain this phenomenon there are several theories which have been proposed which use physical mechanisms that are also important in the dynamics of planetary waves:

NON-LINEAR THEORIES

* Multiple equilibria (Charney and DeVore, 1978; Hart, 1979; Kallen, 1980; Lorenz, 1980; Vickroy and Dutton, 1979). The possibility of the existence of multiple equilibria in a nonlinear dynamic system suggests that the "blocking" phenomena may simply represent dynamic solutions in a different attractor set of a stable equilibrium point which is distinct from the usual case of quasi-periodic flow.

* Wave: wave interaction resonance (Egger, 1978). Blocking action occurs in preferred regions of the standing wave forced by planetary scale heating and topography. Travelling waves near resonance (C ≈ 0) interact nonlinearly to create a smaller-scale, persistent disturbance resembling a blocked flow condition.

LINEAR THEORIES

* Local resonance of Rossby lee waves caused by topography (Kalnay-Rivas, 1980; Faller, 1980). The response of the atmosphere to topographic forcing depends on the local flow condition at the mountain ridge and the existence of a disturbance upstream to deflect the flow.
* Planetary-wave resonance controlled by mean flow conditions, thermal and mechanical forcing (Tung and Lindzen, 1980). Medium-scale, propagating waves are excited by fluctuations in thermal forcing or changing flow conditions over variable topography. These waves are easily trapped (in the vertical) by the zonal wind field, and under the proper mean flow conditions, may be near the resonance for stationary waves, thereby producing a "blocked" condition. Blocking by longer, planetary waves is more unusual, but its influence is felt for a longer period and over a greater area, even penetrating into the stratosphere.
* Unusual thermal forcing drive both exceptionally large amplitude stationary and propagating planetary waves to produce an (apparent) large-scale blocked flow (Austin, 1980). Subsequent steering of cyclonic storms by the planetary mean flow reinforce, intensifies and maintains the blocked flow. Conditions may permit the development of intermediate wave numbers (e.g., wave number 4) which are easily resonant to the usual mean atmosphere flow conditions; this is the usual scale of blocking anticyclones.

In general, theories of blocking depend on the strength of the planetary thermal forcing or the state of the atmosphere (resonance) or the nature of the quasi-equilibrium and its dynamic fluctuations. But these same mechanisms are responsible to some degree for the existence of planetary waves and their

large-scale anomalies. In addition we have already discussed the possible contribution of cyclone-scale disturbances (transient eddies) to the planetary-scale flow.

Therefore, we study the dynamics of planetary-scale waves which are driven primarily by topography and thermal forcing. We use the global, truncated spectral model already developed for this purpose.

2. Review

Recent diagnostic studies, e.g. Van Loon (1973), Lau (1979) and Boettger (1979) indicate that the seasonal climate, as defined in the introduction, is determined largely by the long-wave components (wave number less than or equal to 4). Van Loon (1973) finds, for example, that 96% of the variance of the winter normal 500 mb geopotential height is contained in the first four wave numbers at midlatitudes. Blackmon (1976) performed an analysis of the same field in terms of Fourier series in time and Spherical Harmonics in space, and found most of the variance concentrated in the long-wave, slow moving (quasi-stationary or stationary) part of the spectrum. Lau (1979) finds that the contribution of the stationary components of the local vorticity and heat transport budgets exceeds that of the transient component by a factor of 2 to 5. Similar conclusions are reached by Wallace (1978) in his discussion of the role of stationary versus transient components in maintaining the general circulation.

The transient components are present at all scales. The short scale features (baroclinic waves) contain most of the variance associated with the transient components. Statistically, these waves are correlated with the stationary ones. Boettger (1979), among others, clearly shows increased cyclogenesis east of stationary long wave troughs.

The transient long waves have been analyzed by Madden (1979). They are propagating Rossby waves. They are of some importance to the stratosphere (Charney and Drazin, 1961; Matsuno, 1970), and some slowly moving modes near resonance may contribute to important tropospheric anomalies (Lindzen, 1980).

The stationary long waves are a response to the large-scale atmospheric forcing fields:

(a) orography,

(b) diabatic heating by turbulent heat transfer from the ground, release of latent heat, direct radiational heating and cooling, and radiative transfer within the cloudy atmosphere.

(c) internal mechanical dissipation, and

(d) energy transfer from an ensemble of cyclone-scale disturbances.

The response of the stationary component to forcing was first investigated using linear models on a beta-plane. Charney and Eliassen (1949) considered the effect of orography using a linearized equivalent barotropic model. The 500 mb. geopotential field was decomposed on a latitude circle into a large-scale stationary component and a shorter, transient component. The predicted height field was accurate enough to establish the importance of orographic forcing.

Subsequently, Smagorinsky (1953) treated the effect of sinusoidally distributed heat sources on a simple baroclinic model with constant lapse rate and wind shear, including friction. He found the response of the perturbation height field, with a trough east of the point of maximum heating. These results agree qualitatively with observation.

Since the basic state used by Smagorinsky was not entirely realistic, other investigators have refined his results. Doos (1968) used a lapse rate and wind shear varying with height. His results are not markedly different from those of Smagorinsky. Saltzman (1965) considered heating and orography simultaneously, using a linearized model. Recently, Tung and Lindzen (1979) performed a similar analysis, but using a multiple

perturbation technique. They have proposed an explanation for rare but large anomalies in the planetary waves by a "blocking" mechanism due to a resonance of a nearly stationary Rossby wave.

All these analyses rely on linearized dynamics. However, they are limited by (a) the necessity of prescribing an equilibrium basic state, which is usually assumed to be consistent with some imposed forcing, and (b) by the resonance effects which may be unrealistic. These shortcomings are reviewed by Ashe (1979). Furthermore, the studies are carried out in Cartesian geometry which is not appropriate for planetary waves and which may provide spurious reflections of energy by the lateral boundaries.

General circulation models have also been used to analyze the effects of the forcing fields. Manabe and Terpatra (1974) computed the influence of orography in the GEDL model and found significant differences in the distribution of energy between stationary and transient components. The response of GCMs to thermal forcing at locations in middle latitudes has not been very strong (Kutzbach et al. 1977; Houghton et al. 1974). However, there is some evidence that the thermal forcing from the subtropics strongly influences the atmospheric circulation in the GCM (Chervin, 1980).

The GMCs are, as a rule, unable to reproduce planetary scale, persistent features (Sommerville, 1980), or persistent "blocked" flow, although Miyakoda (1980) has been able to show improvement in this respect. Therefore, it is apparent that studies of simplified models are needed to clarify the important dynamic processes in complex GCM experiments.

Simplified models attempt to lower the order of the system by expansion in series of orthogonal functions or by asymptotic expansion. In some cases analytic solutions are possible (Baer, 1970, 1971); however,

the truncation is necessarily severe. An alternative approach is to use the methods developed for analyzing systems of nonlinear ordinary differential equations. These methods are treated in Minorsky (1962). The methods emphasize the study of the system in phase space in the vicinity of the points where time derivatives vanish (critical points, or steady states). In the case of the atmosphere or simple fluid flows each steady state is identified with a particular flow regime.

Lorenz (1962a, 1962b, 1963a, 1963b) carried out studies motivated by laboratory experiments with rotating flows, where the fluid exhibits several flow regimes determined by the imposed forcing (in this case a thermal gradient and the rotation rate). He found different, steady state solutions as the forcing was changed, i.e., the Hadley and Rossby regimes. The Hadley regime contained a number of subclasses identified by wave numbers. The behavior of the system near critical points was examined to show that transitions between states could occur. For other values of forcing the trajectory in phase space formed by the expansion coefficients is closed, surrounding two steady states (vacillation). For still other values of forcing the trajectory in phase space is chaotic.

Veronis (1963) performed a similar anaylsis for a barotropic, wind-driven ocean in a square basin, with rather realistic results considering the approximations made. Stable steady states were found. Under some conditions of forcing, the system goes into a limit cycle.

These studies suggest that even though the forcing is fixed, a system can execute transitions from one regime to another. This vacillatory behavior is suggestive of the variability of seasonal climate.

Charney and De Vore (1979) applied the methods to an equivalent barotropic model forced by orography and a vorticity source, using a channel

model with high truncation. For certain combinations of forcing, multiple equilibria are found. Three steady states appear for reasonable values of forcing although only two of these are stable. One solution suggests a "blocked" flow pattern, while the other corresponds to more normal conditions of small-amplitude waves. This work is suggestive of some atmospheric conditions although lateral boundaries, truncation and the barotropic model limit the application of these results.

Hart (1979) was able to obtain a set of identical equations using an asymptotic expansion method. This result and others indicate that the results of Lorenz and of Charney and DeVore are not a fortuitous consequence of a particular truncation procedure.

Furthermore, Ashe (1979) has found a steady state for the Lorenz four-variable model in spherical geometry, using modes symmetric about the equator. However, Ashe did not investigate the existence of multiple steady states nor the nature of solutions near equilibrium. The forcing function was obtained from observations, and there was some success in predicting the mean fields.

Charney and Straus (1980) have extended the work of Charney and DeVore to a baroclinic, two-layer channel model. Multiple equilibria were confirmed. The orography is necessary for the equilibria to exist, but the energy comes from the potential energy of the mean flow. Blocked flows, however, require unrealistically large thermal forcing. This may be due to the extreme truncation, to Cartesian geometry, to quasi-geostrophic dynamics, or to idealized forcing.

Spherical geometry appears to be mandatory in the study of planetary waves. Somerville (1980) shows that the use of a global model produces a significant improvement in the predictability of the long waves, even compared to a hemispheric model. A study of the observed global anomalies by Wallace (1980) and Horel and Wallace (1980) finds that teleconnection patterns in the 500 mb. geopotential fields are global in extent. A dynamical experiment by Hoskins (1978), who investigated the response of a linear barotropic model to long-term forcing, showed similar results.

The applicability of quasi-geostrophic dynamics to the long waves was reviewed by Kasahara (1976), who notes from scaling arguments that the divergence is of the same order as the vorticity for long waves. Kasahara suggests the use of the primitive equations, but an alternative approach is also possible. Lorenz (1962a) has simplified the primitive equations based on energetic consistency, rather than on scale analysis. This set of equations is superior to the quasi-geostrophic approximation for planetary wave studies.

3.0 Model Equations

The equations of the model are those of the two-layer energy-conserving model presented by Lorenz (1960). The model consists of prognostic equations for ψ and τ, representing respectively the stream field and its vertical shear, and Θ and σ, which represent potential temperature and its lapse rate. A diagnostic equation is employed to obtain the divergent part of the motion field. We employ the notation of Lorenz (1960).

The model levels are numbered from 0 to 4 with 0 representing the top of the atmosphere ($p = 0$) and 4 representing the ground ($p - p_s = 1000$ mb). Variables are subscripted according to which layer they refer. With this notation, the winds at the upper and lower layers are, respectively,

$$V_1 = \hat{k} \times \nabla(\psi + \tau) + \nabla\chi \tag{3.1}$$

$$V_2 = \hat{k} \times \nabla(\psi - \tau) - \nabla\chi \tag{3.2}$$

The corresponding potential temperature fields are

$$\theta_1 = \theta + \sigma \tag{3.3}$$

$$\theta_3 = \theta - \sigma \tag{3.4}$$

Thus, ψ and Θ represent the stream field and temperature, respectively, at the middle level (500 mb); τ and σ represent their vertical shear. In terms of these variables, the equations for ψ, τ, Θ, and σ are:

$$\frac{\partial}{\partial t}(\nabla^2\psi) = -J(\psi, \nabla^2\psi + f) - J(\tau, \nabla^2\tau) + K_2\nabla^2(\psi - \tau) + \frac{1}{2}\nabla\cdot(f\nabla\chi_0) \tag{3.5}$$

$$\frac{\partial}{\partial t}(\nabla^2\tau) = -J(\tau, \nabla^2\tau + f) + J(\psi, \nabla^2\tau) - K_4\nabla^2\tau + K_2\nabla^2\psi + \nabla\cdot(f\nabla\chi) - \frac{1}{2}\nabla\cdot(f\nabla\chi_0) \quad (3.6)$$

$$\frac{\partial\theta}{\partial t} = -J(\psi, \theta) - J(\tau, \sigma) + h_2(\theta^* - \theta + \sigma) + \nabla\cdot(\sigma\nabla\chi) \quad (3.7)$$

$$\frac{\partial\sigma}{\partial t} = -J(\psi, \sigma) - J(\tau, \theta) + h_2(\theta - \theta^*) + h_4\sigma + \nabla\theta\cdot\nabla\chi \quad (3.8)$$

The constants K_2 and K_4 account for frictional dissipation (exclusive of Ekman layer forcing which is included in (3.9)); and the constants h_2 and h_4 for heat transfer. The function θ^* represents the surface temperature and therefore controls the magnitude and phase of diabatic heating. These equations will be solved on a sphere of radius a. Therefore, there are no lateral boundary conditions. The vertical boundary conditions will be specified as:

(a) At the upper boundary, the vertical velocity is zero.

(b) At the lower boundary the vertical velocity is the sum of that caused by Ekman pumping and of flow over opography of prescribed height h_s. This implies that the term χ_0 is specified by:

$$\nabla^2\chi_0 = -\frac{f_0 g}{\Delta p}\left[\frac{D}{2}\nabla^2(\psi - \tau) + J(\psi - \tau, h_s)\right] \quad (3.9)$$

Where D is a parameter representing the depth of the Ekman layer, $(2K/f)^{1/2}$

A diagnostic equation for the velocity potential χ is obtained from the thermal wind relation

$$bc_p\nabla^2\theta = \nabla\cdot(f\nabla\tau) \quad (3.10)$$

Where b = .124

From equations (3.6), (3.7), and (3.10), we can derive an equation for χ.

$$\nabla\cdot(\sigma\nabla\chi) - (b\zeta_\rho)^{-1}\nabla^{-2}\nabla\cdot f\nabla(\nabla^{-2}(\nabla\cdot\dot{\zeta}\nabla\chi)) = (b\zeta_\rho)^{-1}\nabla^{-2}\nabla\cdot f\nabla((\nabla^{-2}(\frac{\partial}{\partial t}\nabla^2\tau) + \frac{\partial\theta}{\partial t}) \quad (3.11)$$

Equations (3.5) through (3.8) are solved prognostically; (3.11) provides the equations for χ.

3.2 Method of Solution

Equations (3.5) through (3.8) and (3.11) are solved by the spectral method. The prognostic variables are expanded in a series of spherical harmonics. When the series expansions are substituted into the original equations, we convert the partial differential equations into a set of ordinary, coupled nonlinear differential equations, one equation for each coefficient in the series expansion. In practice, the series must be truncated at some point. The method is well-described elsewhere (Platzman, 1960, Merilees, 1968).

In recent years, the transform method has been used to compute nonlinear interactions because of its computational efficiency. The current model uses the interaction coefficient method (Merilees, 1968). This is done for a number of reasons:

(a) In systems with few modes (low-order systems) the computational panalty is not excessive.

(b) The interaction coefficients are essential to analytical work.

(c) The interaction coefficients can be used to filter out certain types of interactions, for instance, wave-wave interactions. Thus, it is possible to linearize the model without reprogramming.

The system of ordinary differential equations which results from the above procedure must be integrated numerically. In the current version of the program, a fourth-order Runge-Kutta-Gill procedure taken from the IBM Scientific Subroutine Package is used.

The model has been programmed in such a way that any combination of modes may be specified. The model user is free to select triangular truncation, trapezoidal truncation, or simply a collection of modes.

3.3 Model Verification

A number of preliminary runs have been made with the spectral model described in the preceding sections. These runs are by no means exhaustive, as their purpose is to serve as a demonstration of the feasibility of the model. The runs all use the same truncation, time step, and initial conditions; but the forcing is different in each run. We now will describe these common elements. In addition, a number of ographic resonance experiments have been performed. These are described in section 4.

3.3.1 Truncation

The modes selected are given in Table 3.1. (called the "12 mode set" hereafter). The numbers are, respectively, the zonal index ℓ and the longitudinal index m of the spherical harmonic

$$Y_\ell^m = N_{m,\ell} P_\ell^m(\varphi,\lambda) e^{im\lambda} \qquad (3.12)$$

Where $N_{m,l}$ is the normalization factor (Platzman, 1960)

The modes selected are a "minimum triangular truncation" plus Y_3^2. This mode was included (a) to give some detail to planetary wave 2, and (b) to provide a nonzero result for the operator $(\nabla\cdot f\vec{v})$ yielding Y_2^2. It

It should be noted that the components of the stream field (ψ, τ) are odd for symmetric flow (with respect to the equator, whereas the components of temperature are even under the same conditions. Therefore, equatorially symmetric conditions require both even and odd modes to be present.

Table 3-1

Modes Used in all Runs

Zonals	Sectorials	Tesserals
0, 0	1, 1	2, 1
1, 0	2, 2	3, 2
2, 0	2, -2	3, -2
3, 0	1, -1	2, -1

3.3.2 Initial Conditions

The zonal components of the streamfunction ψ and its shear τ were chosen so as to yield a reasonable value of the zonal wind at the upper and lower levels. The model then calculates an initial temperature field Θ from the thermal wind equation (3.10). The static stability field (σ) was initially chosen to be a constant 30K, representing a vertical stratification of 30K/500mb in the middle troposphere. Note that the stability is not constant, as the model employs the prognostic equation (3.8) to calculate stability.

3.3.3 Time Step and Run Duration

The time step was chosen by experimentation as a compromise between accuracy (judged by energy conservation properties) and computational load; it was fixed at 1.0 hours. It should be mentioned that the Runge-Kutta algorithm will eventually be replaced by a more suitable method. It is used

because it is self-starting, stable and accurate, but it is time consuming and requires a short time step. Run duration for all verification runs was 20 days. The constants K_2, K_4, h_2, and h_4 were chosen to give a relaxation time for the model of about 5 days. The run duration is thus a factor of 4 larger than this relaxation time and permitted many runs to be made with a reasonable expenditure of computer resources.

3.3.4 Results

A series of runs were made using the initial conditions described in 3.3.2. These runs differ in the forcing used in each case, described below:

Case 1. Unforced (Benchmark run). No friction, no heating, no orography.

Case 2. Orography only. The orographic heights are from Tung and Lindzen (1979)

Case 3. Heating and Friction only.

Case 4. Heating response runs.

Case 5. Heating plus orography (Phase Plane runs).

Based on the output of the unforced run, it was decided to analyze the output as a time mean plus a transient component. This follows standard practice in general circulation and permits one to examine the effects of forcing on the stationary components. Presumably with the low wave numbers employed there is little if any baroclinic activity so that the model is essentially barotropic in the behavior of the low wave numbers. In the absence of forcing we should observe, basically, free Rossby-Haurwitz waves, with phase speed $-2\Omega M/L(L+1)$ for the coefficient of ψ_L^M. In the lowest-order

modes ψ_1^{+1}, ψ_2^{+1}, ψ_2^{+2} this is exactly what we see, with small amplitude and phase speed modulations. These waves will have almost no stationary component. On the other hand, we expect orography or diabatic heating to set up some kind of stationary pattern. This is in fact observed in the runs.

In addition, phase-plane diagrams are obtained for some 2-dimensional subspaces of the 12-dimensional phase space representing this model. The results of the runs are described below.

(1) Case 1. Unforced Case

In this case we can observe the appearance of the abovementioned Rossby-Haurwitz waves after a few days, following the adjustment period in the model. The run verifies conservation of energy and enstrophy to better than .1% in the 20-day period. No stationary components develop. Amplitude and phase speed plots for the nonzonal modes versus time would be a straight horizontal line and are not reproduced.

(2) Case 2. Orography Only

Orography is introduced through the term in psi and tau equations (3.5) and (3.6), of the form

$$\frac{1}{2}\nabla\cdot(f\nabla\chi_o) \qquad (3.13)$$

where χ_o is obtained from equation (3.9). In these runs, the effect of the Ekman layer is not included, i.e. D = 0 in (3.9). Orographic forcing then reduces to

$$\pm\frac{c}{2}\nabla\cdot(f\nabla J(h_s, \psi-\tau)) \qquad (3.14)$$

where h_s is the dimensional height of orography and C is a constant. The value of this constant was -5.0×10^{-5} in a runs. The order

of magnitude of the coefficients of h_s is 400 m. There is a nonzero coefficient for each mode within the truncation limits.

The effects of orographic forcing on the modes ψ_1^1 and ψ_2^1 are the most pronounced (Figures A.2.a and b). A stationary part appears. The magnitude of the stationary part is about 20% of the maximum value of ψ_1^1 and 5% of the value of ψ_2^2. These coefficients now exhibit both amplitude and phase speed modulations, with the maximum of phase speed often coinciding with the minimum of phase speed.

(3) Case 3. Heating and Friction Only

Diabatic heating is modeled with a term proportional to the temperature difference relative to a fixed "ground temperature" Θ^*, in equations (3.7) and (3.8). In the run described here, the function Θ^* was chosen to be identical to Θ ($t = 0$). Thus, the initial contribution of the heating term is zero. As the temperature Θ and σ changes, the temperature differential increases (or decreases) and tends to restore Θ to its initial value. The constants h_2 and h_4 were chosen to be 10^{-6} sec^{-1}.

Friction is introduced into the ψ and τ equations (A.5) and (A.6) by linear terms. The proportionality coefficients used are $K_2 = K_4 = 10^{-6}$ sec^{-1}.

The effect of heating and friction in ψ_1^1 and ψ_2^2 are shown in Figures 3.3.a and 3.3.b and on Θ_2^2 in Figure 3.3.c. For comparison, the unforced behavior of Θ_2^2 is shown in Figure A.4. Except for the initial transient behavior the effect of heating in ψ_1^1 and ψ_2^2 is small. The effect on the temperature mode Θ_2^2 is to smooth out the fluctuations in the amplitude and to introduce nonlinearities in the phase curve. These effects are

reasonable, inasmuch as the thermal forcing is very small and not chosen for realism.

(4) Case 4. Heating Response Runs

In this case, the heating was introduced only through the mode Θ_2^{2*}, i.e. all other modes of Θ^* were set to zero. Twelve separate runs (three sets of four runs each) were performed for this case. In each run the amplitude and phase of Θ_2^{2*} remains constant throughout the run. However, the amplitude and phase of the forcing Θ_2^{2*} changes from run to run. Each set of runs holds θ_2^{2*} at constant phase and varies amplitude. For the next set, the phase is changed from the previous set's value and the amplitude varied. The stationary component of Θ_2^2, $\bar{\Theta}_2^2$, is calculated for each case. The results are summarized in Table A-2. As one would expect from linear forcing, the stationary component $\bar{\Theta}_2^2$ approaches Θ_2^{2*}. The larger the amplitude of forcing, the larger $\left|\bar{\Theta}_2^2\right|$. The phase adjustment of $\bar{\Theta}_2^2$ after 20 days depends on the amplitude of forcing; for large amplitudes of the forcing, the phase of the stationary component almost coincides with that of the forcing.

Table A-2

Response of Stationary Component to Forcing
(After 20 Days)

$\lvert\theta^*\rvert_2^2$	Arg. θ_2^{2*}	$\lvert\bar{\theta}_2^2\rvert$	Arg. $\bar{\theta}_2^2$
2	-45°	2.09	-35.4°
7	-45°	3.88	-51.5°
14	-45°	6.40	-49.8°
21	-45°	8.91	-49.0°
2	45°	1.41	-30.5°
7	45°	2.59	11.5°
14	45°	4.92	26.9°
21	45°	7.38	32.6°
2	135°	0.72	-72.1°
7	135°	1.20	147.5°
14	135°	3.69	137.2°
21	135°	6.21	135.7°

(5) Case 5. Heating and Orography

In this run, the effects of heating and orography were combined. The results are presented in the form of phase subspace plots in terms of the amplitudes of selected coefficients. In Figure 3.5.a we see the amplitudes of ψ_2^2 and ψ_3^2 plotted with time as a parameter. The model is obviously approaching equilibrium, possibly a tight limit cycle as can be seen from the spiral behavior of the phase plane plot.

Figure 3.5.b shows similar behavior for (ψ_2^2, ψ_1^1) subspace.

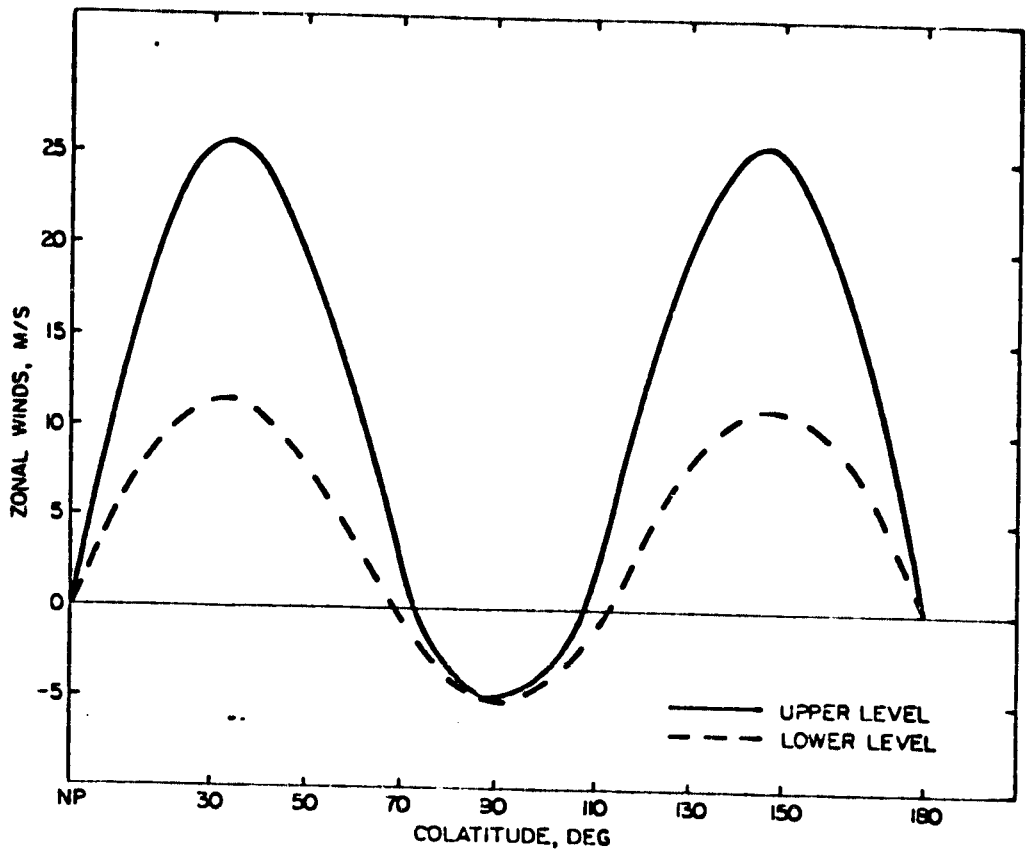

Figure 3.1.a The initial zonal wind field at the upper and lower levels as a function of latitude.

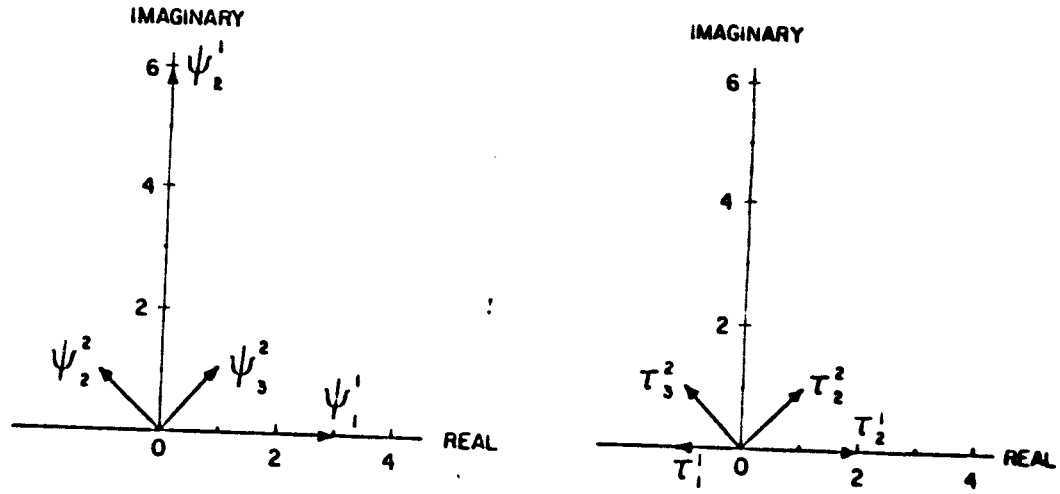

Figure 3.1.b Complex plane representation of the initial eddy components of ψ and τ in units of 10^7 M^2S^{-1}.

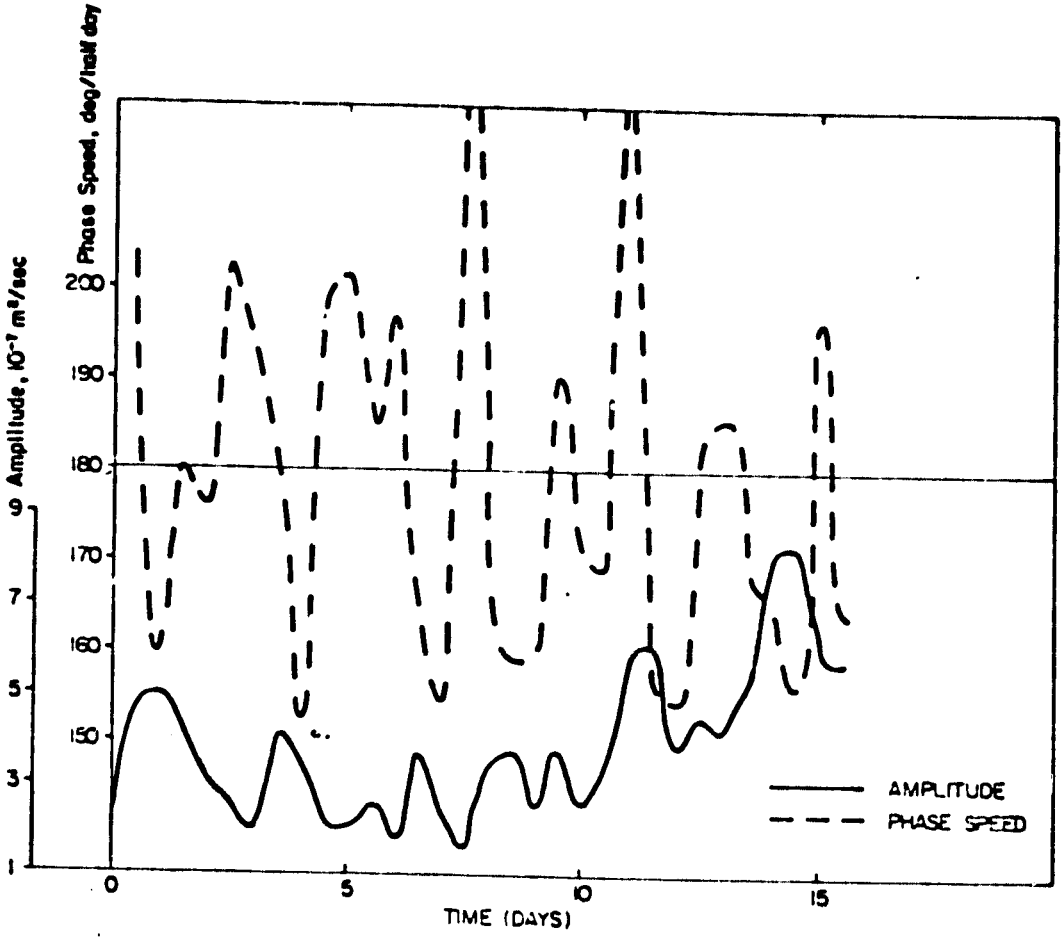

Figure 3.2.a The response of the nonstationary part of ψ_1^1 amplitude and phase speed to orographic forcing only. The stationary part is 1.02×10^7 M^2S^{-1} at a phase of 309^o. The barotropic phase speed is 180^o/halfday.

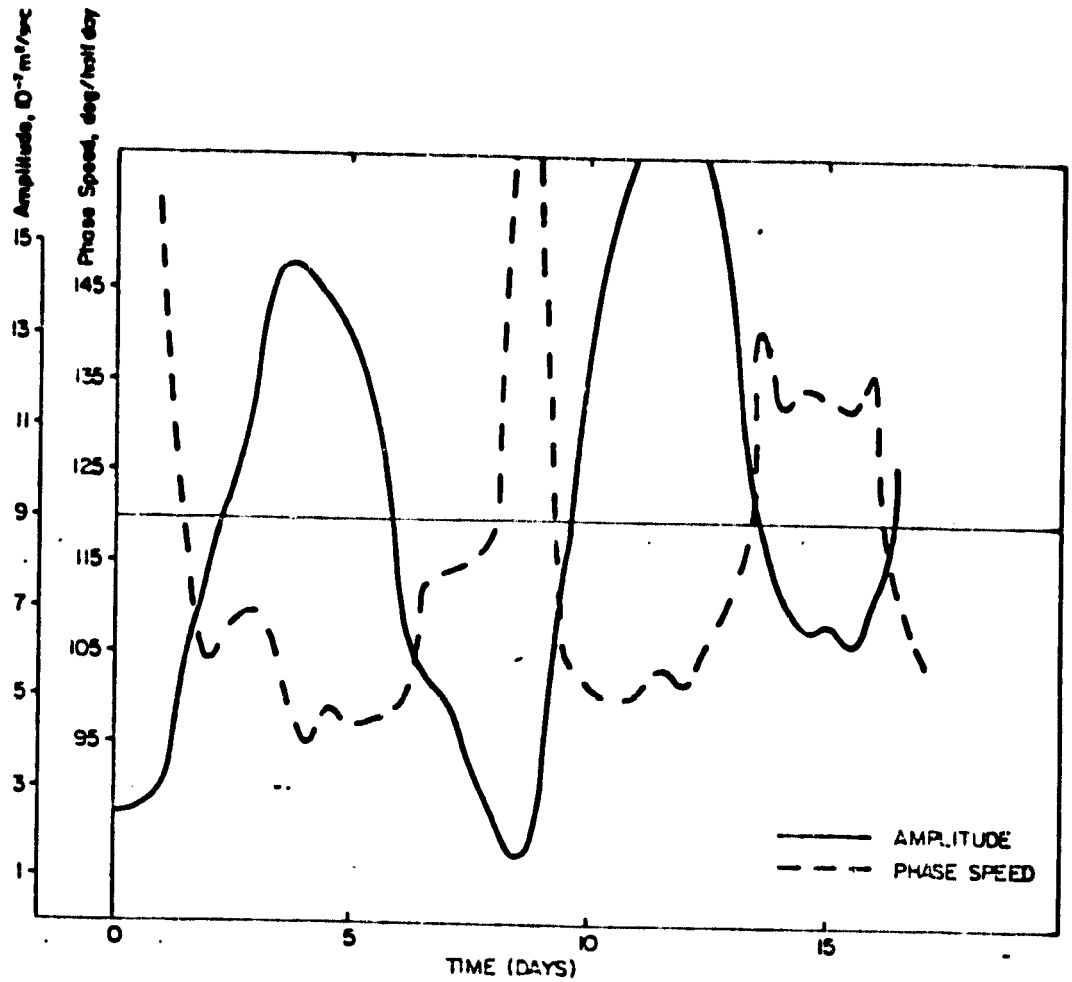

Figure 3.2.b The response of the nonstationary part of ψ_2^2 amplitude and phase speed to orographic forcing. The stationary component is 1.12×10^7 M^2S^{-1} at a phase of 324^o. The barotropic phase speed is 120^o/halfday.

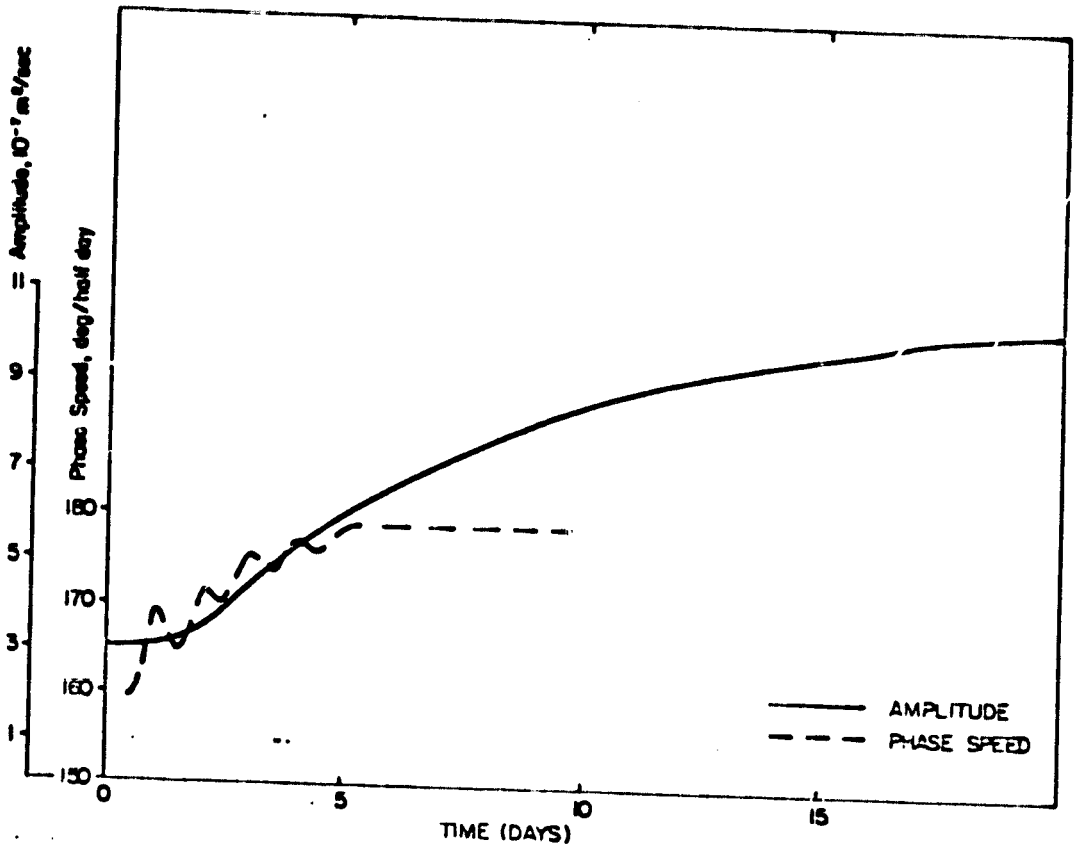

Figure 3.3.a The response of the nonstationary part of ψ_1^1 amplitude and phase speed to heating. The stationary part is negligible.

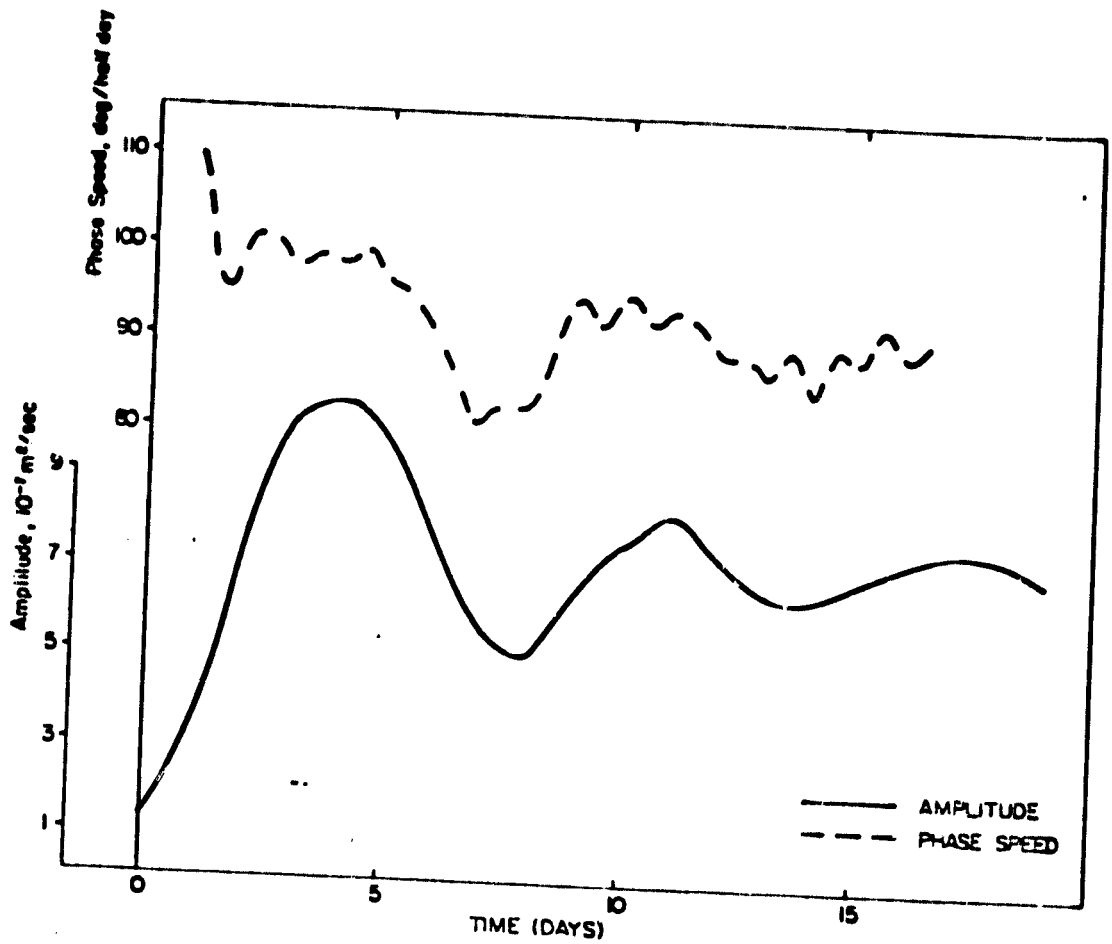

Figure 3.3.b The response of the nonstationary part of ψ_2^2 amplitude and phase speed to heating. The stationary part is negligible.

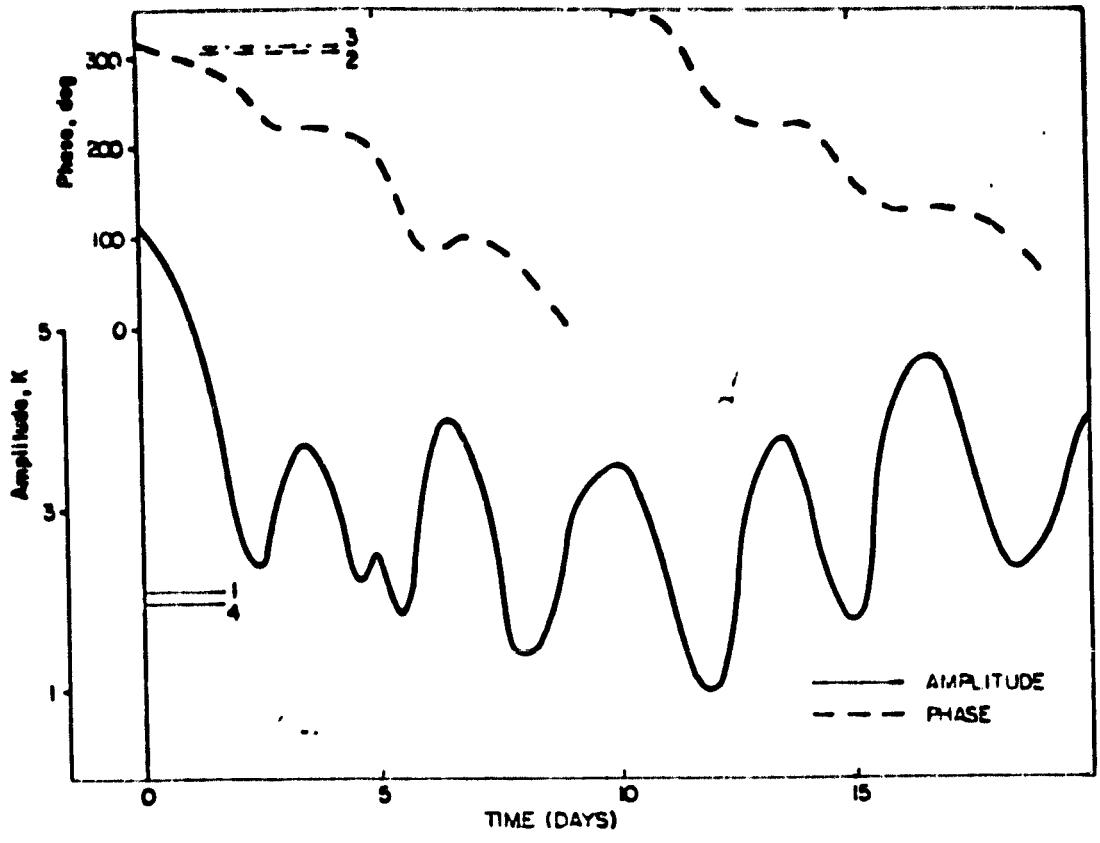

Figure 3.3.c The response of the amplitude and phase of the nonstationary part of θ_2^2 to heating. Solid lines labeled 1 and 4 are the amplitudes of the forcing and of the stationary component, respectively. The broken lines labeled 2 and 3 are the phases of the forcing and of the stationary component, respectively.

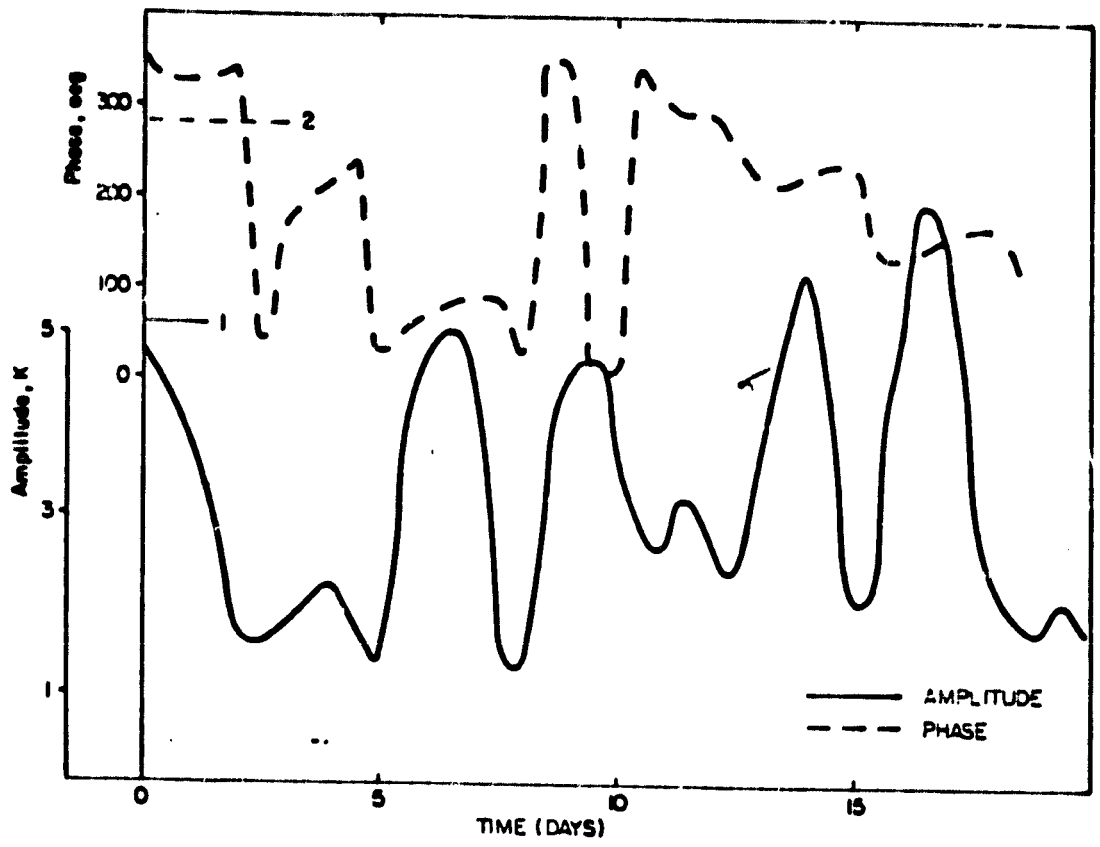

Figure 3.4 As in Figure 3.3.c but for the case of no forcing. Solid line labeled 1 is the amplitude of the stationary component; dashed line labeled 2 is its phase.

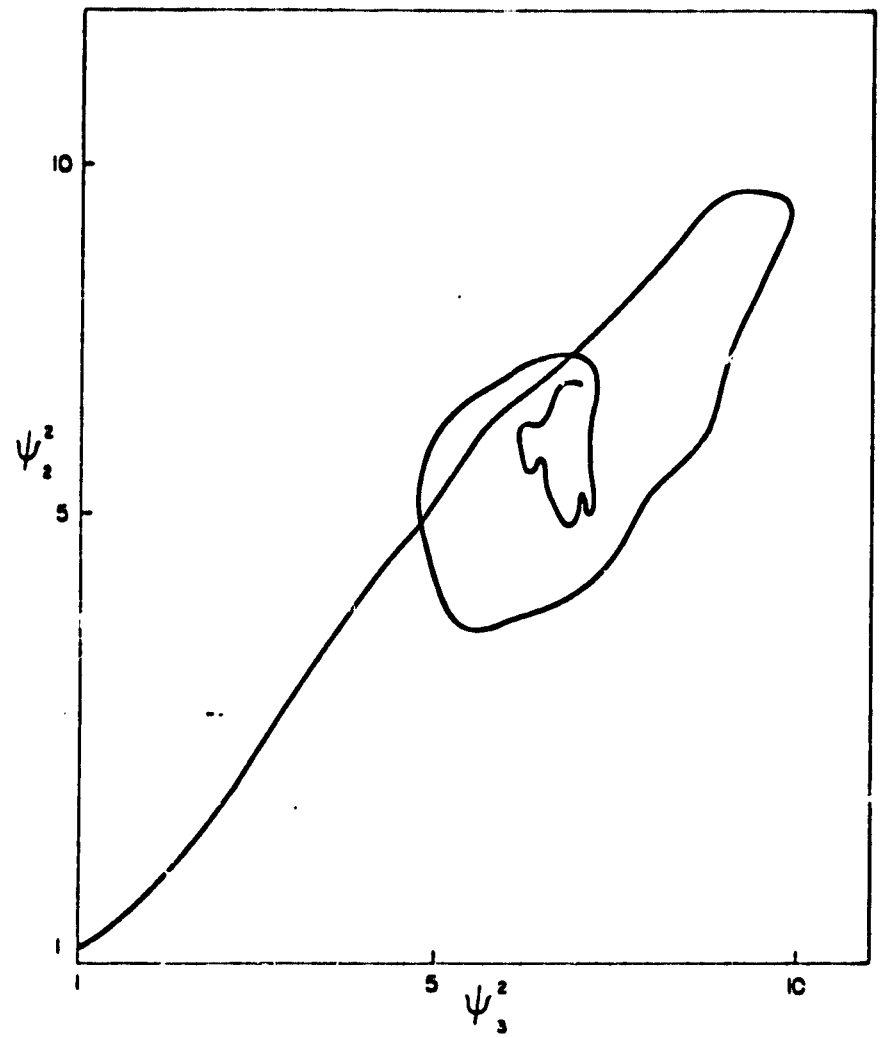

Figure 3.5.a Phase plane plot of ψ_3^2 and ψ_2^2. Trajectory in the phase subspace shows approach to equilibrium as time increases.

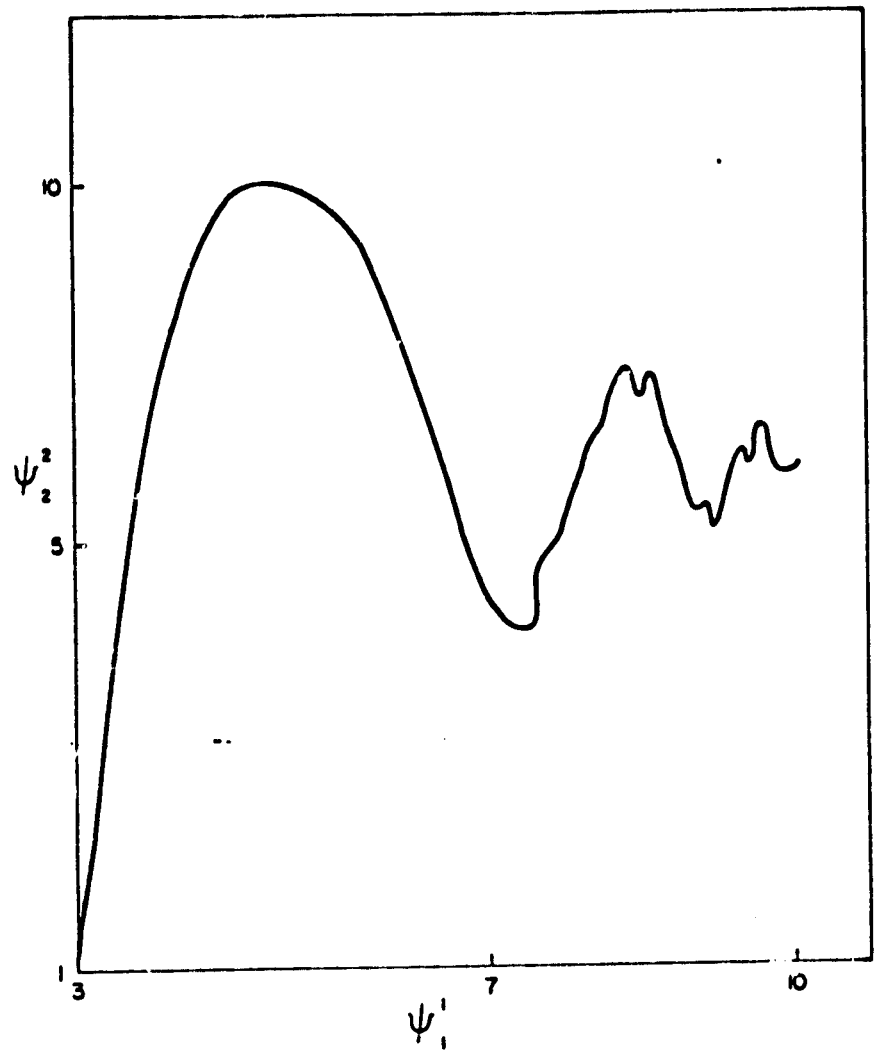

Figure 3.5.b Phase plane plot of ψ_1^1 and ψ_2^2. Trajectory shows approach to equilibrium as time increases.

4.0 Resonance Experiments

4.1 Motivation

The existence of multiple equilibria in approximate, but non-linear, barotropic systems (Charney and DeVore, 1979; Hart, 1979) is intimately connected with the existence of a linear resonance condition. In fact, the equilibrium associated with a large wave amplitude "blocking" flow is located close to the linear resonance point. Consequently, as we will show below, the study of the resonance condition is important for understanding multiple equilibria.

However, it is instructive to begin with a much simpler system which exhibits this type of equilibria, even though it will be in an ad hoc way. Consider the barotropic vorticity equation with forcing on a beta-plane:

$$\frac{\partial}{\partial t}\nabla^2\psi = -J(\psi, \nabla^2\psi + f) + F \qquad (1)$$

where Ψ is the stream function and F some as yet arbitrary forcing function. We can find a solution to (1) on a β-plane of the form (zonal flow plus a single wave):

$$\psi = -\bar{U}y + \psi'(x,t) \qquad (2)$$

Which reduces (1) to the linear partial differential equation

$$\frac{\partial}{\partial t}\left(\frac{\partial^2\psi'}{\partial x^2}\right) = -\beta\frac{\partial\psi'}{\partial x} + \bar{U}\frac{\partial^3\psi'}{\partial x^3} + F \qquad (3)$$

The plane-wave solution for the homogeneous equation is

$$\psi'(x,t) = \psi_0' e^{i(kx-\omega t)} = \psi_0' e^{ik(x-ct)} \quad (4)$$

with c given by the usual Rossby wave dispersion formula.

$$c = \bar{U} - \beta/k^2 \quad (5)$$

We can find a particular solution by setting $\partial\Psi/\partial t = 0$ in eq. (3). Then, if $\bar{\psi}_0'$ is the particular solution

$$\bar{\psi}_0' = \frac{F}{k^2 - \beta/\bar{U}} \quad (6)$$

and we now note that, as $k \to \beta/\bar{U}$ equation (6) becomes resonant. This is a well-known condition discussed, for example, in Dickinson (1980) with respect to orography. In general the solution to (3) is the sum of the stationary wave plus a traveling wave with phase speed given by (5). Resonance corresponds to the case where the traveling wave slows down, and interferes constructively with the stationary wave (as suggested by Tung and Lindzen, 1979).

The unbounded response predicted by eq. (6) is not expected to occur in the atmosphere. (Note that the inclusion of friction would prevent the unbounded resonance in eq. (6)). Instead, nature will act in such a way as to prevent the resonance. This can be accomplished by non-linear interactions between the different waves which will be

present which will modify the zonal flow away from resonance. Thus there will be a nonlinear wave-zonal flow feedback mechanism inhibiting resonance. Therefore, we introduce an ad hoc linear feedback mechanism between the single wave of eq. (2) and the zonal flow, i.e.

$$\bar{U} = A\bar{\psi}_0' + B \tag{7}$$

then we can have multiple equilibrium solutions to the system (6) and (7) as shown in Fig. 4.1. Here, the solution of the system (6), (7) is given by the intersection of the straight line (7) with the resonance curve (6) for a particular value of k.

Fig. (4.1) has been drawn with B>0 and A>0 such that there are three possible solutions (1,2,3). These correspond to the multiple equilibria found by the previously cited authors, who, however, have introduced more than one wave into the problem and physical mechanisms representing the ad hoc constants, A and B. The existence of the equilibria depends on the values chosen for A and B.

Thus, the existence of multiple equilibrium solutions to forced barotropic (and presumably also to baroclinic) models is closely connected with the existence of a resonance condition in a forced wave, and to a feedback mechanism of the wave with the zonal wind. It is of interest, therefore, to use the model described in the previous sections and to attempt to induce a resonant state in this model, both for the baroclinic and barotropic conditions. This work is the subject of the following sections.

4.2 Barotropic Resonance Experiments

We consider the 12-mode set described in section 3. In this set of modes, we restrict ourselves to the barotropic case ($\tau=\sigma=\theta=0$) and further simplify the set by assuming hemispheric symmetry. This is accomplished by setting all even modes of ψ to zero. The remaining modes are given below.

Mode number	1	3	5	7	10	12
M	2	1	0	0	-1	-2
L	3	2	3	1	2	3

We retain the mode (2,2) for the orography. If $c_i = \frac{L_i(L_i+1)}{2}$ then the following eigenvalues are equal:

$$c_1 = c_5 = c_{12} \tag{8a}$$

$$c_3 = c_{10} \tag{8b}$$

The spectral form of the barotropic vorticity equation (1) is the following set of ordinary differential equations.

$$\dot{\psi}_1 = I_{171}\psi_1\psi_7 + H_{251}h_2\psi_5 + \Omega_1\psi_1 \tag{9}$$

$$\dot{\psi}_3 = I_{353}\psi_3\psi_5 + I_{373}\psi_3\psi_7 + H_{2,10,5}\psi_3 h_2 + \Omega_3\psi_3 \tag{10}$$

$$\dot{\psi}_5 = H_{2,12,5}h_2\psi_1 + H_{2L,L,5}h_2\psi_1 \tag{11}$$

$$\dot{\psi}_7 = H_{2,12,7}\, h_2\, \psi_L + H_{11,L,7}\, h_2\, \psi_1 \qquad (12)$$

Where Ψ_i is a mode in the stream field (see table) and

$$I_{ijk} = \frac{c_i - c_j}{c_k} J_{ijk} \qquad (13)$$

$$c_i = \frac{L_i (L_i + 1)}{q^2} \quad \text{is the eigenvalue of ith mode} \qquad (14)$$

J_{ijk} is the Jacobian interaction coefficient, or "coupling integral."

$$\Omega_i = \frac{-2\Omega M_i}{L_i (L_i + 1)} \qquad (15)$$

is the Rossby-Haurwitz phase speed.

H_{ijk} is the coefficient of orographic interaction. The notation $\bar{\Psi n}$ means $(-)^{Mn}\, \Psi n^*$. In general, (8)-(11) would contain other terms (see e.g. Kallen (1979)) but these drop out because of the Eigenvalue relations (8). Thus, in this case we have no wave-wave →zonal flow interactions. Of course, in a two-wave set we cannot have wave-wave-wave interactions.

We can obtain a resonance condition by linearizing (9)-(12), assuming the zonal flow is constant:

$$\psi_5 = \bar{\psi}_5 \tag{16}$$

$$\psi_7 = \bar{\psi}_7 \tag{17}$$

We can then solve for a steady state, analogous to eq. (6), by taking $\frac{d\Psi_1}{dt} = 0$ in eq. (9). The result is

$$\bar{\psi}_1 = \frac{-H_1 \bar{\psi}_5}{I_{171} \psi_7 + \Sigma_1} \tag{18}$$

Where $H_1 = H_{251} h_2$.

Equation (18) is the analog in a spherical spectral system of eq. (6). Since $\bar{\Psi}_1$ is the earth's angular momentum, it is very unlikely that we will ever encounter this particular resonance in practice. However, a different set of modes would exhibit similar behavior (Kallen, 1979). The resonant value of $\bar{\Psi}_7$ (zonal flow) is given by eq. (18):

$$\bar{\psi}_{7R} = -\frac{\Sigma_1}{I_{171}} \approx -34.2 \frac{M^2}{s} \times 10^7 \tag{19}$$

using a reasonable value for the orographic mode h_2 (Tung and Lindzen, 1979) we can plot eq. (18), which is shown as the broken line in Fig. (4.1).

It is interesting to observe the behavior of the system when the nonlinear equations are used. Accordingly, a series of experiments were performed with the model to determine the shape of the resonance curve for the nonlinear case of eqs. (9)-(12). Since the numerical model cannot solve for the steady state, the steady state must be found by averaging. Fig. (4.2) shows the results of these experiments. The solid curve represents $\overline{\Psi}_1$, found by averaging over a period of 30 days. The ordinate is the initial value of Ψ_7, which for practical purposes is the average value of Ψ_7 since it does not change very much over the run. It can be seen that the response curve is broader than that predicted by (18) but that resonance occurs in about the right place. As predicted by (18), the traveling portion of the disturbance was found to slow down as resonance was approached.

4.3 Baroclinic Resonance Experiments

We consider the effect of baroclinicity in the resonance conditions. We will use the 12-mode set, restricted to odd modes in Ψ and τ and even modes in Θ and χ. The stability σ is taken to be constant. In order to simplify the analytical work we will consider only the Ψ and τ equations. This will bypass analysis of the "omega equation" for the variable χ; which is not rigorously justified. However, the principal results will be obtained anyway.

Using the same mode designation as before, we have the following equations:

$$\dot{\Psi}_1 = I_{171}\Psi_1\Psi_7 + I_{171}\tau_1\tau_7 + H_{251}(\Psi_5-\tau_5)h_2 + \sigma_1\Psi_1 \tag{20}$$

$$\dot{\tau}_1 = I_{171}\tau_1\tau_7 + I_{171}\tau_7\Psi_1 + I_{151}\tau_1\Psi_5 + I_{511}\tau_5\Psi_1 + R_1\tau_1 + c_{21}\chi_2 + \tag{21}$$

$$\dot{\Psi}_3 = H_{2,10,3}h_2(\Psi_3^*-\tau_3^*) + \sigma_3\Psi_3 \qquad H_{251}(\Psi_5-\tau_5)h_2 \tag{22}$$

$$\dot{\tau}_3 = H_{2,10,3}h_2(\Psi_3^*-\tau_3^*) + \sigma_3\tau_3 \tag{23}$$

$$\dot{\Psi}_7 = \text{see (11)} \tag{24}$$

$$\dot{\tau}_7 = \text{"} \tag{25}$$

$$\dot{\Psi}_5 = \text{see (12)} \tag{26}$$

$$\dot{\tau}_5 = \text{"} \tag{27}$$

The linearized analysis proceeds by taking the zonal flow and its shear to be constant:

$$\Psi_5 = \bar{\Psi}_5 \qquad \tau_5 = \bar{\tau}_5 \tag{28}$$

$$\Psi_7 = \bar{\Psi}_7 \qquad \tau_7 = \bar{\tau}_7 \tag{29}$$

The equations for the highest order wave mode (mode 1) are

$$\dot{\psi}_1 = (I_{171}\bar{\psi}_7 + \Omega_1)\psi_1 + I_{171}\bar{\tau}_7\psi_1 + H_{251}(\bar{\psi}_5 - \bar{\tau}_5) \quad (30)$$

$$\dot{\tau}_1 = (I_{171}\bar{\psi}_7 + \Omega_1)\tau_1 + I_{171}\bar{\tau}_7\psi_1 + \zeta_1\chi_2 - H_{251}(\bar{\psi}_5 - \bar{\tau}_5) \quad (31)$$

We will now assume that the term χ_2 represents thermal forcing, denoted by χ^*; while the orograhic term will be denoted by H^*. Also letting

$$(I_{171}\bar{\psi}_7 + \Omega_1) = \hat{\psi}_2 \quad (32a)$$

$$(I_{171}\bar{\tau}_7 + \Omega_1) = \hat{\tau}_2 \quad (32b)$$

We have the following set of equations for the wave:

$$\dot{\psi}_1 = \hat{\psi}_2\psi_1 + \hat{\tau}_2\tau_1 + H^* \quad (33)$$

$$\dot{\tau}_1 = \hat{\tau}_2\psi_1 + \hat{\psi}_2\tau_1 + \chi^* - H^* \quad (34)$$

The steady state solution (cf. (18) and (6)) is given by:

$$\bar{\psi}_1 = \frac{-H^*(\hat{\psi}_2 + \hat{\tau}_2) - \hat{\tau}_2 \chi^*}{\hat{\psi}_2^2 - \hat{\tau}_2^2} \tag{35}$$

$$\bar{\tau}_1 = \frac{-H^*(\hat{\psi}_2 + \hat{\tau}_2) + \hat{\psi}_2 \chi^*}{\hat{\psi}_2^2 - \hat{\tau}_2^2} \tag{36}$$

The resonance condition is then

$$\hat{\psi}_2 - \hat{\tau}_2 = 0 \tag{37}$$

Whereas in the barotropic case $\psi_2 = 0$ is the resonance condition (from (18) and 32a). Since for a westerly positive stream flow τ_2 is negative, a higher value of ψ_2 is needed to obtain the resonance than in the barotropic case. That is, the zonal wind required to obtain resonance in the baroclinic case is higher (for negative τ_2 corresponding to winds increasing with height).

A series of numerical experiments with the numerical model were performed to examine the nonlinear resonance case. The experiments consisted of selecting values for mean wind ψ_7 and shear τ_7 and finding the steady state $\bar{\psi}_1$ by averaging over a 30-day period. The results are shown in fig. 5.3, which displays the response of the wave ψ_1 for various values of ψ_7 and τ_7. The results are in agreement with equation (37); we note that as shear increases, a correspondingly high value of ψ_7 is needed to cause a resonant response.

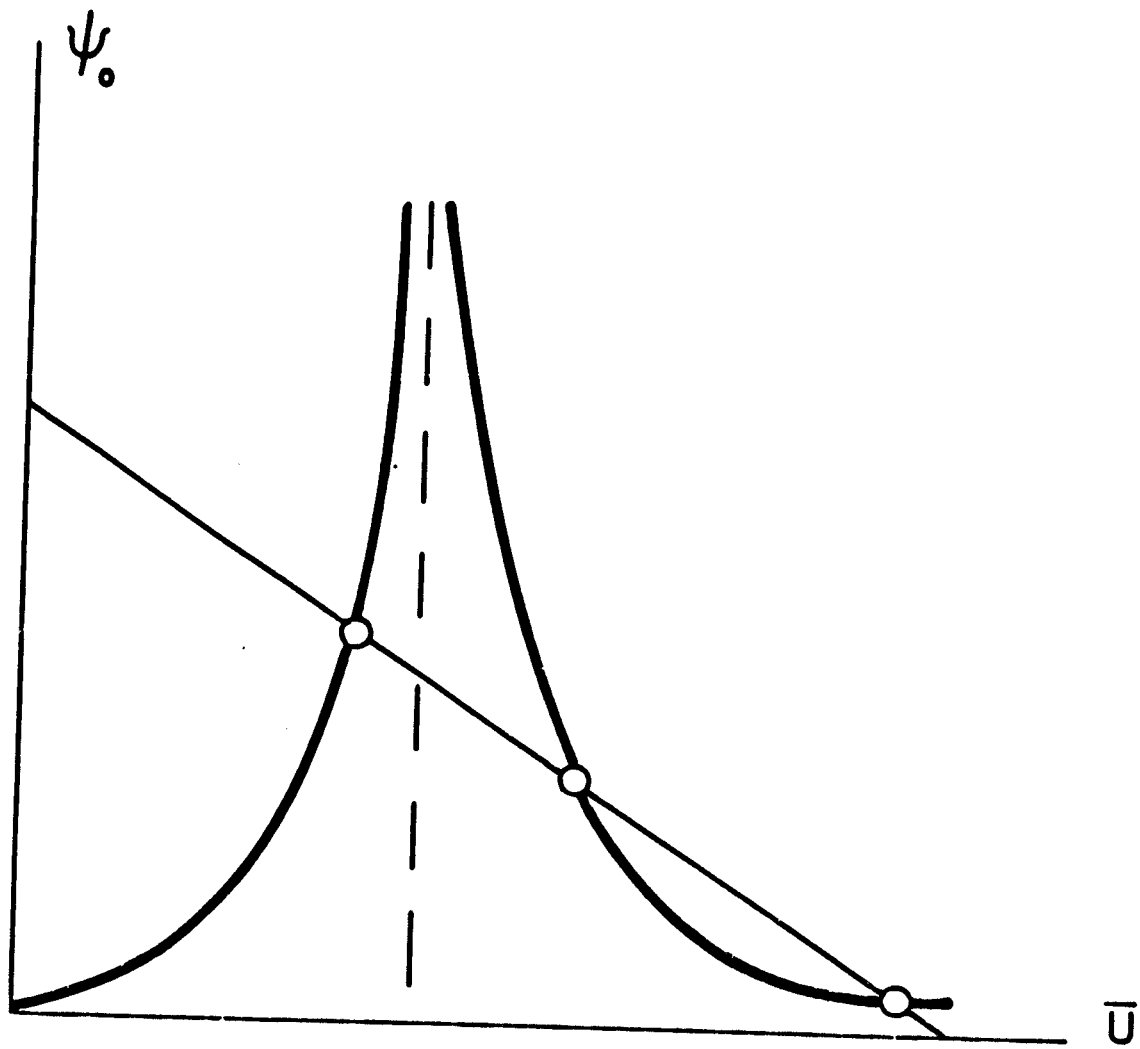

fig 4.1 Schematic illustrating multiple equilibria obtained by solving equations 5.6 and 5.7 simultaneously.

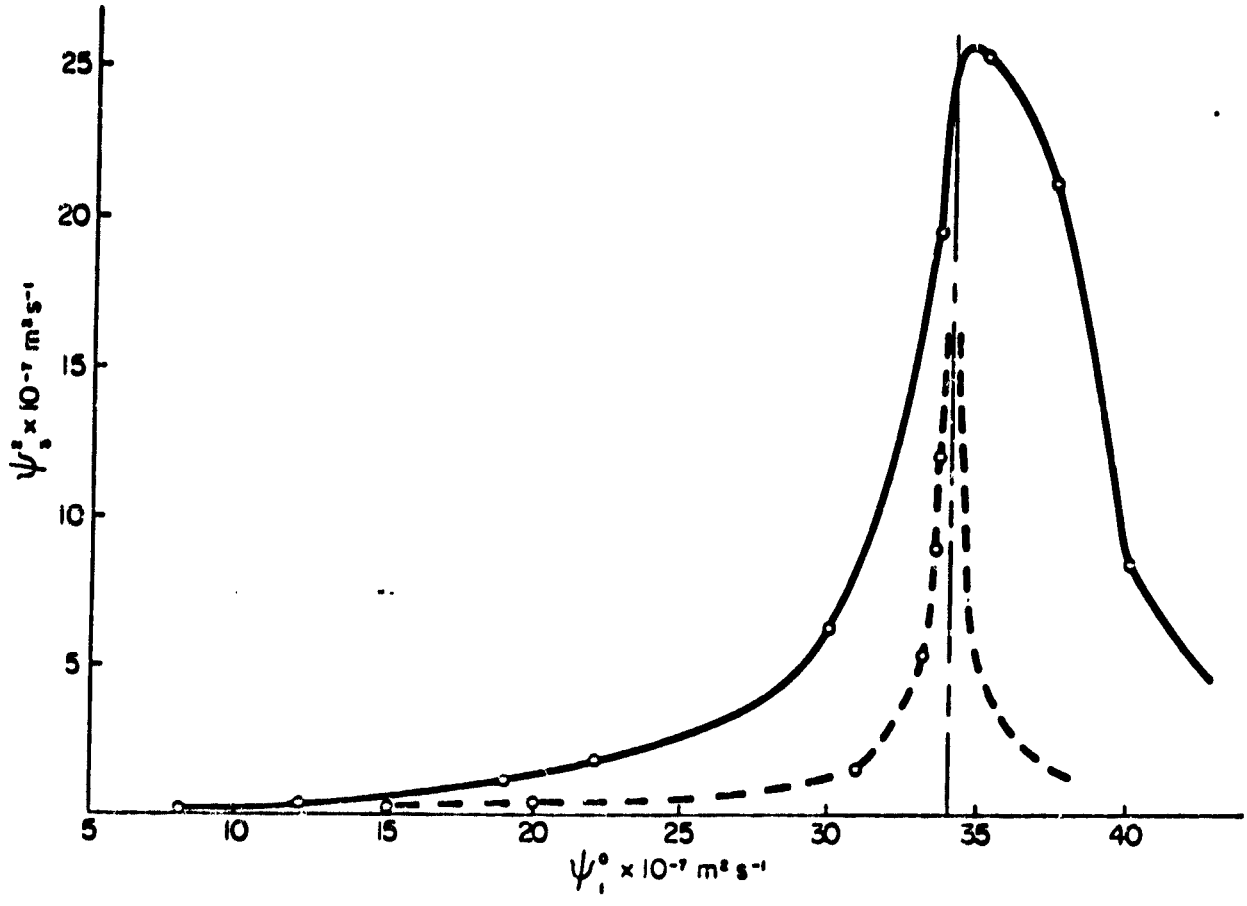

fig 4.2 Amplitude of the stationary component of Ψ_3^2 as a function of the zonal flow Ψ_1^0 for the barotropic case. Dashed line is linear case, solid line is nonlinear result.

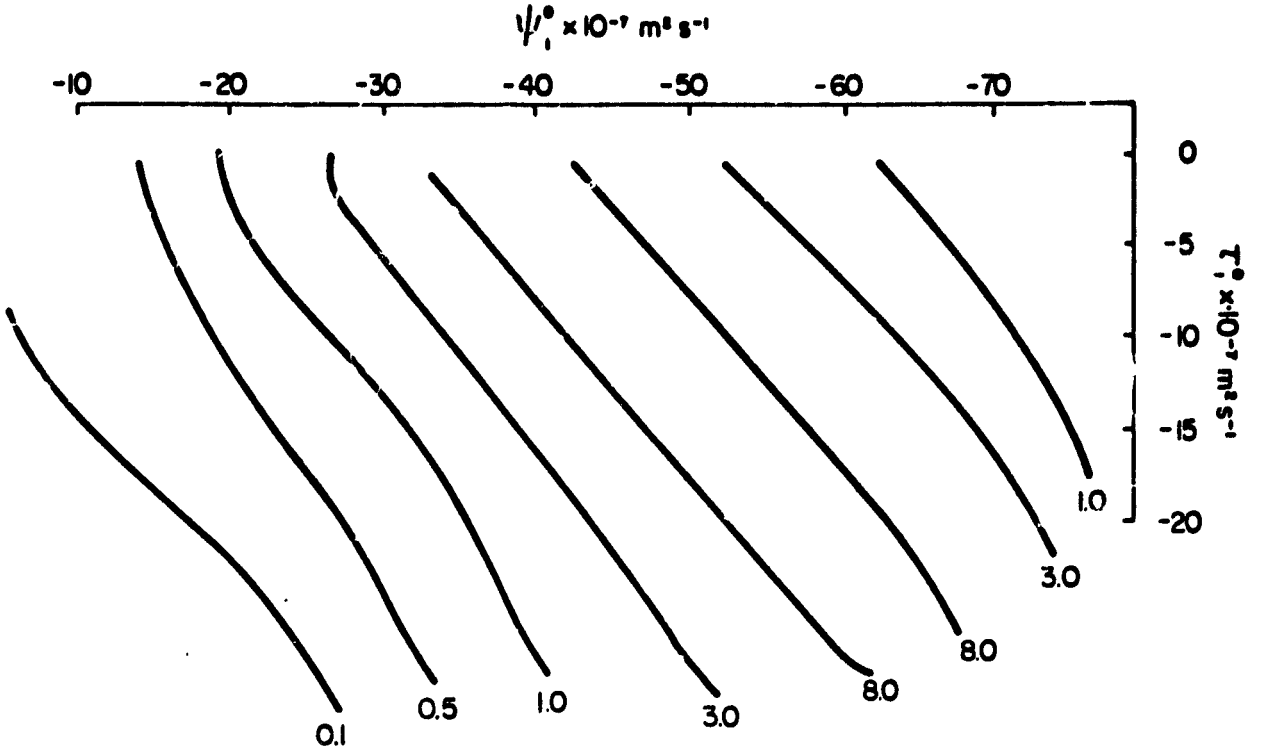

fig 4.3 Amplitude of the stationary component of $\Psi_1(\Psi_3^2)$ as a function of the zonal flow Ψ_1^0 and its shear, τ_1^0.

C - 3

5.0 Conclusions

The model described in section 3 has been verified by demonstrating that the model yields reasonable results. In the absence of any forcing, and with reasonable initial conditions, we find free Rossby waves propagating with the correct phase speed. When orographic forcing is added, a stationary component develops. The nonstationary component has an instantaneous amplitude and phase speed which changes with time. This is to be expected from the interactions with orography. When diabatic heating is added, the response of the stationary temperature field is roughly linear.

The phase plane plots show an approach to equilibrium as one would expect from constant forcing without feedback. Further judgements, based on the limited amount of runs performed thus far and on the lack of verisimilitude of the thermal forcing, would be unwarranted at this time.

The barotropic and baroclinic resonance experiments are intended as preliminary steps in understanding the mechanisms underlying the existence of steady, or quasi-steady, states in the atmosphere. The theory of resonance for the cases covered in the existing literature (zonal flow and two waves), are verified and extended by the model.

The effect of shear on the resonance curves is also investigated. For positive shear (τ) the zonal wind required to obtain resonance is very high.

Further work in this direction will proceed along the lines of investigating more realistic mode structures both in zonal flow and

in the wave structures. Considering first the barotropic case, the addition of more waves raises the possibility of wave-wave-wave interactions, some of which may also produce resonance leading to stationary situations. A guide to this possibility is the numerical results of Egger (1978, 1979) who has simulated blocking situations by wave-wave interactions in a barotropic, forced, channel mode. The extension of this work to spherical coordinates now underway. Further experiments with both barotropic and baroclinic analogs of Egger's experiments is planned. Also, analytical work based on these experiments is being carried out.

The results of this study should have an important bearing on both the atmospheric response to imposed forcing and feedback mechanisms, but also on the nature and existence of multiple equilibria. But these two topics are intimately connected, as we have shown.

Thus we are addressing the fundamental cause of planetary-wave generation and their (nonlinear) interaction with other waves and the zonal flow to form occasional, smaller scale "blocks" in the atmospheric circulation. The role of multiple equilibria in this process involving several scales is of great importance.

6. Multiple Flow Equilibria and Chaotic Behavior

We have undertaken an investigation of the occurrence of multiple stable equilibrium states in simple but heuristically valuable models of large-scale atmospheric flows. Our aim is to expand upon the recent results along these lines of Charney and his colleagues (1,2). They have shown that multiple stable equilibria do occur in highly truncated spectral models of both barotropic and baroclinic flows which are topographically or thermally forced at the lower boundary. By numerical integration of an associated grid-point model for the topographic forcing, having many more degrees of freedom than the spectral model, they have verified the presence of these equilibria. The equilibria can be viewed heuristically as being capable of undergoing transitions among themselves due to small-scale perturbations. From this viewpoint, one of the transitions bears a striking resemblance to the often observed shift of the zonal westerlies to persistent blocking patterns.

Our work centers on several of the difficult mathematical issues involved in analyzing the dynamics of spectral models like those considered by Charney and his colleagues. Ultimately, one would like to characterize the attractor sets of these dissipative, nonlinear dynamical systems. The determination of equilibrium states entails solving relatively large systems of polynomial equations that express the algebraic conditions for an equilibrium. The number of equations and unknowns equals the number of degrees of freedom of the spectral model. The only known systematic solution method for finding all of the isolated solutions of a polynomial system is the so-called homotopy continuation method (3). We have developed a computer implementation of the Li-Yorke homotopy continuation algorithm (4) to provide an appropriate numerical solver for our investigation. Our aim is to use the computer capability to find all of the equilibrium states for Charney-like

models, especially for cases with relatively large numbers of degrees of freedom.

Our solver has been tested on a Charney model having six degrees of freedom. We have thusly rediscovered all the equilibria indicated by Charney and DeVore in (1) for selected model parameters. In (1) it was shown that the problem of solving the particular polynomial systems that arose was reducible to simpler subproblems which enabled the authors to find all of the equilibria in a finite region of the dynamical phase space. We are as yet uncertain if other equilibria exist outside this region and are pursuing the question. The next application of our solver will be to the baroclinic models introduced in (2) where twelve degrees of freedom are involved. In this case it is almost certain that the equilibria already found do not exhaust the totality.

Other efforts under consideration include (a) applying the solver to the global baroclinic model of Rodenhuis, et al. and (b) applying recently discussed techniques (5) for estimating the dimension of the dynamical attractor set to the most meteorologically interesting of the spectral models studied.

REFERENCES

1. J. G. Charney and J. G. DeVore. Multiple Flow Equilibria in the Atmosphere and Blocking, J. Atm. Sci., 36, 1205-1216, 1979.

2. J. G. Charney and D. M. Straus, Form-Drag Instability and Multiple Equilibria in Baroclinic, Orographically Forced Planetary Wave Systems. Preprint.

3. Shui-Nee Chow, John Mallet-Paret, and James A. Yorke, A Homotopy Method for Locating All Zeros of a System of Polynomials. Preprint.

4. Tien-Yien Li and James A. Yorke, A Simple Reliable Numerical Algorithm for Following Homotopy Paths, University of Wisconsin MRC Technical Summary Report #1984, July 1979.

5. Paul Frederickson, James L. Kaplan, and James A. Yorke, The Dimension of the Strange Attractor for a Class of Difference Systems. Preprint.

§ 7. Selected References

Ashe, S., 1979: A nonlinear model of the time-average axially asymmetric flow induced by topography and diabatic heating. J. Atmos. Sci., 36, 109-129

Austin, J. F., 1980: The blocking of middle latitude westerly winds by planetary waves. Quart. J. Roy. Met. Soc., 106, 327-350

Baer, F., 1970: Analytical solutions to low order spectral systems. Arch. Met. Geoph. Biokl. Ser. A, 19, 255-282

------ , 1971: Energetics of low-order spectral systems. Tellus, 23, 218-231

Bell, T. L., 1980: Climate sensitivity from fluctuation dissipation: Some simple model tests. J. Atmos. Sci., 37, 1700-1707

Blackmon, M. L., 1976: A climatological spectral study of the 500 mb geopotential height of the northern hemisphere. J. Atmos. Sci., 33, 1607-1623

---------- R. A. Madden, J. M. Wallace, and D. S. Gutzler, 1979: Geographical variations of the vertical structure of geopotential height fluctuations. J. Atmos. Sci., 36, 2450-2458

Boettger, H., 1979: Spektrale Auswertung des Geopotentials entlang 50 N fuer Winter und Sommer. Meteor. Abhandlung, 3 Institute f. Meteorologie du Freie Universaet, 156 p., Berlin

Charney, J. G. and P. G. Drazin, 1961: Propagation of planetary disturbances from the lower into the upper atmosphere. J. Geoph. Res., 66, 83-109

---------- and A. Eliassen, 1949: A numerical method for predicting the perturbations in the midlatitude wasterlies. Tellus I, 38-54

---------- and J. G. De Vore, 1979: Multiple flow equilibria in the atmosphere and blocking. J. Atmos. Sci., 36, 1205-1216

---------- and D. M. Straus, 1980: Form drag instability and multiple equilibria in baroclinic orographically forced planetary waves. J. Atmos. Sci., 37, 1205-1216

Chervin, R. M., J. E. Kutzbach, D. D. Houghton, and R. G. Gallimore, 1980: Response of the NCAR general circulation model to prescribed changes in ocean surface temperature, Part II: Mid-latitude and subtropical changes. J. Atmos. Sci., 37, 308-322

Dalton, J. A., 1976: The nonlinear, quasi-geostrophic equation. Part II: Predictability, recurrence, and limit properties of thermably forced and unforced flows. J. Atmos. Sci., 33, 1431-1453

Doos, B. 1962: The influence of the exchange of sensible heat with the earth's surface on planetary flow. Tellus 14, 133-147

Gall, R., R. Blakeslee, and R. C. J. Sommerville, 1979: Cyclone scale forcing of ultra long waves. J. Atmos. Sci., 36, 1962-1968

Hart, J. E., 1979: Barotropic quasi-geostrophic flow over anisotropic mountains. J. Atmos. Sci., 36, 1763-1746

Hoskins, B. 1978: Horizontal wave propagation of a sphere. The General Circulation: Theory, Modeling, and Observation. NCAR, Boulder, pp. 144-153

Houghton, D. D., J. E. Kutzbach, M. McClintock, and D. Suchman, 1974: Response of a general circulation model to a sea surface temperature perturbation. J. Atmos. Sci., 31, 857-868

Kalnay-Rivas, E. 1977: A numerical scheme to solve for unstable boundary value problems. Advances Computational Mathametics for Partial Differential Equations. International Assoc. for Math. and Computers in Simulation, R. Vichnevetsky, ed. Brussels

---------- and L. O. Merkien, 1980: A simple mechanism for blocking. MS. submitted for publication, 33 pp.

Kasahara, A., 1976: Normal modes of the ultralong waves in the atmosphere. Mon. Wea. Rev., 104, 609-690

Kutzbach, J. E., R. M. Chervin, D. D. Houghton, 1977: Response of the NCAR GCM to prescribed changes in ocean surface temperature Part I. J. Atmos. Sci., 34, 1200-1213

Lau, N-C., 1979: The observed structure of tropospheric stationary waves and the local balances of vorticity and heat. J. Atmos. Sci., 36, 996-1016

---------- and J. M. Wallace, 1979: On the distributions of horizontal transports by transient eddies in the northern hemisphere wintertime circulation. J. Atmos. Sci., 36, 1844-1861

Leith, C. E., 1975: Climate response and fluctuation dissipation. J. Atmos. Sci., 32, 2022-2026.

Lindzen, R., 1980: NASA-GSFC seminar

Lorenz, E. N., 1962a: Energy and numerical weather prediction. Tellus 22, 364-373

---------- , 1962b: Simplified dynamic equations applied to the rotating-basin experiments. J. Atmos. Sci., 19, 39-51

---------- , 1963a: The mechanics of vacillation. J. Atmos. Sci., 20, 448-464

---------- , 1963b: Deterministic nonperiodic flow. J. Atmos. Sci., 20, 130-141

---------- , 1980: Attractor sets and quasi-equilibrium. J. Atmos. Sci., 37, 1685-1699

Madden, R. A., 1979: Observations of large-scale traveling Rossby waves Rev. Geoph. and Space Phys., 17, 1935-1950

Manabe, S. and T. B. Terpstra, 1974: The effects of mountains on the general circulation of the atmosphere as identified by numerical experiments. J. Atmos. Sci., 31, 3-42

Matsuno, T. 1970: Vertical propagation of planetary waves in the winter northern hemisphere. J. Atmos. Sci., 27, 871-883

Minorsky, N., 1962: Nonlinear Oscillations. Van Nostrand, Princeton, 714pp.

Miyakoda, K., 1980: NASA-GSFC seminar, 10 July 1980

Opsteegh, J. D. and H. M. Van den Dool, 1980: Seasonal differences in the stationary response of a linearized primitive equation model: Prospects for long-range weather forecasting? Ms. 44 pp.

Pedlosky, J. and C. Frenzel, 1980: Chaotic and periodic behavior of finite amplitude baroclinic waves. J. Atmos. Sci., 37, 1177-1196

Saltzman, B. 1970: Large scale atmospheric energetics in the wave number domain. Rev. Geoph. and Space Phys., 8, 289-302

---------- 1965: On the theory of winter-average perturbations in the troposphere. Mon. Wea. Rev., 93, 195-211

Smagorinsky, J. 1953: The dynamical influence of large scale heat sources and sinks on the quasistationary mean motions of the atmosphere. Quart. J. Roy. Meteor. Soc.

Somerville, R. C. J. 1980: Tropical influences in the predictability of ultralong waves. J. Atmos. Sci., 37, 1141-1156

Tung, K. K., and R. S. Lindzen, 1979: A theory of stationary long waves, part I: A simple theory of blocking. Mon. Wea. Rev., 107, 714-734

Van Loon, H., R. L. Jenne, and K. Labitzke, 1973: Zonal harmonic standing waves. J. Geoph. Res., 78, 4463-4471

Veronis, G., 1963: An analysis of wind-driven ocean circulation with a limited number of Fourier components. J. Atmos. Sci., 20, 577-593

Vickroy, J. G. and J. A. Dutton, 1979: Bifurcation and catastrophe in a simple, forced dissipative, quasi-geostrophic flow. J. Atmos. Sci., 36, 42-52

Wallace, J. M. 1978: Maintenance of the zonally averaged circulation: A Eulerian Perspective; A Lagrangian View. The General Circulation: Theory, Modeling and Observations. NCAR, pp 15-39

---------- 1980: NASA-GSFC seminar, 26 June 1980

Webster, P. J. 1972: Response of the tropical atmosphere to local, steady forcing. Mon. Wea. Rev., 100, 518-541

Additional References

Blackmon, M.L. and J. M. Wallace, N-C. Lau and S. L. Mullen, 1977: An Observational study of the northern hemisphere wintertime circulation. J. Atmos. Sci., 34, 1040-1053

Egger, J., 1978: Dynamics of blocking highs. J. Atmos. Sci., 35, 1788-1801.

Lau, N-C, 1979: The structure and energetics of transient disturbances in the northern hempsphere wintertime circulation. J. Atmos. Sci., 36, 982-995

Merilees, P. E., 1968: The equations of motion in spectral form. J. Atmos. Sci., 25, 736-743

Platzman, G. W., 1960: The spectral form of the verticity equation. Jour. Met., 17, 635-644

Faller, A. J. and P. C. Mignerey, 1980. Preliminary laboratory studies of nonlinear Rossby-wave patterns with two mountain ridges. Tech. Note BN-949, Institute for Physical Science and Technology. University of Maryland, 23 pp.

Van den Dool, H. M., 1980: On the role of cloud amount in an energy balance model of the earth's climate. J. Atmos. Sci., 37, 939-946

Cess, R. D., 1976: Climate Change: An appraisal of atmospheric feedback mechanisms employing zonal climatology. J. Atmos. Sci., 33, 1831-1843

Trevisan, A. and H. Buzzi, 1980: Stationary response of barotropic weakly nonlinear Rossby waves to quasi-resonant orographic forcing. J. Atmos. Sci., 37, 947-957

Schneider, S. H., W. M. Washington, and R. M. Chervin, 1978: Cloudiness and climatic feedback mechanism: Effects on cloud amounts of prescribed global and regional surface temperature changes in the NCAR GCM. J. Atmos. Sci., 35, 2207-2221

Wetherald, R. T. and S. Manabe, 1980: Cloud cover and climate sensitivity. J. Atmos. Sci., 37, 1485-1510.

Saltzman, B. and A. D. Vernekar, 1968: A parameterization of the large-scale transient eddy flux of relative angular momentum. Mon. Wea. Rev., 96, 854-857

Stone, P. H. 1974: The meridional variation of heat fluxes by baroclinic waves and their parameterization. J. Atmos. Sci., 31, 444-456

Yorke, J. A. and E. D. York, 1979: Metastable chaos: The transition to sustained chaotic behavior in the model of Lorenz. J. Stat. Phys., 31, 263-277

Kaplan, J. L. and J. A. Yorke, 1979: Preturbulence: A regime observed in a fluid flow model of Lorenz. Commun. Math. Phys., 67, 93-108

Chow, S. N., J. Mallet-Paret and J. A. Yorke, 1978: Finding zeros of maps: Homotopy methods that are constructive with probability one. Math. Comp., 32, 887-899

----------, 1979. A homotopy method for locating all zeros of a system of polynomials. Conf. Proc. on Functional Differential Equations and the Approximation of Fixed Points. Springer Lecture Notes in Math., No. 730, 228-237

VIII. A Simulation of the January Standing Wave Pattern Including the Effects of Transient Eddies

by

J. D. Opsteegh

A. D. Vernekar

Abstract

A steady-state linear, two-level primitive equation model is used to simulate the January standing wave pattern as a response to mountain, diabatic and transient eddy effects. The model equations are linearized around an observed zonal mean state which is a function of latitude and pressure. The mountain effect is the vertical velocity field resulting from zonal flow over the surface topography. The diabatic heating is calculated using parameterized forms of the heating processes. The transient eddy effects, that is the flux convergence of momentum and heat by transient eddies, are computed from observations. Separate responses of the model are computed for each of the three forcing functions.

The amplitude of the response to diabatic heating is small compared to observed values. The vertical structure is highly baroclinic. At the upper level, the phase of the waves is approximately in agreement with the observations. The amplitude of the response to mountain forcing is comparable with observations. The wavelength of the response in the Pacific sector is shorter than observed. The vertical structure is equivalent barotropic. The combined response to diabatic heating and mountain forcing is dominated by the contribution from the mountains. The phase shows some agreement with the observations, but the Aleutian low is located too far to the west and an unrealistic high appears to the west of the dateline.

The amplitude of the response to transient eddy effects is comparable to the observations in middle and low latitudes. At high latitudes the amplitudes are much too large. The assumption of linearity is not valid for strong forcing at high latitudes where the zonal wind is very weak. The vertical structure of the response is almost equivalent barotropic.

A comparison of the responses to mountain and transient eddy effects show an interesting phase relationship. The troughs produced by the transient forcing are found in the lee of the troughs produced by the mountains (very close to the ridge) indicating that transient forcing is organized by the mountain effects.

The combined model response to all three forcing functions shows a good agreement with observations except at very high latitudes.

IX. A Numerical Simulation of the Influence of the Hadley and Ferrell Circulation on Forced Stationary Planetary Waves

by

J. D. Opsteegh

ABSTRACT

The influence of the Hadley and Ferrell circulation on planetary waves, resulting from a local heat source in middle latitudes, the subtropics and the tropics is investigated with a linear steady-state primitive equation model. The model has been linearized around the observed zonally averaged January mean state. This mean state includes the mean meridional circulation (MMC). Both simulations with and and without the MMC have been performed.

It is shown that incorporation of the MMC causes a shift in the resonance wavelength towards waves with lower zonal wavenumber. The inclusion of a small amount of friction has a very significant influence on the quasi-resonant waves. However, it appears that the solution is not sensitive to the particular value of the friction coefficient.

As a consequence of tropical heating a strong Walker circulation can be observed with large meridional gradients in zonal momemtum. This means that the advection of zonal momentum with the mean meridional wind must be an important process and therefore the inclusion of the MMC has a significant influence on the tropical Walker circulation. However, the remote response at middle and high latitudes is only slightly damped and the phase of the mid-latitude planetary waves does not change.

Heating in the sub-tropics generates a strong jet in the tropics. However the structure of this jet is completely different from a Walker ciruclation. It is much more geostrophically tied to the pressure pattern. The Hadley circulation has again a large influence on the strength and position of this jet. But in addition, also the mid-latitude pressure pattern changes significantly.

X. Infrared Radiative Transfer Through A Regular Array of Cuboidal Clouds

by

Harshvardhan

A. INTRODUCTION

There is a need for an adequate radiative parameterization of clouds in climate and general circulation models. To date, all models have utilized plane parallel theory to construct parameterization schemes although a significant portion of the total cloud field is broken. The particular case of monochromatic radiative transfer through isolated cuboidal clouds has been studied in both solar and infrared wavelenths (McKee and Cox, 1974; Davies, 1978; Liou and Ou, 1979, and others). However, in any broken cloud field, each element can not be considered independently as there is cloud-cloud interaction and for incident solar radiation, there may be partial shading of neighboring cloud elements. Ellingson and Kolczynski (1980) have used the technique of Avaste (1969) to compute heating rates in the atmosphere in the presence of an array of black cylindrical clouds.

The present study considers a regular array of identical cuboidal clouds, as in Aida (1977), overlying a non-reflecting surface. Only infrared radiative transfer is considered and the theory of transmission through the array and emission from the cloud field is first developed for black isothermal clouds. The work is then extended to 10μm radiation interacting with a cloud field having prescribed radiative properties. For this, the two stream solution to the isolated cloud problem (Harshvardhan et al., 1980) is used in conjunction with the black cloud results. Computations are made for both fluxes and radiances as a function of the cloud fraction.

B RADIATIVE TRANSFER THROUGH A BLACK ARRAY

Consider an idealized broken cloud field in the form of an extended regular array of cuboids. A portion of this array is illustrated in Fig. 1, from which it follows that the area of the top and bottom face is $A_0 = s^2$ and of each side face, $A_1 = sz^*$. We define the aspect ratio of each element as

$$a = \frac{z^*}{s} = \frac{A_1}{A_0} \tag{1}$$

If the spacing between each element is equal in the x- and y- directions, then the fraction of the field covered by clouds when viewed normally, the cloud fraction, is

$$f = \left(\frac{s}{s+d}\right)^2 \tag{2}$$

For an isothermal cuboid, the monochromatic power emitted by the top face is $\pi B_0 A_0$ and by each side face, $\pi B_0 A_1$ where $B_0(T_0,\lambda)$ is the Planck function. Half the energy emitted by the side faces escapes to space when the cloud is isolated. When the cloud is embedded in a field as in Fig. 1, a fraction, F, of the energy diffusely emitted by each side face is intercepted by the faces of neighboring clouds. In this case, it can be shown that the total power emitted to space by each isothermal cuboid is

$$P = \pi B_0 A_0 \left[1 + 2a\ (1-F)\right] \tag{3}$$

We define the power ratio analogous to emittance in plane parallel theory as

$$p = \frac{P}{\pi B_0 A_0} = 1 + 2a\ (1-F) \tag{4}$$

We also define the effective emittance of a broken cloud array as the power emitted by a region containing the array in the absence of ground emission to the power that would be emitted by the region if it were

entirely covered by a black surface at the same temperature. If there are N identical clouds of tops A_0 as in the present model, then it is evident that the effective emittance is

$$E = \frac{NP}{\pi B_0 A_g} = fp \tag{5}$$

because $f = NA_0/A_g$, where A_g is the total area of the region. The <u>effective transmittance</u> through an array of black clouds is given by energy balance,

$$T = 1-E \tag{6}$$

Thus, the power emitted to space from a broken cloud array at T_0 over a black ground at temperature, T_1, is

$$P_{out} = \pi B_0 A_g E + \pi B_1 A_g T \tag{7}$$

and the flux per unit area of the field is given by

$$M = \frac{P_{out}}{A_g} = \pi B_0 E + \pi B_1 T \tag{8}$$

The above equation is similar to that obtained by the plane parallel theory with E playing the role of the cloud fraction. We therefore introduce the concept of effective cloud fraction, $f_e = E$, such that

$$M = \pi B_0 f_e + \pi B_1 (1-f_e) \tag{9}$$

1. <u>Effective Cloud Fraction</u>

The computation of f_e essentially involves the computation of F as they are related through eqs. (4) and (5). Alternately f_e may be obtained by measuring the transmission of diffuse light through an opaque array. We have attempted both methods, the former by using the theory of angle or configuration factors (Sparrow and Cess, 1978) and the latter by setting up an array of black blocks on a light table and measuring the flux with a Tektronix Model J 16 digital photometer with a cosine corrected remote illuminance probe. The probe was moved around and the mean of a number of readings was used to compute f_e for each configuration. The theory is expected

to give good results as long as shading is not too serious a problem but as f increases it becomes increasingly difficult to estimate F. The results are given in Fig. 2 with a fit to the data and theory given by

$$f_e = \frac{[1+2a(1+0.15f)]f}{1+2af(1+0.15f)} \qquad (10)$$

The curves follow the general pattern of the results presented in Ohvril and Epik (1978) and Ellingson and Kolczynski (1980). It may be noted that as $f \to 0$, $f_e \to (1+2a)f$, which is the correct limit for an isolated cuboid.

2. Fluxes

A consequence of the finite nature of each cloud in the array is to increase the effective cloud fraction because f_e is always greater than f. This implies that energy loss to space from a broken cloud array is less than that computed using the cloud fraction without considering the sides of the clouds. The effective black body emission temperature of a broken cloud array at 255°K overlying a black ground at 290°K is shown in Fig. 3. The curve marked a = 0 is the flat plate or plane parallel case. It is evident that errors of 5° - 10°K can be made for clouds of aspect ratio unity, which is a common value for fair weather cumulus.

Furthermore, there is a change in the cooling rate across the cloud layer because of the radiation intercepted by the sides of the cloud. For a black isothermal cloud in a non-participating atmosphere, it can be shown that

$$\frac{\left(\frac{\Delta M}{\Delta z}\right)_{\text{finite}}}{\left(\frac{\Delta M}{\Delta z}\right)_{\text{infinite}}} = \frac{f_e}{f} \qquad (11)$$

Thus, the cooling rate in the atmospheric window could be two to five times that obtained by the flat plate assumption.

3. Radiances

If the array is composed of black isothermal blocks, the radiance in any direction depends on the field of view obscured by the clouds. When viewed from on top, only the cloud fraction obscures the ground, whereas from any lower observation angle, the sides of the cloud also obscure the ground. This effect is shown in Fig. 4 in which the radiance at $\phi = 0^{o}$ for an isothermal regular array of cuboids of aspect ratio unity is given as a function of zenith angle. The clouds are again at 255^{o}K while the ground is at 290^{o}K. A plot of the brightness temperature when $\phi = 45^{o}$ is also shown for f = 0.1 and 0.2 illustrating the effect of viewing direction. It is seen that the radiance drops off rapidly as more of the clouds and less ground is visible. This suggests that the brightness temperature measured by a satellite instrument can not be related to the cloud top temperature for broken cloud fields without considering the geometry of the array and the viewing angle.

C. MONOCHROMATIC RADIATIVE TRANSFER THROUGH A NON-BLACK ARRAY

Let us now consider a regular cloud array as in Fig. 1 but relax the assumption that the cloud faces are black emitters. We shall consider 10μm radiation and assume the clouds to be water droplets with a C1 size distribution. Furthermore, the clouds are isothermal and the ground is non-reflecting. We shall try and use the results obtained for the black array to solve for fluxes and radiances.

1. Isolated Cloud

The radiation field in an isolated cuboidal cloud has already been obtained using the two stream approximation by Harshvardhan et al., 1980. It is sufficient to note here that fluxes leaving the faces of a cuboid may be expressed in terms of a function, L_0, which is obtained from the solution of a diffusion type equation. If the flux leaving the face is designated M, then at the $X = \frac{s}{2}$ face, $M = M(y,z)$ and so on. We can also obtain the mean flux leaving each face, $\bar{M}$. If the cuboid has equal sides, s, then it is obvious that $(\bar{M})_{X=\frac{s}{2}} = (\bar{M})_{y=\frac{s}{2}}$. Using this information we may construct the boundary conditions to solve the array problem.

2. Boundary Conditions

In the isolated cloud problem it is assumed that the side faces see the ground whereas if the cloud is in an array, the side faces receive flux from neighboring clouds as well as the position of the ground that is visible. If the diffuse emittance from the side faces was independent of position, such that $M(y,z) = \bar{M}$, then the boundary condition on the side face can be shown to be

$$(M)_{x=\frac{s}{2}} = F\bar{M} + (1-F)\frac{B_1}{2} \qquad (12)$$

where F is the angle factor between the face in question and all the other faces visible from it, and B_1 is the ground emission.

However, even if we assume the exiting flux to be diffuse we can not assume that it is uniform and the error introduced by eq. (12) will be considerable as the cloud fraction, f, increases. In the limit, f→1, we know that the input to the side face is exactly the output of the neighboring face, point for point. We have therefore chosen to weigh the boundary conditions as follows

$$(\overleftarrow{M})_{x=\frac{s}{2}} = \phi\ (\overleftarrow{M})_{x=-\frac{s}{2}} + (1-\phi)\left[F\bar{M} + (1-F)\ \frac{B_1}{2}\right] \qquad (13)$$

where $\phi=0$ when $f<f^*$

and $\phi = 1 - \dfrac{4(1-\sqrt{f})^2}{f}$ when $f>f^*$

with $f^* = \frac{4}{9}$

The problem can then be solved as for the isolated cloud using the values of F obtained in the previous section. It may be shown that the upward flux from this array is

$$\frac{2a(1-f)(1+0.15f)f}{1+2af(1+0.15f)}\ \vec{M} + fM\uparrow + \frac{(1-f)}{1+2af(1+0.15f)}\ B_1 \qquad (14)$$

where $\vec{M}$ is the flux out of each side face and $M\uparrow$ is the flux out of the top face.

3. Results

Computations have been made for a=1 and the radiative model mentioned earlier for which the single scattering albedo, $\tilde{\omega}$= 0.64 and asymmetry parameter, g = 0.86 at λ= 10μm. Fig. 5 shows the flux escaping to space from a regular array of cubes of optical depths varying from 0.5 to 20. Results are presented as an effective black body temperature and may be compared with the curve marked

a=1 in Fig. 3 to note the departure from the black case. It is evident that an optical depth of 10 or greater may be approximated quite well by black cuboids.

This is shown further in Fig. 6 in which the radiation at $\phi = 0$ is plotted for various cloud fractions for a regular array of cubes of optical depth 10x10x10. The ground and cloud temperatures are as before and the plot may be compared with Fig. 4 which is the black case. For zenith angles less than 60^0, the two plots are very close indicating that finite cloud fields may be approximated by totally opaque diffuse emitters for purposes of modeling the radiative field exiting the array.

D. Summary

Finite cloud fields have been modeled by a regular array of cuboids. It is shown that the role of the sides of the clouds is very important in computing radiative quantities. Using an approximate technique to solve the isolated cloud problems, results have been obtained for radiative transfer through a participating array of cuboids. One conclusion of this study is that clouds may be modeled by black opaque emitters if the optical dimensions exceed 10 on each side, which is true in the infrared for virtually all cloud fields.

REFERENCES

Aida, M., (1977): "Reflection of Solar Radiation from an Array of Cumuli." J. Met. Soc. Japan, 55, 174-181.

Avaste, O. A., (1969): "Method of Calculating the Coverage of the Sky by the Lateral Parts of Cloud Elements". Radiation and Cloudiness, IFA ANESSR, Tartu.

Davies, R., (1978): "The Effect of Finite Geometry on the Three-Dimensional Transfer of Solar Irradiance in Clouds." J. Atmos. Sci., 35, 1712-1725.

Ellingsor R. G., and E. Kolczynski, (1980): "Cumulus Clouds and Infrared Heating of the Atmosphere." Proceedings of the International Radiation Symposium, Fort Collins, CO., 474-476.

Harshvardhan, J. A. Weinman, and R. Davies, (1980): "Infrared Emission from Broken Clouds." Proceedings of the International Radiation Symposium, CO., 494-496.

Liou, K.-N., and S.-C. Ou, (1979): "Infrared Radiative Transfer in Finite Cloud Layers." J. Atmos. Sci., 36, 1985-1996.

McKee, T. B., and S. K. Cox, (1974): "Scattering of Visible Radiation by Finite Clouds." J. Atmos. Sci., 31, 1885-1892.

Ohvril, H. A., and R. S. Epik, (1978): "Variability of Cloudiness and Radiation Field, IFA ANESSR, Tartu.

Sparrow, E. M., and R. D. Cess, (1978): "Radiation Heat Transfer, McGraw Hill, New York, 366 pp.

FIGURE CAPTIONS

1. Schematic showing regular array of cuboids.

2. Effective cloud fraction, f_e, as a function of the cloud fraction, f, for various aspect ratios.

3. Upward flux from array expressed as effective black body temperature for $T_0 = 255^oK$ and $T_1 = 290^oK$. Aspect ratios are marked on individual curves.

4. Radiance vs. zenith angle expressed as brightness temperature for two azimuth angles, $\phi = o^o$ (—) and $\phi = 45^o$ (---); a=1, $T_0 = 255^oK$, $T_1 = 290^oK$. Cloud fractions marked on individual curves.

5. Same as Fig. 3 but for non-black clouds of unit aspect ratio. Radiative properties given in text. Optical depths marked on individual curves.

6. Same as Fig. 4 but for non-black clouds of unit aspect ratio at $\phi=0^o$. Optical dimensions are 10x10x10. Radiative properties given in text.

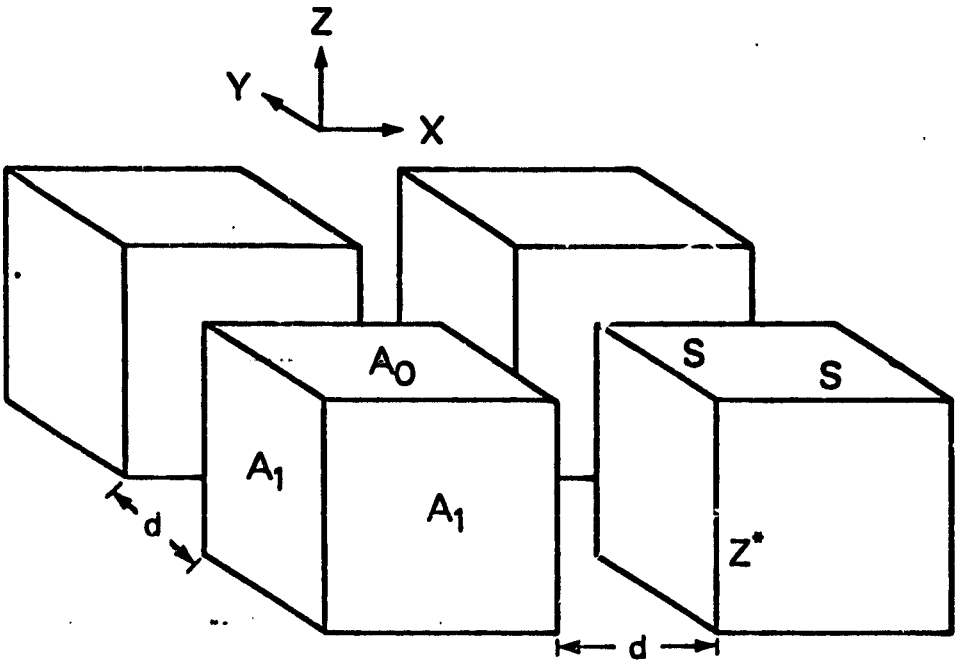

Figure 1

Schematic showing regular array of cuboids.

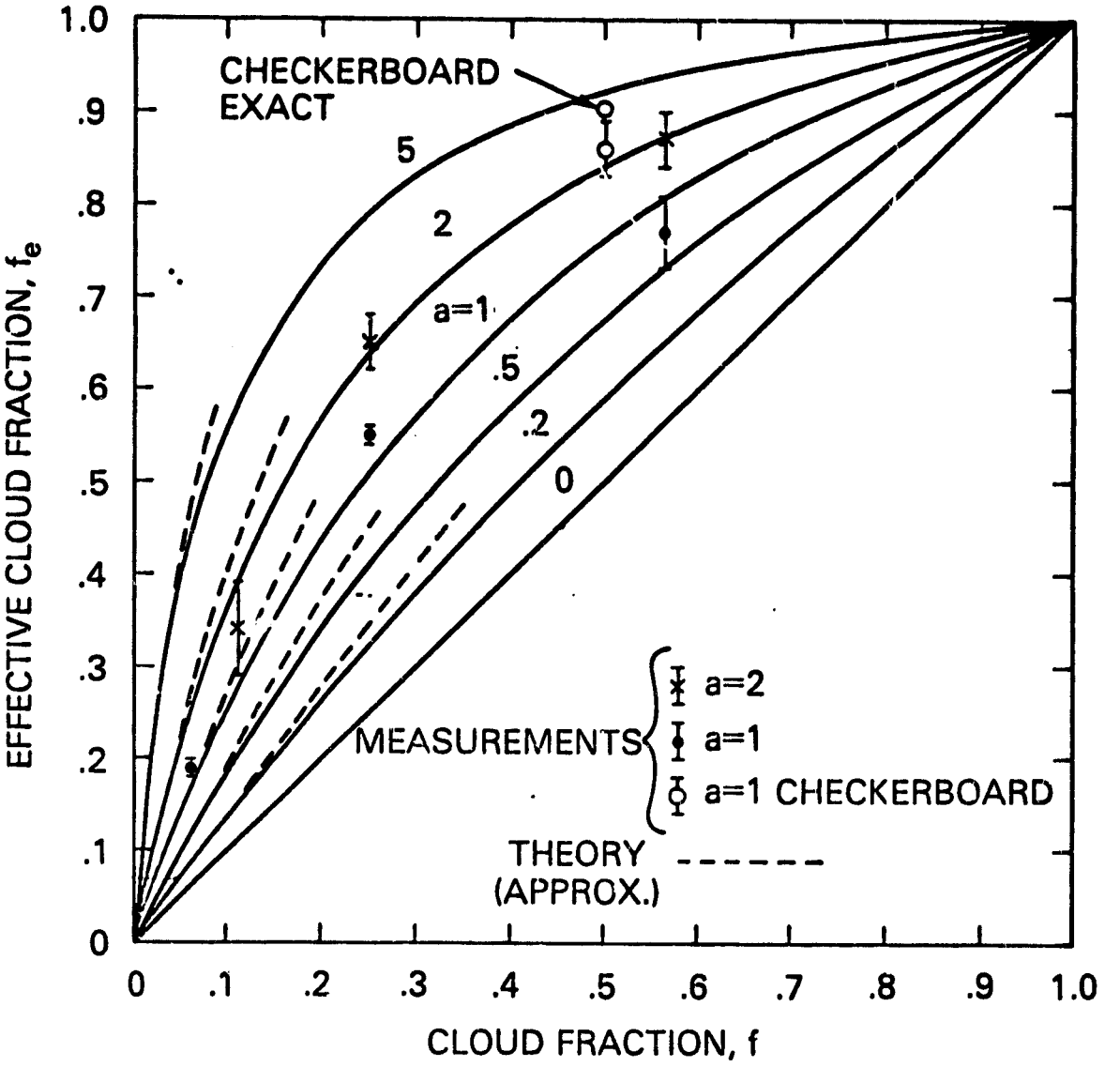

Figure 2

Effective cloud fraction, f_e, as a function of the cloud fraction, f, for various aspect ratios.

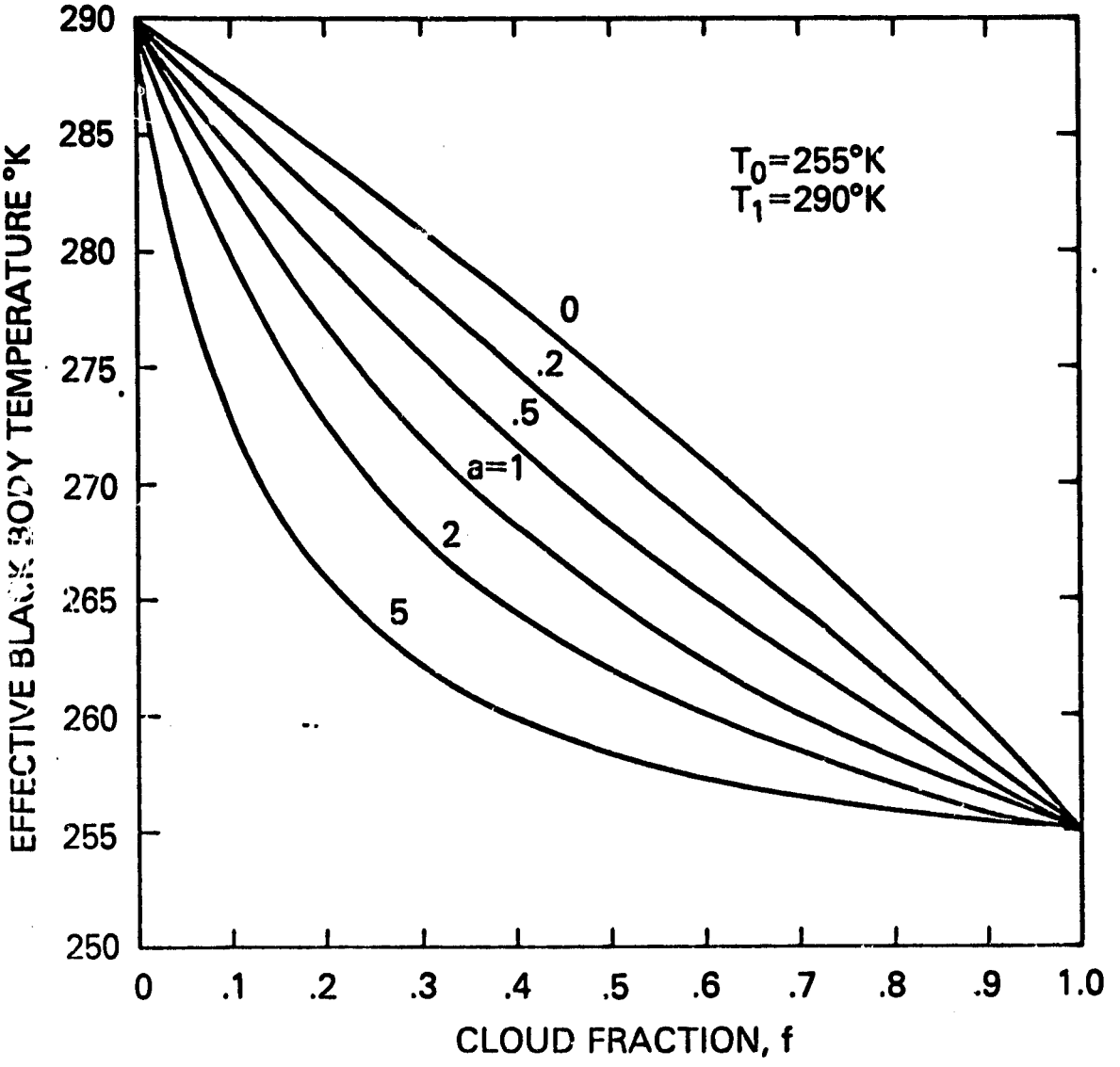

Figure 3

Upward flux from array expressed as effective black body temperature for T_o = 255°K and T_1 = 290°K. Aspect ratios are marked on individual curves.

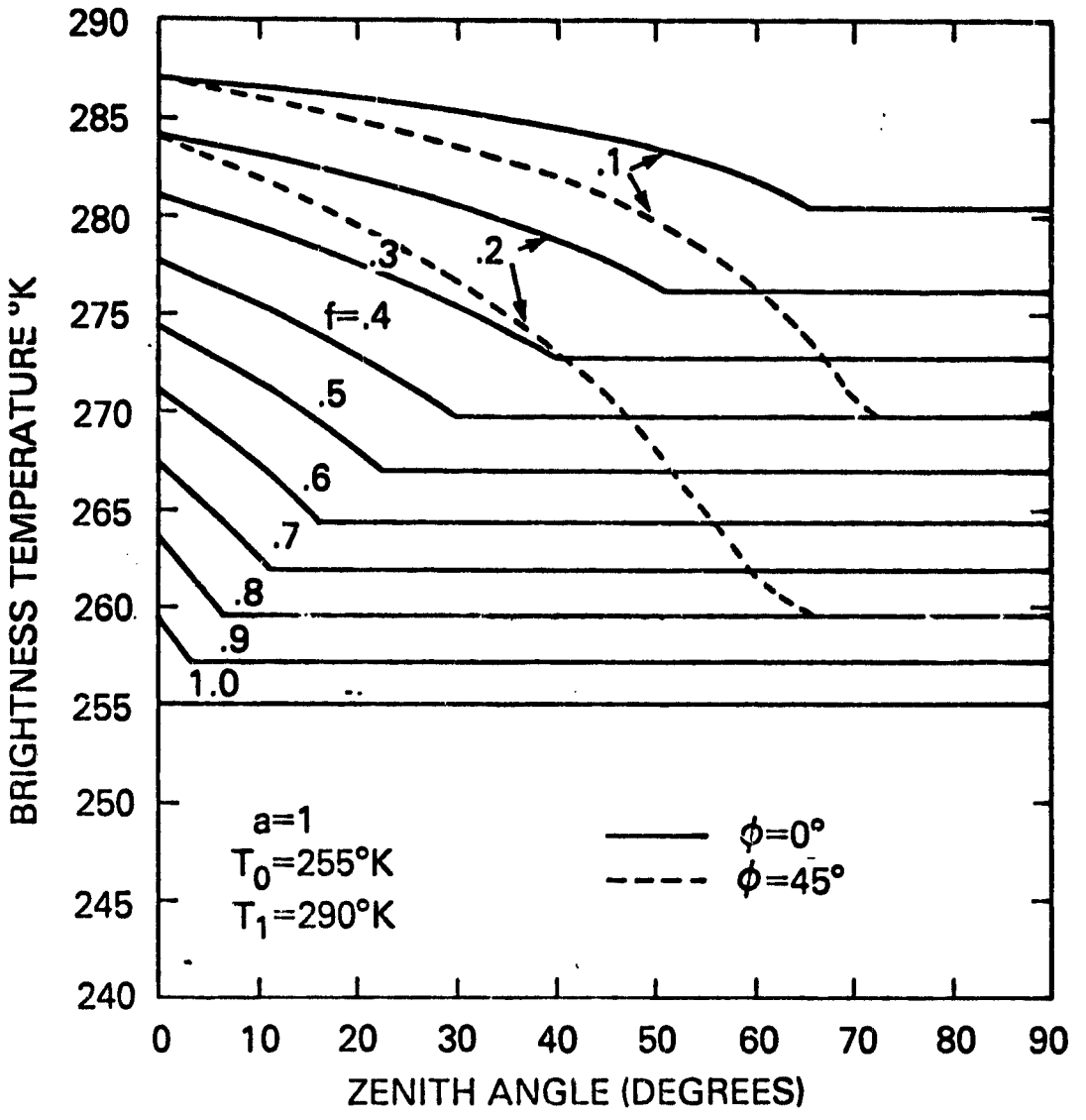

Figure 4

Radiance vs. zenith angle expressed as brightness temperature for two azimuth angles, $\phi = 0^{o}$(—) and $\phi = 45^{o}$(---); a = 1, $T_0 = 255^{o}K$, $T_1 = 290^{o}K$. Cloud fractions marked on individual curves.

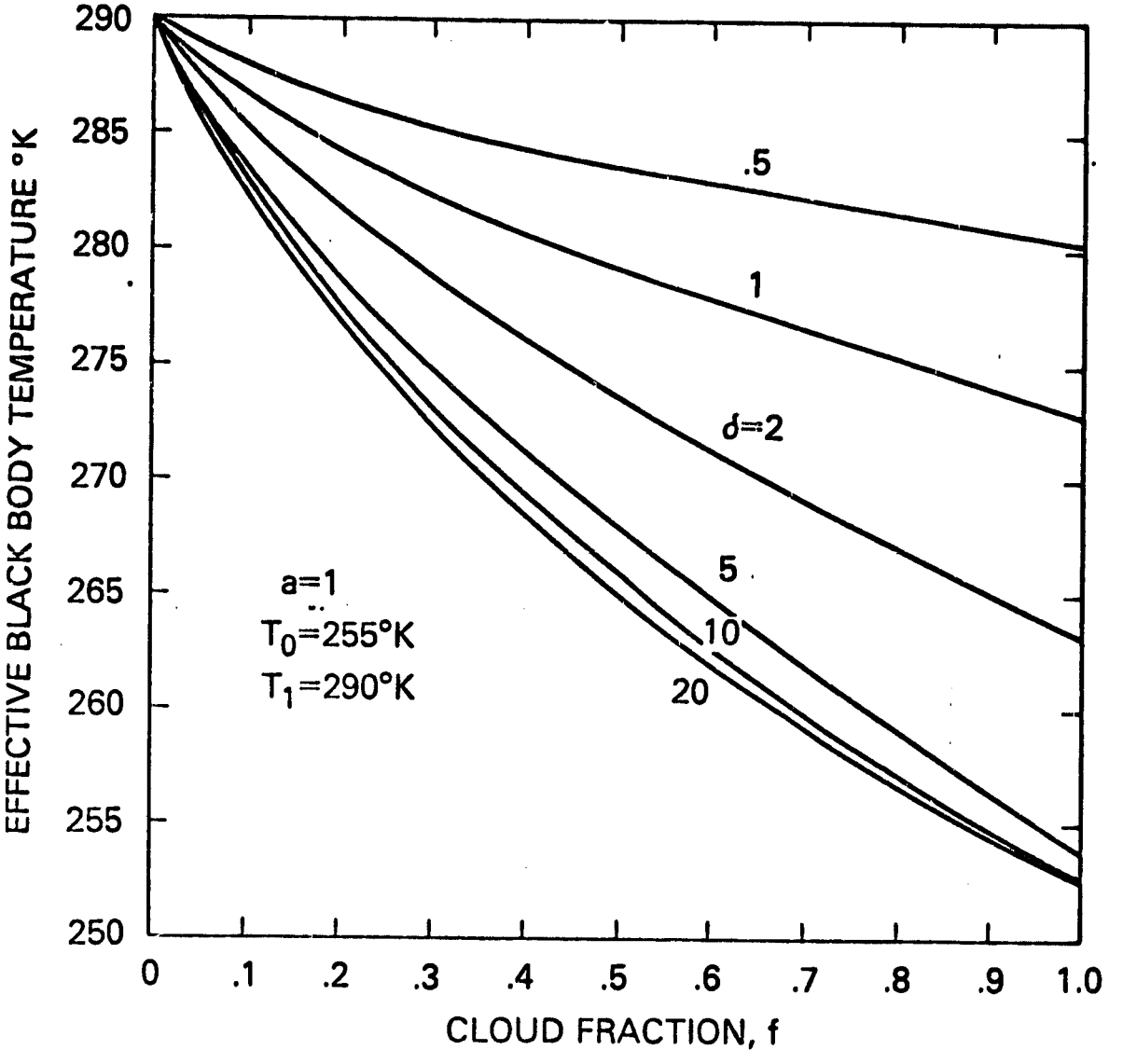

Figure 5

Same as Fig. 3 but for non-black clouds of unit aspect ratio. Radiative properties given in text. Optical depths marked on individual curves.

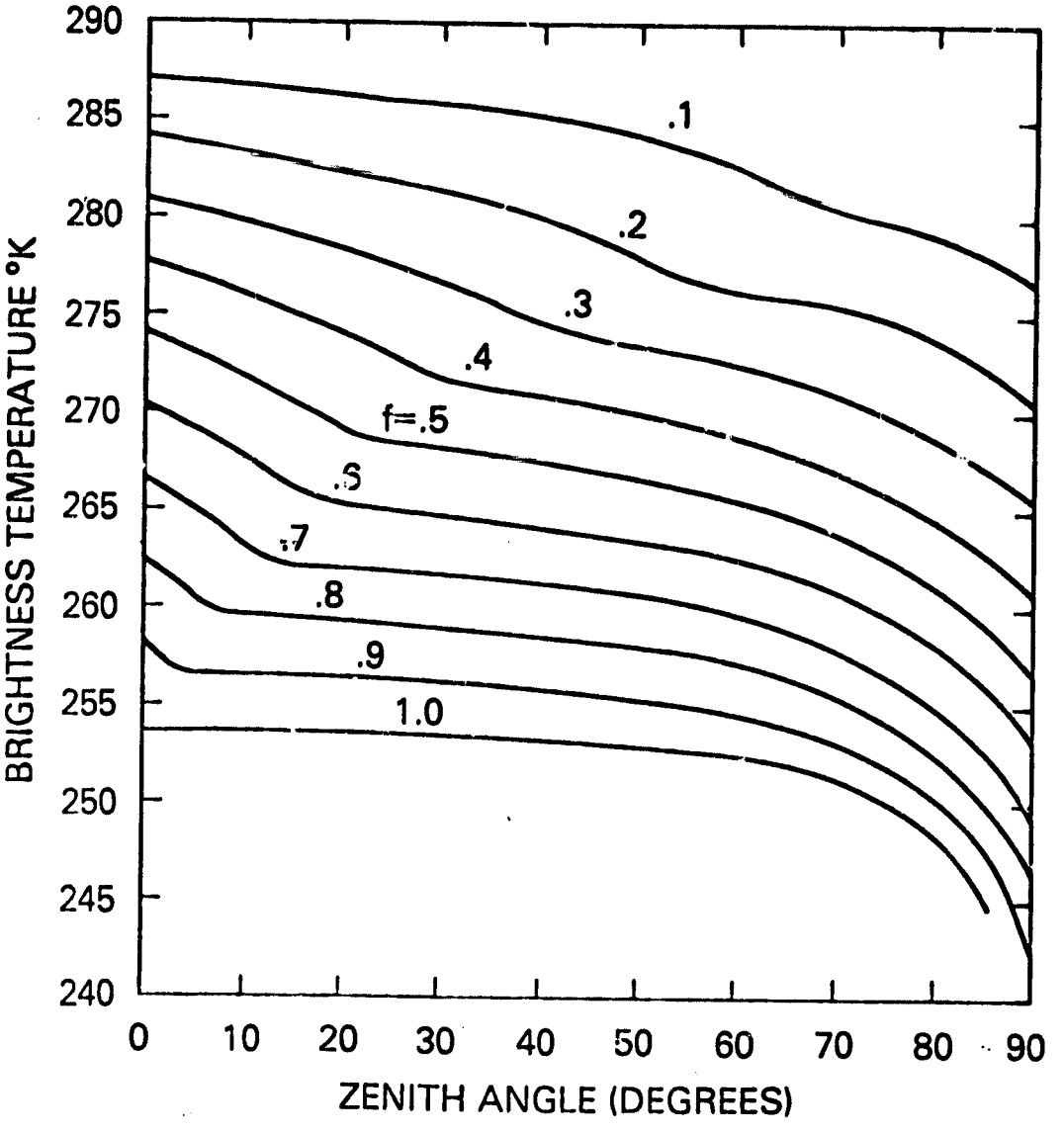

Figure 6

Same as Fig. 4 but for non-black clouds of unit aspect ratio at $\phi = 0^{o}$. Optical dimensions are 10x10x10. Radiative properties given in text.

XI. Retrieving Bouyancy and Pressure Fluctuations from Doppler Radar Observations: A Status Report

by

Tzvi Gal-Chen

Carl E. Hane

1. Introduction

Doppler radars can now measure directly the details of the horizontal wind components. While great uncertainty still exists about the vertical components (Miller, 1978), it appears that under certain circumstances it is also possible to deduce that component as well (Carbone et al., 1980; Clarke et al., 1980; and Gal-Chen, 1979). The radars cannot, however, measure directly the three dimensional structure of thermodynamical variables such as density and pressure fluctuations. These latter variables are nevertheless essential in studies of convective systems. The ideal solution would be to develop instrumentation capable of directly measuring thermodynamical variables with a spatial and time coverage comparable to that of Doppler radars. Unfortunately, the technology for that kind of network does not exist and one must use indirect methods. Recognizing the above cited limitations, several investigators (Hane and Scott, 1978; Leise, 1978; Gal-Chen, 1978; and Chong et al., 1980) have proposed indirect techniques whereby the combined use of the relevant hydrodynamical equations and the observed wind will permit a unique determination of the density and pressure fluctuations.

In this paper the basic methodology for obtaining density and pressure fluctuations is outlined. This is followed by a discussion of possible approaches to verification and error analysis. The last section contains some demonstrations how the method works with real data. Temperature and pressure fluctuation deduced from Doppler radar observations of the boundary layer (Gal-Chen and Kropfli work in progress) are presented. The results of Chong et al. (1980) and Gaillard and Gillet (1980) who used Doppler wind

data to estimate the thermodynamical structure of weak convective cell generated by the passage of a front are also discussed.

2. The Basic Methodology

Because the method has been described in great details elsewhere (Gai-Chen, 1978), only a brief description will be given here. The governing hydrodynamical eqs. for conservation of momentum in x-y-z directions (z-the vertical; x-y-the horizontal directions) are written as:

$$\partial p/\partial x = -\rho_o Du/Dt + f_1 \equiv F \qquad (1)$$

$$\partial p/\partial y = -\rho_o Dv/Dt + f_2 \equiv G \qquad (2)$$

$$\rho g + \partial p/\partial z = -\rho_o Dw/Dt + f_3 \equiv H \qquad (3)$$

where p-pressure fluctuations; ρ-density fluctuations from the basic density-ρ_o; u, v, w-velocities in the x-y-z directions respectively; t-time; f_i $(i = 1, 2, 3)$ - forces other than pressure gradients that can be specified in terms of the observed kinematics (e.g., turbulent friction, coriolis force); g-gravity; Du/Dt, Dv/Dt, Dw/Dt - accelerations in the x-y-z directions respectively. The right hand side of Eqs. (1), (2), and (3) are presumably known or can be calculated from the observed kinematics and are therefore denoted symbolically as F, G, and H.

Inspection of (1) and (2) reveals that the system is overdetermined, it will have a solution if and only if

$$\partial F/\partial y = \partial G/\partial x \qquad (4)$$

If the measurements were error free and the modeling assumptions (e.g., the formulations of turbulent frictions) are exact, then one is assured that (4) is satisfied. In practice (4) is not satisfied and thus (1) and (2) do not have a solution in the usual sense. The system can nevertheless be solved in the least square sense, i.e.,

$$\iint[(\partial p/\partial x - F)^2 + (\partial p/\partial y - G)^2]\, dxdy = \text{Min} \qquad (5)$$

This is a standard variational problem (Courant and Hilbert, 1953, pp. 164-274). The resulting Euler Eq. is a Poisson Eq. for the pressure fluctuations

$$\partial^2 p/\partial x^2 + \partial^2 p/\partial y^2 = \partial F/\partial x + \partial G/\partial y \qquad (6)$$

with the Neumann boundary conditions

$$(\partial p/\partial x)n_x + (\partial p/\partial y)n_y = Fn_x + Gn_y \qquad (7)$$

Here n_x and n_y are the direction cosines of the normal to the boundary. Eq. (6) with the boundary conditions (7) can be solved at each horizontal level where kinematics measurements are available.

Inspection of (7) reveals that if a solution to (6) exists, it is not uniquely determined. Instead, if $p(x, y, z_0)$ is a solution at a particular level $z = z_0$, the $p(x, y, z_0) + c(z_0)$ is also a solution. To remove this spurious component one can subtract from the pressure its horizontal average. Thus, the method allows the estimation of the deviation of the pressure from its horizontal average. The vertical profile of the horizontally averaged pressure need to be estimated by other means (Gal-Chen, 1978).

To deduce the density fluctuations-ρ, one substitutes the calculated pressure fluctuations in Eq. (3). Because only the deviations of the pressure from its horizontal average are given, the same is true for the density; consequently, one modifies the calculated H (Eq. 3) by subtracting from it its horizontal average.

3. Possible Approaches to Verification

a. Statement of the Problem

Because the method outlined in the previous section is indirect, verifications of the derived density and pressure fluctuations are critical. Before discussing verification techniques, it is useful to outline possible error sources. These could be the following:

(1.a) The given kinematics, while qualitatively correct is not accurate enough to allow calculations of derivative of velocity product such as $\partial uw/\partial z$, $\partial vw/\partial z$, $\partial w^2/\partial z$, v^2u, v^2v, v^2w, etc. These quantities are needed in order to estimate F, G, and H (Eqs. (1), (2), and (3)).

(2.a) The scanning rate is not fast enough to capture the temporal evolution. This again, may lead to a significant error in the estimation of F, G, and H (Gal-Chen, 1978).

(3.a) The data is correct, but does not satisfy the particular modeling assumptions. For instance, in the case of a three dimensional cloud model, the turbulent friction parameterization may be wrong and if turbulent friction contribute substantially to the F, G, H estimation (Eqs. (1), (2), and (3)) a serious error may result. Another common source of error is the use of finite differences to estimate spatial and temporal derivatives. At least five points/wavelength are needed to get a fair estimate of the first derivative.

While obviously direct verifications are the most desirable, they are very difficult to come by, particulary, with respect to pressure fluctuations. Consequently, we are concerned in this review on three indirect verifications. They are: numerical simulations; momentum

checking; and time continuity and physical plausibility. These verification methods are only partially objective and a lot remains to be done before one can confidently claim that the technique is verified.

b. Numerical Simulations as a Guide to Verifications

To test the viability of the numerical procedure, and also to get an order of magnitude estimate of the sensitivity of the method to observational errors, numerical models have proven to useful. Gal-Chen (1978) and Hane, Wilhelmson, and Gal-Chen (1981) have used wind data generated by numerical models as a replacement for observations. From this data, they deduced the density and pressure fluctuations and compared them to the "exact" density and pressure. The sensitivity of the method is assessed by inserting simulated errors into the "observed" kinematics, and examining the resulting "error" in the temperature and pressure field. The simulations indicated that errors of $\pm$25 cm/sec for boundary layer studies and $\pm$50 cm/sec for convective storm studies can be tolerated. It was also found that a scanning rate of 2 min/volume for boundary layer observations and 4 min/volume for convective storm studies is acceptable. It must be stressed however, that the numerical simulations do not take into account many other sources of systematic errors such as pulse volume averaging or incorrect lower/upper boundary conditions of the vertical velocity (Carbone et al., 1980). They also by definition cannot evaluate errors which are due to incorrect modeling assumptions.

To simulate boundary layer observations Gal-Chen has used Deardorff (1974a) model. For severe storm simulations, Hane et al. have used the Klemp-Wilhelmson (1978) cloud model. With no errors added the procedure recovers exactly the vertical velocities, buoyancy, and pressure. To test the sensitivity of the procedure to observational errors we have contaminated the data as follows: (a) addition of random noise to the "observed" horizontal velocities ± 15 cm/sec for the boundary layer case and ± 50 cm/sec for the severe storm case. (b) We have taken "observations" which are 2 min apart in the boundary layer case and 4 min apart in the severe storm case. This simulates the fact that radar measurements are non-simultaneous. In both models the actual time step (i.e., interval between successive time integration) is the order of 10 sec. Thus, the models generate data every 10 sec, but we "observed" it every 2 or 4 minutes. The results for the boundary layer case are summarized in Fig. 1 and for the severe storm case in Fig. 2. In Fig. 1 four curves are plotted as a function of z: 1) $\langle|\theta'|\rangle$ here θ' is the potential temperature deviation from the horizontal average, $|\ |$ is a symbol for absolute value and $\langle\ \rangle$ is a symbol for horizontal average; 2) $\langle(|\theta'| - \langle|\theta'|\rangle)^2\rangle^{1/2}$ i.e., the standard deviation associated with $\langle|\theta'|\rangle$; 3) $\langle|\Delta\theta'|\rangle \equiv \langle|\theta' - \theta'_{obs}|\rangle$ where θ'_{obs} is the "observed" potential temperature deviation, $|\Delta\theta'|$ is the "observed" absolute value of the "error"; and 4) $\langle(|\Delta\theta'| - \langle|\Delta\theta'|\rangle)^2\rangle^{1/2}$, the standard deviation of the absolute value of the error. In Fig. 2 we have also plotted the temperature statistics as a function of z. Solid line is the

retrieved temperature, broken line is the standard deviation of the temperature. Short dashed lines (near axis) is the measure of the error (average and standard deviation). From these simulations we have concluded that our procedure may be a viable one.

c. Momentum Checking

It has already been mentioned (section 2) that only under error free conditions the deduced horizontal pressure gradients will exactly balance the right hand side of the horizontal momentum Eqs. (Eqs. (1), (2)); rather they are a least square fit to these equations. The quantity E_r defined by,

$$\frac{\iint[(\partial p/\partial x - F)^2 + (\partial p/\partial y - G)^2]\, dxdy}{\iint[F^2 + G^2]\, dxdy} \equiv E_r, \qquad (8)$$

could be used as a measure of how good the retrieved pressure gradients are. When $E_r = 0$ the fit is perfect. If F, G are generated by white noise then one can show that $E_r = 0.5$. On the other hand, if F, G are perfect (i.e., $\partial F/\partial y = \partial G/\partial x$) but Eq. (6) is solved by second order finite diference approximations rather than exactly, $E_r \approx 0.25$. Overall when $E_r \geq 0.5$ we suspect that the retrieved pressure gradients are virtually useless. It is also worth noting that low E_r values are necessary, but not sufficient indicators of good quality retrieved pressure gradients. For instance one can generate artificially a kinematic flow field which is also potential (i.e., $\nabla \times \vec{u} = 0$) under that condition Eq. (4) is automatically satisfied and consequently the fit is perfect; but incorrect.

Gal-Chen (1978) finds typical E_r values in the order of .1. These values are obtained for simulated boundary layer flows with 100 m horizontal resolutions. The flow fields are perturbed by random white noise of theorder $\pm$15 cm/sec. The scanning rate is of the order of 2 Min/Vol. Gal-Chen and Kropfli, on the other hand, find typical E_r values of the order of .35. The wind data that they have used is based on dual Doppler radar observations of the planetary boundary layer. The spatial resolution is 250 m in the horizontal and 200 m in the vertical. The scanning rate is about 90 Sec/Vol. Table 1 summarizes these results for 5 vertical levels and for selected volume scans. Because time tendencies $\partial/\partial t$ are needed for the calculations of F and G (Eqs. (1) and (2)) one scan is actually a combination of two scans. Thus scan 1 is a combination of scan 1 and 2, etc. Because there is a gap of 100 sec between scan 2 and 3, it is not possible to retrieve the pressure for scan 2. Taking into account the courser resolutions of the radars (compared to the simulated flow) the results are very encouraging. Smaller E_r values could most probably be obtained for more organized convective systems (e.g., severe storms, squall line) provided that one can be assured about the quality of the retrieved vertical velocities.

Clearly, momentum checking is an important simple consistency check that should be used prior to any scientific interpretations of the retrieved pressure.

d. Time Continuity and Physical Plausibility as a Guide for Verification?

This kind of "verification" is necessarily qualitative and subjective and must be pursued with caution and skepticism. In Figs. 3 and 4 we have plotted the pressure fluctuation deviations from its horizontal averages for two scans which are approximately 200 sec apart. The wind data which forms the basis for the pressure retrieval is deduced from a dual Doppler radar measurement taken in September 1978 as part of PROJECT PHEONIX (Kropfli and Hilderbrand, 1980). The height where they are plotted is 500 m above the ground, roughly half the height of the mixed layer for that particular day. The boundary layer at that time seemed to be weakly unstable. Because the larger scale features of wind field have shown some continuity and persistence from scan to scan, it is reasonable to expect the pressure fluctuations to show similar behavior. This is indeed the case. The magnitude of the pressure fluctuations is 0.5 - 2 pascals ($.5 \times 10^{-2}$ - 2×10^{-2} mb) in agreement with values obtained by Deardorff (1974b) for numerically simulated planetary boundary layer flows. The corresponding E_r values (Eq. 8) are 0.33 for the first scan (Fig. 3) and 0.26 for the second scan.

The low E_r values, the time continuity of the pressure field, and the fact that values of the order of 10^{-2} mb are expected for a weakly unstable planetary boundary layer, gives some confidence in the viability of the method. Direct verifications of such low pressure fluctuations is impossible with present technology. On the other hand,

pressure fluctuations play a crucial role in the dynamics of unstable boundary layer (see e.g., Zeman, 1981) and great uncertainty exists about the proper modeling of the pressure terms in the eqs. for the second moments statistics of a turbulent fluid.

As another illustration of the potential of the technique, we present the results of Chong et al. They compute the horizontal gradients of various terms in the vertial Eq. of motion. Fig. 5 presents these components in a horizontal plane which is approximately 2500 m above the ground. The upper part displays the horizontal gradient of the vertical acceleration [$\partial(Dw/Dt)/\partial x$, $\partial(Dw/Dt)/\partial y$]; the middle part is the horizontal gradient of the perturbation potential temperature [$\partial\theta/\partial x$, $\partial\theta/\partial y$]; the lower part is the horizontal gradient of the vertical pressure force [$-\partial/\partial x\ (\partial p/\partial z)$, $-\partial/\partial y\ (\partial p/\partial z)$]. For comparison purposes these gradients are normalized and presented as °K/km. Two distinct relative maxima in the vertical acceleration are apparent, one at the left and one at the right. The left updraft has positive bouyancy associated with it, and a vertical pressure gradient opposite in sign to the bouyancy force. The right updraft has negative bouyancy and again a vertical pressure gradient of a opposite sign. In the former case, the updraft is associated with thermally unstable air which enters the cell from the west, approximately 1500 m above the ground (note the display is for air 2500 m above ground). Thus, in that case, the rising motion is due to thermal instability with pressure gradient as a retarding force. In the latter case, the air enters the cell at an even lower altitude (≈1000 m) where it is thermally stable. In that case the rising

motion is due to pressure gradient forces (probably induced by surface convergence) with bouyancy as a retarding force. The role of the non-hydrostatic pressure as revealed by this study, corresponds closely to that suggested by conceptual models (Cotton, 1975) and seems highly plausible.

Gaillard and Gillet also use dual Doppler radars to study convection forced by the passage of cold fronts. Their retrieved pressure at the lower levels appears to agree qualitatively with surface measurements. It curves out cyclonically at upper levels as is to be expected.

4. Summary and Conclusions

It appears that the combined use of the equations of fluid dynamics and the three dimensional kinematics field derived from multiple Doppler radar observations also permits deduction of pressure and density fluctuations. In order for the method to work several conditions must be satisfied:

(a) high quality wind data that will allow calculations of spatial and temporal first and second derivatives,

(b) sufficiently fast scanning rate to capture the temporal evolutions of the spatial scale resolved by the radars, and

(c) a good fluid dynamical model of the phenomenon under study.

Studies using real data are encouraging. It appears that pressure fluctuations with 30% accuracy can be retrieved. Retrieved temperature and pressure demonstrate the importance of non-hydrostatic pressure gradients in convective dynamics and appear to display continuity and coherence. Firm verification of these results, as well as further technique developments

(particularly in retrievals of vertical velocities) should be pursued with vigor. Almost everything in this vast and difficult problem still remains to be done.

References

Carbone, R. E., R. I. Harris, P. H. Hilderbrand, R. A. Kropfli, L. J. Miller, W. Moninger, R. G. Strauch, R. J. Doviak, K. W. Johnson, S. P. Nelson, P. S. Ray, and M. Gilet, 1980: The multiple Doppler radar workshop, November 1979. Bull. Amer. Meteor. Soc., 61, 1169-1203.

Chong, M., F. Roux, and J. Testud, 1980: A new filtering and interpolating method for processing dual Doppler radar data: Performance in three dimensional wind restitution, ability to derive pressure and temperature fields. Preprints, 19th Conference on Radar Meteorology (Miami Beach), AMS, Boston, pp. 286-293.

Clarke, T. L., F. I. Harris, and C. G. Mohr, 1980: Errors in multiple-Doppler radar-derived wind fields resulting from advection and evolution. Preprints, 19th Conference on Radar Meteorology (Miami Beach), AMS. Boston, pp. 301-306.

Cotton, W. R., 1975: Theoretical cumulus dynamics. Rev. Geophys. Space Phys., 13, 419-448.

Courant, R., and D. Hilbert, 1953: Methods of Mathematical Physics, Vol. 1 Interscience, 561 pp.

Deardorff, J. W., 1974a: Three-dimensional study of the height and mean structure of a heated planetary boundary layer. Bound.-Layer. Meteor., 7, 81-106.

_____, 1974b: Three-dimensional numerical study of turbulence in an entraining mixed layer. Bound.-Layer. Meteor., 7, 199-206.

Gaillard, C., and M. Gilet, 1980: Observation a l'aide d'un systeme de deux radars Doppler d'un tourbillon de moyenne echelle associe a un front froid: Preprints 8th International Conference on Cloud Physics (Clermont-Ferrand France) pp 612-614.

Gal-Chen, T., 1978: A method for the initialization of the anelastic equations: Implications for matching models with observations. Mon. Wea. Rev., 106, 587-606.

_____, 1979: A method for calculating temperature pressure and vertical velocities from Doppler radar observations. Preprints 9th Severe Storms Conference, Kansas City, Amer. Meteor. Soc., 492-496.

Hane, C. E. and B. C. Scott, 1978: Temperature and pressure perturbations within convective clouds derived from detailed air motion information: Preliminary testing. Mon. Wea. Rev., 106, 654-661.

_____, R. B. Wilhelmson, and T. Gal-Chen, 1981: Retrieval of thermodynamic variable within deep convective clouds: experiments in three dimensions, Mon. Wea. Rev. (in press).

Klemp, J. B. and R. B. Wilhelmson, 1978: The simulation of three dimensional convective storm dynamics. J. Atmos. Sci., 35, 1070-1096.

Kropfli, R. A., and P. H. Hildebrand, 1980: Three-dimensional wind measurements in the optically clear planetary boundary layer with dual-Doppler radar. Radio Sci., 15, 3.

Liese, J. A., 1978: Temperature retrieval from dual-Doppler radar wind field data. Preprints, 19th Conference on Radar Meteorology (Atlanta), AMS, Boston, pp. 94-99.

Miller, L. J., 1978: Horizontal airflow and precipitation fall-speed in a convective storm from triple Doppler radar measurements. Preprints, 19th Conference on Radar Meteorology (Atlanta), AMS, Boston, pp. 207-211.

Zeman, O., 1981: Program in the modeling of the planetary boundary layers. In Annual Review of Fluid Dynamics, edited by M. V. Dyke, J. V. Wehausen, and J. L. Lumley, Annual Review, Polo Alto, CA, pp. 253-272.

TABLE CAPTIONS

Table 1: Values of E_r (Eq. 8) for selected scans and vertical levels. It took approximately 100 s to scan a volume. The vertical distance between consecutive scans is 200 m. E_r is a measure of the average relative error of the retrieved pressure gradients.

TABLE 1

LEVEL \ SCAN	1	3	4	5
1	.31	.28	.44	.37
2	.35	.29	.35	.30
3	.33	.26	.38	.32
4	.36	.45	.32	.32
5	.44	.23	.37	.42

FIGURE CAPTIONS

Figure 1. Statistical analysis of the calculated virtual potential temperature deviations $\theta' = \theta - \langle\theta\rangle$ for the boundary layer simulation. Curve A is a vertical profile of $\langle|\theta'|\rangle$; curve B is $\langle(|\theta'| - \langle|\theta'|\rangle)^2\rangle^{1/2}$, i.e., the standard deviation associated with A; curve C is the average "observation error" $\langle|\Delta\theta'|\rangle$; curve D is the standard deviation associated with C.

Figure 2. Same as Figure 1, but for the severe storm simulations. Solid line is for the retrieval temperature, broken line is the standard deviation of the temperature, and short dashed lines (near axis) is the measure of the error.

Figure 3. Pressure deviations (from its horizontal average) for level 3 (≈500 m above the ground) and scan 1 (corresponding to the first 100 s of the experiment). The horizontal resolution is 250 m. The values of the pressure deviations are given in Pascals (1 mb = 100 Pa).

Figure 4. Same as Figure 3, but for scan 3. Scan 3 and scan 1 are approximately 200 s apart. Note that larger scale features do exhibit continuity and persistence from scan to scan.

Figure 5. Horizontal gradient in vertical acceleration of air motion. Horizontal gradient in potential temperature perturbation θ'. Horizontal gradient in vertical pressure force. In order for the three gradients to be comparable, they are all normalized and represented in $^{\circ}K\ km^{-1}$ (Source: Chong et al., 1980)

ORIGINAL PAGE IS
OF POOR QUALITY

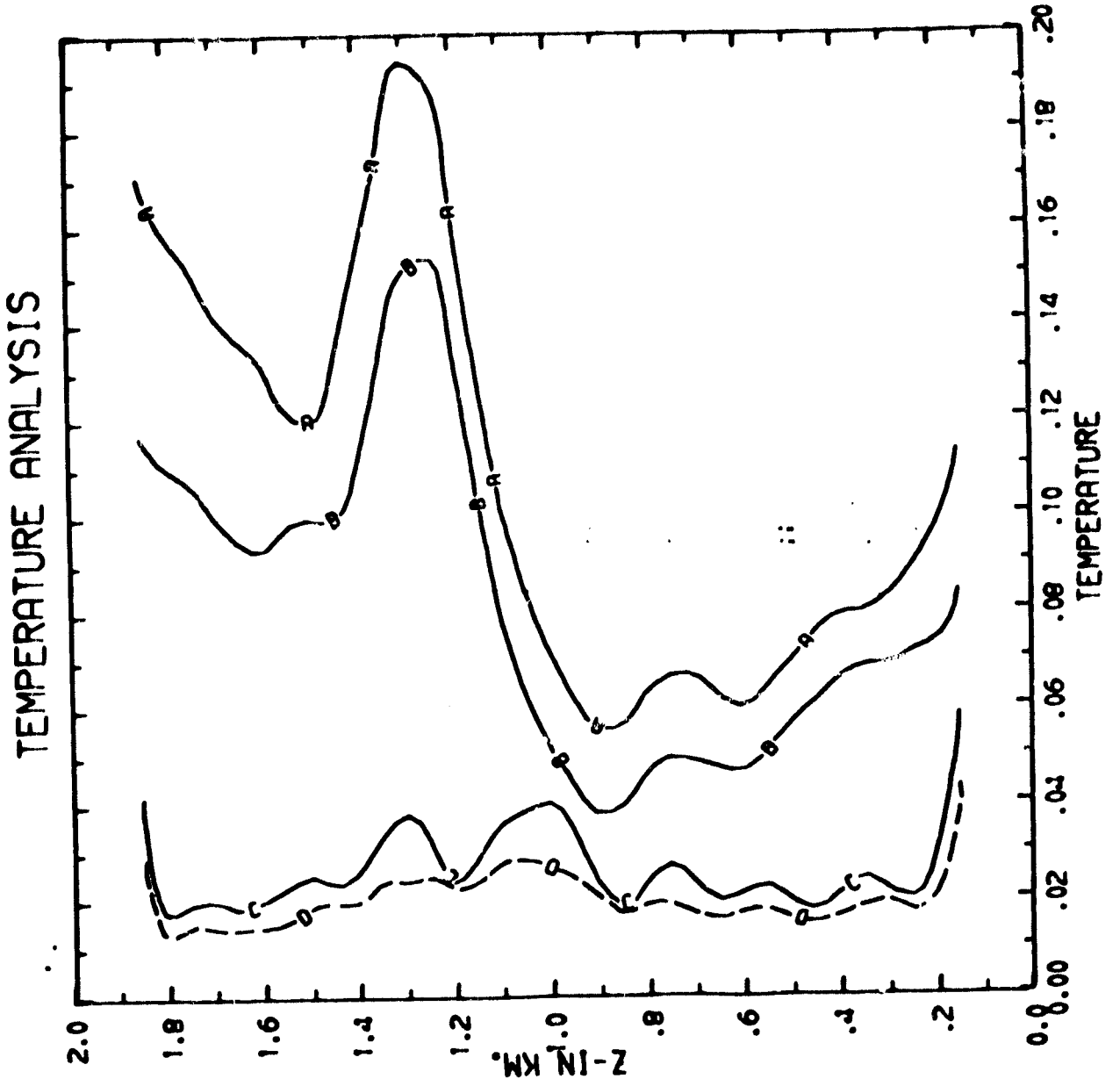

(1)

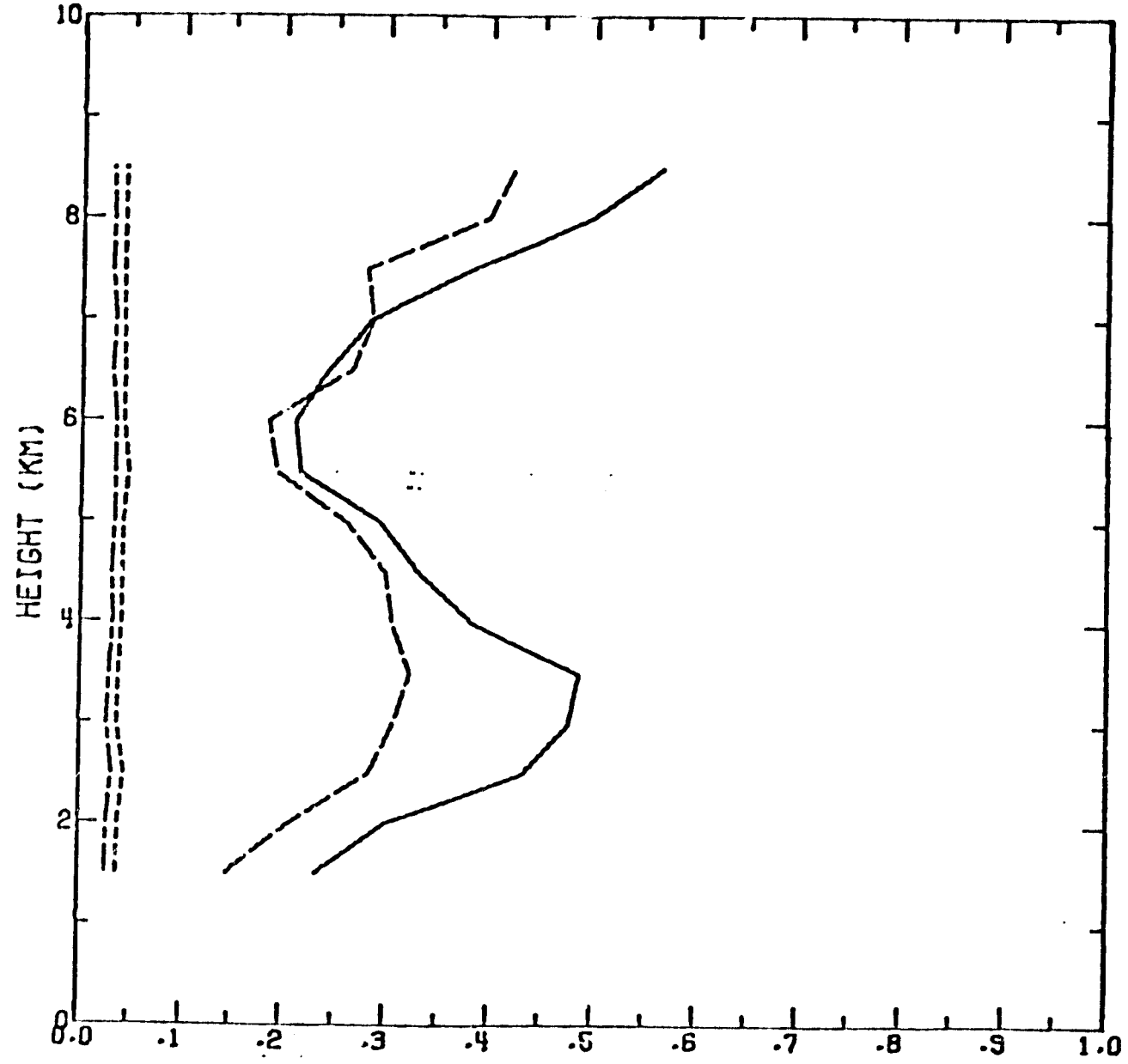
HEIGHT (KM)
10
8
6
4
2
0
0.0
.1
.2
.3
.4
.5
.6
.7
.8
.9
1.0

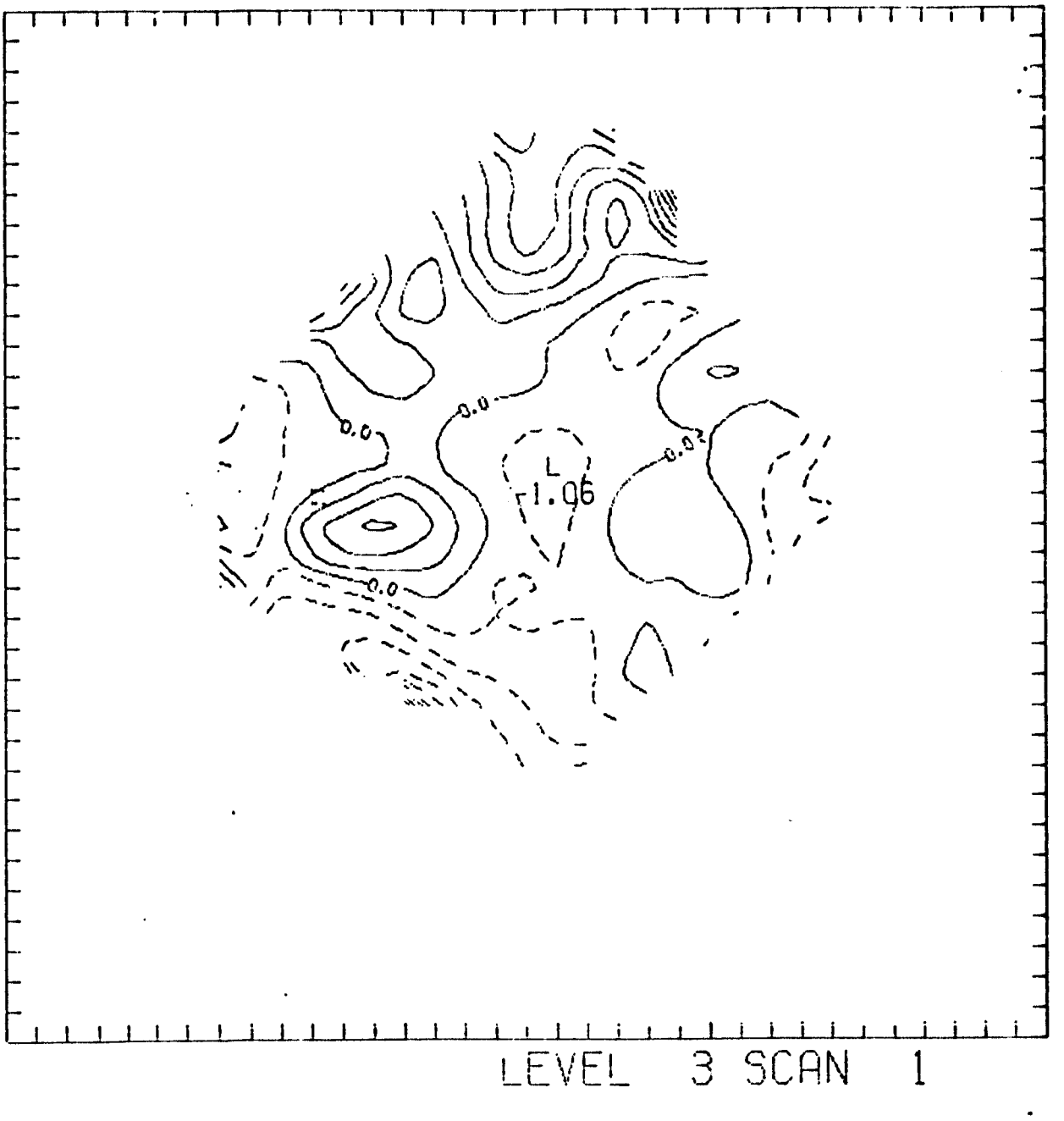

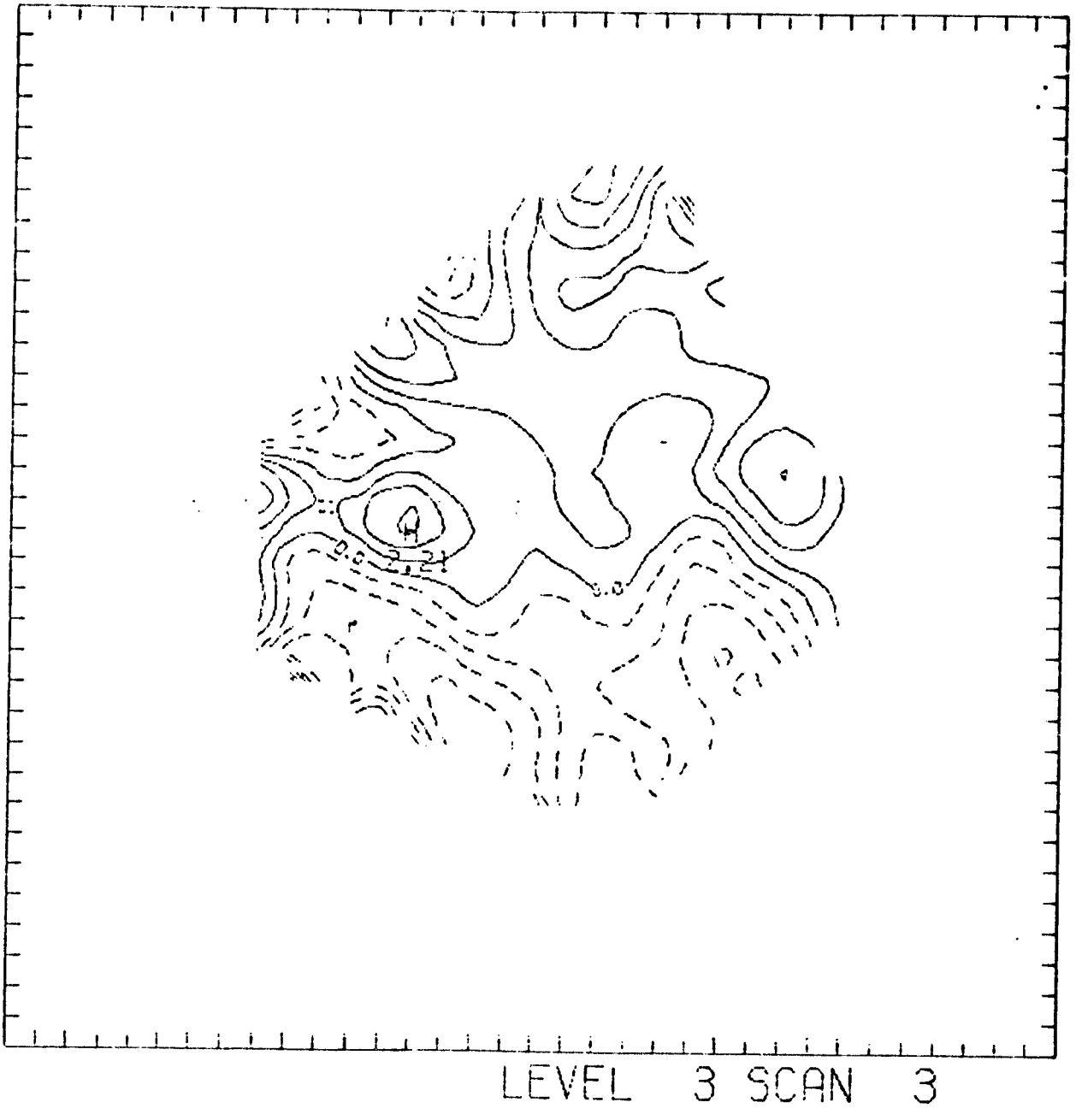

(5)

GRAD HØRIZ ACC VERT
Z1=2KM Z2=3KM
→ 1K/KM

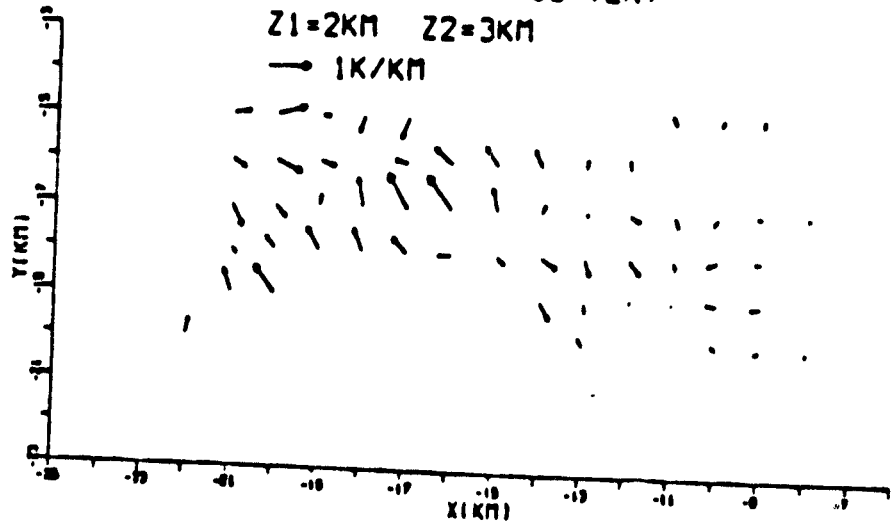

GRAD HØRIZ TEMP PØT
Z1=2KM Z2=3KM
→ 1K/KM

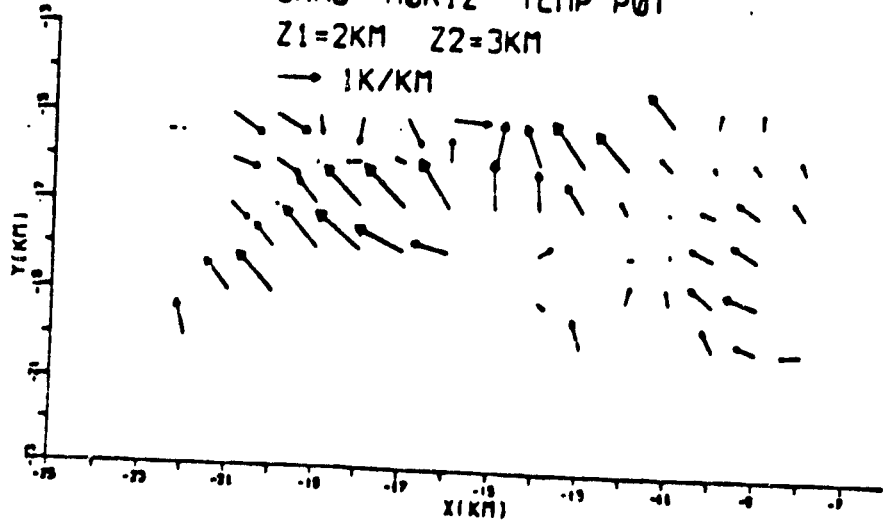

GRAD HØRIZ -DP/DZ
Z1=2KM Z2=3KM
→ 1K/KM